2014

Effect of Thermo-mechanical Processing, Ageing and Compression on Microstructure and Mechanical Properties of near β Ti Alloys Made from Powder

Mansur Ahmed
University of Wollongong, mahmed@uow.edu.au

Effect of Thermo-mechanical Processing, Ageing and Compression on Microstructure and Mechanical Properties of near β Ti Alloys Made from Powder

A thesis submitted to the University of Wollongong as fulfillment for the degree of

Doctor of Philosophy

from

University of Wollongong

by

Mansur Ahmed

B.Sc. (Materials and Metallurgical Engineering)

School of Mechanical, Materials and Mechatronic Engineering

University of Wollongong, Australia

2014

Thesis Certification

I, **Mansur Ahmed**, declare that this thesis, submitted in fulfilment of the requirements for the award of Doctor of Philosophy, in the School of Mechanical, Materials and Mechatronic Engineering, University of Wollongong, is fully my own work unless otherwise stated or referenced. The document has not been submitted for qualifications at any other academic institutions.

Mansur Ahmed

30th August 2014

Acknowledgements

I would like to express my profound indebtedness and heartfelt gratitude to my supervisor Prof. Elena V. Pereloma for her valuable suggestions, constant guidance, encouragement and kind help not only in carrying out the project work and in writing this thesis but also for her support in domestic issues. In spite of her busy schedule, Prof. Elena had time to listen to me and responded back at her earliest possibility whenever I submitted any writing for comments.

I am greatly obliged to my co-supervisor Dr. David Wexler for his time and helpful hand.

Special thanks are given to Dr. Azdiar A. Gazder for his role during early times of my PhD. The involvement of Prof. O.M. Ivasishin and Dr. D.G. Savvakin from the National Academy of Sciences, Ukraine was beneficial to the project and I would like to express my gratitude them for providing the material and their helpful comments. I would also like to acknowledge and thank Associate Prof. Julie M. Cairney and Dr. Tong Li from The University of Sydney for APT work and discussions.

I like to thank Mr. Greg Tillman for his help during metallographic preparation of samples and HF etching. I also wish to thank Mr. Mike Weir, Mr. Andrew Scobie, Mr. Bob De Jong for machining the samples and for assistance with Gleeble tests. Thanks to Dr. Gilberto Casillas for training me on TEM.

Thanks are due to our group members specially, Dr. Ahmed Saleh, Mr. Fayez Alharbi, Mr. Abdullah Al-Shahrani and Dr. Andrii Kostryzhev for their help and encouragement. I would like to express my deepest gratitude to Dr. Liang Chen for informal discussion in our office.

I am very much grateful to my family members who supported me in very crucial times. I would also like to thank other friends for their continuous encouragement.

Finally I wish to record my gratitude to Allah, the most merciful and the most gracious, for giving me the ability to complete the project.

Abstract

The high cost of titanium components restricts wider utilisation of Ti materials. Blended elemental powder metallurgy (BEPM) is a promising cost-effective approach to the manufacturing of Ti products for non-fatigue critical applications. In this series of investigations three near-β Ti alloys (Ti-5Al-5Mo-5V-1Cr-1Fe, Ti-5Al-5Mo-5V-2Cr-1Fe and Ti-10V-3Fe-3Al) produced by BEPM were subjected to different thermo-mechanical processing (TMP) schedules using a Gleeble 3500 simulator. The selected TMP schedules resulted in beneficial reductions in porosity and fragmentation of grain boundary α phase. Selection of specific cooling regimes to room temperature could be used to control the extent of β phase recrystallisation, volume fraction of intragranular α phase and the formation of athermal ω.

To gain a deeper understanding of the resulting phase transformations and of the sequence of microstructural and nanostructural evolution a TMP sample cooled from α+β phase field (800 °C) at 10 Ks^{-1} was investigated using advanced methods of scanning transmission electron microscopy (STEM) coupled with atom probe tomography (APT). Athermal ω and α nuclei were found to be present both separately and interconnected. It was also confirmed by STEM that ω phase was formed via simple atomic displacements in the $<111>_{\beta}$ direction. Compositional fluctuations of Mo were discovered by APT. Possible nucleation sites for α formation were determined to be dislocations, β/ω interfaces and/or regions within ω and Mo-depleted areas.

The evolution of both nanostructure and microstructure during subsequent ageing at 650 °C for 120 s – 28.8 ks after slow heating (0.25 Ks^{-1}) was also investigated by coupling STEM and APT. The early stage of ageing also shows partially transformed ω super cells both individually and in connection with α. It is suggested that α nucleates heterogeneously, preferentially at β/ω interfaces and dislocations. Only a slight compositional difference between β and newly formed α was detected, which supports a displacive-diffusional transformation mechanism. Whereas at shorter ageing times both nucleation and growth of α phase are responsible for the increase in its volume fraction, after 3.6 ks the growth becomes dominant.

Alloying element redistribution between α and β phases during processing (TMP and ageing) were monitored using energy dispersive spectroscopy (EDS) and APT. Consistent with the diffusion-controlled nature of growth of α phase, it was found that the later the stage of α phase formation (coarser α) the more pronounced was the redistribution of alloying elements (e.g. exit of β stabilisers from α phase). The composition of α was found to be affected by the

composition of parent β phase, which varies with the stages of processing. Mo (and sometimes V) pile-up at the α/β interface was especially noticeable after TMP and early stage of ageing.

Mechanical properties of the samples (TMP and aged) were found to be dependent on the α volume, with increases in tensile strength and reductions in ductility with higher α fractions. A significant improvement in mechanical properties was found in the aged after TMP samples compared to the TMP, which can be attributed to the ω-assisted α formation in the aged samples.

The difference in Cr content of the studied alloys (Ti-55521 and Ti-55511) was found to affect the kinetics of α phase formation during isothermal holding in α+β phase field, resulting in a lower amount of α in the higher Cr content alloy.

Deformation behaviour of Ti-10V-3Fe-3Al alloy was determined by room temperature compression testing. It was found that deformation mechanisms in β phase change with varying β phase stability as a function of α phase fraction. With the least stable β phase, in addition to slip, {332}⟨113⟩β deformation twinning along with stress-induced α″ martensite and stress-induced ω were found to be operating deformation mechanisms. With increasing β stability co-existence of {332}⟨113⟩β and {112}⟨111⟩β twinning was found. For samples with higher β stability only {112}⟨111⟩β twinning was noticed while the mechanisms of slip, stress-induced α" and stress-induced ω remain operational. Finally, deformation of samples with maximum β stability was found to occur only by slip.

The findings of the present study have enhanced the understanding of physical metallurgy of near β titanium alloys and will provide a basis for further development of both wrought and cost-effective powder metallurgy route produced alloys.

Declaration on Publications

This thesis includes following chapters that have been prepared as the journal manuscripts.

Chapter 2: M. Ahmed, A.A. Gazder, D.G. Savvakin, O.M. Ivasishin, E.V. Pereloma, "Microstructure evolution and alloying elements distribution between the phases in powder near-β titanium alloys during thermo-mechanical processing, Journal of Materials Science 2012, 47(19), 7013-7025.

Chapter 3: M. Ahmed, D.G. Savvakin, O.M. Ivasishin, E.V. Pereloma, "The effect of cooling rates on the microstructure and mechanical properties of thermo-mechanically processed Ti-Al-Mo-V-Cr-Fe alloys", Materials Science and Engineering A 2013, 576, 167-177.

Chapter 4: M. Ahmed, D.G. Savvakin, O.M. Ivasishin, E.V. Pereloma, " The effect of ageing on microstructure and mechanical properties of powder Ti-5Al-5Mo-5V-1Cr-1Fe alloy", Materials Science and Engineering A 2014, 605, 89-97.

Chapter 5: M. Ahmed, T. Li, G. Casillas, J.M. Cairney, D. Wexler, E.V. Pereloma, "The evolution of microstructure and mechanical properties of Ti-5Al-5Mo-5V-2Cr-1Fe alloy during ageing" under review for publication in Journal of Alloy and Compounds.

Chapter 6: M. Ahmed, D.G. Savvakin, O.M. Ivasishin, E.V. Pereloma, "A comparative study of near-β Ti alloys produced by cost effective blended elemental powder metallurgy technique" in preparation for submission.

Chapter 7: M. Ahmed, D. Wexler, G. Casillas, O.M. Ivasishin, E.V. Pereloma "The influence of β phase stability on deformation mode and compressive mechanical properties of Ti-10V-3Fe-3Al alloy", Acta Materialia, 2015, 84, 124-135.

I, Prof. Elena V. Pereloma, as the principal supervisor declare that the following contributions were made by the candidate, Mr Mansur Ahmed, to each chapter:

Chapter 2: Conducted all the experiments except Gleeble tests and all analysis of data with the help of Dr. Azdiar A. Gazder. Gleeble tests were assisted by Mr. Bob De Jong and Dr. Liang Chen.

Chapters 3, 4 and 6: All the experiments and subsequent analysis were performed by Mansur after training in XRD was received from Dr. Ahmed A. Saleh.

Chapter 5: The experiment and subsequent analysis related to atom probe tomography (APT) were performed by Dr. Tong Li from The University of Sydney. APT data was discussed in joint meetings of all co-authors. High resolution images using Scanning Transmission Electron Microscope (STEM) were acquired and processed by Dr. Gilberto Casillas-Garcia from UOW Electron Microscopy Centre. However, Mansur was responsible for the preparation of APT needles and TEM thin foils used, as well as conducted the conventional TEM after training was received from Drs. Gilberto Casillas and David Wexler. In addition, Mansur was present at STEM sessions and guided Dr. G. Casillas in observations and necessary data acquisition.

Chapter 7: Gleeble tests were performed by Mansur with the assistance of Dr. L. Chen. While STEM was run by Dr. G. Casillas, TEM experiments were carried out by Mansur and co-supervisor Dr. D. Wexler. All the results were analysed by the candidate.

Mansur has reviewed the relevant literature and wrote the first draft of each manuscript. Following the additional data interpretation from the co-authors and their editorial suggestions, Mansur was responsible for submitting each manuscript for publication to the relevant peer-reviewed journals. In all publications, the candidate has responded to the comments raised by editor and reviewer(s) with the assistance of his supervisors.

Mansur Ahmed	Prof Elena V. Pereloma	Dr. David Wexler
29st August 2014	29st August 2014	29st August 2014
Candidate	Principal Supervisor	Co-Supervisor

Contents

List of Tables

Chapter 1

Chapter 2

Chapter 3

Chapter 4

Chapter 5

Chapter 7

List of Figures

Chapter 1

Chapter 2

Chapter 3

Chapter 4

Chapter 5

Chapter 6

Chapter 7

Chapter 1

Introduction

Titanium and its alloys possess superior combination of high specific strength, and corrosion resistance [1]. It is the specific strength (strength-to-weight ratio) that makes titanium so attractive to the aerospace industry where it is most widely used (Fig. 1). Titanium has a density of only 60% of that of steels [1]. On the other hand, the resistance to corrosion has made titanium and its alloys an ideal candidate for use in the chemical, petrochemical industries and marine engineering applications [1, 2]. Additionally, commercially pure titanium and its alloys (with Nb, Zr, and Ta) are non-toxic and are biologically compatible with human tissues and bones [3] which makes them a potential candidate in the biomedical sector as well.

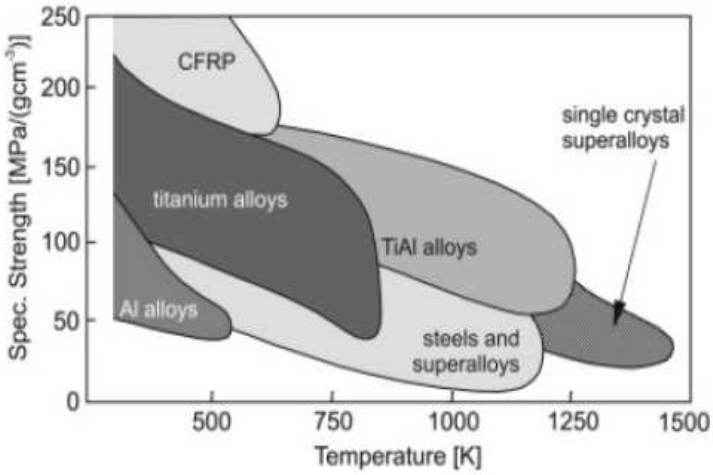

Fig. 1. The specific strength of various structural materials as a function of operating temperature [1].

In spite of the numerous favourable properties of titanium and its alloys, the use of titanium materials has been restricted to limited applications due to their high processing cost. Thus, Ti alloys are mainly used when very high performance is demanded, and as a result, they have found little use compared to steels. In the last few decades researchers have been working on this issue and successfully identified that powder metallurgy is yet to be a commercially well accepted approach, although economically, it is the most attractive method to reduce the cost of titanium alloys production. There are two distinct types of powder metallurgical routes based on the powder used: Pre-alloyed (PA) uses high purity powder and Blended Elemental Powder

Metallurgy (BEPM) uses powder with impurity contents of hydrogen, oxygen etc. However, it is well-established that BEPM is the cheapest way to produce the titanium and titanium alloy products so far [4, 5]. The manufacturing of cost effective titanium alloys allow the expansion of their applications into industries such as the automotive industry, where with increasing fuel prices and environmental concerns, the reduction in weight of vehicles becomes a priority.

In the present study, three near-β titanium alloys (Ti-5Al-5Mo-5V-1Cr-1Fe, Ti-5Al-5Mo-5V-2Cr-1Fe and Ti-10V-3Fe-3Al, wt.%) produced by the cost effective BEPM technique were studied. Ti-5Al-5Mo-5V-1Cr-1Fe alloy is also known as VT22 and is used as aerospace material mostly in Russian aircraft Industries [6, 7] . However, Ti-5Al-5Mo-5V-2Cr-1Fe and Ti-10V-3Fe-3Al alloys are the derivatives of commercial Ti-5Al-5Mo-5V-3Cr and Ti-10V-2Fe-3Al alloys which have been used in aerospace industries to produce landing gear, rotor systems, aero-engines etc. [8]. The capability of attaining high ultimate tensile strength (~1100 MPa) and high cycle fatigue strength (~650 MPa at an R_{ratio}=-1) is the underlying reason for using them in those applications [8]. The Ti-5Al-5Mo-5V-2Cr-1Fe alloy has 2 wt% Cr and 1 wt% Fe instead of 3 wt% Cr and 0.5 wt% Fe in Ti-5Al-5Mo-5V-3Cr, while the concentrations of other alloying elements remained the same. This change allows better densification during sintering without significantly altering the Mo equivalent value, because Fe has the fastest diffusivity of the alloying elements used [9]. Similarly, Ti-10V-3Fe-3Al alloy has 1 wt% more Fe than commercial Ti-10V-2Fe-3Al. Additionally, the segregation of Fe is not occurred which is a significant advantage of PM over the conventional ingot metallurgy technique.

The present work focuses on the microstructure evolution, distribution of alloying elements and mechanical properties arising during the thermo-mechanical processing and ageing. These aspects of near-β titanium alloys are of particular interest as changes in the microstructure and distribution of alloying elements during thermo-mechanical processing affect the end mechanical properties obtained after ageing by influencing the nucleation sites, morphology, size scale and distribution of the α phase. In addition, cold deformation mechanisms will be assessed with respect to the changing of β stability.

1.1. Context of the Body of the Work:

Brief History and uses of Ti-1023, Ti-55511, Ti-5553:

The use of near β alloys is increasing gradually. However, the first application of a β alloy was in the "Lockheed SR 71 Blackbird" in the mid-1960s. About 93% of the aircraft was made of Ti-13V-11Cr-3Mo (B-120VCA) β alloy [8]. In the 1970s, McDonnell Douglas used Ti springs for commercial aircraft fabricated using the same β alloy [8]. But there was a problem of embrittlement under operational stress and at a temperature exceeding 200 °C and with the same alloy. In all aspects, the embrittlement under stress at elevated temperatures is connected with the eutectoid transformation in the Ti- Cr system [6]. As a result, the interest in such alloy had diminished considerably. The development of new generation β titanium alloys was based exclusively on using isomorphous alloying elements e.g. Mo, V, Nb etc. which were applied in the Boeing 777 in the 1990s [8]. Boeing used the Ti-10V-2Fe-3Al alloy for its high strength forging properties in the landing gear and Ti-15V-3Sn-3Cr-3Al alloys for the springs in their aircraft [8]. Unexpectedly, Ti-10V-2Fe-3Al alloy shows some drawbacks e.g., the processing window at the high-strength level is quite narrow and it also suffers from β fleck formation during ingot production [8]. As a solution, Ti-5Al-5Mo-5V-3Cr-0.5Fe was used to replace the Ti-10V-2Fe-3Al alloy in commercial 7E7 aircraft for landing gear application [8]. On the other hand, concurrently Ti-5Al-5Mo-5V-1Cr-1Fe alloy, also known as Russian VT22, had been used by VIAM, the All-Russia Institute of Aviation Materials, to produce landing gear and compressors as this alloy possesses high strength and high weldabililty [8].

The summary of the present state of the scientific literature relevant to near β Ti (especially Ti-55511, Ti-5553 and Ti-1032) alloys and to the present study is as follows:

1.1.1 Effect of Thermo-mechanical processing on the microstructure

During the thermo-mechanical processing of near-β titanium alloys, the phase constituents (α and β) of the microstructure are refined by changing temperature and time. In order to eliminate the influence of the initial microstructure of the as received powder processed alloy, a β phase field solution treatment is performed. The microstructure obtained after β solution treatment consists only grains of β phase. Controlling the β grain size is very important factor as it affects subsequent treatment [10] as well as influences the end mechanical properties after ageing [11]. Lenain *et al*. [10] found in Ti-LCB (Low cost beta) that relatively finer β grain sizes obtained after holding at 810 °C for 600 s enable more α phase to form during subsequent holding α+β phase field whereas relatively coarser β grain sizes obtained after holding at 850 °C for 3.6 ks leads less α phase and a smaller width of α plate (Fig. 2). Indeed, an increase of the β grain size leads to a decrease of the β grain boundary surface area per unit volume and thus offers fewer nucleation sites for the α phase[10].

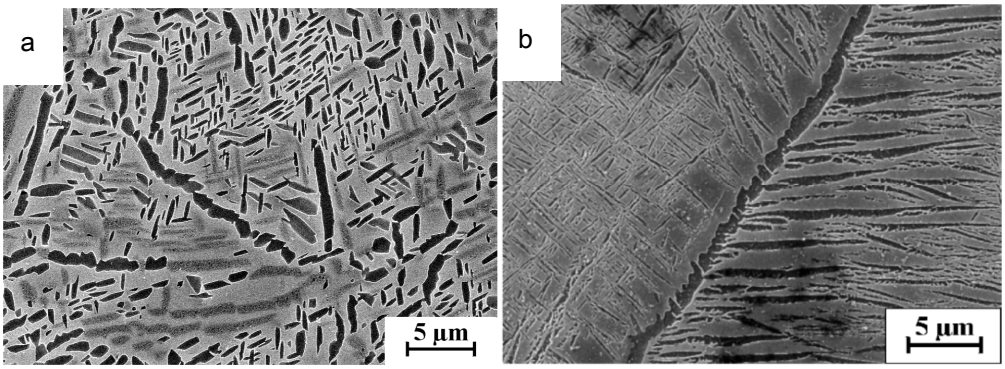

Fig. 2: Microstructures obtained by quenching from 550 °C where β solution treatment was performed (a) at 810 °C for 300s and (b) at 850 °C for 3600 s [10].

In addition, both prolonged exposure at a given temperature and relatively higher temperature at a constant period of time in the β phase field results in coarser β grains [12, 13].

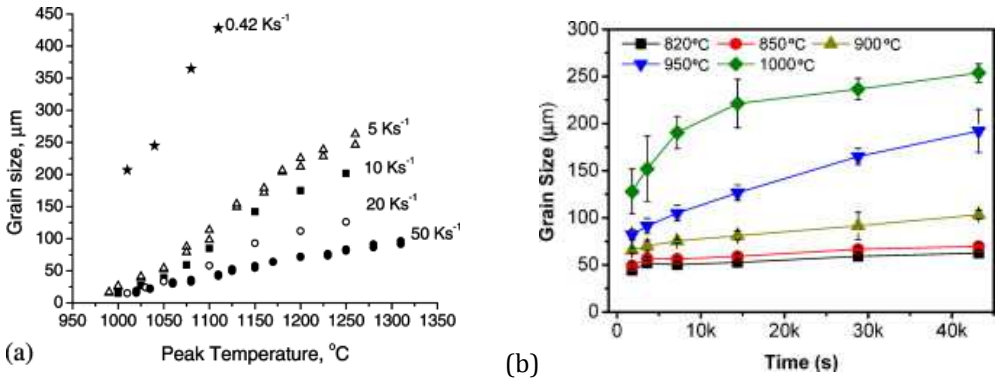

Fig. 3: (a) Measurements of β grain size as a function of peak temperature and heating rate for Ti–6Al–4V (T_β =995 °C) [12]; (b) Variation of β grain size as a function of solution time at different temperatures for Ti–2Al–9.2Mo–2Fe alloy (T_β = 815 °C)[13].

Ivasishin *et al.* [11] have mentioned that near β Ti alloys display more rapid ageing response in the fine-grain condition due to residual defects and/or stresses, which enhance precipitate nucleation and the diffusion of alloying elements.

During sub-transus holding at relatively low temperatures more α phase is obtained than at relatively higher temperatures [14, 15]. On the other hand, at a constant temperature in α+β region, volume fraction of α phase also increases with increasing time [16]. Clement *et al.* [15] observed that with increasing temperature the morphology changed from the acicular α formed at low temperature to globular α phase, as shown in Fig. 4.

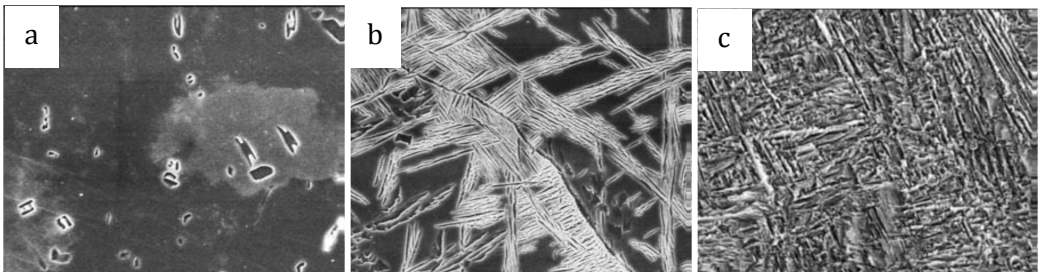

Fig. 4: Morphology of the α phase formed in α+β phase field during holding at 800 °C (a), 700 °C (b) and 500 °C (c) for 3.6 ks in Ti-5333 [15].

Porosity is a common feature in the powder processed materials, and this has significant effects on the mechanical properties. But it has been mentioned that when the porosity level is less than 2% and maximum pore size is small (6 μm), porosity does not affect the tensile mechanical properties [17, 18]. On the other hand, effect of porosity on fatigue properties remains also insignificant provided that the volume of the porosity is less than 1% and the pore size is less than 10 μm [17, 18]. Thus, hot isostatic pressing (HIPping) is performed commonly performed to reduce the porosity during or after the sintering [4, 19]. It has been noticed that when a HIP is performed in the β phase field a higher density product is achieved [20, 21]. However, microstructure after hot deformation consists of deformed β grains with serrated grain boundaries [22]. Table 1 provides some examples of deformation parameters for selected near β Ti alloys in the β phase field.

Table 1: Deformation parameters for several near β alloys hot deformed in the β phase field [22].

Alloy	Temperature range (°C)	β transus temperature (°C)	Strain rate range (s^{-1})
Ti–6Al–4V (Ti–6–4)	1120	995	5×10^{-3}–5
Ti–10V–2Fe–3Al (Ti–10–2–3)	820	800	10^{-3}–10^{-1}
Ti–15V–3Cr–3Sn–3Al (Ti–15–3–3–3)	800–900	760	5×10^{-3}–0.8
Ti–5Al–2Sn–2Zr–4Mo–4Cr (Ti–17)	905–950	885	10^{-3}–10^{0}
Ti–5Al–2Sn–2Cr–4Mo–4Zr–1Fe (Beta-CEZ)	890–1000	890	10^{-2}–10^{-1}

On the other hand, deformation in the two phase field region is performed in Ti alloys to fragment the continuous grain boundary α as the mechanical properties, especially the ductility, greatly depend on it (the presence of continuous grain boundary α) [15, 23]. Deformation temperature is typically T_β – 100 °C or higher, where T_β is the β transus temperature; which conditions the α phase comprises less than 30% [24].

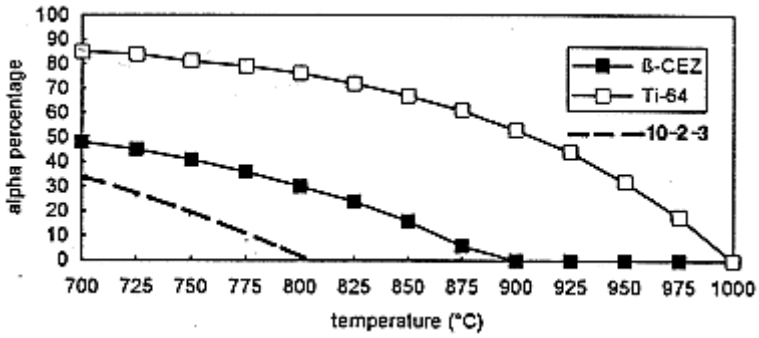

Fig. 5: Variation of α phase volume percentage with temperature[24]

Figure 5 shows the dependency of temperature on the α volume fraction, and can be used to find the appropriate deformation temperature. Table 2 shows the deformation temperature ranges and strain rates of some α+β and near β Ti alloys.

Table 2: Deformation parameters for several *meta*-stable β and β-rich alloys deformed in the α+β phase field [22].

Alloy	Temperature range (°C)	β transus temperature (°C)	Strain rate range (s^{-1})
Ti–6Al–4V (Ti–6–4)	850	995	10^{-3}–10^{-1}
Ti–10V–2Fe–3Al (Ti–10–2–3)	650–790	800	10^{-3}–10^{-1}
Ti–5Al–2Sn–2Zr–4Mo–4Cr (Ti–17)	805–845	885	10^{-3}–10^{0}
Ti–5Al–2Sn–2Cr–4Mo–4Zr–1Fe (Beta-CEZ)	800–850	890	10^{-2}–10^{1}

The presence of α phase has a great influence on microstructure and substructural development during sub-transus deformation [22]. Maeda *et al.* [25] have noticed that α phase is harder than the β phase, and microstructures of α+β can behave as a dispersion of hard particles in a soft matrix. It is mentioned in [26] that strain concentrations develop in the softer β phase surrounding the α phase leading to the formation of small higher misorientation subgrains in comparison to the subgrains formed in the β matrix as the α phase deforms less

than the β phase (Fig. 6). Following sub-boundaries formed in the α phase at higher strains, cusp is developed and β phase penetrates along the α/α sub-boundaries resulting in a more α phase with equiaxed morphology (Fig. 7a). Fig. 7b shows the similar features in the case of Ti-6Al-4V alloy [27]. The matrix phase experiences microstructural changes accompanied by grain elongation and sub-boundaries formation that rises their misorientation continuously; thus forming small recrystallised grains in the vicinity to high angle boundaries surrounded by highly deformed β grain boundaries [22].

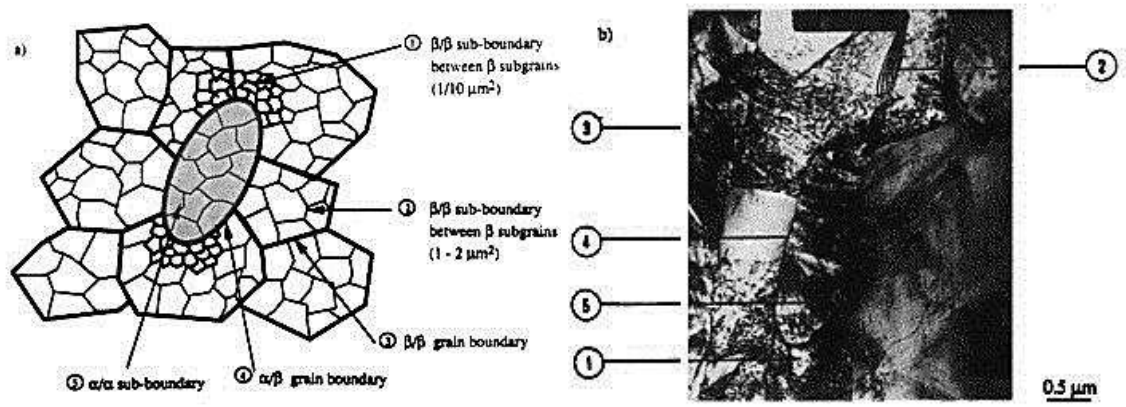

Fig. 6: Schematic and associated TEM image illustrated formation of substructure in the α and β phases during deformation of Ti-5Al-2Sn-2Cr-4Mo-4Zr-1Fe (Beta CEZ) at temperature of 840°C and strain rate of 0.3 s^{-1} [26].

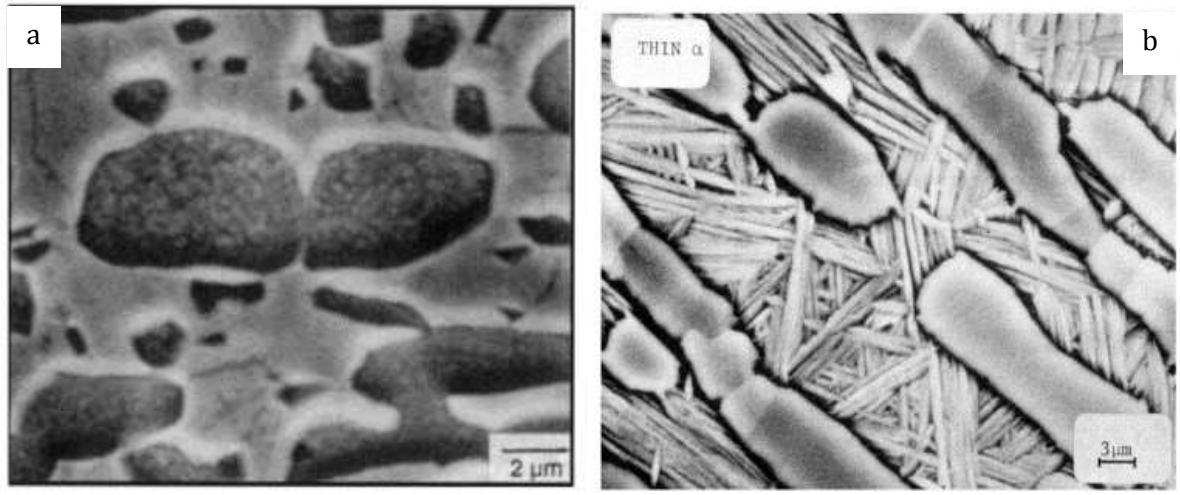

Fig. 7. (a) TEM image showing the formation of cusp and β phase penetration along α/α sub-boundary [28]; (b) Channeling contrast SEM of α plate after 20% deformation in Ti-6Al-4V, followed by annealing at 925°C [27].

Reported investigations describing the influence of cooling rate from the α + β region upon the microstructure appear to be very limited. Jones *et al*. [29] reported the microstructural changes occurred in Ti-5553 alloy after cooling from 800 °C (α+β phase region) using three

different cooling rates (furnace cooling, air cooling and water quenching). It was mentioned that furnace cooling produces more α volume fraction than does air cooled or quenched samples, whereas air cooling and quenching produce approximately the same amounts of α phase.

1.1.2 Effect of ageing on the microstructure and mechanical properties:

In the case of titanium alloys, ageing is a necessary step to increase the final strength of the material by producing fine α particles. The morphologies of α phase were observed to be dependent on the ageing temperature [30]. At low temperatures (~400 °C), fine α lamellae is formed as Widmanstätten basket weave morphology in Ti-10V-2Fe-3Al [30] and Ti-55511 alloys [31]. However, at intermediate temperatures between 400 °C and 650 °C, α precipitates were formed by sympathetic nucleation and are blotchy in nature [30]. At higher temperatures (above 650 °C), a thick grain boundary α is formed along with randomly dispersed intragranular α [30].

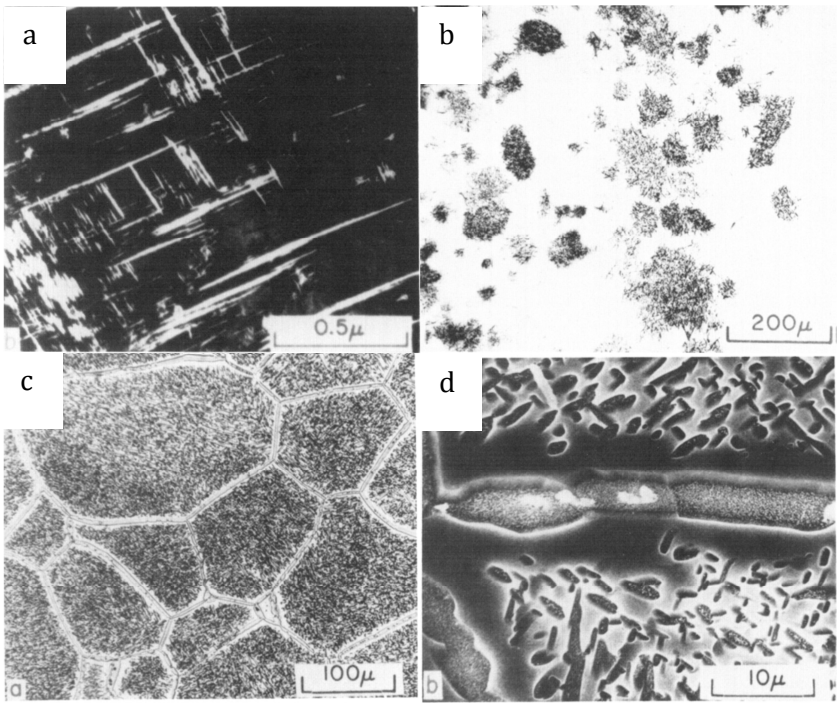

Fig. 8. (a) TEM dark field image showing intragranular widmanstatten basket weave type morphology of α after ageing at 400 °C, (b) the dark etched regions contain sympathetically nucleated α produced after ageing at 450 °C, (c and d) α forms along grain boundary and within the grains above 650 °C [30].

Later on, effect of heating rate to ageing temperature was studied on Ti-55511, Ti-15-3 and Ti-LCB alloys by Ivasishin *et al*. [11, 32]. It was mentioned that fine plate-like α is formed at high temperature (650 °C) ageing using slow heating (0.25 $°Cs^{-1}$) to ageing temperature in VT22

and Ti-LCB alloys [11, 32]. This behaviour was attributed to the precipitation of ω at low temperatures; which serves as nucleation sites for α. At higher heating rates (20 °Cs^{-1}), the formation of ω was avoided; which led to the development of comparatively coarse, plate-like non-uniformly distributed α microstructures with poor ductility (from 7.5% to 3.1% for VT22 alloy). However, no evidence was presented to support this claim.

Figure 9 shows two types of ω precipitated in Ti alloys; athermal ω during rapid quenching from high temperature and isothermal ω during low temperature ageing [33, 34]. Athermal ω precipitates are typically ~2-10 nm size, whereas isothermal ω is around 10 nm [35, 36]. The morphology of ω particles depends on the composition of the alloys and ω/β misfit, e.g. ellipsoidal in the alloys containing Mo or Nb with low misfit and cuboidal with Cr or V and high misfit [37, 38].

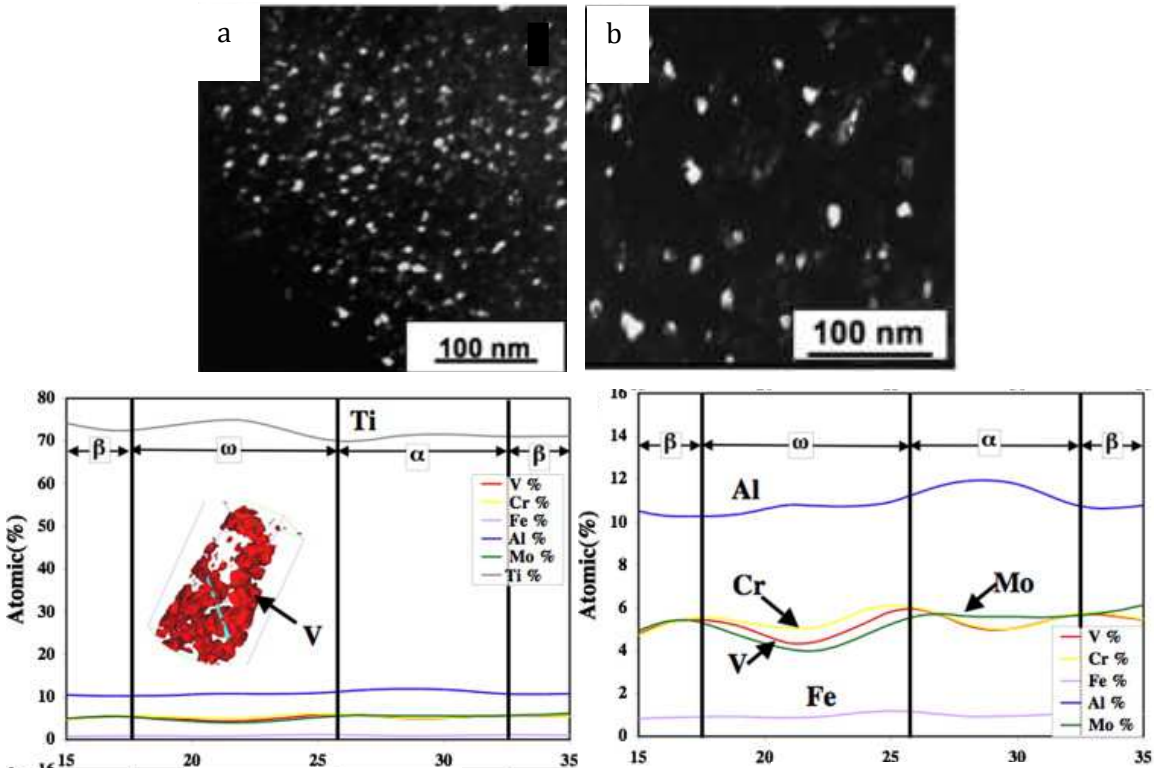

Fig: 9. DF image showing (a) athermal ω and (b) isothermal ω particles and (c-d) corresponding compositional changes for isothermal ω [34].

Recently, some dedicated research to investigate the ω-assisted α nucleation in Ti-5553 and Ti-9Mo has been performed [33, 34]. Aberration-corrected Scanning TEM (STEM) was employed to reveal the atomic collapse of the β phase to form the ω phase in the direction of ⟨111⟩ (Fig. 9) [33]. Simultaneously, atom probe tomography (APT) was used to observe the

composition fluctuations with the formation of ω phase (Figs 9 and 10). It was also mentioned that formation of isothermal ω is associated with depletion in alloying elements present in the studied alloys [33, 34]. Despite using the aberration corrected STEM, Devaraj *et al.* [33, 35, 39] could not find an ω motifs connection with α phase. Additionally, no statistical analysis was applied to identify the presence of clustering/compositional variations.

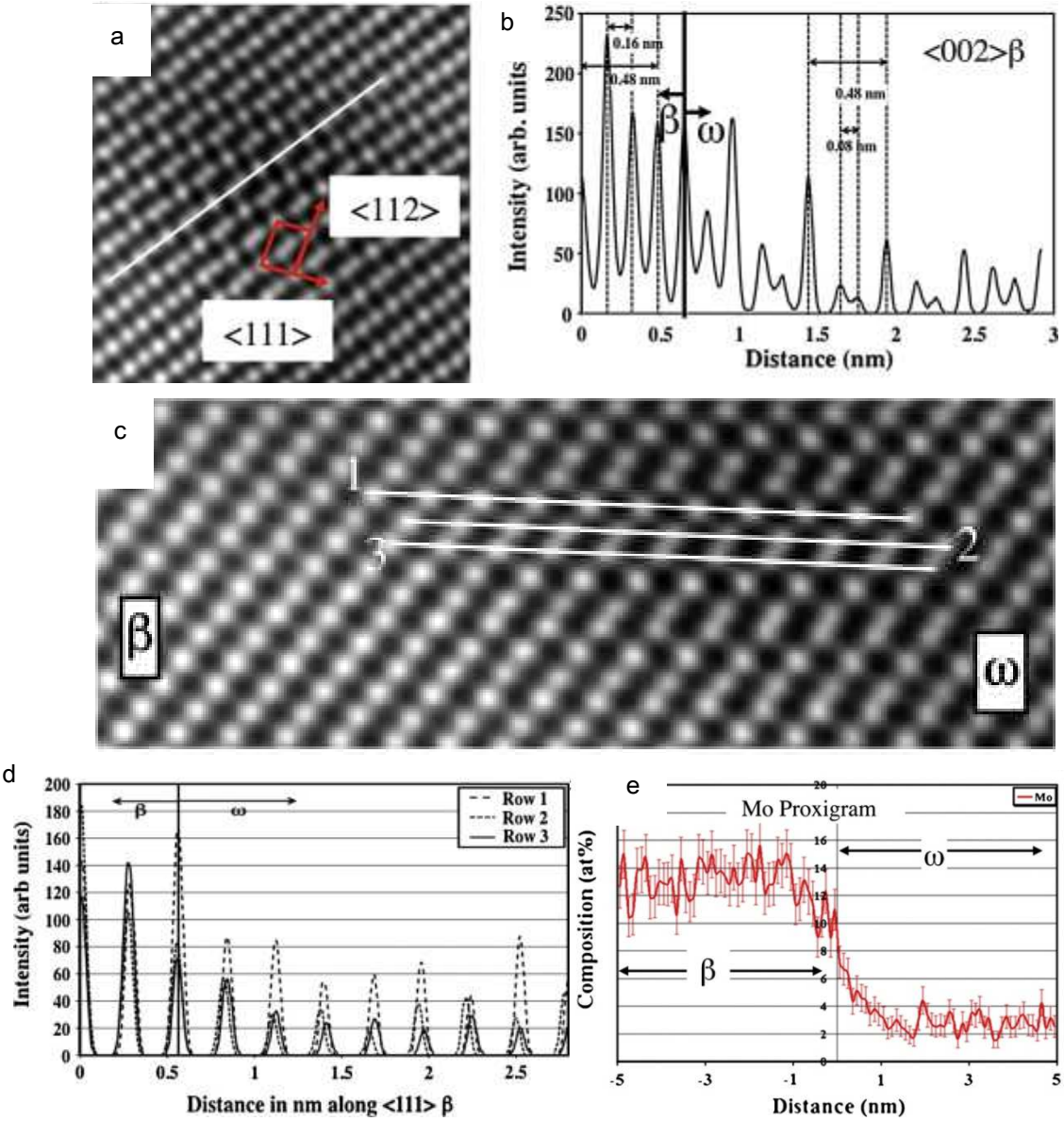

Fig. 10. (a) High Resolution STEM image delineating ω motif; (b) intensity profile along the line in (a) shows the atomic collapse in the <002> direction; (c) HR STEM image with the region of interest; (d) superimposed intensity profile along the lines 1, 2, 3 in (c) shows that atoms in the lines 2 and 3 moves along <111> direction.; (e) the proxigram shows the compositional transitions occurred due to the formation of ω[33].

However, it is mentioned that α possibly nucleates within ω [40], at the ω/β interface [34, 41] or near this interface in β phase [42]. In another study [43], it was reported that Mo

piles-up at the interface at initial stage of ageing and low diffusivity of Mo was attributed to such event. However, pile-up diminished with prolonged ageing time. However, mechanical properties of such conditions were not measured to see the influence of α, which supposedly nucleated at ω.

A summary of the mechanical properties, yield strength (YS), ultimate tensile strength (UTS) and total elongation (T.E) after ageing of Ti-5553 and its derivative is given in Table 3. All near β titanium alloys display a reduction in ductility with increasing ageing time. The reasons behind the observation have been explained as (i) the increased strain localisation in the aged matrix and, (ii) the higher yield stress difference between the α phase and β matrix [44]. The combination of the above phenomena leads to early crack nucleation and poor ductility. In highly β stabilised alloys, e.g. Ti-15-3 or Beta C, duplex ageing comprising either high-low or low-high ageing temperature sequences result in inhomogeneous secondary α phase precipitation. Duplex ageing allows for higher strength attainment in shorter ageing times than those achieved by single-step ageing [45]. In this regard, some authors have shown an improvement in ductility after duplex ageing [46], while others found that it did not affect ductility [47, 48].

Table 3: Mechanical properties of near-β alloys after ageing.

Composition (wt%)	Processing stages	YS (GPa)	UTS (GPa)	T.E. (%)	Ref.
Ti-5Al-5Mo-5V-1Cr-1Fe	820°C (1–2 h), 750°C (2–3 h), 600°C (4 h)	1.07–1.12	1.12–1.16	9–12	[6]
	820°C (1–2 h), 790°C (2–3 h), 600°C (4 h)	1.15–1.21	1.24–1.29	8–12	
	820°C (1–2 h), 750°C (2–3 h), 570°C (8 h)	1.1–1.2	1.17–1.25	8–14	[49]
	950°C (0.5 h), RT (30% def.), 750°C, 538–640°C (8 h)	1.24–1.75	1.35–1.75	0.3–7.5	[32]
	840°C (4 h), HIP (1133 K), 570°C (0.25–5 h)	–	1.23	10.7	[50]

Composition (wt%)	Processing stages	YS (GPa)	UTS (GPa)	T.E. (%)	Ref.
	840°C (3 h), 750°C (3 h), 580°C (4 h)	–	1.21	15.9	[51]
	860°C (3 h), 750°C (3 h), 570°C (8 h)	–	1.21	15	
Ti–5Al–5Mo–5V-3Cr–0.5Fe	821°C(3 h), 621°C(6 h)	1.24	1.31	18	[52]
Ti–5Al–5Mo–5V–3Cr-0.4Si	-	1.09	1.19	4.5	[53]
Ti–5Al–5Mo–5V–3Cr	-	1.08	1.15	5.3	
Ti–5Al–5Mo–5V–3Cr-0.6Fe	804°C (1h), 610°C (8h) 804°C (1h), 660°C (8h) 832°C (1h), 610°C (8h) 832°C (1h), 660°C (8h)	1.21 1.10 1.21 1.10	1.29 1.16 1.33 1.19	7 13 5 9	[54, 55]
Ti–5Al–5Mo–5V–3Cr-0.6Fe	-	1.21-1.24	1.27-1.30	11-14	

1.1.3 Phase transformations:

1.1.3.1 Diffusional β→α transformation

During high temperature annealing in the α+β phase field in the thermo-mechanical processing and ageing, β phase transforms to α phase by means of diffusion. Three types of α phase are formed in near-β Ti alloys in terms of their formation sites. They are: (i) grain boundary α precipitating at β grain boundaries and growing by kink-on-ledge mechanism along grain boundaries [56], (ii) intergranular α, which grows from the grain boundary into the β grains, and (iii), intragranular α, which nucleates and grows within the β grains and which can be sub-divided into primary and secondary α depending on the size scale and order of nucleation and growth.

There are two opinions about the mechanism of nucleation and growth of intergranular α laths. The first opinion held by Mullins and Sekerka [57], ascribes their formation to the instability at α/β interface formed by the perturbation wavelength. Inter-granular α has the same orientation as the grain boundary α during the growth stage. Subsequently, through the pinch-off mechanism a boundary between the inter-granular α and grain boundary α is generated. The second opinion states that intergranular α is sympathetically nucleated on the grain boundary α [58]. In the latter case, the nucleated α comprises a different variant than the grain boundary α.

Once the nucleation of α phase occurred, questions regarding its growth mechanism and the obstacles it requires to overcome during the growth needs to be addressed. The study by Furuhara and Maki [59] illustrates how the transformation strains are accommodated by the ledge mechanism in Ti-Cr alloys. It was mentioned that structural growths ledges are formed, which merge to form super-ledges in order to make up the shear strain. Glissile dislocations introduced onto the interface through diffusion or plastic deformation have the same spacing as the height of the growth ledges. Thus, they can glide on the common slip planes between the precipitate and the matrix during the migration process of the interface. Precipitation of certain selected variants is another mechanism to reduce transformational strains. Self-accommodation via variant selection occurs by having the direction of maximum misfit nearly parallel to the Burgers vector of the dislocation in the case of precipitation on dislocations [60].

However, the most commonly observed orientation relationship between the α and β phases is the Burgers orientation relation (OR) [61], although others like Pitsch-Schrader [62], Potter [63], and Rong-Dunlop [64] have been also noted. A summary of ORs are listed below:

Burgers OR: $(0001)_\alpha$ // $\{011\}_\beta$; $<11\bar{2}0>_\alpha$ //$<1\bar{1}1>_\beta$; $\{1\bar{1}00\}_\alpha$ // $\{121\}_\beta$ (1)

Pitsch-Schrader OR: $(0001)_\alpha$ // $\{011\}_\beta$; $<11\bar{2}0>_\alpha$ // $<100>_\beta$; $\{1\bar{1}00\}_\alpha$ // $\{0\bar{1}1\}_\beta$ (2)

Potter OR: $(0001)_\alpha$ 2° from $\{011\}_\beta$; $<11\bar{2}0>_\alpha$ //$<1\bar{1}1>_\beta$; $\{1\bar{1}00\}_\alpha$ // $\{110\}_\beta$ (3)

Rong-Dunlop OR: $(0001)_\alpha$ // $\{021\}_\beta$; $<11\bar{2}0>_\alpha$ // $<100>_\beta$; $\{1\bar{1}00\}_\alpha$ // $\{0\bar{1}2\}_\beta$ (4)

Solute redistribution occurs during growth of the α phase. Typically β stabilising alloying elements e.g. Mo, V, Fe, Cr etc. diffuse out of the α phase during growth of the α phase. On the other hand, α stabilisers e.g. Al, O, etc. diffuse into the favourable the α phase. Thus, growth of α phase depends on the diffusivities of the solutes present in the system. It was mentioned in [43] that partitioning of alloying elements is dependent on the heat-treatment. In the case of Ti-5553 alloy, pronounced partitioning of the alloying elements occurred between the α and β phases when sample was processed at high temperature annealing in the α+β phase field (either by step quenching to 700°C or furnace-cooling from super-transus temperature)[43]. On the other hand, such pronounced partitioning was not observed when sample was aged at 400 °C after β solution treatment followed by quenching. Due to lower

diffusivity of the elements growth of the α and partitioning of the alloying elements restricted at relatively low ageing temperature of 400 °C [43].

1.1.3.2 Displacive shuffle transformation (β→ω)

The formation of ω from the β phase is believed to occur via atomic shuffle. There are several different theories about the formation of the ω phase [65, 66]. The orientation relationship between β and ω can be described as [67]:

$\{111\}_\beta$ // $\{0001\}_\omega$ and $<11\bar{2}0>_\omega$ // $<011>_\beta$ (5)

From the above relationship, two things could be assumed. Firstly, it enables an estimate of the lattice parameter of the ω in terms of the β phase such that:

$a_\omega = \sqrt{2}\, a_\beta$ and $c_\omega = (\sqrt{3}/2)\, a_\beta$ (6)

where a and c are the lattice parameters; suffix β and ω indicates the corresponding phase

Secondly, there are four possible crystallographic variants of the ω structure in the bcc parent crystal as there are four sets of <111> directions.

On these bases, a mechanism of ω formation was developed called the Linear Fault Mechanism. It is a hard sphere model proposed by Sass *et al.* [65] and is based on the development of ω within the β lattice. According to the model, initially there is an ABCABC… stacking sequence of open bcc β structure that generates a three-fold axes along the $<111>_\beta$ direction. The ω forms on collapsing two adjacent $(111)_\beta$ planes (which is similar to applying equal and opposite shears to the $(011)_\beta$ planes in the $<111>_\beta$ direction) through a distance of one-sixth of the separation of the $(111)_\beta$ planes [65].

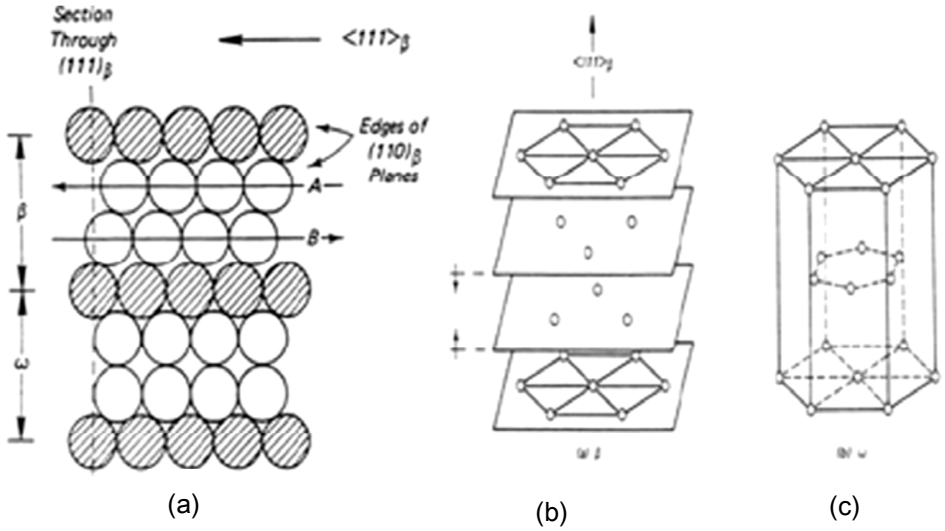

Fig. 11: (a) Linear fault model for ω phase transformation showing a $(101)_\beta$ section through the bcc crystal and depicting the transformation of ω phase as a displacement of adjacent $(110)_\beta$ planes [68] (b) and (c) the movement of atoms in β to form ω as seen from the $<111>_\beta$ direction [69].

The atomic movement that needs to occur to bring about a β to ω phase transformation is illustrated in Fig. 11 [68, 69]. When this collapse is completed, a six-fold symmetry is created along the $<111>_{\beta}$ direction along which this collapse has taken place. On the other hand, if the collapse is incomplete, the trigonal symmetry is not lost. Upon this transformation, there is an overall 3% contraction of the $(110)_{\beta}$ planes (initial separation = (2×1.414)D; final separation = (1 + 1.723)D; where D is the assumed diameter of the atom in the hard sphere model) [69]. However, it is mentioned in [69] that this theory is only valid to explain the effect of the composition on the formation of ω. This model fails to explain the reversibility of ω (change of curvilinear diffuse reflections to straight lines) with temperature.

Using the soft Phonon Mechanistic Model developed by de Fontaine [66], the effect of both temperature and composition on athermal ω phase can be explained. This model shows a bcc lattice comprising of $\{111\}_{\beta}$ planes stacking perpendicular to the [111]β direction. On that was superimposed a longitudinal phonon propagating in the <111>β direction. This phonon had a maximum amplitude of $2/3[111]_{\beta}$, and the ordinates (or local amplitudes) at the points where the curve intersects the lattice planes specify the magnitude and direction of the corresponding lattice plane. Thus in order to form ω from β, the plane at position '0' would not move while the planes at '1/3' and '2/3' would move towards the intermediate '1/2' position; again the plane at position '1' would not move and so on (Fig. 12a) [66]. This model worked perfectly due to the fact that the ω instability caused by the transverse sinusoidal displacement wave of amplitude 1/3 <112> β is equivalent to this longitudinal sinusoidal phonon displacement wave of 2/3<111>β [67]. It is evident from Fig. 12a that the wave nature of these displacements is equivalent to the spinodal decomposition, except that displacement waves are involved instead of compositional waves. As a result of this displacement, three dimensionally, the stacking sequence of the (111) β planes changes from ABCABC… to AB′AB′…, where A planes are unchanged but the B′ planes have a trigonal nearest neighbour arrangement of atoms [70]. Fig. 12b demonstrates this change of stacking sequence from β to incomplete (of trigonal symmetry) and complete (of hexagonal symmetry) ω transformation [69]. Additionally to explain the athermal ω phenomenon, the usage of this model leads to the possibility of a continuum of incomplete ω states intermediate between the original β and the completely transformed ideal ω phases. Thus the reciprocal lattice streaking effect of the early stage ω could be attributed to these 2/3<111>β phonons, caused by the instability of the crystal due to the variation of its composition or temperature. In addition, the reversible temperature phenomena leading to change of curvilinear diffuse reflections to straight lines of athermal ω could be explained comprehensibly by this model [67]. The beauty of this model is that it identifies the

most possible instability that may arise in a bcc structure to be the one leading to the β to ω transformation. This transformation can thus be linked with the equilibrium transformation of titanium from high temperature bcc to low temperature hcp structure.

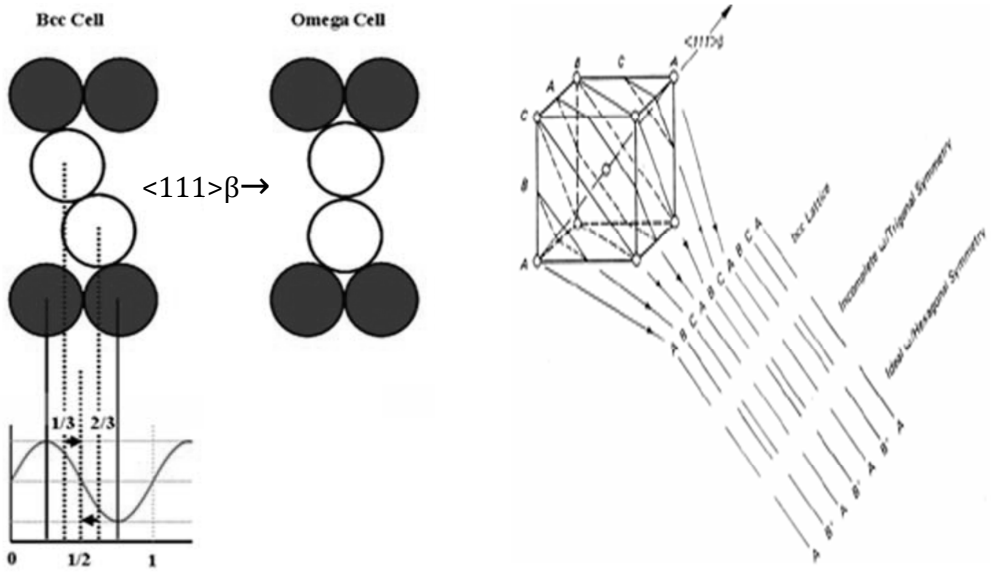

Fig. 12: (a) Sinusoidal displacement wave along with the β and ω atomic stacking [66]; (b) β to ω transformation explained in terms of displacement wave mechanism. The transformation could be incomplete or complete [69].

1.1.3.3 Martensitic Phase transformation (β → α′, α′′)

Both α' and α" are the products of the martensitic transformation [69]. While α' is hexagonal in structure, α" has the orthorhombic structure. The α' martensite only forms by quenching (athermal martensite), but α" can also form on application of external forces (stress induced or strain induced martensite) [71]. Neelakantan *et al.* [72] have developed the following equation based on the Ghosh and Olson [73] approach to estimate the athermal martensite start temperature.

M_s= 1156-150Fe-96Cr-49Mo-37V-17Nb-7Zr+15Al (7)

Here, M_s is martensite start temperature in K, the amount of the alloying elements is in wt. %. It is evident from the eq. (7) that, athermal martensite formation will be hindered with increasing β stabilisers through lowering M_s. thus, external forces will be then required to obtain α".

Two independent theories [74, 75] have been proposed for martensite formation based on the postulation that diffusion does not occur and atomic correspondence is sustained during transformation. Herein strains of a combination of two invariant lattice planes can achieve their essential lattice change either in the habit plane (which is the interface between martensite and the parent phase) or on an invariant plane through a simple complimentary shear [76].

However, these hypothesis are hardly valid when alloying elements are added to the pure metal as alterations in the elastic parameters of the system result in a changing of the conditions under which athermal transformation occurs [69]. Of even greater significance is the local effect of alloying to prevent the movement of atomic planes which could hamper the microstructure of the transformed product itself and change the rate of reaction [69].

The activation energy for the process is reducible by the $\beta \rightarrow \alpha'$ transformation process with the following shear systems [77]

$[111]_\beta \left(11\bar{2}\right)_\beta \equiv \left[2\bar{1}\bar{1}3\right]_{\alpha'} \left(\bar{2}112\right)_{\alpha'}$ and

$[111]_\beta \left(\bar{1}01\right)_\beta \equiv \left[2\bar{1}\bar{1}3\right]_{\alpha'} \left(\bar{1}011\right)_{\alpha'}$

A transformation which maintains the orientation relationship can only be achieved via a series of contractions and expansions of the β lattice in order to form the α′ phase. They are registered below [69]:

1. a 10% contraction along $[100]_\beta$ which corresponds to $\left[2\bar{1}\bar{1}0\right]_{\alpha'}$
2. a 10% expansion along $\left[0\bar{1}1\right]_\beta$ which corresponds to $\left[0\bar{1}10\right]_{\alpha'}$
3. a 1% expansion along $[011]_\beta$ which corresponds to $[0001]_{\alpha'}$

The other form of martensite in Ti alloys is with the orthorhombic α″ structure. This is demonstrated when the Burgers orientation is written in terms of the orthorhombic crystal lattice such that the OR between the β and α′ phases becomes:

$(001)_p // (001)_m$ and $[\bar{1}10]_p // [\bar{1}10]_m$ (8)

Where, p and m represent the parent and matrix, respectively [71]. The relationship between β and α″ could also be described via the same relationship.

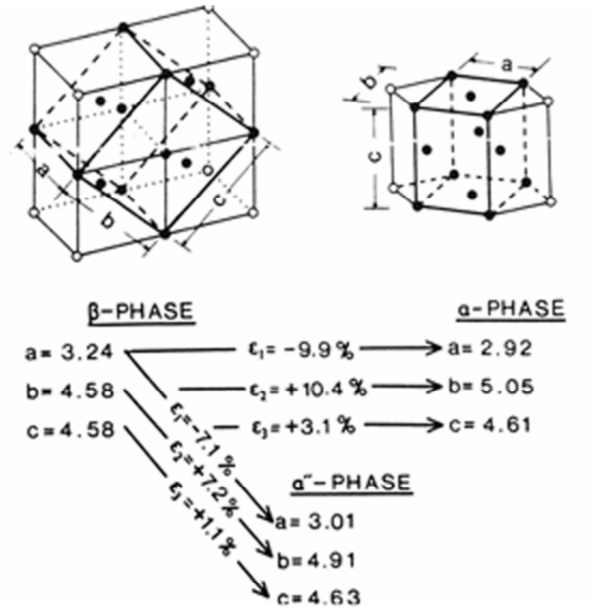

Fig. 13: An illustration of how the lattices of α, β and α′′ phases are interrelated. Also shown are the transformation strains for β–>α and β–> α′′ transformations [78].

Figure 13 shows the interrelation between three lattices (a, b, and c) as represented in the orthorhombic system [78]. The following crystallographic orientations have been found between β and α" in quenched Ti-Nb alloy by Hatt and Rivlin [79]:

- $[100]_{\alpha''}$ 2° from $<001>_{\beta}$
- $[010]_{\alpha''}$ 2° from $<110>_{\beta}$
- $[001]_{\alpha''}$ // $<1\bar{1}0>_{\beta}$ (9)

1.1.3.4. Effect of oxygen on phase transformation and mechanical properties:

Oxygen is an important interstitial element which considerably affects the phase transformation and mechanical properties in the case of titanium and its alloys. The formation of ω phase is suppressed in Ti alloys containing α stabilisers, such as oxygen and aluminium [80]. The starting temperature of ω formation decreases with increasing oxygen content (Fig. 14a). Thus, ω phase can be avoided using sufficient amount of oxygen content. On the other hand, oxygen accelerates the β → α+β phase transformation through increasing the β transus temperature due to oxygen being a strong α stabiliser. Microstructural features occurring due to oxygen are of particular importance because they play a key role in deciding the mechanical properties, especially ductility, in Ti alloys. In binary Ti-Al alloys [81], an intermetallic α_2 (Ti_3Al) forms with a certain amount of oxygen content. It has also been reported that oxygen not only enhances the formation of α_2 precipitation but also increases its volume fraction [81]. The

critical level of oxygen was found to be around 1300 ppm for the ductile-to-brittle transition in Ti–8Al. However, this α_2 could not be always the cause for displaying the ductile-to-brittle transition. For instance, the ductile-to-brittle transition of Ti–6Al–2V alloy occurred at a much higher oxygen level (0.65 wt.% oxygen) and with absence of the formation of such α_2 precipitation [82]. A very recent study [83] also showed that nanosized α_2-type clusters were formed in Ti-6Al-4V alloy with 0.49 wt.% of oxygen (Fig. 14b). Thus, it can be concluded that each alloy shows ductile-to-brittle transition phenomenon at a distinct oxygen content and it may or may not be associated with the presence of α_2 phase.

For the case of martensitic transformation, it has been reported that the formation of α' phase with hcp structure is induced or promoted by high concentration of oxygen in Ti alloys [84]. The martensitic transformation temperature increases with oxygen similar to the β transus temperature.

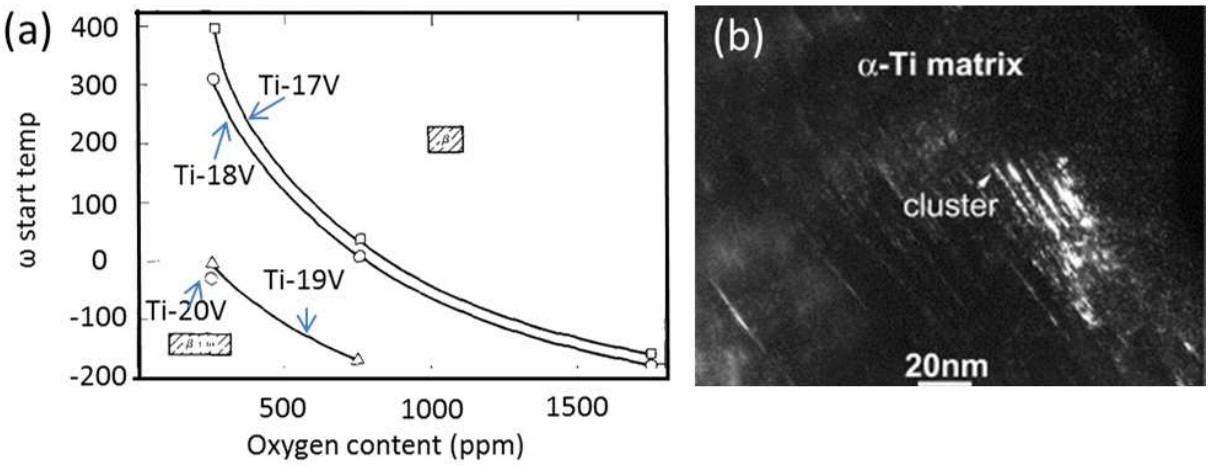

Fig. 14: (a) Omega formation start temperature as a function of oxygen [80] and (b) α_2 cluster in α Ti [83].

The summary of the influence of oxygen content on the ductility of β/near β Ti alloy is shown in the following Fig. 15. It is evident from Fig. 15a that each of the alloys has different amount of oxygen content to show the poor ductility. For example, while Ti-15Mo-3Al-2.8Nb-0.2Si shows 5% elongation at oxygen content of 0.33 wt.%, Ti-35Nb-0.7Ta-2Zr displays similar amount of elongation with 0.53 wt.%. Fig. 15b shows the elongation of Ti-6Al-4V alloy, processed using different technique, with respect to oxygen content. It is clear that manufacturing processing also governs the ductility. The dashed circle in Fig. 15b shows the low ductility and the underlying reason was in the microstructural constituents. Microstructure of those alloys contains α' (martensite) which causes the low ductility even with 0.15 wt.% of

oxygen. Hence, it can ultimately be concluded that influence of oxygen on the ductility is microstructure dependent.

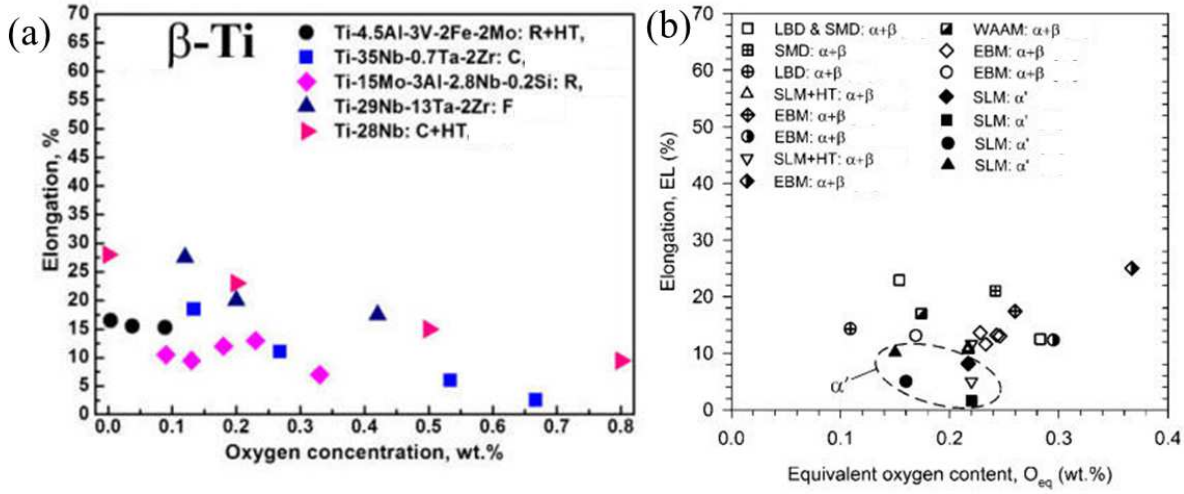

Fig. 15: (a) The effect of oxygen on tensile elongation for β Ti alloys [84] and (b) the effect of oxygen on elongation in Ti-6Al-4V alloy manufactured by different processing technique [84].

1.1.4 Cold deformation mechanisms in near-β Ti alloys

Deformation mechanisms of near β Ti alloys, e.g., Ti–Nb–Ta–Zr–O (gum metal series), Ti-Mo, Ti-V and Ti-15V-3Cr-3Sn-3Al alloys, show the dependencies on the β phase stability. For instance, Ti–Nb–Ta–Zr–O system experiences {332}⟨113⟩β deformation twinning [85] and stress-induced α′′ martensite [86] in Ti–21Nb–0.7Ta–2Zr–1.2O (at. %) alloy. By increasing Nb content to 2 at%, the deformation mechanism changed to stress-induced α′′ martensite formation, 1/2⟨111⟩ dislocations slipping, stress-induced ω phase and {112}⟨111⟩β deformation twinning [86-89]. With further increasing the β stability by additional 2 at% Nb, it was found that only dislocation glide occurs during deformation. The above results indicate that the deformation mechanism of Ti–Nb–Ta–Zr–O system is dependent on the β stability [85]. It is proposed that the presence of deformation mechanisms after deformation depends upon the electronic properties (metal d orbital energy level $\overline{Md}$ and bond order= $\overline{Bo}$) of the elements used (Fig. 14) [90]. However, it is pertinent to mention that these alloys do not contain any α during deformation.

On the other hand, near β Ti alloys (Ti-5Al-2Sn-5Zr-4Mo-2Cr-1Fe (β-Cez) and Ti-10V-2Fe-3Al) containing α phase (before deformation) show only stress-induced α″ martensitic transformation on deformation [16, 91-96]. It is also mentioned in [16, 95] that Ti-10V-2Fe-3Al alloy containing more than 50% of prior α phase does not transform into α" martensite by applying an external stress.

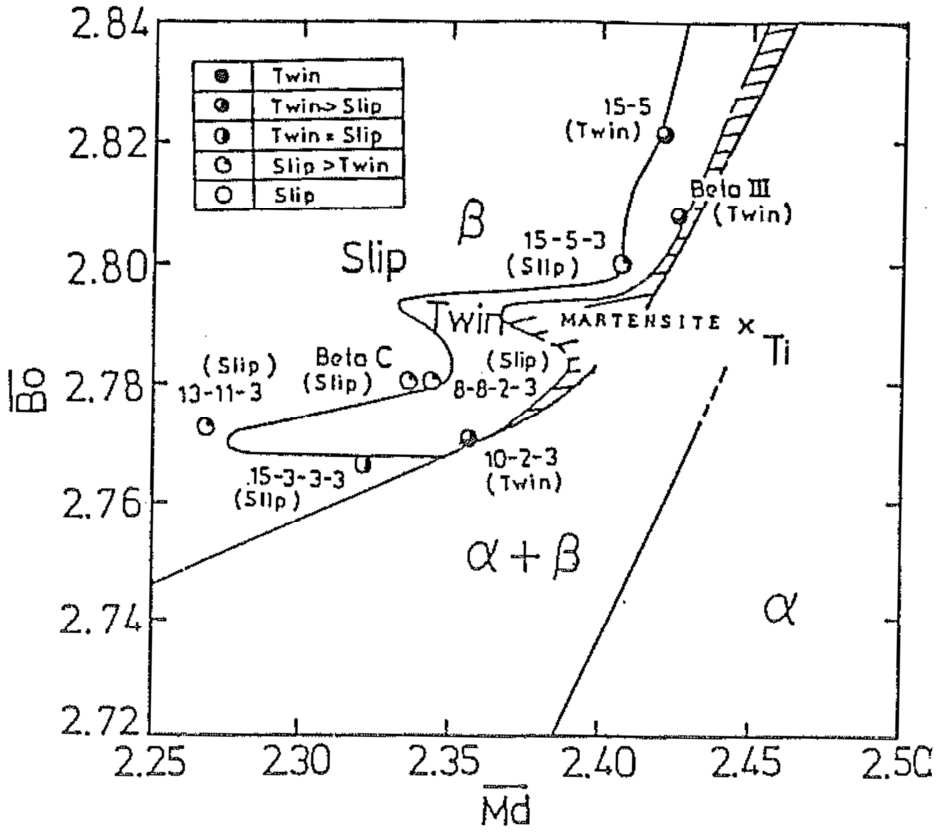

Fig. 16: Slip/twin boundary and the martensite region in $\overline{Bo}$ vs $\overline{Md}$ map [90].

1.2 Objectives of the thesis:

A systematic study of near β Ti-alloys manufactured by the BEPM technique is needed in order to compare microstructural evolution and product mechanical properties with those resulting from other conventional synthesis and processing methods. In addition, there is a lack of information in the literature on the compositional transitions occurring during thermo-mechanical processing and subsequent ageing of BEPM manufactured Ti. Furthermore, the influence of cooling rates during thermo-mechanical processing on microstructure and mechanical properties has not been investigated. In addition, ω-assisted α phase nucleation and its effect on the mechanical properties are not yet fully understood. Finally, the cold deformation behavior of a range of near β Ti alloys containing a prior α phase has not been examined in details.

Addressing the above, three near β (Ti-55511, Ti-55521, and Ti-1033) alloys produced by BEPM were chosen for this project. The objectives of the present study are as follows:

- To evaluate the effect of TMP parameters on the microstructural evolution and on the re-distribution of alloying elements between the phases.
- To investigate the influence of cooling rate on the microstructure and mechanical properties.
- To study the effect of a single-step high temperature ageing with a slow heating rate on the evolution of microstructure and mechanical properties. In addition, to examine the phase transformations taking place during ageing using advanced experimental techniques of HR STEM and atom probe tomography.
- To examine the influence of Cr content on the aforementioned subjects.
- To assess the effect of β phase stability on the deformation behaviour of Ti-1033 alloy at room temperature.

1.3 Materials and Experimental Procedures:

1.3.1 Materials:

The Ti-alloys used in the present study were sourced from the Institute for Metal Physics of National Academy of Sciences, Ukraine.

A cost effective BEPM technique was employed to manufacture the alloys via the following general procedure: Hydrogenated Ti containing 3.5 wt.% hydrogen was blended with 50Al–50V (wt.%) master alloy powder and Mo, Cr, Fe elemental powders to achieve the required compositions of the alloys. The details about the powder size, grade, purity and supplier of the materials used is presented in the Table 4.

Table 4: The detailed information about the powders used in the study.

Materials	Size (μm)	Grade	Purity (%)	Source
TiH_2	≤100	-	-	ZTMC*
Al	≤40	AD 0	99.5	-
Mo	40-63	MPC	99.5	-
V	≤40	VnM-1	99.4	-
Cr	≤40	H-99	99.0	-
Fe	≤40	3.200.26	99.3	-

*Zaporozhje Titanium & Magnesium Combine, Ukraine

Thereafter, the blended powders were die pressed using steel dies at room temperature under a pressure of 650 MPa to form bar-shaped green compacts. The obtained size of the green compacts was 10X11X100 mm as rectangular bar. The nominal chemical composition of the alloys used in the present study is as follows:

Table 5: The nominal composition of the alloys used in present study (in wt.%).

Alloys	Al	Mo	V	Cr	Fe
Ti-55511	5	5	5	1	1
Ti-55521	5	5	5	2	1
Ti-1033	3	-	10	-	3

The compacts of Ti-55511 and Ti-55521 alloys used in Chapters 2, 3, 4, 5 and 6 were sintered in two steps comprising; heating at $10°Cs^{-1}$ to 1020°C for 3600 s followed by holding at 1250°C for 21600 s. Green compacts of Ti-1033 alloy used in Chapter 7 were also sintered in two steps consisting of holding at $10°Cs^{-1}$ to 1020°C for 900 s, then holding at 1250°C for 14400 s. The Density of the sintered samples was measured by Archimedes technique using distilled water.

1.3.1.1 Materials Processing:

In the present study, a Gleeble 3500 thermo-mechanical simulator configured under pocket jaw mode was employed for processing the materials used. A K-type thermocouple (a combination of Chromel and Alumel) was spot welded to the specimens at their longitudinal mid-point. Tantalum sheets and graphite were attached to both sides of the samples. The specimens were placed between copper jaws and resistance heated. All Gleeble tests were conducted in a vacuum of $\sim 3.89\times10^{-4}$ torr to prevent high temperature oxidation and atmospheric contamination.

The dimensions of the samples used in Chapter 2 were 4 mm diameter and 6 mm length while sample dimensions of 8 mm diameter and 12 mm length were utilised for the experiments described in Chapters 3-7.

Following the thermo-mechanical processing, samples were encapsulated into a quartz tube under vacuum in order to protect from the high temperature oxidation. Thereafter, the samples were heated in a tube furnace at 0.25 Ks^{-1} to 650 °C for ageing.

However, the actual composition of the alloys was measured after ageing for Ti-55521 and thermo-mechanical processing for Ti-1033 using Inductively Coupled Plasma Atomic Emission Spectroscopy (ICP-AES), Leco at Spectrometer Services Pty Ltd. The following Table 6 shows the actual compositions.

Table 6: The composition of the alloys after the processing (wt.%±0.01).

	Ti	Al	Mo	V	Cr	Fe	O
Ti-55521	Bal.	5.35	4.78	4.50	1.88	1.05	0.38
Ti-1033	Bal.	3.00	-	9.54	-	2.97	0.27

As the oxygen amount shown in Table 6 was measured after entire processing, thus it can be assumed that the oxygen content after the BEPM was definitely lower than the amount shown.

The following table delineates the various schedules used in the present study:

Table 7. Heat treatments cycles employed in the present study.

Alloy	β phase	β phase	α+β phase	α+β phase	Cooling condition	Ageing 650°C	Chapter
Ti-55511 Ti-55521	950°C (120s)	-	-	-	WQ	-	2
	950°C (120s)	900°C (25%)	-	-	WQ	-	
	950°C (120s)	900°C (25%) (40%)	750°C (1800s)	-	WQ	-	
	950°C (120s)	900°C (40%)	750°C (1800s)	-	WQ	-	
	950°C (120s)	900°C (25%)	750°C (1800s)	750°C (40%)	WQ	-	
Ti-55511 Ti-55521	950°C (120s)	900°C (25%)	800°C (1800s)	800°C (60%)	10 Ks^{-1}	-	3
	950°C (120s)	900°C (25%)	800°C (1800s)	800°C (60%)	1 Ks^{-1}	-	
Ti-55511	950°C (120s)	900°C (25%)	800°C (600s)	800°C (60%)	10 Ks^{-1}	3.6 ks 7.2 ks 14.4 ks 28.8 ks	4
Ti-55521	950°C (120s)	900°C (25%)	800°C (600s)	800°C (60%)	10 Ks^{-1}	120 s 3.6 ks 14.4 ks 28.8 ks	5
Ti-1033	900°C (5min)	850°C (25%)	725°C 700°C 675°C 650°C 625°C 500°C (300s)	-	WQ	N/A	7

For experiments described in Chapter 7, samples were thereafter strained to 0.4 at a strain rate of 0.001 s^{-1} at ambient temperature.

1.3.2 Materials characterisation techniques:

1.3.2 (i) Optical Microscopy (Chapter 7):

Samples were prepared for metallography after cutting perpendicular to the deformation direction. Then the samples were hot mounted under a pressure of 7.17 MPa at 150 °C for 480 s. The mounted samples were rough ground using 500 and 1200 SiC papers, fine ground with a 15μm diamond disc, followed by fine polishing with colloidal silica suspension. Thereafter, the polished samples were etched to reveal the microstructures using Kroll's reagent (2 ml HF, 5 ml HNO_3 and 93 ml H_2O).

The microstructures were examined with a Leica DM4500 P LED high-end polarisation microscope with intelligent light and contrast management. Several microstructures were acquired randomly from the interested regions.

1.3.2 (ii) Scanning Electron Microscopy (Chapters 2-7):

After processing, the samples were cut perpendicular to the deformation direction and then hot mounted under a pressure of 7.17 MPa at 150 °C for 480 s. The mounted samples were rough ground using 500 and 1200 SiC papers, fine ground with a 15μm diamond disc, followed by fine polishing with colloidal silica suspension. Thereafter, the polished samples were etched to reveal the microstructures using Kroll's reagent (2 ml HF, 5 ml HNO_3 and 93 ml H_2O).

All scanning electron microscopy (SEM) observations reported in Chapters 2-7 were undertaken on a JEOL JSM 7001F Field Emission Gun—Scanning Electron Microscope (FEG-SEM), fitted with Energy Dispersive X-ray Spectrometer (EDS) system. Bruker - AXS XFlash detector was used in Chapter 2 while Oxford Instruments AZtec software was utilised in Chapters 2 and 3. The operation was carried with an accelerating voltage of 15 kV and working distance of 15 mm. Both the back scattered electron (BSE) and secondary electron (SE) modes were employed for imaging. Several microstructures were acquired randomly from the interested regions.

In Chapter 2, a probe current was chosen to provide an EDX count rate of approximately 25 kcps, so as to ensure good statistics. X-ray maps were then acquired for 14.4 ks using an image resolution of 1200×1024 pixels and a dwell time of 12 ms. The X-ray line scans were thereafter analysed in the X-ray maps using an interactive standardless PB-ZAF analysis whereby the elements were set and an appropriate Bremsstrahlung background was selected to obtain an optimum fit before quantification was performed. The accuracy of the compositional

measurement was ±5 %. At least 30 X-ray line scans were performed for each phase composition, whereas each x-ray line scan was a combination of numerous points. Moreover, the EDS spectra did not overlap.

1.3.2 (iii) X-ray Diffraction (Chapters 3 and 4):

X-ray diffraction investigations were conducted using a PANalytical X'Pert PRO Multipurpose diffractometer (MPD) with Cu Kα radiation (λ=0.154 nm) filtered with Ni-monochromator at 45 mA and 40 kV. Polished samples of 15 mm diameter were oriented normal to the deformation axis. Diffraction patterns were obtained under a continuous scanning mode over the 2θ range of 30–90°, with 0.01° step size and 490 s resulting acquisition time. In order to characterise the instrumental broadening a standard polycrystalline silicon sample was used. X-ray line profile analysis was performed by Rietveld fitting.

The modified Rietveld

The method consists of a modelling of diffraction profiles through pseudo-Voigt (pV) function using the programme LS1[97]. The crystal structure of the materials and microstructural parameters, e.g. lattice parameters, crystallite size and microstrain, are simultaneously refined through the LS1 programme. In the programme, Fourier transform of the pV function is used to fit the broadening of the peaks profile. An isotropic model is assumed, which is called the Popa model [98] where the lattice constants, volume weighted crystallite size and microstrain are concomitantly used as the fitting parameters. Since the samples are heavily deformed, the preferred orientation of the crystallites has been corrected in order to obtain the best fit by maintaining the following function, [99]:

$$p(\alpha) = (r^2 cos^2\alpha + r^{-1} sin^2\alpha)^{-3/2} \quad (10)$$

Here, α is the angle between the preferred orientation vector and the normal to the planes generating the diffracted peak and r is a refinable parameter. In all conditions, the diffraction profiles were fitted up to 100° (2θ) using the above mentioned approach because of the very low intensity of the peaks above 100°.

The Goodness of fit (GoF) indicates the quality of the fitting which is expressed as follows:

$$GoF = R_{wp}/R_{exp} \quad (11)$$

Here, R_{wp} is the weighted residual profile and R_{exp} is the expected profile.

1.3.2 (iv) Transmission Electron Microscopy (Chapters 6 and 7):

Disks with ~0.2 mm thickness were cut perpendicular to deformation direction using Electric Discharge Machining (EDM). Thereafter, disks were thinned to ~80 μm by polishing using 1200, 2400 and 4000 SiC grit papers. Thin foils for TEM were prepared using a Struers Tenupol-5 twin jet electropolisher with an electrolyte containing 5-7% of HClO4 in CH3OH. Electropolishing conditions were maintained at ~80 mA and -30°C for all conditions.

In the present studies described in Chapters 6 and 7, two transmission electron microscopes (TEM) were used. Conventional TEM was performed on a JEOL JEM-2011 at an accelerating voltage of 200 kV. Bright field (BF) and dark field (DF) images and selected area diffraction patterns (SADP) were taken using a Gatan Orius CCD camera and analysed using Gatan's Digital Micrograph software.

A JEOL ARM200F with a probe-corrected operated at 200 kV equipped with a cold field emission gun was used to acquire images. High-angle annular dark field (HAADF) images were acquired with 50 and 180 mrad inner and outer collection angles respectively, while BF images used 11 mrad collection angles. Both images were recorded with a dwell time of 38 μs, and convergence semi-angle of 25 mrad resulting in a probe current of 35 pA. A Centurio SSD Energy Dispersive X-ray Spectrometer (EDS) detector with an active area of 100 mm^2 was featured in the microscope. EDS spectra were acquired with a probe current of 290 pA. Dr Gilberto Casillas from Electron Microscope Centre, University of Wollongong operated the JEOL ARM200F.

1.3.2 (v) Atom Probe Tomography (Chapter 6):

The square cross-section (0.2×0.2 mm^2) rods with a minimum 10 mm length were prepared using EDM. Thereafter, atom probe specimens were prepared by electropolishing in a solution containing perchloric acid (5%), 2-butoxyelethnol (35%) and methanol at 30V at -40°C. The relatively blunt electropolished tips were sharpened in Zeiss Auriga Focused Ion Beam (FIB), reducing the radius to less than 100 nm. Atom probe experiments were conducted in a Cameca LEAP 4000X-SI™ instrument located at The University of Sydney by Dr Tong Li. Data acquisition was carried out in the laser pulsing mode at a specimen temperature of 50 K with a target evaporation rate of 5 ions per 1000 pulses, a pulse rate of 250 kHz, laser energy of 70 pJ and a laser spot size of approximately 2 μm. The wavelength of the UV laser was 355 nm. The APT data were reconstructed and analysed using the commercial IVAS 3.6.6™ software. Atom probe maps, iso-concentration surfaces, composition profiles and proxigrams were used for visualisation of phases and solute distribution/composition analysis. The error bars in the proxigrams have been calculated based on the statistical errors associated with APT [100].

1.3.3 Mechanical Testing Methods:

1.3.3 (i) Tensile Test (Chapters 3, 4 and 5):

Tensile specimens were machined by EDM into sub-sized tensile specimens (Chapters 2, 3 and 4) of gauge length 5.1 mm; width 2.18 mm and thickness 0.9 mm. Tensile tests were carried out with a μ-Tweezer Tensile Module (Kammrath & Weiss, GmbH) at a constant speed of 1.7 mm min^{-1} at room temperature. Three samples were tested per condition.

Work hardening behaviour of the samples was determined by fitting the stress-strain curves using rational polynomial functions via 2D-TableCurve. Pearson IV (a, b, c, d, e, f) equation was used to fit the curves.

1.3.3 (ii) Microhardness Tests (Chapter 3):

A Leitz RZD-DO Vickers microhardness tester was used to measure the microhardness value of the samples. 0.5 kg load was applied and twenty indentions were taken to obtain the average values.

1.4. Overview of the Chapters 2 to 7

The results obtained from the present study are given in the subsequent chapters and are summarized below

Chapter 2 describes the effect of the thermo-mechanical processing parameters on the microstructure evolution and distribution of alloying elements between the phases in the case of Ti-55511 and Ti-55521 alloys. The microstructure and phase compositions of the samples quenched from different stages of processing were analysed using FEGSEM with EDS. Microstructures were refined through thermo-mechanical processing in both alloys. The evolution of volume fraction of the phases and their compositions at each stage of TMP were determined. The effects of solute diffusion rates and Cr content on these processes were also highlighted.

These results were published in **Journal of Materials Science** 2012, 47(19), 7013-7025.

Chapter 3 illustrates the influence of cooling rates (10 Ks^{-1} and 1 Ks^{-1}) from α+β phase field to room temperature during thermo-mechanical processing on the microstructure evolution and mechanical properties in Ti-55511 and Ti-55521 alloys. Microstructural changes were observed using scanning electron microscopy and X-ray diffraction line profile analysis. Information about dislocation density, microstrain and stored energy of different crystallographic planes in both α and β phases has been obtained and discussed in relation to the cooling rates. Tensile properties of the samples processed under different cooling rates were also measured and related to the observed microstructures.

These results were published in **Materials Science and Engineering A** 2013, 576, 167-177.

Chapter 4 describes the effect of the ageing time at 650 °C on microstructure-mechanical property interrelationships in Ti-55511 alloy. FEGSEM coupled with EDS and μ tweezer tensile module testing was used to investigate microstructural evolution and mechanical behaviour. With increasing time at 650 °C more secondary α phase was formed. Tensile properties were found to be dependent on the α phase volume fraction. Significant elemental partitioning was noticed with increasing ageing time. The modified Crussard–Jaoul method was applied to characterise the work hardening behaviour of the alloy and three stages have been found.

These results were published in **Materials Science and Engineering A** 2014, 605, 89-97.

In **Chapter 5,** using state-of-the art techniques of scanning transmission electron microscopy (STEM) and atom probe tomography (APT), microstructural evolution, phase transformations and alloying elements distributions occurred during thermo-mechanical processing and subsequently ageing of Ti-55521 alloy were investigated. Effects of accelerated cooling during TMP and slow heating on the phase transformations were evaluated and discussed in detail. Based on the results, nucleation sites for α were suggested for TMP and early stage of ageing. Pile-up of the slowest diffusing solutes near the α/β interface was noticed in the β matrix. Significant improvement in mechanical properties was recorded after ageing compared to unaged TMP.

These results have been submitted for publication in **Journal of Alloys and Compounds**, 2014 (under review).

Chapter 6 discusses a comparative study between Ti-55511 and Ti-55521 alloys with respect to ageing treatment. The ageing was performed at 650°C from 3.6 ks to up to 28.8 ks. Thereafter, the alloys were characterised using scanning electron microscopy and tensile testing. Microstructure-properties relationships were established. The empirical relation between VHN and YS has been derived for Ti-55511 and Ti-55521 alloy, respectively. The effect of Cr content on β→α phase transformation and subsequently on mechanical properties has been highlighted.

These results were presented at the International Titanium Powder Processing Conference, Dec 2-4, 2013, NZ and will be submitted to **Materials Science and Technology**, 2014.

Chapter 7 describes the dependency of the beta phase stability on deformation behavior. Variation in beta phase stability was achieved by controlling the volume fraction of α phase. Room temperature compression tests were performed to determine the deformation mode. Microstructural features induced by compression were identified using transmission electron microscopy. Change in β phase stability was reflected in the twinning mode while stress-induced ω, and martensite along with slip were unchanged. An expansion of martensite area of the $\overline{Bo}$-$\overline{Md}$ phase stability diagram is proposed based on these findings.

These results have been published for publication in **Acta Materialia**, 2015, 84, 124-135.

References

[1] M. J. Donachie, *Titanium: a technical guide*: ASM International, 1988.

[2] Leyens C. and Peter M., *Titanium and Titanium alloys : Fundamentals and Application*: WILEY-VCH.

[3] M. J. Donachie, *Titanium: A Technical Guide*: ASM International, 2000.

[4] M. Hagiwara and S. Emura, Blended elemental P/M synthesis and property evaluation of Ti-1100 alloy, Materials Science and Engineering: A, 352 (2003) 85-92.

[5] O. M. Ivasishin, V. M. Anokhin, A. N. Demidik, and D. G. Savvakin, cost-effective blended elemental powder metallurgy of titanium alloys for transportation application, Key Engineering Materials 188 (2000) 55-62.

[6] V. N. Moiseev, Beta-titanium alloys and prospects of their development, Metal Science and Heat Treatment, 40 (1998) 482-485.

[7] V. N. Moiseev, High-strength titanium alloys for large parts of aircraft engines, Metal Science and Heat Treatment, 42 (2000) 81-83.

[8] R. R. Boyer and R. D. Briggs, The use of β titanium alloys in the aerospace industry, Journal of Materials Engineering and Performance, 14 (2005) 681-685.

[9] G. Neumann and C. Tuijn, "Chapter 4 Self-Diffusion and Impurity Diffusion in Group IV Metals," in *Pergamon Materials Series*. vol. Volume 14, N. Gerhard and T. Cornelis, Eds., ed: Pergamon, 2008, pp. 149-213.

[10] Lenain A., Clément N. , Véron M. , and Jacques P. J. , Characterisation of the phase transformations in a metastable β titanium alloy, Materials Science Forum, 539 - 543 (2007) 3712-3717.

[11] O. M. Ivasishin, P. E. Markovsky, S. L. Semiatin, and C. H. Ward, Aging response of coarse- and fine-grained β titanium alloys, Materials Science and Engineering: A, 405 (2005) 296-305.

[12] O. M. Ivasishin, S. L. Semiatin, P. E. Markovsky, S. V. Shevchenko, and S. V. Ulshin, Grain growth and texture evolution in Ti–6Al–4V during beta annealing under continuous heating conditions, Materials Science and Engineering: A, 337 (2002) 88-96.

[13] D.-G. Lee, C. Li, Y. Lee, X. Mi, and W. Ye, Effect of temperature on grain growth kinetics of high strength Ti–2Al–9.2Mo–2Fe alloy, Thermochimica Acta, 586 (2014) 66-71.

[14] A. Lenain, N. Clément, P. J. Jacques, and M. Véron, Characterization of the α phase nucleation in a two-phase metastable β titanium alloy, Journal of Materials Engineering and Performance, 14 (2005) 722-727.

[15] N. Clément, A. Lenain, and P. Jacques, Mechanical property optimization via microstructural control of new metastable beta titanium alloys, JOM Journal of the Minerals, Metals and Materials Society, 59 (2007) 50-53.

[16] C. Li, X. Wu, J. H. Chen, and S. van der Zwaag, Influence of α morphology and volume fraction on the stress-induced martensitic transformation in Ti–10V–2Fe–3Al, Materials Science and Engineering: A, 528 (2011) 5854-5860.

[17] W. Hongtao, Z. Z. Fang, and S. Pei, A CRITICAL REVIEW OF MECHANICAL PROPERTIES OF POWDER METALLURGY TITANIUM, International Journal of Powder Metallurgy, 46 (2010) 45-57.

[18] C. G. McCracken, C. Motchenbacher, and D. P. Barbis, REVIEW OF TITANIUM-POWDER-PRODUCTION METHODS, International Journal of Powder Metallurgy, 46 (2010) 19-26.

[19] K. Zhang, J. Mei, N. Wain, and X. Wu, Effect of Hot-Isostatic-Pressing Parameters on the Microstructure and Properties of Powder Ti-6Al-4V Hot-Isostatically-Pressed Samples, Metallurgical and Material Transactions A, 41 (2010) 1033-1045.

[20] H. Jiang, K. Zhang, F. A. Garcia-Pastor, M. H. Loretto, D. Hu, P. J. Withers, M. Preuss, and X. Wu, Microstructure and properties of hot isostatically pressed powder and extruded Ti25V15Cr2Al0·2C, Materials Science and Technology, 27 (2011) 1241-1248.

[21] F.-C. Yen and K.-S. Hwang, Shape memory characteristics and mechanical properties of high-density powder metal TiNi with post-sintering heat treatment, Materials Science and Engineering: A, 528 (2011) 5296-5305.

[22] I. Weiss and S. L. Semiatin, Thermomechanical processing of beta titanium alloys—an overview, Materials Science and Engineering: A, 243 (1998) 46-65.

[23] C. Sauer and G. Luetjering, Thermo-mechanical processing of high strength β-titanium alloys and effects on microstructure and properties, Journal of Materials Processing Technology, 117 (2001) 311-317.

[24] Y. Combres and B. Champin, presented at the Beta Titanium Alloys in the 1990s, Warrendale, PA, 1993.

[25] T. Maeda and M. Okada, presented at the Titanium 1995: Science and Technology, London, 1995.

[26] A.-M. Chaze and F. Montheillet, presented at the Beta Titanium Alloys, Editions de la Revue de Metallurgie,, Paris, 1994.

[27] I. Weiss, F. H. Froes, D. Eylon, and G. E. Welsch, Modification of alpha morphology in Ti-6Al-4V by thermomechanical processing, Metallurgical Transaction A, 17 (1986) 1935-1947.

[28] Y. Combres and B. Champin, presented at the Metallurgy and Technology of Practical Titanium Alloys, Warrendale, PA, 1994.

[29] N. G. Jones, R. J. Dashwood, D. Dye, and M. Jackson, Thermomechanical processing of Ti–5Al–5Mo–5V–3Cr, Materials Science and Engineering: A, 490 (2008) 369-377.

[30] T. W. Duerig, G. T. Terlinde, and J. C. Williams, Phase transformations and tensile properties of Ti-10V-2Fe-3AI, Metallurgical Transaction A, 11 (1980) 1987-1998.

[31] S.-z. Zhang, Z.-q. Liu, G.-d. Wang, L.-q. Chen, X.-h. Liu, and R. Yang, Microstructural evolution during aging of Ti-5Al-5Mo-5V-1Cr-1Fe alloy, Journal of Central South University of Technology, 16 (2009) 354-359.

[32] O. M. Ivasishin, P. E. Markovsky, Y. V. Matviychuk, S. L. Semiatin, C. H. Ward, and S. Fox, A comparative study of the mechanical properties of high-strength β-titanium alloys, Journal of Alloys and Compounds, 457 (2008) 296-309.

[33] A. Devaraj, S. Nag, R. Srinivasan, R. E. A. Williams, S. Banerjee, R. Banerjee, and H. L. Fraser, Experimental evidence of concurrent compositional and structural instabilities leading to ω precipitation in titanium–molybdenum alloys, Acta Materialia, 60 (2012) 596-609.

[34] S. Nag, R. Banerjee, R. Srinivasan, J. Y. Hwang, M. Harper, and H. L. Fraser, ω-Assisted nucleation and growth of α precipitates in the Ti–5Al–5Mo–5V–3Cr–0.5Fe β titanium alloy, Acta Materialia, 57 (2009) 2136-2147.

[35] A. Devaraj, R. E. A. Williams, S. Nag, R. Srinivasan, H. L. Fraser, and R. Banerjee, Three-dimensional morphology and composition of omega precipitates in a binary titanium–molybdenum alloy, Scripta Materialia, 61 (2009) 701-704.

[36] Y. Ohmori, T. Ogo, K. Nakai, and S. Kobayashi, Effects of ω-phase precipitation on β→α, α″ transformations in a metastable β titanium alloy, Materials Science and Engineering: A, 312 (2001) 182-188.

[37] M. J. Blackburn and J. C. Williams, Trans. Met. Soc. AIME, 242 (1968) 2461.

[38] G. M. Pennock, H. M. Flower, and D. R. F. West, presented at the Titanium'80 Science and Technology, 1980.

[39] A. Devaraj, S. Nag, and R. Banerjee, Alpha phase precipitation from phase-separated beta phase in a model Ti–Mo–Al alloy studied by direct coupling of transmission electron microscopy and atom probe tomography, Scripta Materialia, 69 (2013) 513-516.

[40] F. Prima, P. Vermaut, G. Texier, D. Ansel, and T. Gloriant, Evidence of α-nanophase heterogeneous nucleation from ω particles in a β-metastable Ti-based alloy by high-resolution electron microscopy, Scripta Materialia, 54 (2006) 645-648.

[41] T. Furuhara, T. Maki, and T. Makino, Microstructure control by thermomechanical processing in β-Ti–15–3 alloy, Journal of Materials Processing Technology, 117 (2001) 318-323.

[42] S. Azimzadeh and H. J. Rack, Phase transformations in Ti-6.8Mo-4.5Fe-1.5Al, Metallurgical and Materials Transactions A, 29 (1998) 2455-2467.

[43] S. Nag, R. Banerjee, J. Y. Hwang, M. Harper, and H. L. Fraser, Elemental partitioning between α and β phases in the Ti–5Al–5Mo–5V–3Cr–0.5Fe (Ti-5553) alloy, Philosophical Magazine, 89 (2009) 535-552.

[44] G. Terlinde, T. Duerig, and J. Williams, Microstructure, tensile deformation, and fracture in aged ti 10V-2Fe-3Al, Metallurgical and Materials Transaction A, 14 (1983) 2101-2115.

[45] Ankem S. and Seagle S., "Heat treatment of metastable beta titanium alloys," in *Beta Titanium Alloys of the 1980's*, Boyer R.R. et al (Eds)TMS, Warrandale,PA, USA, 1984, p. 107.

[46] N. Niwa and H. Takatori, "Effect of Duplex aging after cold working on the mechanical properties of Ti-10V-3Cr-3Sn-3Al," presented at the Titanium '92, Science and Technologies, Warrandale, PA, 1993.

[47] J. Wang and X. Duan, "A study of the duplex aging of Ti-10V-1Fe-1Cr-3Al near-beta alloy," presented at the 6th world conference on Ti France, 1988.

[48] D. Buttinelli, F. Felli, G. D. Festa, and A. J. Querales, "Effect of heat treatments on the fatigue behavior of the Beta-C Ti alloy," presented at the Titanium '92, Science and Technology, Warrandale, PA, 1993.

[49] V. N. Moiseev, N. V. Sysoeva, and M. I. Ermolova, Heat treatment of granulated VT22 alloy, Metal Science and Heat Treatment, 38 (1996) 42-45.

[50] V. N. Moiseev, N. V. Sysoeva, and T. V. Ishun'kina, Metallurgy of granules of high-strength titanium alloys, Metal Science and Heat Treatment, 37 (1995) 248-250.

[51] A. M. Parshin, S. S. Ushkov, and I. I. Yarmolovich, Cracking of titanium alloy VT22 during aging, Metal Science and Heat Treatment, 15 (1973) 313-316.

[52] J. Huang, Z. Wang, and K. Xue, Cyclic deformation response and micromechanisms of Ti alloy Ti–5Al–5V–5Mo–3Cr–0.5Fe, Materials Science and Engineering: A, 528 (2011) 8723-8732.

[53] D. Qin, Y. Lu, Q. Liu, and L. Zhou, Effects of Si addition on mechanical properties of Ti–5Al–5V–5Mo–3Cr alloy, Materials Science and Engineering: A, 561 (2013) 460-467.

[54] J. C. Fanning, Properties of TIMETAL 555 (Ti-5Al-5Mo-5V-3Cr-0.6Fe), Journal of Materials Engineering and Performance, 14 (2005) 788-791.

[55] S. L. Nyakana, J. C. Fanning, and R. R. Boyer, Quick reference guide for β titanium alloys in the 00s, Journal of Materials Engineering and Performance, 14 (2005) 799-811.

[56] Furuhara T. and Aaronson H. I., Crystallography and interfacial structure of proeutectoid α grain boundary allotriomorphs in a hypoeutectoid Ti-Cr alloy, Acta Metallurgica et Materialia, 39 (1991) 2887-2899.

[57] Mullins W.W. and Sekerka R.F., Morphological stability of a particle growing by diffusion or heat flow Journal of Applied Physics, 34 (1963) 323-329.

[58] H. I. Aaronson, G. Spanos, R. A. Masamura, R. G. Vardiman, D. W. Moon, E. S. K. Menon, and M. G. Hall, Sympathetic nucleation: an overview, Materials Science and Engineering: B, 32 (1995) 107-123.

[59] Furuhara T. and Maki T., Accommodation of transformation strain during the growth of precipitates, Scripta Materialia, 34 (1996) 929-934.

[60] Furuhara T. and Maki T., Variant selection in heterogeneous nucleation on defects in diffusional phase transformation and precipitation, Materials Science and Engineering: A, 312 (2001) 145-154.

[61] W.G. Burgers, On the process of transition of the cubic-body-centered modification into the hexagonal-close-packed modification of zirconium, Physica, 1 (1934) 561-586.

[62] Pitsch W. and Schrader A., Arch. Eisenhutt Wes., 29 (1958) 715.

[63] D.I. Potter, The structure, morphology and orientation relationship of V3N in α-vanadium, Journal of the Less Common Metals, 31 (1973) 299-309.

[64] W. Rong and G. L. Dunlop, The crystallography of secondary carbide precipitation in high speed steel, Acta Metallurgica, 32 (1984) 1591-1599.

[65] S. L. Sass, The structure and decomposition of Zr and Ti b.c.c. solid solutions, Journal of the Less Common Metals, 28 (1972) 157-173.

[66] D. De Fontaine, Mechanical instabilities in the b.c.c. lattice and the beta to omega phase transformation, Acta Metallurgica, 18 (1970) 275-279.

[67] D. De Fontaine, N. E. Paton, and J. C. Williams, The omega phase transformation in titanium alloys as an example of displacement controlled reactions, Acta Metallurgica, 19 (1971) 1153-1162.

[68] I. A. Bagariatskii, G. I. Nosova, and T. V. Tagunova, Factors in the Formation of Metastable Phases in Titanium-Base Alloys, Soviet Physics Doklady, 3 (1958) 1014.

[69] Boyer R.R., Welsch G., and Collings E.W., *Materials Properties Handbook: Titanium Alloys*: ASM Handbook, 1994.

[70] D. de Fontaine and O. Buck, A Monte Carlo simulation of the omega phase transformation, Philosophical Magazine, 27 (1973) 967-983.

[71] Duerig T.W. and Williams J.C., "Microstructure and properties of beta Titanium alloys," in *Beta Titanium alloys in the 80's: proceedings of the symposium*, Atlanta, GA, United States, 1984, pp. 19-67

[72] S. Neelakantan, P. E. J. Rivera-Díaz-del-Castillo, and S. van der Zwaag, Prediction of the martensite start temperature for β titanium alloys as a function of composition, Scripta Materialia, 60 (2009) 611-614.

[73] G. Ghosh and G. B. Olson, Kinetics of F.C.C. → B.C.C. heterogeneous martensitic nucleation—I. The critical driving force for athermal nucleation, Acta Metallurgica et Materialia, 42 (1994) 3361-3370.

[74] Bowles J. S. and Mackenzie J. K., The crystallography of martensite transformations I, Acta Metallurgica, 2 (1954) 129-137.

[75] M. S. Wechsler, D. S. Liebeman, and T. A. Read, Trans. AIME, 197 (1953) 1503.

[76] S. C. Wang, M. Aindow, and M. J. Starink, Effect of self-accommodation on α/α boundary populations in pure titanium, Acta Materialia, 51 (2003) 2485-2503.

[77] Otte H.M., *The Science, Technology and Application of Titanium, 645-657,1970*

[78] T. W. Duerig, J. Albrecht, D. Richter, and P. Fischer, Formation and reversion of stress induced martensite in Ti-10V-2Fe-3Al, Acta Metallurgica, 30 (1982) 2161-2172.

[79] B. A. Hatt and V. G. Rivlin, Phase transformations in superconducting Ti-Nb alloys, Journal of Physics D: Applied Physics, 1 (1968) 1145.

[80] N. E. Paton and J. C. Williams, The influence of oxygen content on the athermal β-ω transformation, Scripta Metallurgica, 7 (1973) 647-649.

[81] J. Y. Lim, C. J. McMahon, D. P. Pope, and J. C. Williams, The effect of oxygen on the structure and mechanical behavior of Aged Ti-8 Wt pct Al, Metallurgical Transaction A, 7 (1976) 139-144.

[82] Z. Liu and G. Welsch, Effects of oxygen and heat treatment on the mechanical properties of alpha and beta titanium alloys, Metallurgical Transaction A, 19 (1988) 527-542.

[83] M. Yan, M. S. Dargusch, T. Ebel, and M. Qian, A transmission electron microscopy and three-dimensional atom probe study of the oxygen-induced fine microstructural features in as-sintered Ti–6Al–4V and their impacts on ductility, Acta Materialia, 68 (2014) 196-206.

[84] M. Yan, W. Xu, M. S. Dargusch, H. P. Tang, M. Brandt, and M. Qian, Review of effect of oxygen on room temperature ductility of titanium and titanium alloys, Powder Metallurgy, 57 (2014) 251-257.

[85] S. Kuramoto, T. Furuta, J. Hwang, K. Nishino, and T. Saito, EBSP Analysis on Microstructure of Gum Metal after Plastic Deformation, Journal of the Japan Institute of Metals and Materials, 69 (2005) 953-961.

[86] T. Furuta, S. Kuramoto, J. H. Hwang, K. Nishino, and T. Saito, Elastic Deformation Behavior of Multi-Functional Ti--Nb--Ta--Zr--O Alloys, Materials Transactions, 46 (2005) 3001-3007.

[87] R. J. Talling, R. J. Dashwood, M. Jackson, and D. Dye, On the mechanism of superelasticity in Gum metal, Acta Materialia, 57 (2009) 1188-1198.

[88] R. J. Talling, R. J. Dashwood, M. Jackson, S. Kuramoto, and D. Dye, Determination of () in Ti–36Nb–2Ta–3Zr–0.3O (wt.%) (Gum metal), Scripta Materialia, 59 (2008) 669-672.

[89] H. Xing, J. Sun, Q. Yao, W. Y. Guo, and R. Chen, Origin of substantial plastic deformation in Gum Metals, Applied Physics Letters, 92 (2008) -.

[90] M. Morinaga, N. Yukawa, T. Maya, K. Sone, and H. Adachi, "Theoritical Design of Titanium alloys," presented at the Sixth world conference on Titanium alloys, Cannes, France, 1988.

[91] T. Grosdidier, Y. Combres, E. Gautier, and M. J. Philippe, Effect of microstructure variations on the formation of deformation-induced martensite and associated tensile properties in a β metastable Ti alloy, Metallurgical and Materials Transactions A, 31 (2000) 1095-1106.

[92] T. Grosdidier and M. J. Philippe, Deformation induced martensite and superelasticity in a β-metastable titanium alloy, Materials Science and Engineering: A, 291 (2000) 218-223.

[93] T. Grosdidier, C. Roubaud, M.-J. Philippe, and Y. Combres, The deformation mechanisms in the β-metastable β-Cez titanium alloy, Scripta Materialia, 36 (1997) 21-28.

[94] T. Grosdidier, C. Roubaud, M.-J. Philippe, S. Zaefferer, M. Zandona, E. Gautier, and Y. Combres, Structure/Deformation Relationship in a ß Metastable Ti-Alloy, Journal of Physics IV France, 06 (1996) C1-435-C1-444.

[95] C. Li, J. H. Chen, X. Wu, W. Wang, and S. van der Zwaag, Tuning the stress induced martensitic formation in titanium alloys by alloy design, Journal of Materials Science, 47 (2012) 4093-4100.

[96] S. Neelakantan, D. San Martin, P. E. J. Rivera-Díaz-del-Castillo, and S. van der Zwaag, Plasticity induced transformation in a metastable β Ti-1023 alloy by controlled heat treatments, Materials Science and Technology, 25 (2009) 1351-1358.

[97] L. Lutterotti and P. Scardi, Simultaneous structure and size–strain refinement by the Rietveld method, Journal of Applied Crystallography, 23 (1990) 246-252.

[98] N. Popa, The (hkl) Dependence of Diffraction-Line Broadening Caused by Strain and Size for all Laue Groups in Rietveld Refinement, Journal of Applied Crystallography, 31 (1998) 176-180.

[99] W. Dollase, Correction of intensities for preferred orientation in powder diffractometry: application of the March model, Journal of Applied Crystallography, 19 (1986) 267-272.

[100] M. K. Miller, *Atom Probe Tomography: Analysis at the Atomic Level*: Springer US, 2000.

Chapter 2

Microstructure evolution and alloying elements distribution between the phases in powder near-β titanium alloys during thermo-mechanical processing

J Mater Sci (2012) 47:7013–7025
DOI 10.1007/s10853-012-6652-3

Microstructure evolution and alloying elements distribution between the phases in powder near-β titanium alloys during thermo-mechanical processing

Mansur Ahmed · Azdiar A. Gazder · Dmytro G. Savvakin · Orest M. Ivasishin · Elena V. Pereloma

Received: 20 April 2012 / Accepted: 8 June 2012 / Published online: 26 June 2012

Abstract In the present study, two powders near-β Ti alloys having a nominal composition of Ti-5Al-5Mo-5V-XCr-1Fe (X = 1–2, wt%) were studied. The alloys were produced via the blended elemental powder metallurgy technique using hydrogenated Ti powder. Microstructure evolution and the distribution of the alloying elements between the phases were investigated after each step of thermo-mechanical processing (TMP). Microstructures were refined through the TMP in both alloys. Porosity was reduced with deformation at 1173 K (900 °C) in the β phase field. The $\beta \rightarrow \alpha$ phase transformation occurred during soaking at 1023 K (750 °C) in the $\alpha + \beta$ phase field. Fragmentation of the continuous grain boundary α occurred because of the 40 % deformation at 1023 K (750 °C). Variation in the concentration of the alloying elements in each phase took place through the diffusion during soaking in the $\alpha + \beta$ phase field, e.g. exit of β-stabilisers from the α-phase. However, the α phase remained supersaturated with β stabilisers. Deformation had no influence on the distribution of the alloying elements. An addition of 1 % Cr content slightly affects the amount of the α phase formed and β grain size, but it has no noticeable effect on the distribution of the alloying elements between the phases.

M. Ahmed (✉) · A. A. Gazder · E. V. Pereloma
School of Mechanical, Materials & Mechatronic Engineering, University of Wollongong, Wollongong, NSW 2522, Australia
e-mail: ma960@uowmail.edu.au

D. G. Savvakin · O. M. Ivasishin
Institute for Metal Physics, National Academy of Sciences Ukraine, UA-03142 Kiev, Ukraine

Introduction

Near β-Ti alloy VT22 and its modified compositions are used for aerospace applications in landing gear parts (e.g. as bogie beams and lower and upper torque links) and in the compressors of aero-engines because of their high strength (1100–1260 MPa) and fracture toughness (66–77 MPa $m^{1/2}$), reasonably good ductility (8–14 %), favourable fatigue strength, as well as corrosion resistance properties [1, 2]. In order to increase the affordability of titanium alloys through reduction in production costs, near-net shape powder metallurgy techniques are fast becoming the most preferred production route compared with conventional techniques. This is mainly because powder metallurgy-based processes return significantly higher material yield by minimising waste [3, 4]. Amongst the powder metallurgy methods for Ti alloy production, the blended elemental powder metallurgy (BEPM) technique is regarded as the most cost effective which can produce alloy having high density with a uniform distribution of the alloying elements throughout the matrix after sintering [5, 6]. If the BEPM is undertaken with Ti powder only, then an additional hot isostatic pressing (HIP) step is necessary to achieve high density after sintering. On the other hand, if hydrogenated Ti powder is used in BEPM, then additional HIP step is not required. Thus, the production cost can be reduced further. Ivasishin et al. [7] produced Ti-6Al-4V alloy via the BEPM technique using hydrogenated Ti powder avoiding any additional HIP step and obtained a high density ($\sim$99 %) in the powder alloy after sintering.

In general, near-β Ti alloys respond to heat treatment, such that the grain boundary α (α_{GB}) phase, the *inter*-granular and *intra*-granular α phases, and the β grains are the microstructural constituents obtained through thermo-mechanical

processing (TMP). The size, shape and the amount of the various phases can be modified by varying the TMP parameters. Sauer and Luetjering [8] utilised various processing schedules to achieve microstructures in two high strength β-alloys: β-CEZ and Ti-6246. They produced a bimodal microstructure using a TMP technique known as $\alpha + \beta$ processing. The schedule involved β annealing treatment, hot deformation in the $\alpha + \beta$ two phase field, followed by a holding in the $\alpha + \beta$ phase field. During the cooling to room temperature from the β-annealing temperature and the heating to $\alpha + \beta$ hot deformation temperature from room temperature, large equiaxed β grains surrounded by a continuous α phase were produced. The plastic deformation in the $\alpha + \beta$ phase field produced dislocation density which serves as nucleation site of α phase during subsequent cooling to room temperature. Thereafter, the $\alpha + \beta$ holding produced acicular α phase via $\beta \rightarrow \alpha$ phase transformation. However, the above mentioned $\alpha + \beta$ processing produced a microstructure comprising equiaxed β grains along with continuous α phase and acicular α phase. The continuous grain boundary α surrounding the β grains is deleterious for ductility because the strain is localised in the continuous α leading to crack nucleation and fractures at grain boundaries [9–11]. In order to minimise the effect of continuous grain boundary α, Clement et al. [10] suggested two possible preventive measures which are (i) to apply $\alpha + \beta$ hot forging to the alloy after holding in the $\alpha + \beta$ phase field, and (ii) to apply cold forging before ageing. Weiss and Semiatin [12] reported that the $\alpha + \beta$ hot deformation should be performed while the volume fraction of the α phase is $\leq$30 %.

There are very few findings on the distribution of the alloying elements between the phases (α and β) during TMP. The distribution of the alloying elements depends on their solubility, diffusion rate, as well as the time allowed for diffusion to take place. Nag et al. [13] studied elemental partitioning between the α and β phases in Ti-5Al-5Mo-5V-3Cr alloy. Using 3D atom probe tomography, they found that all the alloying elements partitioned pronouncedly between the phases during sub-transus annealing through the diffusion of the alloying elements. Mo piled up more at the interfaces because of its slow diffusivity than other alloying elements during step-quenching to 973 K (700 °C) and holding for 1800 s which can play a vital role in growth kinetics of α phase.

In this study, a traditional Ti-5Al-5Mo-5V-1Cr-1Fe (VT22) alloy was chosen as it is produced via the cost-effective BEPM method using powder for the first time, and a modified VT22 (Ti-5Al-5Mo-5V-2Cr-1Fe) alloy was also selected since the Cr content controls the grain size during heat treatment in the β phase field [14], in addition to reducing the amount of α phase [15, 16] formed during soaking in the $\alpha + \beta$ phase field resulting in improved ductility [17]. However, if more Cr ($\geq$ 2 wt%) is added to the alloy, then the Mo equivalent is further increased ($Mo_{eq.} = 1 \times Mo + 0.67 \times V + 1.6 \times Cr + 2.9 \times Fe - 1 \times Al$, the amount which determines the β stability of the alloy). The greater Mo equivalent results in steeper β-transus gradient, which makes the processing window narrower and more difficult to control [18]. The aim of the present study is to examine the microstructure's evolution and the distribution of the alloying elements between the phases of two near-β Ti alloys during TMP. The nominal compositions of the alloys are Ti-5Al-5Mo-5V-XCr-1Fe (X = 1−2) (in wt%). The two alloys will hereafter be referred to as Ti-55511 and Ti-55521 alloys, respectively, throughout the text. Other objectives include reducing the harmful effect of the continuous grain boundary α and understanding the effect of additional Cr content in Ti-55521 alloy.

Materials and experimental procedure

Hydrogenated Ti powder containing 3.5 wt% hydrogen was blended with 50Al–50V (wt%) master alloy powder and Mo, Cr, Fe elemental powders to achieve the required compositions of the Ti-5Al-5Mo-5V-1Cr-1Fe (Ti-55511) and Ti-5Al-5Mo-5V-2Cr-1Fe (Ti-55521) alloys. The size of each alloying element's powder was less than 40 μm with the exception of Mo (40–63 μm). Thereafter, the blended powders were die pressed at room temperature under a pressure of 650 MPa to form bar-shaped green compacts. The compacts were then sintered in two steps comprising heating at 1293 K (1020 °C) for 3600 s, followed by heating at 1523 K (1250 °C) for 21600 s. The average compositions (in wt%) of the two as-sintered alloys determined by Energy dispersive spectroscopy (EDS) are given in Table 1.

Cylindrical samples with a diameter of 4 mm and length of 6 mm were machined from the sintered bars. A Gleeble 3500 thermo-mechanical simulator in pocket jaw mode was employed for the TMP of both alloys. A K-type thermocouple (a combination of Chromel and Alumel) was

Table 1 The average composition of the as-sintered alloys determined by EDS (Energy Dispersive Spectroscopy) (in wt %)

Alloy	Al	Mo	V	Cr	Fe	Ti
Ti-55511	4.75 ± .05	3.95 ± .08	4.00 ± .03	0.70 ± .03	0.75 ± .04	Bal.
Ti-55521	4.90 ± .04	4.00 ± .05	3.90 ± .06	1.60 ± .05	0.90 ± .07	Bal.

spot welded to the specimens at their longitudinal midpoint. The specimens were placed between copper jaws and resistance heated. The entire TMP schedule (Fig. 1) was conducted in a vacuum of 3.8×10^{-4} torr to prevent high temperature oxidation and atmospheric contamination. The samples for analysis were water quenched after four steps of the TMP schedule described below:

(i) Step I: heating at 10 Ks^{-1} to 1223 K (950 °C), hold for 120 s
(ii) Step II: Step I + Cooling at 35 Ks^{-1} from 1223 K (950 °C) to 1173 K (900 °C) where 25 % deformation took place
(iii) Step III: Step II + Cooling at 35 Ks^{-1} from 1173 K (900 °C) to 1023 K (750 °C), 1800 s soaking
(iv) Step IV: Step III + 40 % deformation at 1023 K (750 °C).

In addition, the fifth sample was processed similar to the one as in step III, but with 40 % deformation at 1173 K (900 °C). This schedule is termed Step III(a) hereafter.

The samples of both alloys were prepared for metallography after cutting perpendicular to the deformation direction. Then, the samples were hot mounted under a pressure of 7.17 MPa at 423 K (150 °C) for 480 s. The mounted samples were rough ground using 500 and 1200 SiC papers, fine ground with a 15 μm diamond disc, followed by fine polishing with colloidal silica suspension. Thereafter, the polished samples were etched to reveal the microstructures using Kroll's reagent (2 ml HF, 5 ml HNO_3 and 93 ml H_2O).

A JEOL JSM 7001F Field Emission Gun—Scanning Electron Microscope (FEG-SEM), equipped with a 127 eV Bruker-AXS XFlash detector energy dispersive X-ray spectroscopy (EDS) system, was used for semi-quantitative compositional analysis to find out the variation in the concentration between the phases. The accelerating voltage was 15 kV, and a probe current was chosen to provide an EDX count rate of approximately 25 kcps, so as to ensure good statistics. X-ray maps were then acquired for 14.4 ks using an image resolution of 1200 × 1024 pixels and a dwell time of 12 ms. The X-ray line scans were then analysed in the X-ray maps using an interactive standardless PB-ZAF analysis whereby the elements were set and an appropriate Bremsstrahlung background was selected to obtain an optimum fit before quantification was performed. The accuracy of the compositional measurement was ± 5 %. At least 30 X-ray line scans were performed for each phase composition, whereas each x-ray line scan was a combination of numerous points. Moreover, the EDS spectra did not overlap. Back-scattered electron (BSE) mode was used for microstructure imaging. The porosities and area fractions of the different phases of both alloys were measured using secondary electron images of the microstructures and MATLAB image processing program. The β grain size and the width of the grain boundary α were measured using Image Tool 3.0 software.

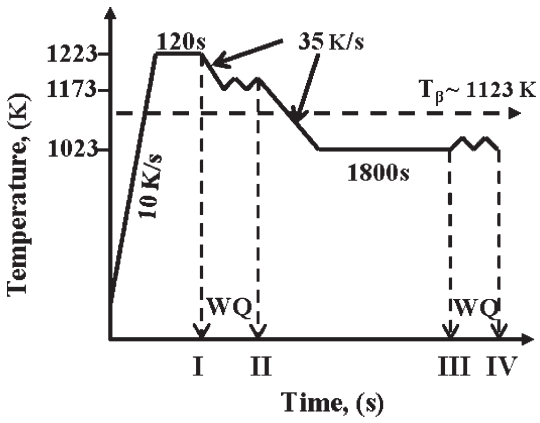

Fig. 1 A schematic illustration of the TMP schedule employed in the present study

Results

Microstructure characterisation

Microstructure of the as-sintered material

The BSE microstructures of the as-sintered samples for the two alloys are shown in Fig. 2. Three types of α phase were present in the microstructure of the as-sintered alloys: (i) a grain boundary α phase, (ii) an *intra*-granular α phase that nucleates and grows inside the β grains, and (iii) an *inter*-granular α phase that nucleates from the grain boundary α phase and grows into the β grains. For the purposes of this study, the *intra*-granular and *inter*-granular α phases are collectively termed the 'α phase' throughout the text. In the as-sintered samples, the width of the grain boundary α phase was 2.58 ± 1.34 μm in the Ti-55511 alloy and 2.52 ± 0.65 μm in the Ti-55521 alloy. The grain boundary α phase around the β grain was continuous in both alloys. The average β grain sizes for the Ti-55511 and Ti-55521 alloys were 74 ± 17 and 70 ± 14 μm, respectively. Both alloys still contained ~2 % porosity in the as-sintered form.

Microstructure after annealing and deformation in the β phase field

The BSE microstructures of the Ti-55511 and Ti-55521 near-β Ti alloys after annealing at 1223 K (950 °C) for 120 s (step I) and 25 % deformation at 1173 K (900 °C) (step II) are shown in Fig. 3. Tables 2 and 3 indicate the area fractions of the porosity and all the constituent phases,

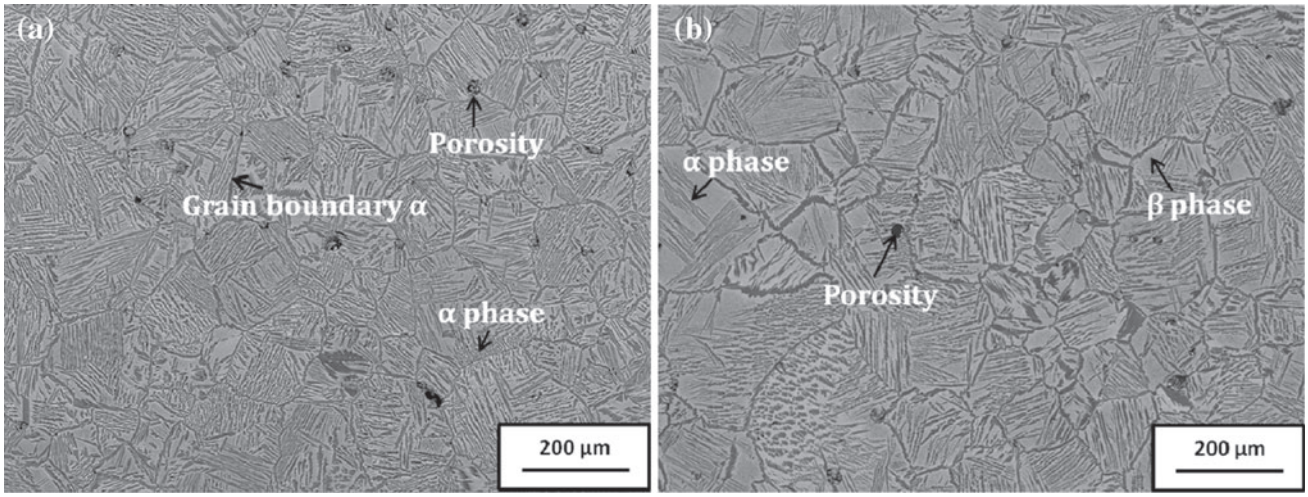

Fig. 2 Back-scattered electron images of the as-sintered microstructures of (**a**) Ti-5Al-5Mo-5V-1Cr-1Fe (Ti-55511) and (**b**) Ti-5Al-5Mo-5V-2Cr-1Fe (Ti-55521) alloys. The α phase in Fig. 2(**a**) indicates *inter*-granular α, and the α phase in Fig. 2(**b**) indicates *intra*-granular α

the width of the grain boundary α phase, as well as the average β grain size of the Ti-55511 and Ti-55521 alloys, respectively after each TMP step. Since the appearance of a wide and continuous grain boundary α phase is deleterious for ductility [9–11], this was partially negated by near dissolution of the α phase during annealing for 120 s at 1223 K (950 °C), which is above the β-transus temperature (~1123 K (850 °C) for the Ti-55511 alloy [19]). Prolonged heating at the super-transus temperature was deliberately avoided to minimise the coarsening of the β grains. The area fractions of the porosity after β-annealing were 1.9 and 1.7 % for the Ti-55511 and Ti-55521 alloys, respectively. As a result of annealing in the β phase field during Step I, the average β grain size was 73 ± 12 and 68 ± 9 μm in the Ti-55511 and Ti-55521 alloys, respectively, which are nearly constant in comparison with as-sintered condition. The area fractions of grain boundary α phase were 0.7 and 0.8 % in the Ti-55511 alloys and Ti-55521 alloys, respectively. The width of the grain boundary α phase reduced to 0.99 ± 0.35 μm in the

Table 2 The amount of porosity, β grain size and the various phases in the Ti-55511 alloy after thermo-mechanical processing steps

TMP Step	Porosity (%)	β grain size (μm)	Width of α_{GB} phase (μm)	Area fractions (%)	
				Grain boundary α-phase (α_{GB})	α phase
I	1.9	73 ± 12	0.99 ± 0.35	0.7	0.5
II	0.3	56 ± 18	0.65 ± 0.15	1.5	1.3
III	0.1	58 ± 16	1.05 ± 0.34	3.6	34.1
III(a)	0.1	–	0.76 ± 0.26	3.2	34.7
IV	0.07	–	0.67 ± 0.22	2.1	35.9

Table 3 The amount of porosity, β grain size and the various phases in the Ti-55521 alloy after thermo-mechanical processing steps

TMP Step	Porosity (%)	β grain size (μm)	Width of α_{GB} phase (μm)	Area fractions (%)	
				Grain boundary α-phase (α_{GB})	α phase
I	1.7	68 ± 9	1.01 ± 0.28	0.8	0.5
II	0.6	54 ± 15	0.92 ± 0.31	2.3	1.4
III	0.1	55 ± 18	1.15 ± 0.37	3.7	29.6
III(a)	0.1	–	0.87 ± 0.23	3.4	31.9
IV	0.03	–	0.88 ± 0.25	3.1	32.3

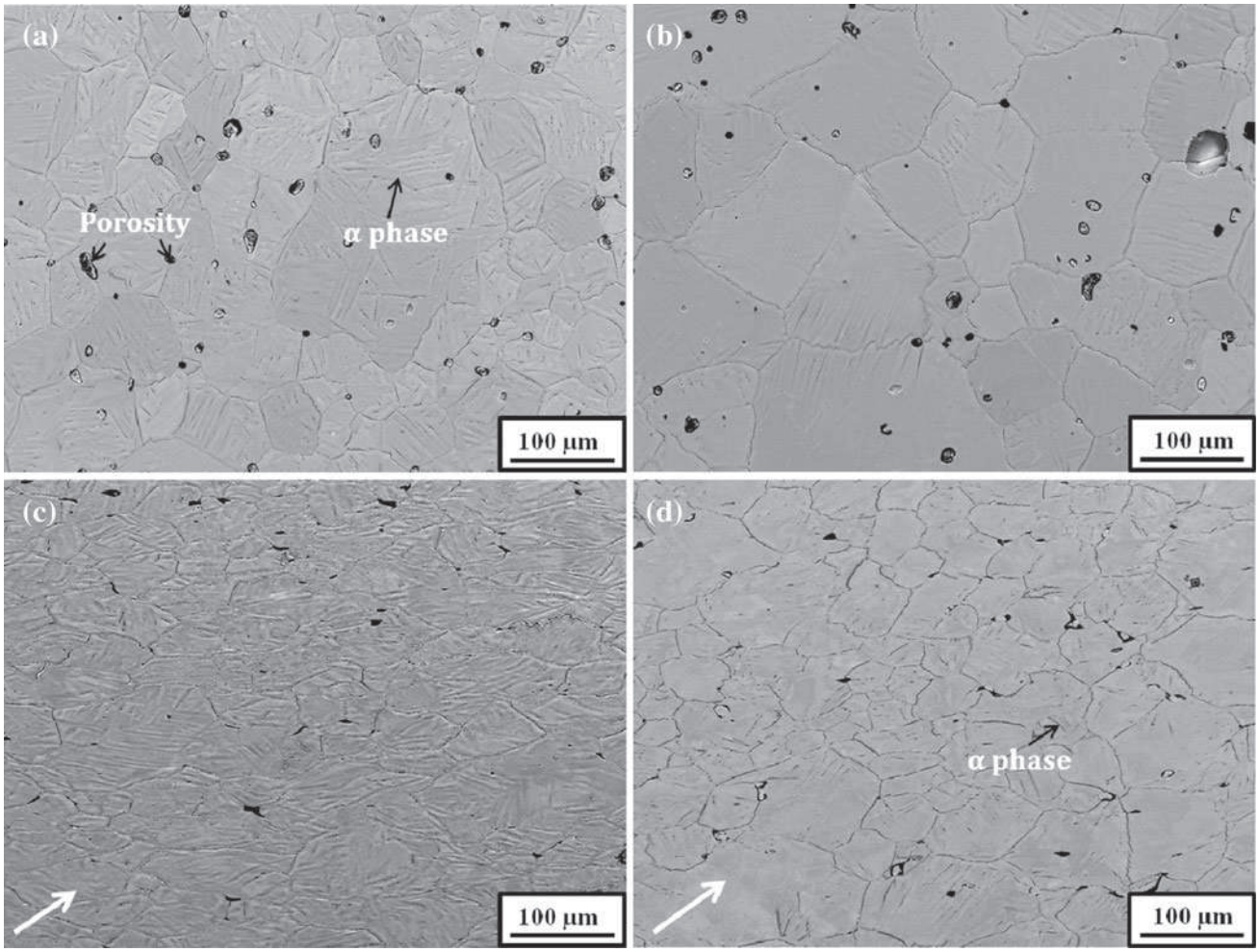

Fig. 3 Back-scattered electron images of (**a**, **c**) Ti-55511 and (**b**, **d**) Ti-55521 alloys after (**a**, **b**) step I and (**c**, **d**) step II of the thermo-mechanical processing. *White arrow* in (**c**, **d**) denotes the deformation direction

Ti-55511 and to 1.01 ± 0.28 μm in the Ti-55521 alloys compared with the as-sintered condition (Fig. 5). In addition, the area fraction of the α phase was 0.5 % for both alloys (Fig. 3(a, b)).

Figure 3(c, d) is the representative microstructures after step II (25 % deformation at 1173 K (900 °C) + step I) of both alloys. The direction of deformation is marked by a white arrow in Fig. 3(c, d). Deformation in the β phase field (Step II) significantly reduced the amount of porosity in both alloys in comparison with step I. The measured porosities were 0.3 and 0.6 % for the Ti-55511 and Ti-55521 alloys, respectively. A significant reduction in the average β grain size (56 ± 18 and 54 ± 15 μm for the Ti-55511 and for the Ti-55521 alloys, respectively) was also observed after step II. The area fraction of grain boundary α phase increased to 1.5 % in the Ti-55511 alloy and 2.3 % in the Ti-55521 alloy as a result of β grains getting subdivided because of the deformation at 1173 K (900 °C). The area fraction of α phase also increased to 1.3 and 1.4 % in the Ti-55511 and Ti-55521 alloys, respectively. An obvious reduction in the width of the grain boundary α phase and α phase is clearly visible in the microstructures when compared with the as-sintered condition and step I. The reduced width of the grain boundary α phase was 0.65 ± 0.15 and 0.92 ± 0.31 μm in both alloys, respectively, after step II (Fig. 5). Although, continuous grain boundary α phase was still predominant in the microstructures of both alloys, localised regions containing fragmented grain boundary α phase was also seen.

Microstructure after soaking and deformation at α + β phase field

The BSE microstructures of the studied alloys after step III (Fig. 4(a, b)), step IIIa (Fig. 4(c, d)), and step IV (Fig. 4(e, f)) are shown in Fig. 4. The microstructures after soaking in α + β phase field show the transformation of β phase to the α phase along with a broadening of the width of the α constituents. The microstructures of the alloys were refined during soaking at 1023 K (750 °C) for 1800 s.

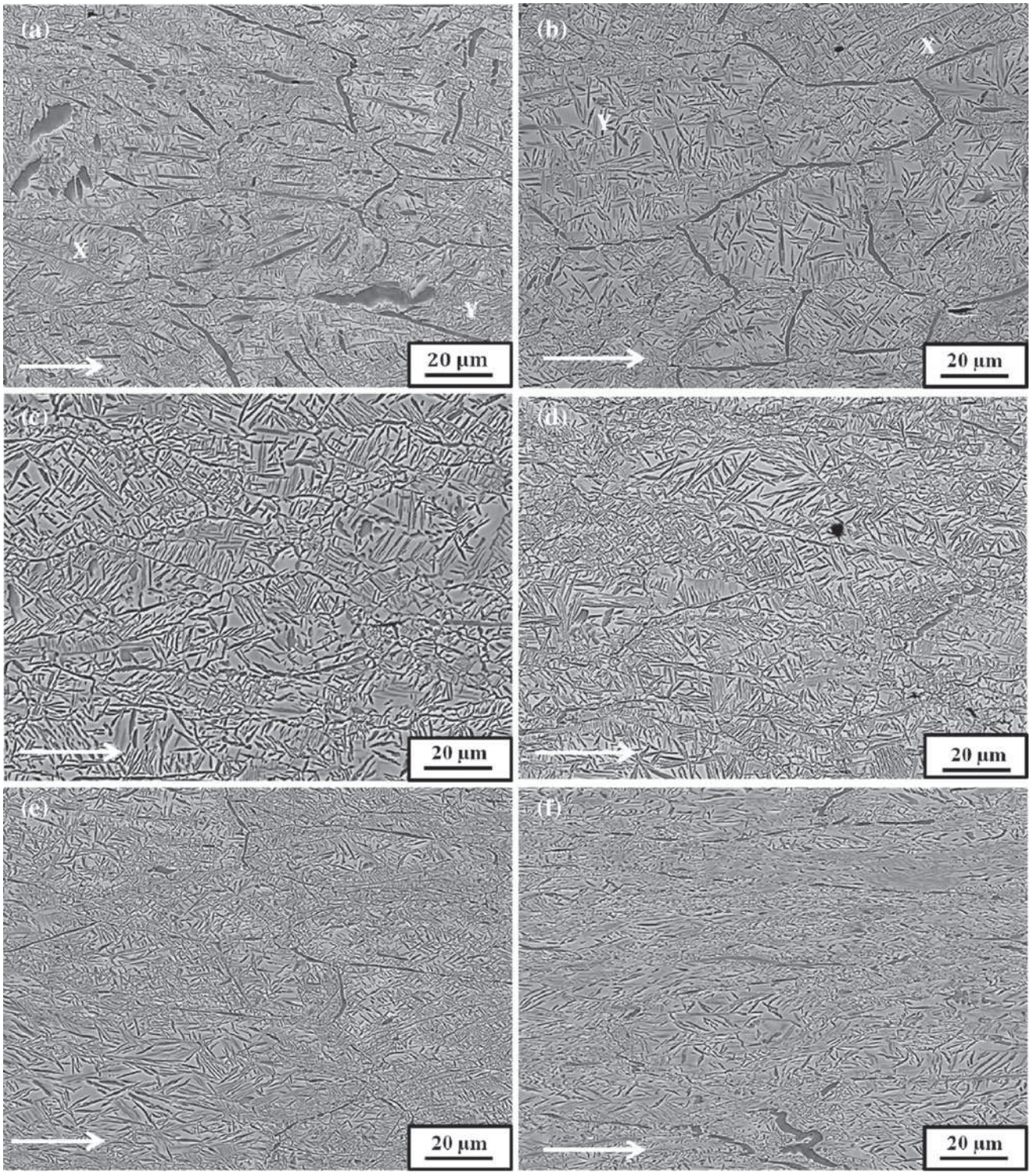

Fig. 4 Back-scattered electron images of (**a**, **c**, **e**) Ti-55511 and (**b**, **d**, **f**) Ti-55521 alloys after (**a**, **b**) step III, (**c**, **d**) step III (**a**) and (**e**, **f**) step IV of the thermo-mechanical processing. X in Figures (**a**), (**b**) indicates the colony and Y in Figures (**a**), (**b**) indicates the basket-weave morphologies. *White arrows* indicate the deformation direction

Figure 4(a, b) corresponds to the microstructures of the Ti-55511 and Ti-55521 alloys, respectively, after step III of TMP. Step III processing resulted in a reduction of the porosity to 0.1 % for both alloys. The β grain size was 58 ± 16 μm in the Ti-55511 alloy and 55 ± 18 μm in the Ti-55521 alloy which remained approximately constant in

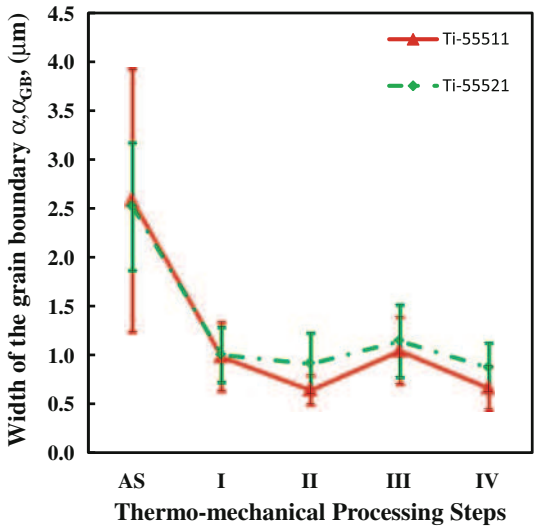

Fig. 5 Variation of the width of the grain boundary α (α_{GB}) phase with the thermo-mechanical processing steps. Step III (**a**) is not plotted in the above Figure because of its different parameters. The width of the grain boundary α after step III (**a**) is presented in the Tables 2 and 3 for both alloys. *AS* as-sintered

comparison with step II. The area fraction of the grain boundary α increased slightly to 3.6 % in the Ti-55511 alloy and 3.7 % in the Ti-55521 alloy due to the broadening of width of the grain boundary α phase. The width of the grain boundary α phase increased to 1.05 ± 0.34 and 1.15 ± 0.37 μm in the both alloys, respectively, after step III (Fig. 5). On the other hand, the area fraction of the α phase increased most noticeably to 34.1 % in the Ti-55511 alloy and 29.6 % in the Ti-55521 alloy. The α phase had both, colony-type (marked with the letter 'X' in Fig. 4(a, b)) as well as basket weave type (marked with the letter 'Y' in Fig. 4(a, b)) morphologies in both alloys.

The microstructures shown in Fig. 4(c, d) are obtained after step III(a) processing for both alloys, respectively. The area fraction of porosity was ~0.1 % in both alloys and remained constant in comparison with step III. The β grains were elongated along the direction of deformation as a result of higher deformation (40 %) at 1173 K (900 °C). The area fractions of grain boundary α phase were 3.2 and 3.4 % in the Ti-55511 and Ti-55521 alloys, respectively. The widths of the grain boundary α phase were 0.76 ± 0.26 and 0.87 ± 0.23 μm in the Ti-55511 and Ti-555521 alloys, respectively, which are lower than that of the step III due to the narrowing of the width of the grain boundary α phase (Tables 2 and 3). The area fractions of the α phase were 34.7 and 31.9 % in the Ti-55511 Ti-55521 alloys, respectively, after step III(a). A slight increment in the area fractions of α phase was observed in the Tables 2 and 3 after step III(a) in comparison with those after step III.

Figure 4(e, f) shows the microstructures of both alloys after step IV which consisted of an additional 40 % deformation at 1023 K (750 °C) in the β phase field after step III. The area fractions of the porosity decreased slightly to 0.07 and 0.03 % in the Ti-55511 and Ti-55521 alloys, respectively, as a result of deformation at 1023 K (750 °C). The area fractions of the grain boundary α phase were reduced to 2.1 and 3.1 % in the Ti-55511 and Ti-55521 alloys, respectively, through the fragmentation along with a narrowing of their width. The measured widths of the grain boundary α were 0.67 ± 0.22 and 0.88 ± 0.25 μm in the Ti-55511 and Ti-55521 alloys, respectively. While the narrowing of the grain boundary α phase was predominant in the Ti-55511 alloy, the fragmentation of the same phase was more in the Ti-55521 alloy. The area fractions of the α phase increased slightly to 35.9 and 32.3 % in the Ti-55511 and Ti-55521 alloys, respectively.

Distribution of alloying elements between the phases

Figures 6 and 7 show the X-ray elemental maps of the different alloying elements for the Ti-55511 and Ti-55521 alloys, respectively, after step IV processing. The alloying elements are found to be distributed rather uniformly throughout the β matrix phase. The histograms in Figs. 8, 9, 10 indicate the compositional variation in the alloying elements in the grain boundary α (Fig. 8), α phase (Fig. 9) and β phase (Fig. 10) after each TMP step for the Ti-55511 alloy (Figs. 8(a), 9(a), 10(a)) and for the Ti-55521 alloy (Figs. 8(b), 9(b), 10(b)). The diffusion rates of the alloying elements in α- and β-Ti at 1023 K (750 °C) are shown in Table 4 obtained from [20–23]. From the Table 4, it is clear that Fe is the fastest diffusive element, and Mo has the slowest diffusivity in β-phase. The diffusion rate of Cr is slower than that of Fe, but faster than that of other alloying elements (Al, Mo and V). V and Al have approximately similar diffusion rates, which are intermediate between Cr and Mo ones. The solubility of the alloying elements in both α-Ti and β-Ti at 1023 K (750 °C) processing temperature is shown in Table 5 obtained from [24]. The solubility in descending order of the alloying elements is Mo > V > Cr > Fe > Al in β-Ti; and Al > Mo > Cr > V > Fe in α-Ti.

Distribution in grain boundary α phase

The changes in the amount of alloying elements in the grain boundary α phase after each TMP step are shown in Fig. 8(a) for the Ti-55511 alloy and in Fig. 8(b) for the Ti-55521 alloy. The extent of α-stabilising alloying element (Al) remained approximately constant throughout the TMP in the Ti-55511 alloy. In contrast, the amount of Al increased slightly after step III and thereafter remained

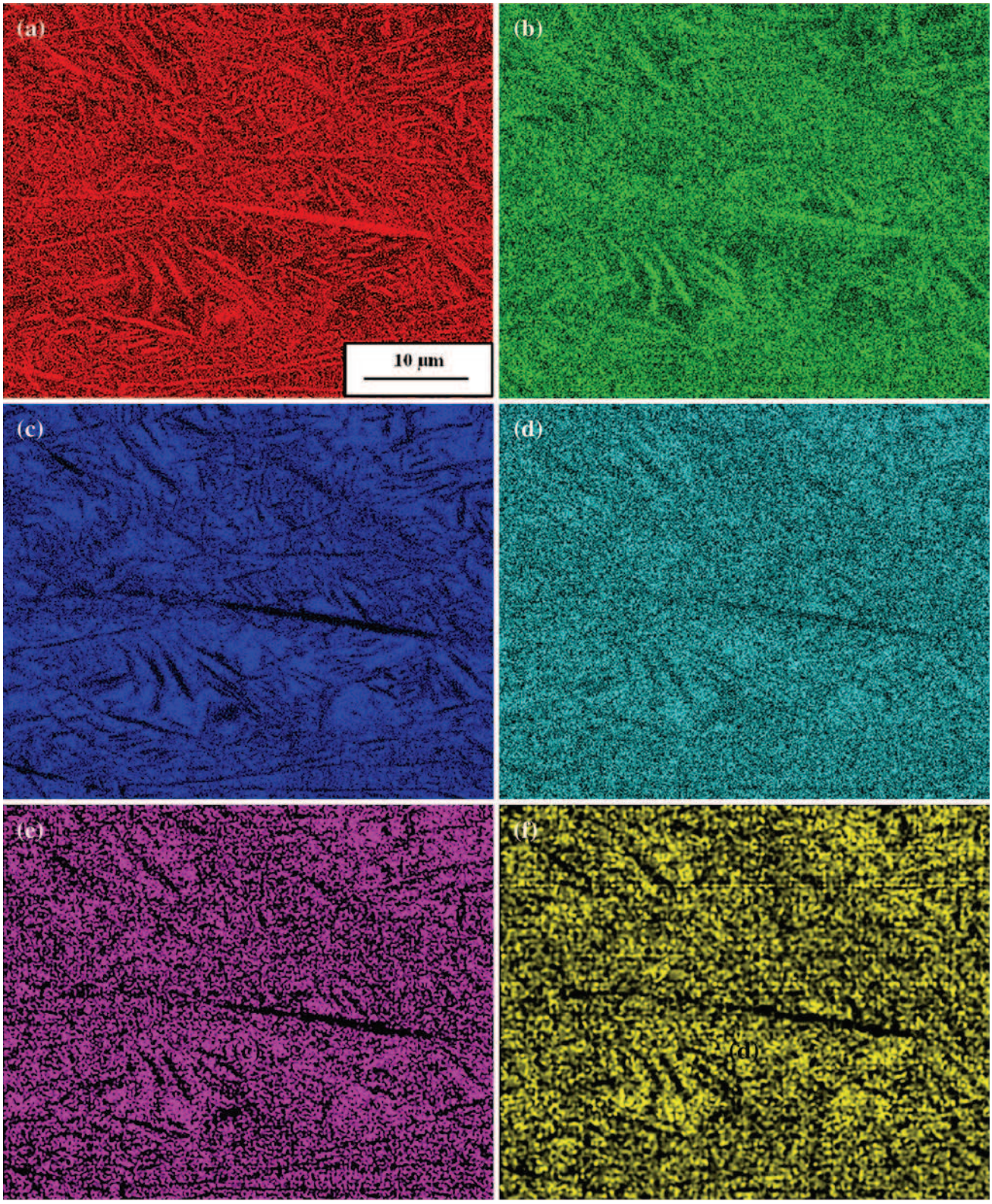

Fig. 6 X-ray elemental maps of Ti-55511 alloy after step IV corresponding to SEM image in (**a**) Ti, (**b**) Al, (**c**) Mo, (**d**) V, (**e**) Cr and (**f**) Fe

constant in the Ti-55521 alloy. The amount of β stabilising element, Mo, reduced slightly after step III in the Ti-55511 alloy. In contrast, the Mo content remained approximately constant throughout the processing steps in the case of the Ti-55521 alloy. A significant decrease in the amount of V, Cr and Fe was observed in both alloys after step III. The

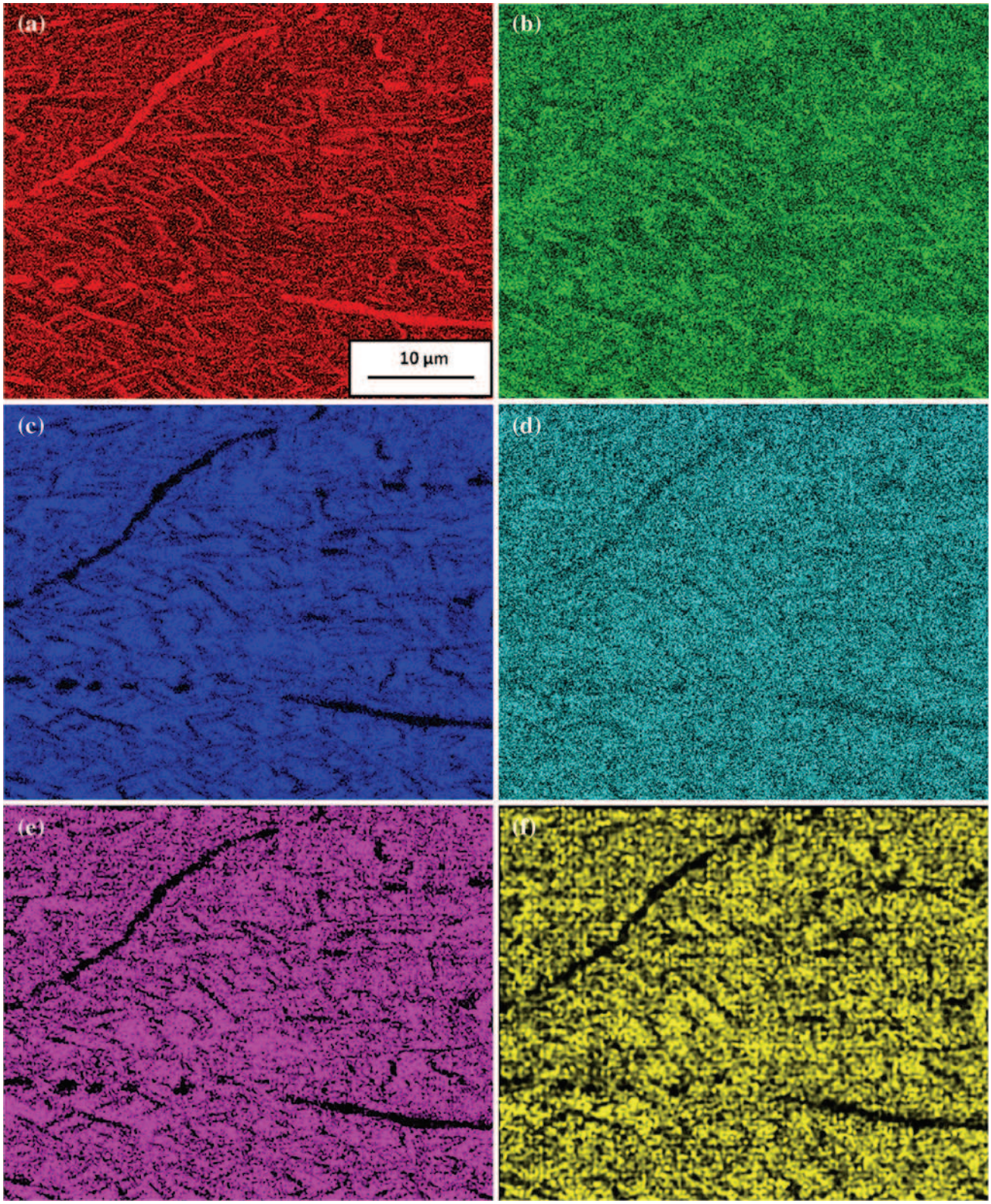

Fig. 7 X-ray elemental maps of Ti-55521 alloy after step IV corresponding to SEM image in (**a**) Ti, (**b**) Al, (**c**) Mo, (**d**) V, (**e**) Cr and (**f**) Fe

amounts of α-stabilising alloying element (Al) and β-stabilising alloying elements (Mo, V, Cr and Fe) were approximately the same after steps III and III(a) in both alloys. In addition, there was no deviation in the concentration of the alloying elements after steps III and step IV in both alloys.

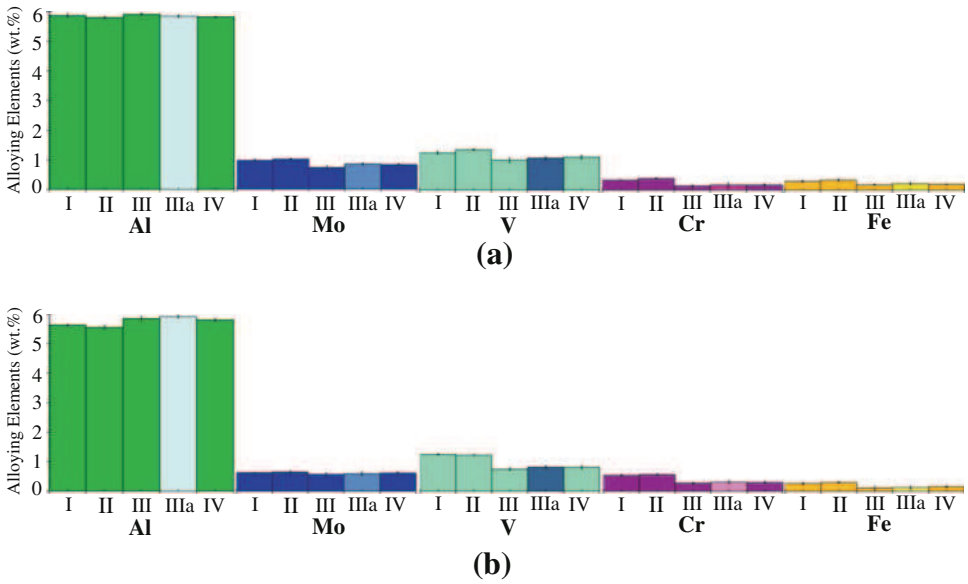

Fig. 8 Variation in grain boundary α phase (α_{GB}) alloy composition with thermo-mechanical processing through Steps I to IV in: (**a**) Ti-55511 and (**b**) Ti-55521 alloys

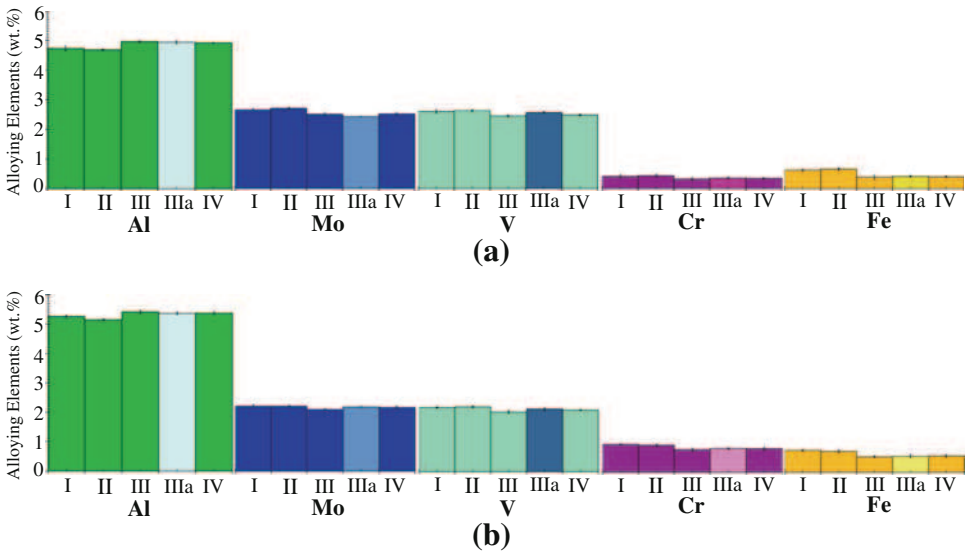

Fig. 9 Variation in the α phase (α) alloy composition with thermo-mechanical processing through Steps I to IV in: (**a**) Ti-55511 and (**b**) Ti-55521 alloys

Distribution in α phase

The variation of the concentration of the alloying elements in the α phase is shown in Fig. 9(a, b) for both alloys. It could be seen from the histograms of all alloying elements that, there was approximately no variation in the alloying elements' contents in α phase after steps I and II in both alloys. The amount of Al content in α phase increased slightly after step III for both alloys. Thereafter, it remained approximately constant after step IV. Between steps III and III(a), there was no change in Al content for both alloys. The concentration of Mo and V was not changed throughout the TMP except slight reduction that occurred after step III in both alloys. In the case of both the alloys, the amounts of Cr and Fe decreased after step III and remained thereafter constant during subsequent processing. There was approximately no variation in the concentrations of the β-stabilising alloying elements after steps III and III(a) in both alloys.

Distribution in beta (β) phase

Figure 10(a, b) indicates the variation in β phase alloy composition with TMP from step I to step IV in the Ti-55511 and Ti-55521 alloys, respectively. From the histogram for the α stabiliser, there was approximately no variation in the Al content between step I and step II for both alloys. However, the amount of Al content reduced significantly after step III, and remained thereafter constant after step IV in both alloys. Also, there was no variation in the Al concentration after steps III and III(a) for both alloys. Similarly, the main variation in the concentration of

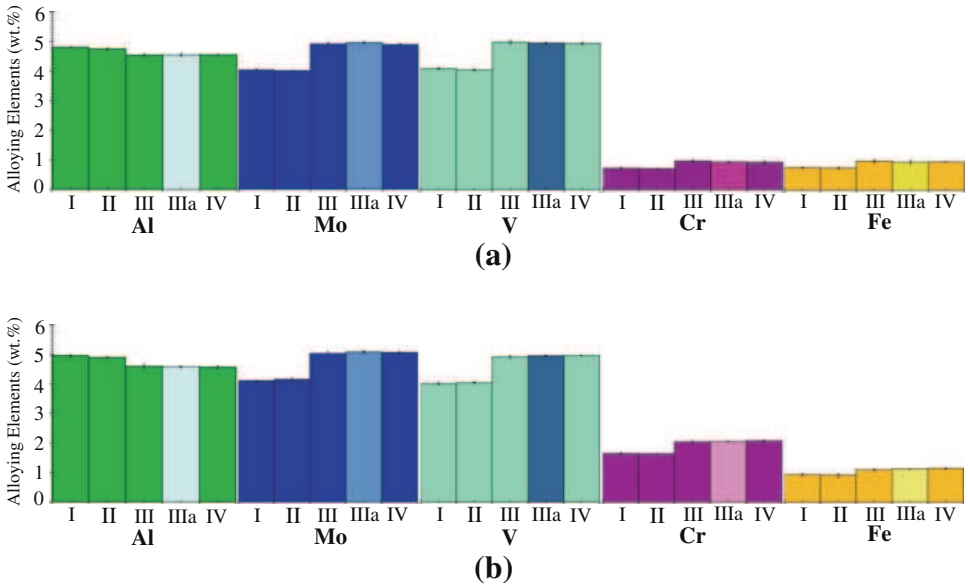

Fig. 10 Variation in β phase (β) alloy composition with thermo-mechanical processing through Steps I to IV in: (**a**) Ti-55511 and (**b**) Ti-55521 alloys

Table 4 Diffusion rates of the alloying elements in α-Ti and β-Ti at 1023 K (750 °C) [20–23]

Temperature	Matrix phase	Al ($\times 10^{-14}$ m^2/s)	Mo ($\times 10^{-14}$ m^2/s)	V ($\times 10^{-14}$ m^2/s)	Cr ($\times 10^{-14}$ m^2/s)	Fe ($\times$ 10^{-14} m^2/s)
1023 K	β-Ti	0.48 ± 0.05	0.05 ± 0.01	0.52 ± 0.03	1.40 ± 0.11	13.5 ± 0.13
	α-Ti	10^{-4}	–	–	0.65	9.6

Table 5 Solubilities of the alloying elements in α-Ti and β-Ti at 1023 K (750 °C) [24]

Temperature	Matrix phase	Al (wt%)	Mo (wt%)	V (wt%)	Cr (wt%)	Fe (wt%)
1023 K	β-Ti	0	<15	<9	<8	<7
	α-Ti	<9	<0.5	<0.3	<0.15	<0.047

β stabilisers (Mo, V, Cr and Fe) took place after step III. However, as expected, the distribution trend for the β stabilisers was the opposite one for the Al, i.e., their amount increased after step III and remained approximately constant thereafter. Between step III and step III(a), no variation in the concentration of β stabilisers was also observed in β phase for both alloys.

Discussion

Microstructure characterisation

In the present study, the microstructure evolution during TMP is investigated with respect to the area fraction of the porosity, the β grain size and the constituent phases. Through the TMP, the microstructures of the two alloys were refined in terms of β grain size as well as α phases (grain boundary α and α phase). The significant amount of porosity inherited from sintering was closed through applying deformation at 1173 K (900 °C) for both alloys. Porosity was also reduced during step III by healing pores through the activated diffusion at high density of crystal defects formed during deformation of step II [5]. The average β grain size was slightly coarser in the Ti-55511 alloy after steps I to III in comparison with the Ti-55521 alloy. Zhao et al. [14] reported the effect of Cr on reducing the β grain coarsening in Ti-25V-15Cr-0.2Si alloy compared to Ti-25V-10Cr-0.2Si alloy. No β grain growth was observed after step III because residual pores as well as the α phase presented at this stage prevented it. β grain sizes corresponding to the Steps III(a) to IV were not recorded in Tables 2 and 3 because the β grains were elongated along the deformation direction after steps III(a) and IV. The average width of the grain boundary α decreased after step II for both alloys because of the deformation at high temperature in the β phase field (Fig. 5). The width of the grain boundary α increased after step III because of the soaking at 1023 K (750 °C) and thereafter decreased with further processing. During step III, the area fraction of the grain

boundary α increased (2.1 % for the Ti-55511 and 1.4 % for the Ti-55521 alloys) slightly because of the coarsening of the grain boundary α, as the average width increased from 0.65 ± 0.15 to 1.05 ± 0.34 μm in the Ti-55511 alloy and from 0.92 ± 0.31 to 1.15 ± 0.37 μm in the Ti-55521 alloy (Fig. 5). Interestingly, the area fraction of the grain boundary α decreased after step IV. It may have two reasons: (i) through the reduction of the width of the grain boundary α and (ii) some fragmented parts of the grain boundary α were considered as α phase because of their size and shape. There was still a very small amount of the α phase (0.50 % in both alloys) present in the microstructure after step I because 120 s annealing time in the β phase field (1223 K) was insufficient to dissolve the α phase completely which carried over from the sintering stage. However, 120 s annealing time was used to minimise the β grain growth. Deformation during steps II and IV increased the area fraction of the α phase; there may have two reasons: (i) increase in dislocation density which serve as nucleation sites for α phase and (ii) the fragmented grain boundary α was considered as α phase because of their size and shape. The soaking at 1023 K (750 °C) in the α + β phase field for 1800 s resulted in 32.8 % α phase in the Ti-55511 alloy and 28.2 % in the Ti-55521 alloy through the progress of diffusion-controlled β → α phase transformation. In comparison, the amount of α phase produced in the Ti-55521 alloy was less than in the Ti-55511 alloy during step III. It is due to the effect of the 1 % additional Cr content in the Ti-55521 alloy on the β phase transformation to α phase. As additional 1 % Cr increased the Mo equivalent of the alloy which ultimately lowered the β transus temperature [12] of the Ti-55521 alloy compared to that for Ti-55511 alloy. So, the temperature difference between the β transus temperature to soaking temperature (750 °C) in the α + β phase field is larger for the Ti-55511 alloy than for the Ti-55521 alloy. Thus, more α phase formed in Ti-55511 alloy than in Ti-55521 alloy. Previous studies [25, 26] of the Ti-10 V-2Fe-3Al and Ti-LCB alloys, have also found that larger amount of α phase formed when the temperature difference between the β transus temperature and soaking temperature in the α + β phase field was also larger. Higher amount of α phase (34.7 % for the Ti-55511 alloy and 31.9 % for the Ti-55521 alloy) was obtained after step III(a) than after step III. Higher amount of deformation (40 % vs. 25 %) in the β phase field created more dislocations which serve as nucleation sites for the α phase during subsequent soaking at 1023 K (750 °C). Thus, more α phase obtained after step III(a) than step III.

Alloying elements distribution between the phases

Diffusivity of the alloying elements is calculated in binary system (Ti-X, where X = alloying elements). If more than one alloying element is added to the system, then diffusivity of all alloying elements change [20, 27]. Yang et al. [27] mentioned that diffusivity of a fast diffusion element is decreased by adding less diffusive element and diffusivity of less diffusive element increase simultaneously. It was reported in [20] that the addition of 4.36 wt% of Al to Ti decreased the diffusivity of Cr from 2.839×10^{-16} to 1.183×10^{-16} m^2/s (~2.4 times) at 874 K (601 °C) because Al has lower diffusivity than Cr in Ti. According to the diffusion rate of Fe and Cr in α-Ti from Table 4, Fe should move at least 6.6 μm and Cr should move 1.71 μm distances during 1800 s of soaking at 1023 K (750 °C). These distances are much smaller than the width of grain boundary α after step III, and it is clear that this time is not sufficient to remove the supersaturation of Fe and Cr in grain boundary α. Thus, β stabilising alloying elements of the grain boundary α could not reach the equilibrium concentration after step III, because of insufficient time, indicated in Table 5. From Figs. 8, 9, 10, it is clear that phase transformation from β phase to α phase occurred during TMP of step III through the diffusion of the alloying elements resulting in change in the composition and area fraction of the phases. With the formation of the α phase during step III, the area fraction of α phase increases. The newly formed α which was produced during step III may either increase or decrease the composition of the entire α phase (entire α phase = the newly formed α which formed during step III + existing α which existed before step III). It depends on the composition and area fraction of the newly formed α and the existing α phase. If the newly formed α has higher concentration of alloying elements with larger area fraction than the existing α phase, then the result is an increment in the alloy composition of the entire α phase. On the other hand, if the newly formed α is depleted in alloying elements and represents larger area fraction than the existing α phase, then this will decrease the alloy composition of the entire α phase. As a result of the above described process, as well as of diffusion of the β stabilisers out of the α phase, the composition of the phases changed significantly after step III (Figs. 8, 9, 10).

During step III and step III (a), the β stabilisers diffused into the favoured β phase and diffused out of the α phase. This phenomenon is also a factor to increase the β stabilisers content in the β phase. It is also noticeable that the concentration of the β stabilisers is higher in the α phase than in the grain boundary α phase. As β → α phase transformation is diffusion controlled [28], the first portions of newly formed α phase will have relatively high content of β stabilising alloying elements, which inherited from the parent phase and had insufficient time to diffuse out. However, with time these β stabilisers will diffuse out of the α phase for this phase to achieve equilibrium composition indicated in Table 5. However, time may not be

sufficient to reach the equilibrium composition, thus the α phase remains saturated with β stabilisers. On the other hand, the α phase formed at higher temperature (step I and step II) will have higher concentration of Al than α phase formed at lower temperature at 1023 K (750 °C). This is due to the depletion of the Al in remaining β phase as a result of initial α phase transformation. As there was no variation in the concentration of the alloying elements after Steps I and II, and steps III and IV, so it can be said that deformation in either β or α + β phase field had no effect on the distribution of alloying elements between the phases for both alloys. In addition, higher deformation in the β phase field did not affect on the distribution of the alloying elements.

Conclusions

Microstructure and distribution of alloying elements of two near β titanium alloys (Ti-55511 and Ti-55521) after TMP showed that

- As a result of TMP, porosity reduced to 0.07 % for Ti-55511 alloy and 0.03 % for Ti-55521 alloy. Most of the residual porosity has been closed during deformation at 1123 K (900 °C) in the β phase field.
- Owing to the soaking at 1023 K (750 °C) in the α + β phase region for 1800 s, 32.8 % α phase is obtained in Ti-55511 alloy and 28.2 % in Ti-55521 alloy. Fragmentation of continuous grain boundary α phase occurred through deformation in the α + β phase field. The morphology of the α phase and the distribution nature of the alloying elements between the phases was approximately the same in both alloys.
- Elemental partitioning between the phases is observed in the alloys. Phase transformation from β to α phase occurred through diffusion of the alloying elements. Higher concentration of β-stabilising alloying elements was in α phase than in the grain boundary α phase. In the case of both alloys, β-stabilising alloying elements could not reach their equilibrium content in α phase because of insufficient time. Higher deformation in the β phase field as well as deformation in two-phase field had no effect on the variation of the alloying elements in the phases for the studied alloys.
- From the above discussion, it follows that alloying with additional 1 % Cr content slightly reduces the amount of α phase formed, as well as β grain size, whereas the distribution of the alloying elements between the phases was not affected.

Acknowledgements This study was supported by the Engineering Materials Institute strategic grant. The authors acknowledge the technical support during Gleeble tests by Mr. B. De Jong and Dr. L. Chen, UOW and use of UOW Electron Microscopy Centre, in particular JEOL 7001F, which was purchased with ARC support (LE0882613). Mr. Mansur Ahmed gratefully acknowledges the University of Wollongong Postgraduate Award (UPA) and the useful discussions with Mr. M. Reid, UOW.

References

1. Moiseev VN (1998) Met Sci Heat Treat 40:482
2. Moiseev VN (2000) Met Sci Heat Treat vol. 42:81
3. Froes FH, Eylon D (1990) Int Mater Rev 35:162
4. Moxson V, Senkov ON, Froes FH (1998) Int J Powder Metall 34:45
5. Carman A, Zhang LC, Ivasishin OM, Savvakin DG, Matviychuk MV, Pereloma EV (2011) Mater Sci Eng A 528:1686
6. Savvakin DG, Carman A, Ivasishin OM, Matviychuk MV, Gazder AA, Pereloma EV (2012) Metall Mater Trans A 43:716
7. Ivasishin OM, Savvakin DG, Moxson VS, Bondareva KA, Froes FH (2002) Mater Technol Adv Perform Mater 17:20
8. Sauer C, Luetjering G (2001) J Mater Process Tech 117:311
9. Chesnutt J, Froes FH (1977) Metall Mater Trans A 8:1013
10. Clement N, Lenain A, Jacques PJ (2007) JOM 59:50
11. Terlinde G, Duerig T, Williams J (1983) Metall Mater Trans A 14:2101
12. Weiss I, Semiatin SL (1998) Mater Sci Eng A 243:46
13. Nag S, Banrjee R, Hwang JY, Harper M, Fraser HL (2009) Philos Mag 89:535
14. Zhao YQ, Xin SW, Zeng WD (2009) J Alloys Compd 481:190
15. Polmear IJ (2006) Light alloys from traditional alloys to nanocrystals, 4th edn. Elsevier, Amsterdam
16. Banerjee S, Mukhopadhyay P (2007) Phase transformations: example from titanium and zirconium alloys. Elsevier, Amsterdam
17. Terlinde G, Rathien HJ, Schwalbe KH (1988) Metall Trans A 19A:1037
18. Jones NG, Dashwood RJ, Dye D, Jackson M (2008) Mater Sci Eng A 490:369
19. Zhang SZ, Liu ZQ, Wang GD, Chen LQ, Liu XH, Yang R (2009) J Cent South Univ Technol 16:354
20. Nakajima H, Ogasawara K, Yamaguchi S, Koiwa M (1990) Mater Trans JIM 31:249
21. Neumann G, Tuijn C (2008) Self-diffusion and impurity elements diffusion in pure metals: handbook of experimental data 14:149. Elsevier, Amsterdam
22. Gibbs GB, Graham D, Tomlin DH (1963) Philos Mag 8:1269
23. Lee SY, Iijima Y, Hirano KI (1991) Mater Trans JIM 32:451
24. Massalski TD, Okamoto H, Subramanian PR, Kasprzak L (eds) (1990) Binary alloys phase diagrams. ASM International, Materials Park
25. Lenain A, Clement N, Veron M, Jacques P (2007) Mater Sci Forum 3712:539–543
26. Li C, Wu X, Chen JH, Zwaag SV (2011) Mater Sci Eng A 528:5854
27. Yang YF, Luo SD, Schaffer GB, Qian M (2011) Mater Sci Eng A 528:6719
28. Ivasishin OM, Markovsky PE (1996) JOM 48:48

Chapter 3

The effect of cooling rates on the microstructure and mechanical properties of thermo-mechanically processed Ti-Al-Mo-V-Cr-Fe Alloys

Materials Science & Engineering A 576 (2013) 167–177

Contents lists available at SciVerse ScienceDirect

Materials Science & Engineering A

journal homepage: www.elsevier.com/locate/msea

The effect of cooling rates on the microstructure and mechanical properties of thermo-mechanically processed Ti–Al–Mo–V–Cr–Fe alloys

Mansur Ahmed [a,*], Dmytro G. Savvakin [b], Orest M. Ivasishin [b], Elena V. Pereloma [a,c]

[a] School of Mechanical, Materials and Mechatronic Engineering, University of Wollongong, NSW 2522, Australia
[b] Institute for Metal Physics, National Academy of Sciences of Ukraine, UA-03142 Kiev, Ukraine
[c] Electron Microscopy Centre, University of Wollongong, NSW 2519, Australia

ARTICLE INFO

Article history:
Received 7 November 2012
Received in revised form
15 March 2013
Accepted 29 March 2013
Available online 11 April 2013

Keywords:
Ti alloys
Cooling rate
X-ray diffraction
Microstructure
Mechanical properties

ABSTRACT

Two near-β titanium alloys, Ti–5Al–5Mo–5V–1Cr–1Fe and a modified one containing 2 wt% Cr (Ti–5Al–5Mo–5V–2Cr–1Fe) were produced from Ti hydride precursor powders via the cost-effective blended elemental powder metallurgy technique. The effects of two cooling rates (10 K s^{-1} and 1 K s^{-1}) during thermo-mechanical processing on the microstructure and mechanical properties were investigated using X-ray diffraction and scanning electron microscopy. X-ray line profile analysis revealed that dislocation densities and microstrain in β-Ti phase are higher than in α-Ti phase for all cases. In both alloys, slower cooling results in an increase in α volume fraction and promotes morphology of continuous grain boundary α phase. A lower total elongation is obtained in both alloys under slower cooling which could be accounted for by the continuous morphology of α phase. Overall, Ti–5Al–5Mo–5V–1Cr–1Fe displays higher ultimate tensile strength and total elongation compared to Ti–5Al–5Mo–5V–2Cr–1Fe, regardless of the cooling rate.

1. Introduction

Ti based alloys are used in the aerospace, automotive and medical industries due to their attractive properties, particularly high strength-to-density ratios [1–3]. Extensive research has been carried out in order to reduce the production costs, particularly over the last decade [4–6]. One of the most promising cost-effective powder metallurgical techniques is the blended elemental powder metallurgy (BEPM) method [7]. A number of Ti based alloys [7–12] have been produced using powder metallurgy technique where an additional processing step called the hot isostatic pressing (HIP) is used in order to increase relative density or reduce the residual porosity. This results in an extra processing cost which compromises the cost savings of powder metallurgy technique. Ye et al. [13] have thereafter used uniaxial hot pressing at much lower pressure (~15 MPa for Ti64) than HIP (~150 MPa for Ti64) in the α/β phase transformation range in order to replace the HIP. This approach has reduced processing cost compared to the HIP but it still remains expensive. Later on, only the press-and-sinter method has been employed in [14–18] which unfortunately produced the density close to ~90% only. Finally, Ti hydride powder is used with BEPM technique without HIP. In this method a uniform network of fines pores, which form during cold compaction of brittle TiH_2 powder particles, are healed upon sintering. Due to $TiH_2 \rightarrow Ti+2H$ phase transformation high density of crystal lattice defects evolve which accelerates the synthesis. The evolution of atomic hydrogen promotes mass transfer through the inter-particle boundaries which reduces surface oxides/residual porosity. The obtained sintered density was close to ~99% by using Ti powders containing 3 wt% hydrogen [19]. This is considered to be the lowest cost powder metallurgy technique. The studied alloys have been produced using this methodology. Near-β Ti alloys are used in the aerospace industries particularly due to their deep hardenability, high strength and creep properties. A near-β Ti alloy consists typically of two phases: hard α phase and soft β phase. Several investigations have been carried out on the effect of the thermal processing on the microstructure and mechanical properties. In [4,20,21], the influence of α phase morphology on the mechanical properties has been analysed. It is reported in [20,21] that globular shaped α phase has positive effect on the mechanical properties, especially on ductility.

X-ray diffraction line profile analysis (XRDLPA) and transmission electron microscopy (TEM) are used to determine the crystallite dimensions, lattice microstrain and dislocation densities of the submicron grains in the microstructure. The results obtained through TEM analysis are locally accurate but may not be representative of the bulk material. In contrast, XRDLPA involves significantly larger sample volumes and is useful provided that the volume fractions of relevant phases are high enough to result in clear XRD peaks for analysis. For materials containing two or

* Corresponding author. Tel.: +61 2 4221 5798; fax: +61 2 4221 3662.
E-mail address: ma960@uowmail.edu.au (M. Ahmed).

0921-5093/$ - see front matter © 2013 Elsevier B.V. All rights reserved.
http://dx.doi.org/10.1016/j.msea.2013.03.083

more phases, it generally is more convenient to use XRD as the peaks of the constituent phases appear distinctly in the profile. Several XRDLPA investigations have been performed on steels [22–26], Cu [27–29] and Zr [30,31] alloys. In contrast, a fewer number of investigations using the XRDLPA have been performed on Ti alloys [32–34]. Glavicic et al. [32] have used X-ray line profile analysis to examine the slip activity in commercially pure Ti. Later on, they have measured dislocation densities for individual α and β phases in Ti–6Al–4V alloy [33]. Deformed microstructures of boron doped Ti–6Al–4V alloys have been characterised in terms of crystallite size and dislocation density using variance and the modified Rietveld method [34] with findings that the dislocation densities are higher in β phase than in α phase [22,23].

In the present study, two near-β titanium alloys, Ti–5Al–5Mo–5V–1Cr–1Fe (Ti-55511) and a variant containing 2 wt% Cr (Ti-55521) were produced via the BEPM technique using Ti hydride powder. The Ti-55511 alloy is selected because of its use in aerospace industries [35] and this is the first attempt for this alloy production using cost-effective BEPM technique. A novel Ti-55521 alloy is chosen because increased Cr contents reduce the amount of α phase [36,37] during soaking in α+β phase field potentially results in improvements in ductility [21]. The aim of the present work is to characterise the microstructure and mechanical properties of the alloys subjected to the thermo-mechanical processing (TMP). In particular, the effects of Cr addition and two cooling rates are investigated.

2. Experimental and analysis methods

2.1. Materials

Hydrogenated (3.5 wt% H) Ti powders were mixed with elemental Mo, Cr, Fe (<40 μm) and Al–V master alloy powders (40–63 μm) in order to obtain the required alloy composition. The powders were blended and die pressed under 650 MPa to form green compacts. The green compacts were thereafter sintered by heating to 1293 K for 3600 s followed by heating to 1523 K for 21,600 s in order to distribute the alloying elements throughout the matrix uniformly. The results obtained after sintering have shown in [38] that all the alloying elements distributed homogeneously throughout the matrix after sintering step II (1523 K for 21,600 s). The sintered compacts were provided by Institute for Metal Physics, National Academy of Sciences, Ukraine. Thereafter, a Gleeble 3500 thermo-mechanical simulator with modest vacuum ($\sim 3.8\times10^{-4}$ Torr) in pocket jaw mode was employed for the TMP.

The TMP schedule is shown in Fig. 1 and involved the heating of cylindrical samples (12 mm length × 8 mm diameter) to 1223 K at 10 K s^{-1} and holding for 120 s, then cooling at 35 K s^{-1} to 1173 K where a 25% length reduction takes place. This is followed by cooling at 35 K s^{-1} to 1073 K where after the hold for 1800 s a deformation to 60% reduction is applied. After deformation, the samples are given a final cool to room temperature at either of the two selected cooling rates; 10 K s^{-1} or 1 K s^{-1}. The samples are cut perpendicular to the deformation direction and prepared using conventional metallographic techniques. The polished samples are etched using Kroll's reagent (2 ml HF, 5 ml HNO_3 and 93 ml H_2O) in order to reveal the microstructure.

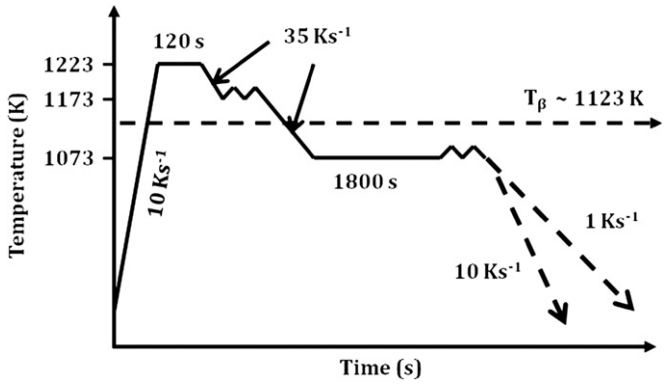

Fig. 1. A schematic diagram of the thermo-mechanical processing schedules.

2.2. X-ray data acquisition

X-ray diffraction investigations were conducted using a PANalytical X'Pert PRO Multipurpose diffractometer (MPD) with Cu Kα radiation ($\lambda=0.154$ nm) filtered with Ni-monochromator at 45 mA and 40 kV. Polished samples of diameter 15 mm were oriented normal to the deformation axis. Diffraction patterns were obtained under a continuous scanning mode over the 2θ range of 30–160°, with 0.01° step size and 490 s resulting acquisition time. In order to characterise the instrumental broadening a standard polycrystalline silicon sample was used.

2.2.1. Method of X-ray diffraction line profile analysis

Diffraction from a crystalline material provides information about both periodic and internal crystalline features. In the diffraction pattern such information can be inferred from calculations related to peak position, peak shape and peak width. Broadening of the peaks can occur due to a decrease in crystallite size, and/or due to microstrain within the crystallite. The width of the diffraction peaks also depends on the instrumental factors. Other factors such as dislocation density, slip activity [32], and the presence of stacking faults can also affect the shape and/or position of diffraction peaks [27]. Warren [39], Randle and Engler [40] developed the XRDLPA approach for the analysis of the microstructure, which was later followed by others [28,41–45] with some modifications making it possible to determine the crystallite size and microstrain in materials reliably. Similarly to [16,23], the modified Rietveld [46] method has been used in order to characterise microstructures in this investigation. The brief algorithms of the modified Rietveld method used are presented below.

2.2.1.1. The modified Rietveld method. The modified Rietveld method consists of a modelling of diffraction profiles through pseudo-Voigt (pV) function using the programme LS1 [46]. The crystal structure of the materials and microstructural parameters, e.g. lattice parameters, crystallite size and microstrain, are simultaneously refined through the LS1 programme. In the programme, Fourier transform of the pV function is used to fit the broadening of the peaks profile. An isotropic model is assumed, which is called the Popa model [47] where the lattice constants, volume weighted crystallite size and microstrain are concomitantly used as the fitting parameters. Since the samples are heavily deformed, the preferred orientation of the crystallites has been corrected in order to obtain the best fit by maintaining the following function, $P(\alpha)$ [48]:

$$P(\alpha) = (r^2\cos^2\alpha + r^{-1}\sin^2\alpha)^{-3/2} \quad (1)$$

Here, α is the angle between the preferred orientation vector and the normal to the planes generating the diffracted peak and r is a refinable parameter. In all conditions, the diffraction profiles were fitted up to 100° (2θ) using the above mentioned approach because of the very low intensity of the peaks above 100°.

The Goodness of fit (*GoF*) indicates the quality of the fitting which is expressed as follows:

$$GoF = R_{wp}/R_{exp} \tag{2}$$

Here, R_{wp} is the weighted residual profile and R_{exp} is the expected profile.

2.2.1.2. The calculation of dislocation density and stored energy. The amount of dislocation density depends on the value of crystallite size and microstrain of crystallographic planes peaks. The value of dislocation density, $\langle p\rangle$, is thereafter calculated using the following equation obtained from [49]

$$\langle\rho\rangle = \frac{3\sqrt{(2\pi)}\langle\in_L^2\rangle^{1/2}}{D_s b}. \tag{3}$$

Here, D_s is the crystallite size, $\langle\in_L^2\rangle^{1/2}$ is the microstrain and b is Burger's vector. Burger's vector for hexagonal closed packed planes (b_{hcp}) and for body-centered cubic planes (b_{bcc}) is

b_{hcp} = lattice parameter of basal plane (a) which is 0.293 nm in the present study; (3.1)

$$b_{bcc} = \frac{\text{lattice parameter}}{2}\left|\langle hkl\rangle\right| \tag{3.2}$$

Finally, stored energy (E_s) due to the inhomogeneous microstrain is calculated using the Stibitz relationship [50]:

$$E_s = 1.5Y\frac{(\Delta d/d)^2}{1+2v^2}. \tag{4}$$

Here, Y is Young's modulus of the material. The value of Y is equal to 116 GPa [51] for hcp-Ti and 68 GPa [52] for bcc-Ti. The value of Poisson's ratio (ν) is equal to 0.32 for hcp-Ti [53] and 0.23 for bcc-Ti [54]. The value of stored energy (E_s) is expressed in J mol^{-1} assuming the molar volume 10.46 cm^3 mol^{-1}. The relative change in lattice spacing ($\Delta d/d$) is derived from the broadening of the peak [55]:

$$(\Delta d/d) = w/2\tan\theta \tag{4.1}$$

Here, w is the broadening of the peaks and θ is the half of the Bragg angle (2θ) corresponding to the peak.

2.3. Microstructure and mechanical properties

A JEOL-JSM 7001F Field Emission Gun-Scanning Electron Microscope (FEG-SEM) was used to investigate the microstructures of the samples. Operating at 15 kV and 15 mm working distance both the back scattered electron and secondary electron modes were employed for imaging. TMP samples were machined into sub-sized tensile specimens (Fig. 2) of gauge length 5.1 mm; width 2.18 mm and thickness 0.9 mm. Tensile tests were carried out with a μ-Tweezer Tensile Module (Kammrath & Weiss, GmbH) at a constant speed of 1.7 mm min^{-1} at room temperature. In order to understand the work hardening behaviour of the samples and to find the m-values (work hardening exponent) of different stages of the plastic regions in the stress–strain curves of the samples, stress–strain curves were fitted using rational polynomial functions via 2D-TableCurve.

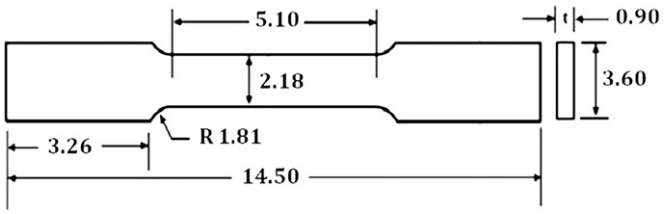

Fig. 2. A schematic of the tensile specimens (two dimensional) with dimensions. All dimensions are in mm.

Table 1
The values of agreement indices of the Rietveld fitting for the alloys at different cooling conditions.

Alloy	Cooling rate (K s^{-1})	Residual weighed profile (R_{wp}), %	Goodness of fit (*GoF*)
Ti-55511	10	9.1	1.6
	1	8.8	0.9
Ti-55521	10	7.4	1.0
	1	7.9	0.9

3. Results

3.1. X-ray line profile analysis and phase transformation

A summary of agreement indices of the Rietveld fitting for all samples is shown in Table 1. The obtained value of residual weighted profile (R_{wp}) is in between 7.4% and 9.1% as well as Goodness of fit (*GoF*) is lying between 0.9 and 1.6. Fig. 3 indicates X-ray diffraction patterns and associated Rietveld fitting for all samples where peaks from α and β phases with *Miller–Bravais* indices are clearly exhibited. The intensity difference between the experimental and the Rietveld fitting is also plotted under the diffraction patterns. The trend of the X-ray diffraction patterns is similar for the samples cooled at the same rate for both alloys. For both alloys, there is an obvious reduction in β planes peaks intensities for the samples cooled at 1 K s^{-1} compared to those for the samples cooled at 10 K s^{-1}. On the other hand, α planes peaks intensities show opposite character to β planes peaks. The 2θ position of all β planes peaks shifts slightly to the right in the diffraction profiles compared to those of the pure unalloyed β-Ti.[1] The similar results indicating the shift of β planes peaks to the right have been found in other Ti alloys, e.g. Ti–25V–15Cr–0.2Si [56] and Ti–30Zr–5Al–3V [57].

Tables 2 and 3 are the summary of the Rietveld analyses, indicating values of lattice parameter, crystallite size and microstrain of the several α and β planes, respectively. Dislocation density and stored energy values is calculated using Eqs. (3) and (4) and also included in Tables 2 and 3. In Table 2, only basal lattice parameter (a) of hcp lattice is given because prism lattice parameter (c) could easily be obtained from the c/a ratio. The c/a ratio of hcp lattices has been calculated using the following equation [58]:

$$\frac{c}{a} = \frac{\sqrt{3}}{2}\frac{\sin\theta_{(h0\bar{h}0)}}{\sin\theta_{(000l)}}\frac{l}{h} \tag{5}$$

Here, $\sin\theta_{(h0\bar{h}0)}$ is equal to $\sin\theta_{(10\bar{1}0)}$ and $\sin\theta_{(000l)}$is equal to $\sin\theta_{(0001)}$ in the present study. By using Eq. (5), the c/a ratio ($\sim$1.6) is calculated for all samples which are similar to those for an unalloyed α-Ti. Thus, it may be claimed that alloying and cooling rates did not influence the c/a ratio of hcp lattices. On the other hand, the average of the β-Ti lattice parameter is 0.3235 nm for both alloys, which is slightly less than that for the unalloyed β-Ti

[1] PDF Reference Code: 03-065-5970.

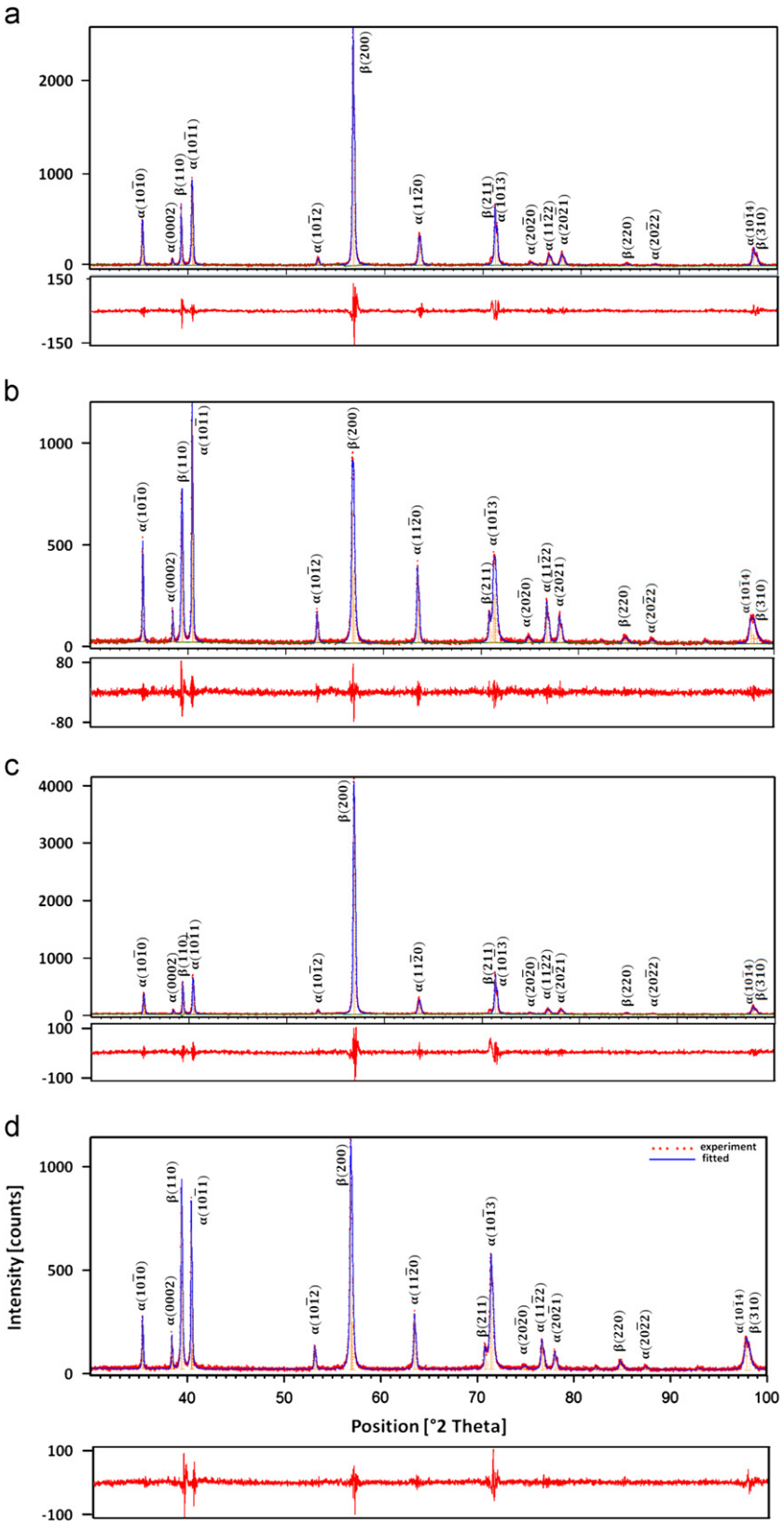

Fig. 3. X-ray diffraction patterns and Rietveld fitting of (a and b) Ti-55511 and (c and d) Ti-55521 alloys cooled at 10 K s^{-1} (a and c) and 1 K s^{-1} (b and d), respectively. Difference between the experiment and Rietveld fitting is shown below each pattern.

(0.3311 nm). For both alloys, a slightly larger reduction in the bcc lattice parameter is obtained for slow cooling rate (1 K s^{-1}). On the other hand, the Ti-55521 alloy has slightly smaller bcc lattice parameter than Ti-55511 alloy.

In this study, the dominant lattice planes α(10$\bar{1}$0), α(0002), α(10$\bar{1}$1), α(10$\bar{1}$2), and α(11$\bar{2}$0) in the diffraction profiles are analysed. In both alloys, the crystallite size of α planes peaks is found to be higher for the samples cooled at 1 K s^{-1} compared to

Table 2
The values of lattice parameters (a and c *), crystallite size (D_s), microstrain $(\langle\varepsilon_L^2\rangle)^{1/2}$, dislocation density $\langle p\rangle$ and local stored energy (E_s) obtained from the Rietveld analysis and other formula for several α planes.

Miller indices	Alloy	Cooling rate (K s^{-1})	a (nm)	D_s (nm)	$(\langle\varepsilon_L^2\rangle)^{1/2}$ ($\times 10^{-4}$)	$\langle p\rangle \pm 0.02$max ($\times 10^{14}$ m^{-2})	E_s (J mol^{-1})
$(10\bar{1}0)$	Ti-55511	10	0.293	165 ± 9	10.5	1.65	3.4
		1	0.293	219 ± 12	7.9	0.94	1.9
	Ti-55521	10	0.293	135 ± 5	11.2	2.15	3.9
		1	0.293	175 ± 7	8.4	1.24	2.2
(0002)	Ti-55511	10	0.293	111 ± 6	7.7	1.80	1.8
		1	0.293	371 ± 13	5.5	0.38	0.95
	Ti-55521	10	0.293	88 ± 3	9.1	2.68	2.6
		1	0.293	197 ± 8	6.1	0.80	1.2
$(10\bar{1}1)$	Ti-55511	10	0.293	192 ± 6	10.3	1.39	3.3
		1	0.293	234 ± 17	7.4	0.82	1.7
	Ti-55521	10	0.293	178 ± 3	10.7	1.56	3.5
		1	0.293	198 ± 11	8.1	1.06	2.0
$(10\bar{1}2)$	Ti-55511	10	0.293	181 ± 12	14.3	2.05	6.3
		1	0.293	211 ± 5	6.2	0.76	1.2
	Ti-55521	10	0.293	97 ± 7	19.7	5.26	11.8
		1	0.293	206 ± 8	8.9	1.12	2.5
$(10\bar{2}0)$	Ti-55511	10	0.293	134 ± 10	15.2	2.94	7.1
		1	0.293	193 ± 2	9.2	1.24	2.6
	Ti-55521	10	0.293	117 ± 8	17.3	3.83	9.2
		1	0.293	146 ± 6	10.6	1.88	3.4

* Lattice parameter, $c = 1.6 \times a$ (for hcp).

Table 3
The values of lattice parameter (a), crystallite size (D_s), microstrain $(\langle\varepsilon_L^2\rangle)^{1/2}$, dislocation density $\langle p\rangle$ and local stored energy (E_s) obtained from the Rietveld analysis and other formula for several β planes.

Miller indices	Alloy	Cooling rate (K s^{-1})	a (nm)	D_s (nm)	$(\langle\varepsilon_L^2\rangle)^{1/2}$ ($\times 10^{-4}$)	$\langle p\rangle \pm 0.05$ ($\times 10^{14}$ m^{-2})	E_s (J mol^{-1})
(110)	Ti-55511	10	0.3238	143 ± 5	11.4	2.61	2.3
		1	0.3233	92 ± 9	18.8	6.68	6.3
	Ti-55521	10	0.3233	179 ± 3	9.6	1.75	1.6
		1	0.3230	108 ± 14	16.3	4.93	4.8
(200)	Ti-55511	10	0.3238	147 ± 12	9.9	1.56	1.7
		1	0.3234	79 ± 6	13.6	4.00	3.3
	Ti-55521	10	0.3234	187 ± 9	8.4	1.04	1.3
		1	0.3230	102 ± 10	12.9	2.94	2.9
(310)	Ti-55511	10	0.3238	82 ± 7	11.1	1.99	2.2
		1	0.3232	28 ± 6	13.5	7.09	3.7
	Ti-55521	10	0.3233	68 ± 5	16.8	3.64	5.0
		1	0.3231	46 ± 8	18.3	5.85	6.8

that for the samples cooled at 10 K s^{-1}. This is accompanied by the reduction in crystallite microstrain after slower cooling. Thus, dislocation density and local stored energy in the α lattice planes is lower for both alloys cooled at 1 K s^{-1} compared to those cooled at 10 K s^{-1}. On the other hand, α crystallite size of the Ti-55521 alloy is always smaller and the microstrain is larger than those for the Ti-55511 alloy under the respective cooling condition. As a result, the dislocation density and stored energy are found to be higher in the Ti-55521 compared to Ti-55511 alloy under the respective cooling rate. In the case of β peaks, β (110), β (200), and β (310) lattice planes are analysed. Despite of the good intensity, β (211) plane is not analysed as it overlaps with α$(10\bar{1}3)$ peak. In both alloys, the crystallite size of β planes peaks decreases for the samples cooled at 1 K s^{-1} compared to the samples cooled at 10 K s^{-1}. There is an increase in microstrain of β crystallite of the samples cooled at 1 K s^{-1}. Consequently, the dislocation density and local stored energy of the β planes are found to be higher for both alloys cooled at 1 K s^{-1}. However, after similar processing the β crystallite size is larger for the Ti-55521 alloy compared to the Ti-55511 alloy. Dislocation density and stored energy are found to be a bit higher for the Ti-55521 alloy. Overall, the dislocation densities and microstrain in β planes peaks are higher than those in α planes peaks.

3.2. Microstructural development

Fig. 4 represents the microstructures of both alloys for all cooling conditions. The microstructures consist of both α and β phases with α phase displaying different morphologies: lamellar shape and globular shape. The lamellar shape α can later form basket weave structure if they lie in different planes, as can be seen in Fig. 4f in the areas denoted by circles. Within the basket weave structure in Fig. 4f, there are also visible arrangements of triangular-shaped α consisting of three interconnected α lamellae. There are also some parallel α lamellae arrangements, indicated by a rectangular box in Fig. 4f. In both alloys, recrystallised β grains are visible in the microstructures under both cooling conditions, but it is more pronounced after slower cooling. In the case of both

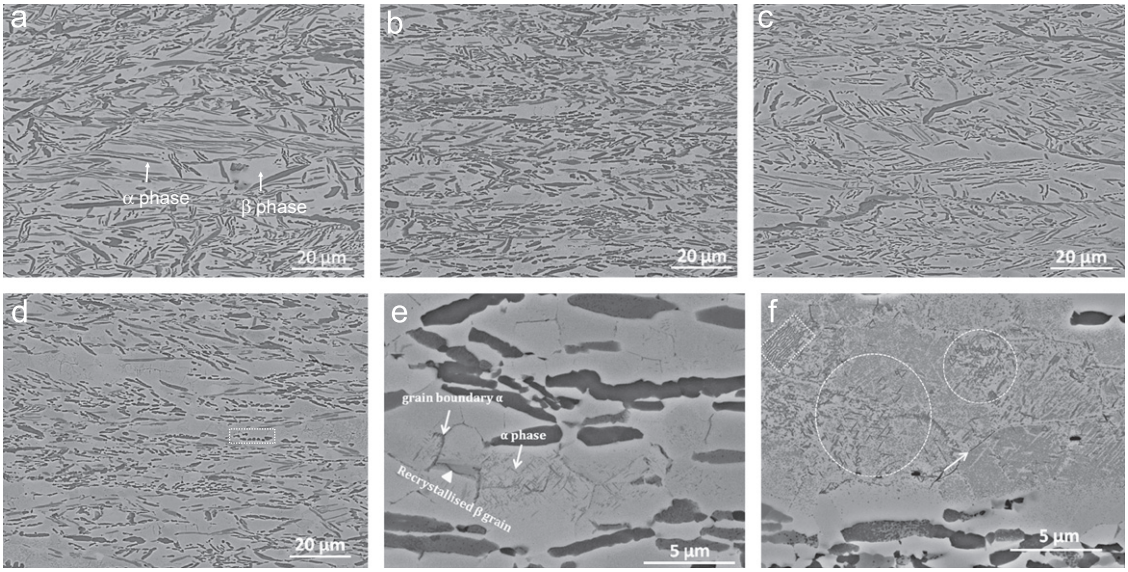

Fig. 4. The microstructures of the alloys showing α and β phases. (a) Ti-55511 alloy cooled at 10 K s^{-1}, (b) Ti-55511 alloy cooled at 1 K s^{-1}, (c) Ti-55521 alloy cooled at 10 K s^{-1}, and (d) Ti-55521 alloy cooled at 1 K s^{-1}. (e) Enlarged view of Ti-55521 alloy cooled at 1 K s^{-1} showing interconnected grain boundary α phase. (f) Initiation of the grain boundary α phase formation (arrow marked) and triangular shaped α phase (circle marked)—in Ti-55511 alloy. Parallel lamellar α in the top left corner (indicated by rectangular box).

alloys cooled at 1 K s^{-1}, the microstructures also reveal a continuous network of grain boundary α formed at the β grain boundaries. In addition, there are fine α lamellae lying inside the recrystallised β grains which also form a basket weave structure. Microstructural observations, such as those shown in Fig. 5 (indicated by a rectangular areas and an arrow), reveal that the α phase formation first takes place at the interface of the β phase crystals, and with time, the remaining β phase surrounded by the newly formed α, transforms into the α phase.

The porosity of the alloys is reduced from ~2% after sintering to ~0.10% after TMP [38]. Table 4 indicates that the amount of α phase varies with the alloy composition and cooling rates. A maximum volume fraction of α phase of 54 ± 2% is obtained in the case of Ti-55511 alloy cooled at 1 K s^{-1}, whereas the minimum amount of α phase (34 ± 3%) is obtained in the case of Ti-55521 alloy cooled at 10 K s^{-1}. Regardless of the cooling rate, Ti-55521 alloy contains a lesser amount of α phase compared to Ti-55511 alloy. On the other hand, both alloys show a higher amount of α phase for the samples cooled at 1 K s^{-1} compared to those cooled at 10 K s^{-1}.

3.3. Mechanical properties

Fig. 6 shows the engineering stress versus strain curves of both alloys for all cooling conditions. The shape of these curves is quite similar for all samples. A summary of the mechanical properties based on Fig. 6 is also given in Table 4. A maximum ultimate tensile strength (UTS) of 1189 ± 7 MPa is obtained in the case of Ti-55511 alloy cooled at 1 K s^{-1}, whereas a maximum total elongation of 9.85 ± 0.05% is obtained in the case of Ti-55511 alloy cooled at 10 K s^{-1}. For the same cooling conditions, Ti-55511 alloy displays a higher UTS compared to Ti-55521 alloy. On the other hand, specimens subjected to 10 Ks^{-1} cooling rate show lower UTS values compared to those cooled at 1 K s^{-1}. Table 5 shows Vickers micro-hardness values for α and β phases from which 0.2% offset yield strength of the samples is calculated using the rule of mixtures.[2] Table 5 also clearly indicates that estimated 0.2% offset yield strength correlates well with the experimental data.

[2] Rule of mixtures, Total strength = vol. fraction of phase 1 × strength of phase 1+vol. fraction of phase 2 × strength of phase 2.

The work hardening behaviour is analysed using the modified Crussard–Jaoul (C–J) model [59–63], as the samples contain two phases similar to dual phase steel for which this model was developed. The modified C–J model uses the following Eq. (6) which is known as the Swift equation [59]:

$$\varepsilon = \varepsilon_0 + C_s\sigma^m \tag{6}$$

Here, σ is the true stress, ε is the true strain, m is the work hardening exponent and C_s is the material constant. The logarithmic form of the differential Swift equation with respect to ε gives the following:

$$\ln(d\sigma/d\varepsilon) = (1-m)\ln\sigma - \ln(C_s m) \tag{7}$$

It can be seen that Eq. (7) represents the linear relation between logarithmic form of work hardening rate, $\ln(d\sigma/d\varepsilon)$, and logarithmic form of true stress, $\ln\sigma$, where $(1-m)$ is the slope of the line. The logarithm of work hardening rate, $\ln(d\sigma/d\varepsilon)$, versus logarithm of true stress, $\ln\sigma$, is plotted for all the samples in Fig. 7a. The trend of the curves for all samples is quite similar. Each of the curves is segmented into three distinct stages as per depicted in Fig. 7b (stage I, stage II and stage III), with a maximum slope in stage II and a minimum one in stage III. A summary of the results obtained from Fig. 7a is presented in Table 6, where the work hardening exponent (m) values corresponding to each stage are given together with the transition true stress and true strain values. The maximum value of the work hardening exponent is obtained for stage II (m_{II}) and the minimum work hardening exponent is obtained for stage III (m_{III}) in all the samples. Regardless of cooling conditions, the values of transition strain from stage I to stage II and stage II to stage III are slightly higher for the Ti-55511 alloy compared to the Ti-55521 alloy.

4. Discussion

4.1. X-ray line profile analysis and phase transformation

The effect of slower cooling (1 K s^{-1}) on the β to α phase transformation can easily be understood from the diffraction profiles. A reduction in relative intensities of the β peaks and an increase in relative intensities of the α peaks for the samples

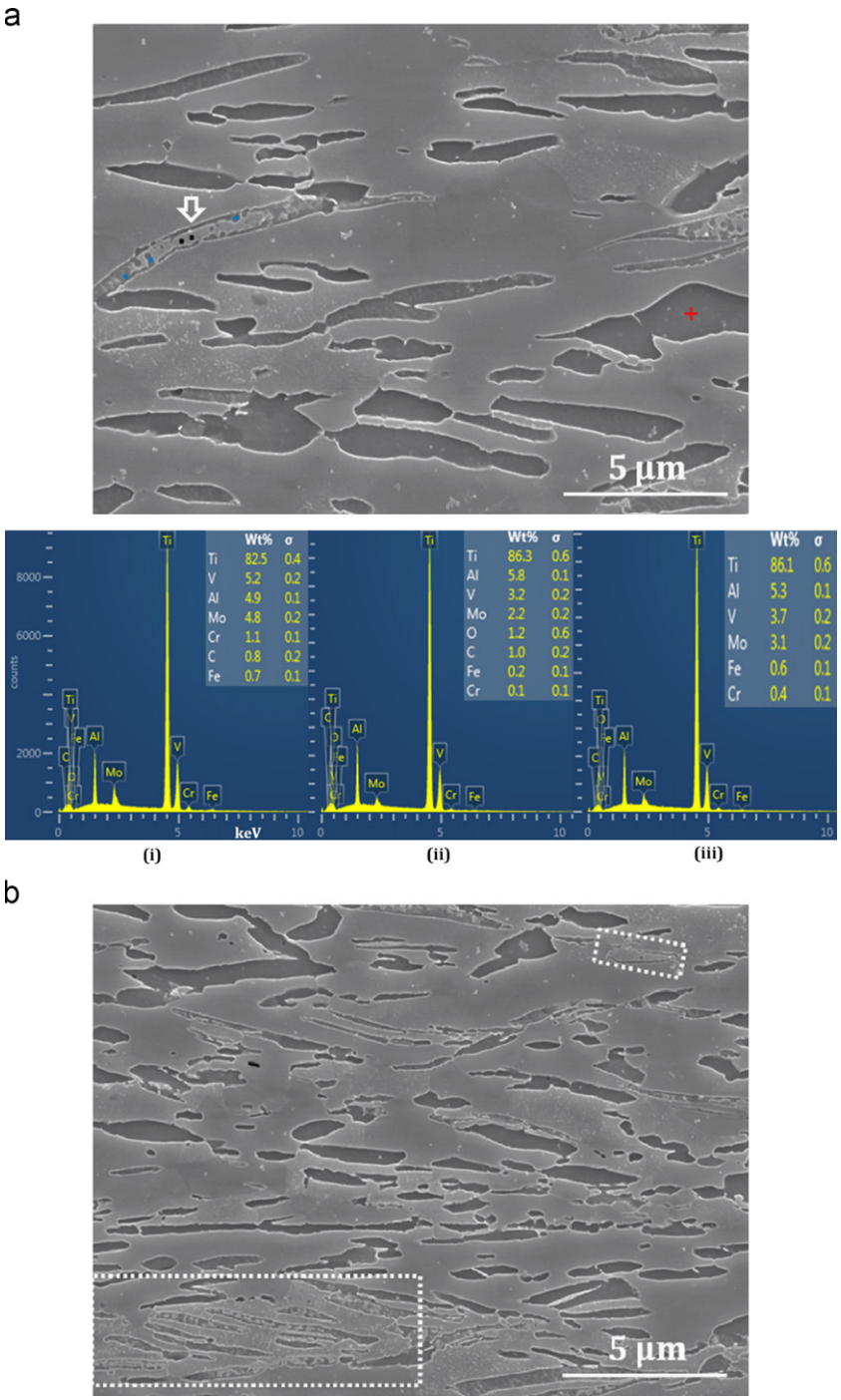

Fig. 5. The examples of different morphologies of α and β phases with corresponding EDX profiles indicating the progress of β→α transformation. The arrow head in (a) and rectangular boxes in (b) indicate the fields of interest in the microstructure. For (a): (i) the composition of untransformed β corresponds to the "black dot" in the region indicated by an arrow; (ii) the composition of transformed α corresponds to the "blue dot" in the same region, and (iii) the composition of α phase taken from the area identified by "+" in (a). (For interpretation of the references to colour in this figure legend, the reader is referred to the web version of this article.)

Table 4
The volume fractions of α phase (V_α), 0.2% offset yield strength (σ_Y), ultimate tensile strength (σ_{UTS}), uniform elongation (el_{uni}) and total elongation (el_{Tot}) of the alloys at different processing conditions.

Alloy	Cooling rate (K s^{-1})	V_α (%)	σ_Y (MPa)	σ_{UTS} (MPa)	el_{uni} (± max 0.05 %)	el_{Tot} (± max 0.1%)
Ti-55511	10	46 ± 2	1102 ± 9	1142 ± 15	4.4	9.85
	1	54 ± 2	1141 ± 15	1189 ± 7	6.5	9.40
Ti-55521	10	34 ± 3	1031 ± 19	1091 ± 11	4.6	8.30
	1	41 ± 2	1053 ± 10	1116 ± 9	4.8	7.85

cooled at 1 K s^{-1} compared to those cooled at 10 K s^{-1} indicates β to α phase transformation. Ivasishin and Markovsky [64] have also mentioned that β to α phase transformation occurs during cooling in Ti alloys. The position of the β planes peaks shifts to the right resulting in smaller bcc lattice parameter. This is the effect of the presence of those alloying elements which have smaller atomic radii Al (143 pm), Mo (139 pm), V (134 pm), Cr (128 pm), and Fe (126 pm) compared to elemental Ti (147 pm). The same reason is mentioned in [56,57] for Ti–25V–15Cr–0.2Si and Ti–30Zr–5Al–3V alloys, respectively. As Ti-55521 alloy contains 1% more Cr, which has a much smaller atomic radius compared to elemental Ti, this results in an expected slightly smaller bcc lattice parameter than that for Ti-55511 alloy. On the other hand, hcp lattice parameters are not affected by the alloying elements because hcp phase contains α stabiliser Al (143 pm) as a main alloying element, which has a closer atomic radius to Ti (147 pm) compared to those of β stabilising alloying elements.

Under both cooling conditions, Ti-55521 alloy contains a smaller α crystallite size than Ti-55511 alloy. This is attributed to the slower rate of α phase transformation [37] caused by the presence of additional β-stabilising Cr and insufficient time for diffusion of β stabilisers out from the newly formed α. The restoration process after deformation (annihilation of dislocations, formation of dislocation cell structure) in α phase is found to be more advanced in the samples cooled at 1 K s^{-1}; as such samples remain a longer time at high temperatures compared to those cooled at 10 K s^{-1}. This, in turn results in less density of dislocations [34] and larger crystallite size of α in these specimens. Similar to the findings in [34], the β (110) plane has a higher dislocation density and microstrain compared to those of the α(10$\bar{1}$1) plane. There are two reasons for this observation: (i) the bcc crystal structure of β phase has more active slip systems than

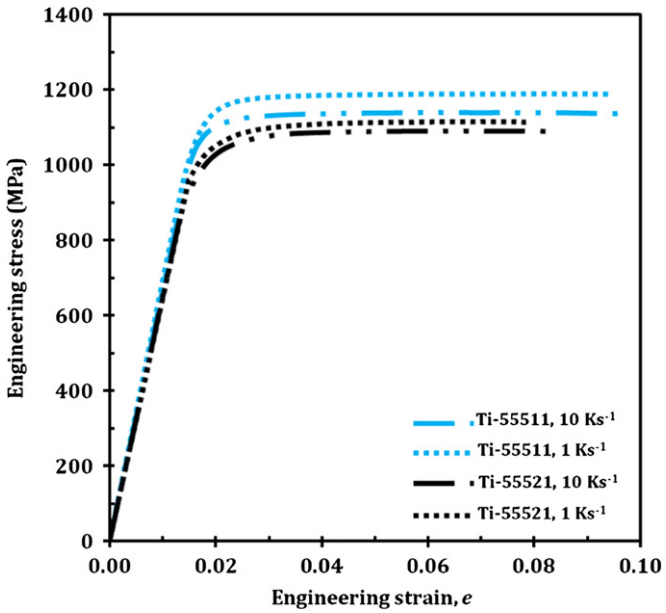

Fig. 6. The engineering stress versus engineering strain curves for both alloys under all cooling conditions.

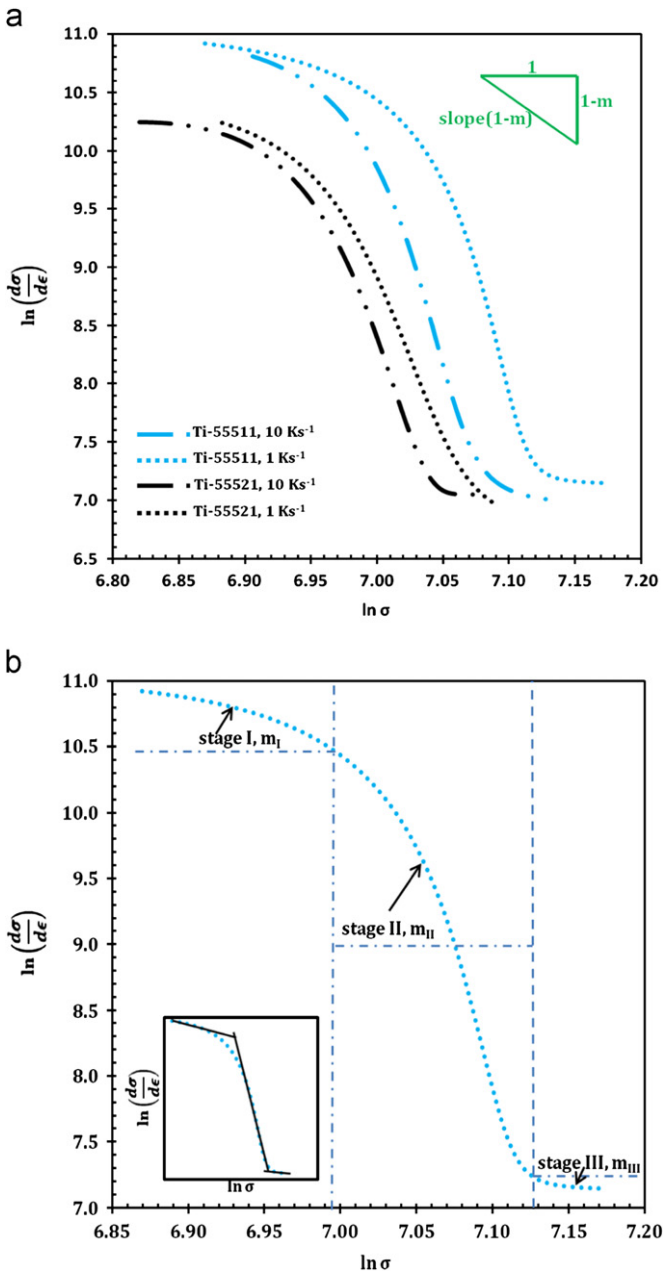

Fig. 7. (a) ln(dσ/dε) versus ln σ curves for both alloys under all cooling conditions where σ denotes true stress. (b) Representative illustration of ln(dσ/dε) versus ln σ curve for the Ti-55511 alloy cooled at 1 K s^{-1} showing three different work hardening stages (m_I, m_{II}, and m_{III}). The inset in (b) depicts the lines across the stages from where value for the slope (1−m) is obtained.

Table 5
The relationships between hardness, yield strength and volume fractions of phases present in the alloys.

Phase	VHN (H_v)	Calculated strength (MPa), $\sigma \approx H_v/3$	Alloy	Cooling rate (K s^{-1})	V_α (%)	Estimated 0.2% offset yield strength	Experimental 0.2% offset yield strength
α	434 ± 9	1416	Ti-55511	10	46 ± 2	1099 ± 12	1102 ± 9
β	253 ± 6	830		1	54 ± 2	1146 ± 12	1141 ± 15
α	431 ± 7	1409	Ti-55521	10	34 ± 3	1033 ± 17	1031 ± 19
β	257 ± 5	840		1	41 ± 2	1073 ± 11	1053 ± 10

Table 6
The value of work hardening exponent (m), transition true stress (σ_{tr}) and transition true strain (ε_{tr}) between the stages.

Alloy	Cooling rate (K s^{-1})	Stage I, m_{I}	Stage II, m_{II}	Stage III, m_{III}	$m_{\mathrm{I}} \rightarrow m_{\mathrm{II}}$		$m_{\mathrm{II}} \rightarrow m_{\mathrm{III}}$	
					σ_{tr} (MPa)	ε_{tr}	σ_{tr} (MPa)	ε_{tr}
Ti-55511	10	6.47	38.58	4.58	1092	0.018	1196	0.048
	1	9.56	45.72	5.91	1137	0.017	1240	0.045
Ti-55521	10	3.86	30.02	2.51	997	0.017	1139	0.046
	1	4.37	35.91	3.64	1016	0.016	1161	0.044

the hcp α phase. Thus, dislocation assisted slip activities during deformation at 1073 K occurs mostly in the β phase [65]. In addition, (ii) the remaining β phase is subjected to two deformations at 1173 K and 1073 K, whereas the α phase formed during holding at 1073 K is subjected only to single deformation (1073 K) and the α phase formed during cooling is not deformed. The increase in stored energy/dislocation density in the β planes at 1 K s^{-1} cooling rate could also be related to two concurrent phenomena taking place during cooling. Firstly, after the hot deformation at 1073 K, partial recrystallisation occurs in the remaining β phase [66] at high temperature during cooling. This results in the reduction of dislocation density. Recrystallisation of the whole remaining β phase is not completed due to the short time at high temperature during cooling. Secondly, the formation of a hard α phase inside the recrystallised β grains (Fig. 4e) during cooling has constrained the β phase resulting in high dislocation density at slower cooling than at faster cooling due to the higher volume fraction of α phase formed (Table 4). It appears that the second event plays a more dominant role, as a net effect is of a higher stored energy in slow cooled samples compared to that in the samples cooled at 10 K s^{-1}. A lower amount of α formed on cooling at 10 K s^{-1} due to a shorter time available results in less constrained β grains with lower stored energy.

4.2. Microstructural development

As a result of 60% deformation at 1073 K, globular shaped α phase is formed through breaking up of α lamellae, which formed previously during both cooling to and holding at 1073 K. Partial recrystallisation occurs during cooling of the heavily deformed (60%) β structure. It is more pronounced in the samples cooled at 1 K s^{-1} as more time is available. If multiple α phase crystals nucleate at the β grain boundaries in line, thereafter the grain boundary α is formed. It seems that during slower cooling (1 K s^{-1}), α phase nucleates preferably at β grain boundaries resulting in the presence of the interconnected grain boundary α (Fig. 4e). Sauer and Luetjering [67] have also mentioned that continuous α phase can be formed at β grain boundaries after cooling from the recrystallised temperature. The unusual phase transformation behaviour in Fig. 5 can be explained by observing the composition profile for the α and β phases, which shows that the newly formed α phase and the remaining inside β phase contain localised impurities, e.g. C and O. The higher concentrations of interstitial C and O are in α phase because they are α stabilisers, whereas the remaining β contains only traces of C and/or O. It could be proposed that due to the fast diffusion of interstitials C and O in the nuclei of α, the remaining β areas become more stable delaying the full transformation to α phase. On the other hand, the composition of the majority fully transformed α phase shows no O and/or C (Fig. 5aiii). This suggests that the areas showing unusual phase transformation behaviour (large bottom left corner in Fig. 5b) may have originally contained some oxide or carbide in the form of a surface layer on some powder particles [38].

Due to the addition of 1% more Cr in the Ti-55521 alloy less α phase is formed (Table 4) than in the Ti-55511 alloy, as this extra Cr content increases the Mo equivalent according to the following equation:

$$\mathrm{Mo}_{\mathrm{equivalent}} = 1 \times [\mathrm{Mo}] + 0.67 \times [\mathrm{V}] + 1.6 \times [\mathrm{Cr}] + 2.9 \times [\mathrm{Fe}] - 1 \times [\mathrm{Al}] \quad (8)$$

Weiss and Semiatin [68] have reported that the β-transus temperature decreases with increasing Mo equivalent. The 1% Cr has increased the Mo equivalent value to 9.45 for Ti-55521 alloy from 7.85 for Ti-55511 alloy. This difference in Mo equivalent reduces the β-transus temperature from ~1123 K [1] in the Ti-55511 alloy to ~1093 K for the Ti-55521 alloy [68]. Thus, the under cooling between the β-transus temperature and holding temperature of 1073 K is larger for the Ti-55511 alloy compared to that for the Ti-55521 alloy resulting in a higher volume fraction of α phase in Ti-55511 alloy. The similar results were obtained in [69] for Ti–10V–2Fe–3Al alloy where 50% of α volume fraction is formed by isothermal holding at 973 K for 1800 s and only 8.1% of α volume fraction is formed by isothermal holding at 1073 K for 1800 s. On the other hand, as the β to α phase transformation is a diffusion controlled transformation [64], the longer time available for transformation the higher volume fraction of the α phase formed. This is why for both alloys a larger volume fraction of α phase is obtained at relatively slower cooling rate of 1 K s^{-1} compared to that after 10 K s^{-1} cooling.

4.3. Mechanical properties

The strength of the alloy depends upon the properties and amounts of the phases present in the microstructure. Thus, the observed variation in strength could be explained by considering the changes in the volume fraction of α phase due to either processing difference (cooling rate) or compositional difference (wt% of Cr). Since α phase is harder than β phase, there is nearly a linear relationship between the strength and the amount of α phase (Table 5).

Although the amount of the α phase controls the strength of an alloy, its morphology affects the ductility. Terlinde et al. [21] have claimed that a change in shape from lamellae to globular of α phase increases the total elongation/ductility in Ti–10V–2Fe–3Al alloy. On the other hand, it has been reported that continuous networking nature of α phase deteriorates the total elongation/ductility [20,70,71]. In the present study, a reduction in total elongation is obtained for the samples cooled at 1 K s^{-1} cooling rate in both alloys, despite the presence of ~4% of globular-shaped α phase. This relatively low amount of the globular-shaped α may be insufficient to have a significant effect on the properties improvement, especially when the microstructures contain continuous and interconnected grain boundary α. Regardless of the cooling rate, the Ti-55521 alloy exhibited a lower total elongation compared to the Ti-55511 alloy. The possible reason for this is the

presence of more interconnected grain boundary α in the remaining β phase in Ti-55521 alloy compared to Ti-55511. This can be explained by the slower kinetics of α formation due to smaller under cooling below β transus, resulting in more free β grain boundaries available for α formation during cooling.

The modified C–J model has been applied to analyse the work hardening behaviour in the present study as it is generally used for two-phase materials [59–61]. It is mentioned in [61,62,72] that three stages in the work hardening behaviour depend upon the amount and type of the constituents present in the microstructure. Stage I corresponds to the plastic deformation of β phase that work hardens due to the glide of dislocations and formation of pile ups in the vicinity of the hard α phase grains which serve as barriers to dislocation motion and initially do not deform plastically. Consequently, strain gradient exists between the phases and within the β matrix. The higher the amount of α present, the more areas of high strain exist around α phase, and β phase work hardens faster, which corresponds to higher m_I. Stage II corresponds to the plastic deformation of soft β phase restrained between the hard α crystals, which continue to deform elastically. Stage III indicates the non-homogenous plastic deformation of both phases. The increase in m_I and m_{II} values with increasing the volume fraction of α in both alloys is in agreement with the literature [61,63,72], which also links the work hardening in the stage I with dislocation density, dislocation distribution and mobility of dislocations in the soft β phase.

5. Conclusions

The effects of final cooling rates, from 1073 K to room temperature, after TMP of two near-β Ti alloys on the microstructural parameters, phase transformation and mechanical properties were investigated. The following conclusions can be drawn:

- A β lattice distortion compared to unalloyed Ti is observed in both alloys and is attributed to the addition of the alloying elements. However, there is no effect of cooling rate on β lattice distortion. The α lattice parameters are unchanged in all experimental conditions.
- The slower final cooling results in a larger α crystallite sizes in both alloys, which is attributed to the annihilation of dislocations and formation of dislocation cell structure. Dislocation density is always found to be higher in the remaining β phase regardless of the cooling rates and alloy composition because (i) β phase is subjected to two high temperature deformations and (ii) ease of slip in the bcc crystal structure.
- The extent of β grain recrystallisation and continuous grain boundary α phase formation is more pronounced when the alloys are cooled slowly (1 K s^{-1}). Both cooling rates and Cr content affect the volume fraction of α, which subsequently influences the strength of the studied alloys. Among all the samples, the Ti-55511 alloy cooled at 10 K s^{-1} shows the highest total elongation with moderate UTS. For both alloys, slowly cooled samples showed a reduced total elongation. This is attributed to the formation of interconnected grain boundary α phase. The work hardening behaviour of the samples in all conditions is characterised by three distinct stages.

Acknowledgements

This work is funded by the Engineering Materials Institute strategic grant. The use of UOW Electron Microscopy Centre facilities, in particular JEOL 7001F, which was purchased with ARC support (LE0882613) is being acknowledged. The authors are grateful to Dr. A.A. Gazder for modification of tensile stage. One of the authors (Mansur Ahmed) would like to acknowledge the University Postgraduate Award (UPA) with International Postgraduate Tuition Award (IPTA) for his PhD study.

References

[1] O.M. Ivasishin, P.E. Markovsky, Yu.V. Matviychuk, S.L. Semiatin, C.H. Ward, S. Fox, J. Alloys Compd. 457 (2008) 296–309.
[2] O.M. Ivasishin, P.E. Markovsky, S.L. Semiatin, C.H. Ward, Mater. Sci. Eng. A 405 (2005) 296–305.
[3] O.M. Ivasishin, P.E. Markovsky, Yu.V. Matviychuk, S.L. Semiatin, Metall. Mater. Trans. A 34 (2003) 147–158.
[4] T. Saito, H. Takamiya, T. Furuta, Mater. Sci. Eng. A 243 (1998) 273–278.
[5] T. Saito, T. Furuta, Curr. Adv. Mater. Process., Iron Steel Inst. Jpn. 4 (1991) 1738–1739.
[6] F.H. Froes, D. Eylon, Int. Mater. Rev. 35 (1990) 162–184.
[7] M. Hagiwara, S. Emura, Mater. Sci. Eng. A 352 (2003) 85–92.
[8] K. Zhang, J. Mei, N. Wain, X. Wu, Metall. Mater. Trans. A 41 (2010) 1033–1045.
[9] W. Smarsly, Y.T. Lee, G. Welsch, Metall. Mater. Trans. A 16 (1985) 1831–1834.
[10] H. Jiang, K. Zhang, F.A. Garcia-Pastor, M.H. Loretto, D. Hu, P.J. Withers, M. Preuss, X. Wu, Mater. Sci. Technol. 27 (2011) 1241–1248.
[11] M.D. McNeese, D.C. Lagoudas, T.C. Pollock, Mater. Sci. Eng. A 280 (2010) 334–348.
[12] F.-C. Yen, K.-S. Hwang, Mater. Sci. Eng. A 528 (2011) 5296–5305.
[13] B. Ye, M.R. Matsen, D.C. Dunand, Acta Mater. 58 (2010) 3851–3859.
[14] V.A. Druz, V.S. Moxson, R. Chernenkoff, W.F. Jandeska Jr., J. Lynn, Met. Powder Rep. 61 (2006) 16–21.
[15] N. Zhang, P.B. Khosrovabadi, J.H. Lindenhovius, B.H Kolster, Mater. Sci. Eng. A 150 (1992) 263–270.
[16] J.C. Hey, A.P. Jardine, Mater. Sci. Eng. A 188 (1994) 291–300.
[17] D.G. Morris, M.A. Morris, Mater. Sci. Eng. A 110 (1989) 139–149.
[18] S.M. Green, D.M. Grant, N.R. Kelly, Powder Metall. 40 (1997) 43–47.
[19] O.M. Ivasishin, D. Eylon, V.I. Bondarchuk, D.G. Savvakin, Defect Diffusion Forum 277 (2008) 177–185.
[20] G.T. Terlinde, T.W. Duerig, J.C. Williams, Metall. Mater. Trans. A 14 (1983) 2101–2115.
[21] G. Terlinde, H.J. Rathjen, K.H. Schwalbe, Metall. Mater. Trans. A 19 (1988) 1037–1049.
[22] A Sarkar, A. Bhowmik, S. Suwas, Appl. Phys. A—Mater. Sci. Process. 94 (2009) 943–948.
[23] T. Ungár, M. Victoria, P. Marmy, P. Hanák, G. Szenes, J. Nucl. Mater. 276 (2000) 278–282.
[24] T. Shintani, Y. Murata, Acta Mater. 59 (2011) 4314–4322.
[25] X. Tian, Y. Zhang, Mater. Sci. Eng. A 516 (2009) 73–77.
[26] M.R. Movaghar Garabagh, S. Hossein Nedjad, H. Shirazi, M. Iranpour Mobarekeh, M. Nili Ahmadabadi, Thin Solid Films 516 (2008) 8117–8124.
[27] A Chanda, M. De, J. Alloys Compd. 313 (2000) 104–114.
[28] T. Ungar, H. Mughrabi, D. Rönnpagel, M. Wilkens, Acta Metall. 32 (1984) 333–342.
[29] F. Székely, I. Groma, J. Lendvai, Mater. Sci. Eng. A (309–310) (2001) 352–355.
[30] P.S. Chowdhury, A. Sarkar, P. Mukherjee, N. Gayathri, M. Bhattacharya, P. Barat, Mater. Charact. 61 (2010) 1061–1065.
[31] T. Ungár, O. Castelnau, G. Ribárik, M. Drakopoulos, J. Béchade, L.T. Chauveau, A. Snigirev, I. Snigireva, C. Schroer, B. Bacroix, Acta Mater. 55 (2007) 1117–1127.
[32] M.G. Glavicic, A.A. Salem, S.L. Semiatin, Acta Mater. 52 (2004) 647–655.
[33] M.G. Glavicic, S.L. Semiatin, Acta Mater. 54 (2006) 5337–5347.
[34] A Sarkar, S. Roy, S. Suwas, Mater. Charact. 62 (2011) 35–42.
[35] R. Boyer, R. Briggs, J. Mater. Eng. Perform. 14 (2005) 681–685.
[36] S. Banerjee, P. Mukhopadhyay, Phase Transformations: Examples from Titanium and Zirconium Alloys, Elsevier, Amsterdam, The Netherlands, 2007.
[37] M. Ahmed, A.A. Gazder, D.G. Savvakin, O.M. Ivasishin, E.V. Pereloma, J. Mater. Sci. 47 (2012) 7013–7025.
[38] A Carman, L.C. Zhang, O.M. Ivasishin, D.G. Savvakin, M.V. Matviychuk, E.V. Pereloma, Mater. Sci. Eng. A 528 (2011) 1686–1693.
[39] B.E. Warren, X-ray Diffraction, second ed., Courier Dover Publications, Mineola, NewYork, 1990.
[40] V. Randle, O. Engler, Introduction to Texture Analysis: Macrotexture, Microtexture and Orientation Mapping, second ed., CRC Press, Taylor & Francis Group, Boca Raton, FL, 2009.
[41] P. Scardi, M. Leoni, Acta Crystallogr. Sect. A 58 (2002) 190–200.
[42] D. Balzar, H. Ledbetter, J. Appl. Crystallogr. 26 (1993) 97–103.
[43] E.J. Mittemeijer, P. Scardi, Diffraction Analysis of the Microstructure of Materials, Springer, Berlin-Heidelberg, 2004.
[44] T. Ungár, A. Borbély, Appl. Phys. Lett. 69 (1996) 3173–3175.
[45] R.L. Snyder, H.J. Bunge, J. Fiala, Defect and Microstructure Analysis from Diffraction in International Union of Crystallography Monographs on Crystallography no. 10, 1999.
[46] L. Lutterotti, P. Scardi, J. Appl. Crystallogr. 23 (1990) 246–252.
[47] N. Popa, J. Appl. Crystallogr. 31 (1998) 176–180.
[48] W. Dollase, J. Appl. Crystallogr. 19 (1986) 267–272.
[49] R.E. Smallman, K.H. Westmacott, Philos. Mag. 2 (1957) 669–683.

[50] G.R. Stibitz, Phys. Rev. 49 (1936) 862–863.
[51] H. Ledbetter, H. Ogi, S. Kai, S. Kim, M. Hirao, J. Appl. Phys. 95 (2004) 4642–4644.
[52] A.N. Timoshevskii, S.O. Yablonovskii, O.M. Ivasishin, Funct. Mater. 19 (2012) 266–271.
[53] E.S. Fisher, M.H. Manghnani, J. Phys. Chem. Solids 32 (1971) 657–667.
[54] Y.T. Lee, M. Peters, G. Welsch, Metall. Mater. Trans. A 22 (1991) 709–714.
[55] B.D. Cullity, S.R. Stock, Elements of X-ray diffraction, third ed., Prentice Hall, Upper Saddle River, New Jersey, 2001.
[56] Y.Q. Zhao, S.W. Xin, W.D. Zeng, J. Alloys Compd. 481 (2009) 190–194.
[57] S.X. Liang, M.Z. Ma, R. Jing, Y.K. Zhou, Q. Jing, R.P. Liu, Mater. Sci. Eng. A 539 (2012) 42–47.
[58] H.M. Otte, A.L. Esquivel, Trans. Metall. Soc. AIME 233 (1965) 1276–1280.
[59] W. Nie, X. Wang, S. Wu, H. Guan, C. Shang, Sci. China Technol. Sci. 55 (2012) 1791–1796.
[60] A. Kumar, S.B. Singh, K.K. Ray, Mater. Sci. Eng. A 474 (2008) 270–282.
[61] F.H. Samuel, Mater. Sci. Eng. 92 (1987) L1–L4.
[62] A. Bag, K.K. Ray, E.S. Dwarakadasa, Metall. Mater. Trans. A 30 (1999) 1193–1202.
[63] H. Paruz, D.V. Edmonds, Mater. Sci. Eng. A 117 (1989) 67–74.
[64] O.M. Ivasishin, P.E. Markovsky, JOM 48 (1996) 48–52.
[65] M.K. Kumar, I. Samajdar, N. Venkatramani, G.K. Dey, R Tewari, D. Srivastava, S. Banerjee, Acta Mater. 51 (2003) 625–640.
[66] B.B. Rath, R.J. Lederich, C.F. Yolton, F.H. Froes, Metall. Mater. Trans. A 10 (1979) 1013–1019.
[67] C. Sauer, G. Luetjering, J Mater. Process. Technol. 117 (2001) 311–317.
[68] I. Weiss, S.L. Semiatin, Mater. Sci. Eng. A 243 (1998) 46–65.
[69] C. Li, X. Wu, J.H. Chen, S. van der Zwaag, Mater. Sci. Eng. A 528 (2011) 5854–5860.
[70] J. Chesnutt, F. Froes, Metall. Mater. Trans. A 8 (1977) 1013–1017.
[71] N. Clément, A. Lenain, P.J. Jacques, JOM 59 (2007) 50–53.
[72] R.A. Kot, B.L. Bramfitt, Fundamentals of dual-phase steels, in: Proceedings of the Symposium, Metallurgical Society of AIME, 1981.

Chapter 4

The effect of ageing on microstructure and mechanical properties of powder Ti-5Al-5Mo-5V-1Cr-1Fe alloy

Materials Science & Engineering A 605 (2014) 89–97

Contents lists available at ScienceDirect

Materials Science & Engineering A

journal homepage: www.elsevier.com/locate/msea

The effect of ageing on microstructure and mechanical properties of powder Ti–5Al–5Mo–5V–1Cr–1Fe alloy

Mansur Ahmed [a,*], Dmytro G. Savvakin [b], Orest M. Ivasishin [b], Elena V. Pereloma [a,c]

[a] School of Mechanical, Materials & Mechatronic Engineering, University of Wollongong, NSW 2522, Australia
[b] Institute for Metal Physics, National Academy of Sciences of Ukraine, UA-03142 Kiev, Ukraine
[c] Electron Microscopy Centre, University of Wollongong, NSW 2519, Australia

ARTICLE INFO

Article history:
Received 13 September 2013
Received in revised form
20 January 2014
Accepted 10 March 2014
Available online 18 March 2014

Keywords:
Powder Ti-55511
Ageing
Microstructure
X-ray diffraction
Mechanical properties

ABSTRACT

The thermo-mechanically processed powder Ti–5Al–5V–5Mo–1Cr–1Fe alloy was aged at 923 K for 1–8 h in order to investigate the effect of ageing time on the microstructure–mechanical properties relationships. The microstructures of the alloy after ageing consist of the both primary and secondary α phases with retained β matrix phase. The shift of β peaks in X-ray pattern with ageing time indicates an increase in lattice parameter distortion due to diffusion into the retained β phase of more β stabilisers with smaller atomic radius compared to the elemental Ti. The tensile test results indicate that the sample aged for 1 h has achieved the best combination of mechanical properties with ultimate tensile strength of 1194 MPa and total elongation of 14.1% among all the experimented conditions. The modified Crussard–Jaoul method is applied to characterise the work hardening behaviour of the alloy.

1. Introduction

The main reasons for using Ti alloys in the fields of aerospace, chemical and medical applications are their high strength with reasonable ductility, high strength-to-weight ratio, good fatigue strength and corrosion resistance [1]. The conventional casting is so far the most commonly used method for the production of Ti alloys for different aerospace parts, e.g. landing gears, airframe, compressor discs and blades, spacers and gas turbine engines [2,3]. However, castings inherit some essentially unavoidable defects, such as macro-segregation, micro-segregation, porosity, solidification shrinkage and second phase inclusions [3–5]. In addition, only ~10% of the material's initial weight is utilised [6] resulting in high processing costs. On the other hand, powder metallurgy provides a significant cost reduction in the production of Ti alloys [7,8] making them more affordable, which may lead to a wider spread of their applications in many fields. Moreover, using powder metallurgy technique nearly full density products could be manufactured [8,9]. The blended elemental powder metallurgy (BEPM) technique is one of the cost effective techniques for production of Ti alloys [7,8].

Microstructure of near-β Ti alloys (e.g. Ti–5Al–5Mo–5V–1Cr–1Fe (Ti-55511)) consists of α and β phases where the amount and morphology of α phase to a large extent control the mechanical properties [10]. Moreover, heat treatment is used to modify the microstructure of this category alloys. Ageing is the final and inevitable processing step which is used to improve the mechanical properties [10]. Ageing of Ti-55511 is usually performed at high temperature ($>$ 623 K) where preferable nucleation sites for α nucleation already exist such as dislocations, or ω phase [11]. Ohmori et al. [12] have mentioned that α precipitates nucleate at ω/β interfaces, whereas Zhang et al. [13] have reported that fine α phase nucleates at ω particles. This ω phase is formed during slow heating to ageing temperature [14]. Nag et al. [15] have noticed that ω phase is very fine nanometre sized precipitates and the elemental concentration variation is considered to be responsible for its formation. Thus, the availability of such large number of nucleation sites results in fine α precipitation which is associated with both high strength and ductility [16]. Hence, high temperature ageing with slow heating rate to ageing temperature has been used in the present study.

Most of the previous investigations mentioned only the mechanical properties of cast Ti55511 alloy during ageing [11,17–21], while some others reported only microstructural changes without providing data on the mechanical properties [13,22]. Mechanical properties of cast/wrought Ti-55511 alloy after ageing at different conditions are listed in Table 1; they are dependent on the complete processing schedule. Although a limited data on the microstructure–mechanical properties relationships of aged (cast/wrought) Ti-55511 is available [14,23], the detailed and systematic analysis of these relationships is lacking. Thus, the aim of the present study is

* Corresponding author. Tel.: +61 2 42215798; fax: +61 2 42213662.
E-mail address: ma960@uowmail.edu.au (M. Ahmed).

http://dx.doi.org/10.1016/j.msea.2014.03.030
0921-5093/

Table 1
Mechanical properties of Ti-55511 alloy and its derivatives after ageing.

Composition (wt%)	*Processing stages*	*YS (GPa)*	*UTS (GPa)*	*T.E. (%)*	*Ref.*
Ti-55511	1093 K (1–2 h), 1023 K (2–3 h), *873 K (4 h)*	1.07–1.12	1.12–1.16	9–12	[17]
	1093 K (1–2 h), 1063 K (2–3 h), *873 K (4 h)*	1.15–1.21	1.24–1.29	8–12	[17]
	1093 K (1–2 h), 1023 K (2–3 h), *843 K (8 h)*	1.1–1.2	1.17–1.25	8–14	[18]
	1223 K (0.5 h), RT (30% def.), 1223 K, *811–913 K (8 h)*	1.24–1.75	1.35–1.75	0.3–7.5	[14]
	1113 K (4 h), HIP (1133 K), *843 K (0.25–5 h)*	–	1.23	10.7	[21]
	1113 K (3 h), 1023 K (3 h), *853 K (4 h)*	–	1.21	15.9	[19]
	1133 K (3 h), 1023 K (3 h), *843 K (8 h)*	–	1.215	15	[19]
Ti–6.5A–3Mo–2.5Fe–0.5Cr–0.5Mn	1143 K(1 h), *673 K(0.25–5 h)*	0.96–1.27	1.01–1.4	5.1–11	[20]
Ti–5Al–5Mo–5V–1Cr–1Fe–0.3C	1133 K(3 h), 1023 K(3 h), *853 K(8 h)*	–	1.29	16.6	[21]
Ti–5.4Al–5Mo–2.9V–1.3Cr–0.9Fe	1023 K (1 h), *823 K (10 h)*	1.28	1.45	8	[23]

Key: RT=room temperature; UTS=ultimate tensile strength; YS=yield strength; HIP=hot isostatic pressing; T.E.=total elongation. Italics in column 2 indicates the ageing treatment.

to evaluate the effect of ageing time on the microstructure–mechanical properties relationships of Ti-55511 alloy produced by cost effective (BEPM) process.

2. Materials and experiments

In order to obtain the required alloy composition, Ti powders containing 3.5 wt% hydrogen were combined with elemental Mo, Cr, Fe (<40 μm) and 50Al–50V master alloy powders (40–63 μm). Thereafter the green compacts were prepared through blending and die pressing under 650 MPa. The sintering of green compacts was done by two steps (i) heating to 1293 K for 1 h followed by (ii) heating to 1523 K for 6 h to assist the distribution of the alloying elements homogeneously in the matrix. The as-sintered material contains of about 2 vol% residual porosity which was determined using the Archimedes method [24].

Thermo-mechanical processing (TMP) was conducted using a Gleeble[1] 3500 thermo-mechanical simulator. Tests were carried out under $\sim 3.8 \times 10^{-4}$ Torr vacuum to avoid atmospheric contamination. The dimensions of the cylindrical sample used for the TMP was 12 mm length and 8 mm diameter. The samples were heated to 1223 K at 10 K s^{-1} and held for 120 s. Afterwards, the samples were cooled down to 1173 K at 35 K s^{-1} and deformed to 25% reduction followed by cooling to 1073 K at 35 K s^{-1}. Thereafter the samples were held for 600 s at 1073 K followed by 60% reduction at 1073 K. Eventually, the samples were cooled to room temperature at 10 K s^{-1}. After the TMP, the samples were encapsulated into a quartz tube under vacuum in order to protect against high temperature oxidation. Thereafter, the samples were placed into a tube furnace[2] and heated at 0.25 K s^{-1} to 923 K and held for 1 h, 2 h, 4 h and 8 h. The entire heat treatment cycle is shown in Fig. 1.

The microstructures were investigated using scanning electron microscopy (SEM). The specimens for SEM observations were cut normal to the deformation direction and prepared by using conventional metallographic techniques. After polishing, the samples were etched in a solution of 2 ml hydrofluoric acid, 5 ml nitric acid and 93 ml distilled water (Kroll's reagent) to reveal the microstructure. SEM observations were carried out using a JEOL-JSM 7001F Field Emission Gun-Scanning Electron Microscope (FEG-SEM) operating at 15 kV voltage and 10 mm working distance and equipped with an XMax Oxford Instruments energy dispersive X-ray spectrometer (EDS). The sub-sized tensile test specimens with gauge length 5.1 mm; width 2.18 mm and thickness 0.9 mm were machined using the electrical discharge machine (EDM). A μ-Tweezer Tensile

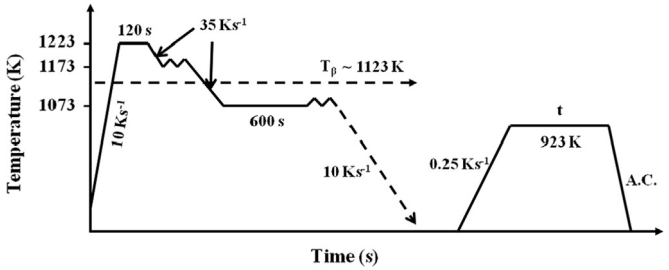

Fig. 1. The illustration of the heat treatment cycle used in this study. Here *t* indicates the ageing time which is 1 h, 2 h, 4 h and 8 h. A.C. stands for air cooling.

Module[3] at a constant speed of 1.7 mm min^{-1} at room temperature was used to perform the tensile test. The stress–strain curves were fitted using rational polynomial functions (via a programme called Table Curve5.1) which were utilised to find the *m*-values of the plastic regions of the samples.

A PANalytical X'Pert PRO Multipurpose diffractometer (MPD) with Cu Kα radiation (λ=0.154 nm) filtered with Ni-monochromator operating at 45 mA and 40 kV was used to investigate the material using X-ray diffraction. The dimension of the samples was ~15 mm diameter which was oriented parallel to the deformation axis. Under a continuous scanning mode, the diffraction patterns were acquired over the 2θ range of 30° to 90°. The step size and the acquisition time were 0.01° and 490 s respectively. A standard polycrystalline silicon sample was used in order to characterise the instrumental broadening. The lattice parameters of the hcp crystal structure were calculated precisely using Cohen's method [25]. The volume fraction of α phase was calculated using direct comparison method [25]. The Rietveld method was applied to characterise the different crystallographic planes (e.g. crystallite size and microstrain) of α and β phases using X'pert HighScore Plus software. The algorithms behind Rietveld method used in the present study are described elsewhere [26]. Thereafter, the dislocation density of the crystallographic planes was calculated from the numerical value of crystallite size and microstrain using the standard equations [27,28].

3. Results and discussion

3.1. The evolution of microstructure

After TMP, the microstructure of Ti-55511 alloy consists of primary α and β phases (Fig. 2a). This condition has been used

[1] Dynamic Systems Inc.
[2] GSL-1600-80X, MTI Corporation
[3] Kammrath & Weiss, GmbH

as ageing precursor. α Phase has different morphologies in TMP sample: globular and lamellae which form basket weave structure. The fragmentation of grain boundary α occurs during high temperature deformation at 1073 K. Partial β recrystallisation and fine α lamellae were produced during cooling to room temperature, which has also been reported in [27]. From XRD data, the volume fraction of α phase was calculated to be $26 \pm 4\%$, so that the microstructure can further be optimised during ageing.

Fig. 2b–e shows the microstructures of Ti-55511 alloy after ageing at 923 K for 1 h, 2 h, 4 h and 8 h, respectively. The microstructures consist basically of primary α, secondary α and retained β phases. The morphology of the secondary α phase precipitated during ageing is shown in Figs. 2 and 3. It is evident that recrystallisation of the deformed β phase occurs during ageing (Fig. 3b–e). Similarly, the recrystallisation of deformed β phase is reported in [29]. It appears that the morphology of fine secondary α is almost similar for all the aged samples showing basket weave structure which precipitated homogeneously. It also shows that the fine secondary α precipitated both intragranularly and at the grain boundaries of recrystallised β phase which supports the investigation by Zhang et al. [13]. The applied high temperature deformation increases the dislocation density of β phase as glide occurs easily in bcc structure, thus resulting in more nucleation sites for α precipitates [27,30]. The amount of fine secondary α phase is the identifying difference among the aged samples, as it increases with ageing time from 44% after 1 h to 62% after 8 h ageing (Table 2). The width and length of fine secondary α for 1–4 h aged samples are 0.08–0.12 μm and ~0.6 μm, respectively.

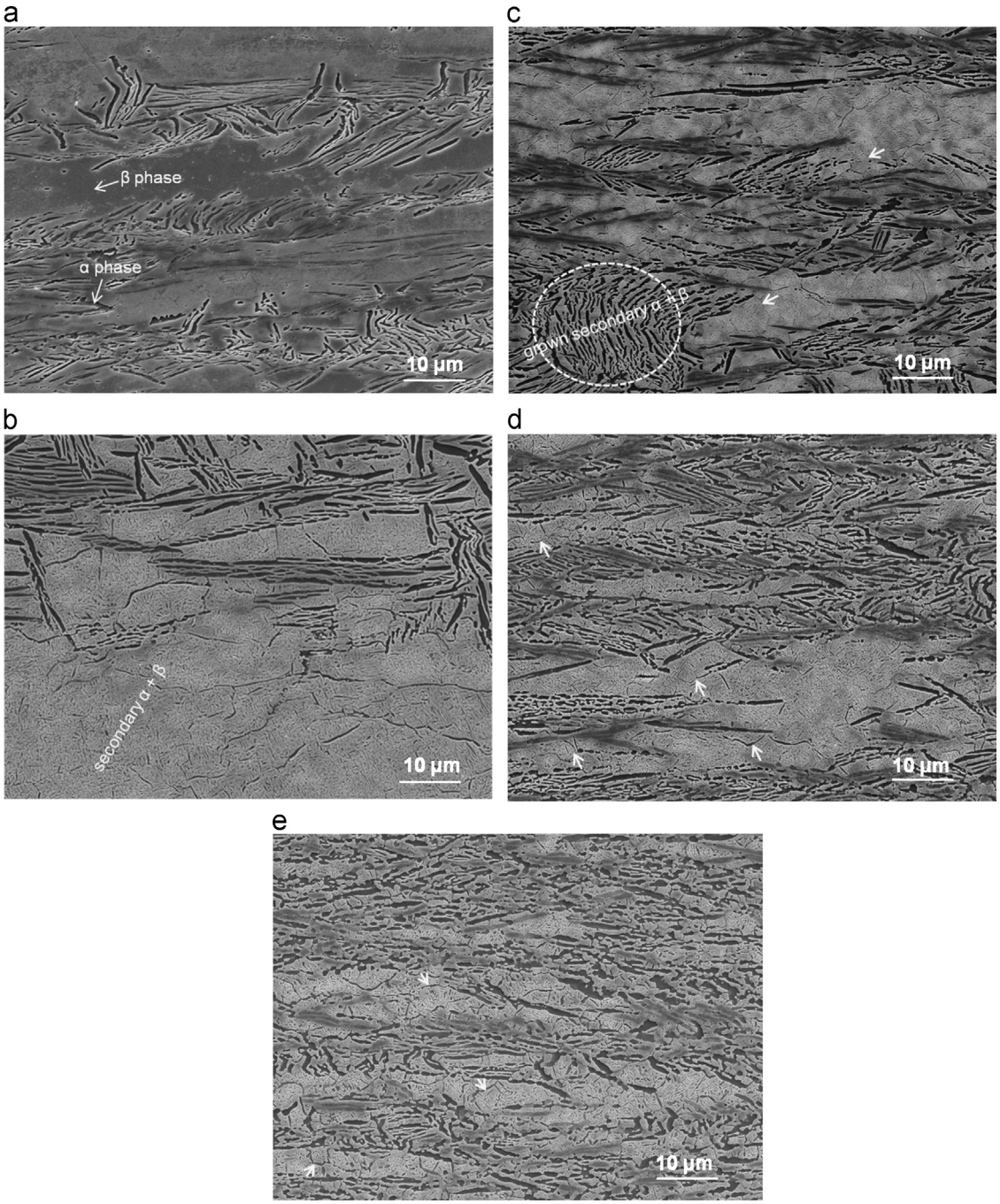

Fig. 2. The microstructures of Ti–5Al–5Mo–5V–1Cr–1Fe alloy after TMP (a) and ageing at 923 K (b–e) for 1 h, 2 h, 4 h and 8 h, respectively. White coloured arrows in Fig. 2(c–e) indicate the recrystallisation of β phase during ageing.

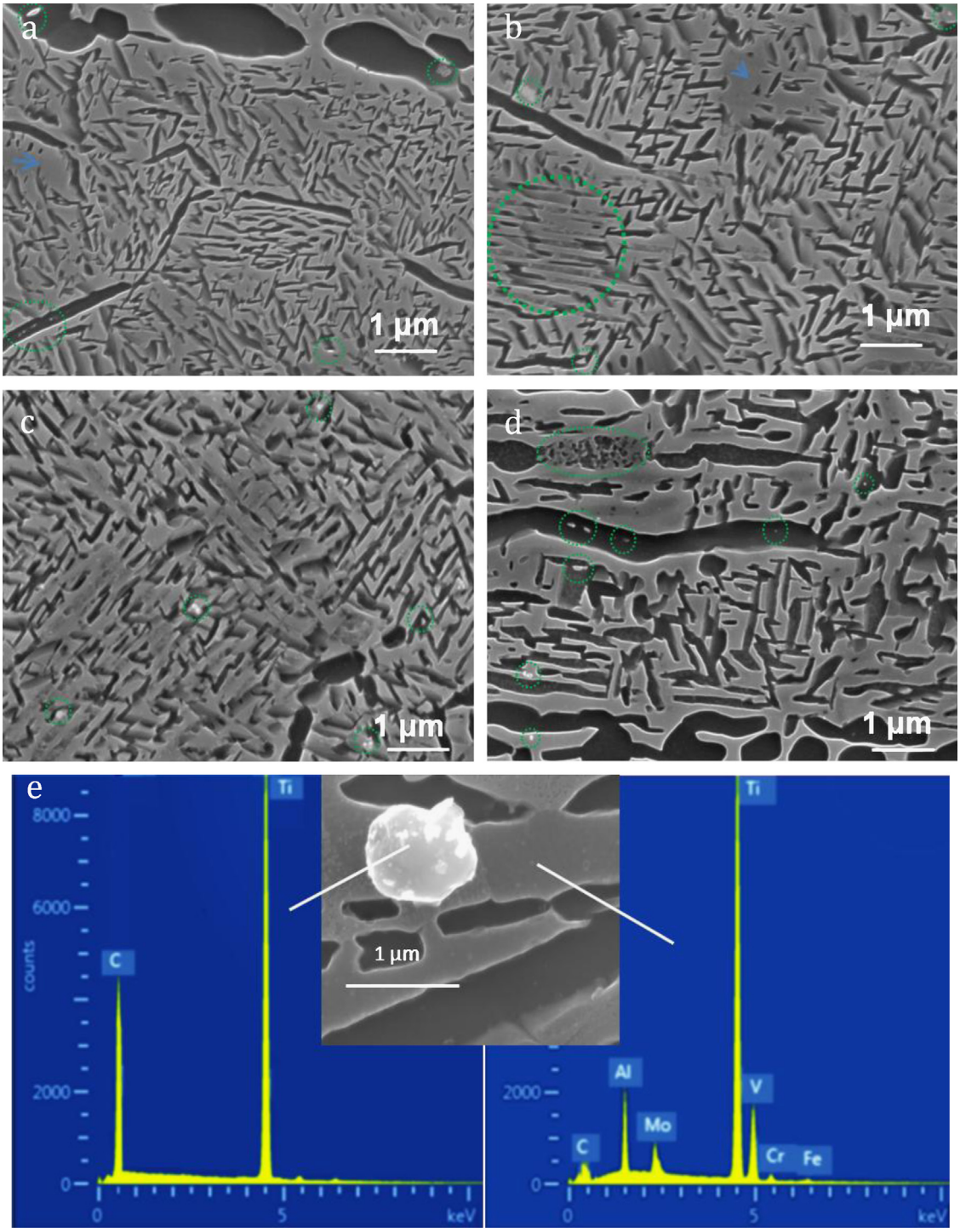

Fig. 3. Morphology of the secondary α produced during ageing for 1 h (a), 2 h (b), 4 h (c), and 8 h (d). The small green circles show the white colour particles, which were identified as titanium carbide based on EDS analysis (e). The blue arrows in (a) and (b) show the retained β phase. The large green circles in (b) and (d) indicate the region not fully transformed into single α. (e) shows the EDS analysis of the white particles (left) and β matrix phase (right). Inset of (e) shows enlarged view of titanium carbide particle. (For interpretation of the references to colour in this figure legend, the reader is referred to the web version of this article.)

On the other hand, fine secondary α in the sample aged for 8 h has grown by coalescing adjacent α lamellae (Fig. 3d) which returned the width and length of ~0.2 and 0.5 μm respectively. Since nucleation and growth of fine secondary α is a continuous process, the growth seems dominant after 4 h ageing. It is mentioned in [22], that the growth of the α phase could be due to (i) the increase of diffusional mobility of atoms at the temperature of ageing and (ii) the need to decrease surface-to-volume ratio of needle-like α particles in order to reduce the total energy of the system. In the present study no α'' phase appears contrarily to the findings by Shevel'kov [22], because shorter ageing times used were not sufficient to produce large concentration gradients within β phase. The obtained microstructures are in good agreement with the existing literature [13,14,31,32]. Beyond this, there is an important microstructural feature showing the incomplete phase transformation in a single α lamellae (Fig. 3b and d). The similar result is also obtained in our previous investigation [27] where it has been proved that the segregation of C and/or O is

Table 2
The volume fraction of α phase (V_α), 0.2% proof strength ($\sigma_{0.2\%}$), ultimate tensile strength (σ_{UTS}), uniform elongation (el_{uni}) and total elongation (el_{tot}) of the Ti-55511 alloy at different ageing conditions.

Alloy	Ageing condition (h)	V_α (%)	$\sigma_{0.2\%}$ (MPa)	σ_{UTS} (MPa)	el_{uni} ($\pm$ max. 0.5%)	el_{tot} (%)
Ti-55511	0	26 ± 4	1009 ± 13	1103 ± 30	5.8	10.2 ± 0.9
	1	44 ± 5	1120 ± 15	1194 ± 24	10.1	14.1 ± 1.1
	2	51 ± 6	1165 ± 19	1243 ± 26	8.5	12.5 ± 1.3
	4	56 ± 6	1219 ± 22	1287 ± 29	7.1	11.2 ± 1.9
	8	62 ± 4	1247 ± 18	1298 ± 16	6.8	11.0 ± 0.8

All strength and elongation shown in the table are engineering strength and engineering elongation.

responsible for this event. As C and O are α stabilisers, formation of their segregation into the β matrix reduce Mo equivalent. Thus, such local region is more stable β (due to the increased β-transus temperature [33]) resulting in a delay in the $\beta \rightarrow \alpha$ transformation compared to the area containing no C and/or O segregation.

White spherical shaped particles of typically 100–200 nm in size are present in the microstructures in both α and β phases (Fig. 3). However, some of them reach up to 1 μm size (Fig. 3e inset). From the comparison of EDS spectra of β matrix and a white particle, it is clear that the main elements in the particle are titanium and carbon. Thus, it is assumed to be a titanium carbide particle (Fig. 3e). There is no effect of ageing on these particles in terms of their size and morphology (Fig. 3). The presence of similar white titanium carbide particles in β-Ti alloys is reported in the literature [20,32,34]. In another study [35], the effect of carbon content on structural changes in α phase in Ti–5Al–5Mo–5V–3Cr alloy has been discussed but they do not mention the presence of such particles. The reason for titanium carbide formation can be understood from the electronic configuration of Ti i.e. [Ar] $3d^2$ $4s^2$. Sung and Tai [36] have reported that transition metals react with carbon by overlapping their d-orbitals with carbon p-orbitals, and thus the reactivity of carbon and metals is mainly determined by metal electronic state and specifically by number of vacant electron in d-orbitals. In the present case, as the number of the electron vacancy in d-orbitals in titanium increases compared to other elements (Mo/V/Cr/Fe), the reactivity also increases which lead to the formation of titanium carbide. This is why titanium carbide can easily form depending upon the availability of carbon. In the present study, carbon may be picked up unexpectedly during either processing (TMP/ageing) or from the original powder.

3.2. Phase composition and their dependency on the elemental diffusion

The compositional variation of the phases with respect to the ageing time is depicted in Fig. 4. It is clear from the histogram for primary α that the amount of the β stabilising alloying elements depletes with the ageing time whereas the concentration of α stabiliser Al increases (Fig. 4a). This is attributed to the diffusion of the β stabilisers out of the primary α phase. The observed increase in the concentration of β stabilising elements in fine secondary α with increase in ageing time is associated with the formation of secondary α from more enriched β phase. As β stabilisers diffuse out of fine secondary α formed during ageing, the β phase becomes enriched. This enriched retained β phase acts as the parent phase for producing secondary α at later stages of ageing. Consequently, each secondary α produced at the next stage of ageing has more β stabilisers than the previous one (Fig. 4).

Solid state diffusion is the mechanism responsible for mass transfer resulting in the observed compositional difference in the phases with the ageing time. The effective diffusion distance of an element can be estimated by the following equation [37]:

$$x = \sqrt{Dt} \quad (1)$$

where x is the effective diffusion distance (or path), D is the diffusivity of element herein and t is the diffusion time. The diffusivity D of an element depends upon the temperature and activation energy which also varies with the temperature. However, the diffusivity can be calculated using the following equation [38]:

$$D = D_0 \exp(-Q/RT) \quad (2)$$

where D_0 is the pre-exponential diffusion constant, Q is the activation energy for diffusion, T is the diffusion temperature and R is the ideal gas constant. Using the above Eqs. (1) and (2), the diffusion distances for Fe and Cr has been estimated in α-Ti at ageing temperature (923 K). The calculated diffusion path for Fe is 12.8–27.3 μm for 1 h using the following range for Fe diffusivity $D = 4.54 \times 10^{-14}$ to 2.08×10^{-13} m^2 s^{-1} [38]. Furthermore, for similar condition the estimated diffusion distance for Cr is 1.37–1.85 μm when $D = 5.18 \times 10^{-16}$ to 9.48×10^{-16} m^2 s^{-1} [38]. Unfortunately, there is no diffusivity information available for V and Mo in α-Ti. On the other hand, the effective diffusion distance for Al in β-Ti is 0.2 μm for similar condition using $D = 9.94 \times 10^{-18}$ m^2 s^{-1} [38]. Considering the concentration of Fe and Cr in primary α phase, it can easily be realised that the actual diffusion distance is reasonably shorter than the calculated one (12.8–27.3 μm and 1.37–1.85 μm after 1 h, respectively) because primary α phase has width of 0.4–0.6 μm and some Fe and Cr are still remained in it (Fig. 4a). This is attributed to the reduction of the diffusivity of the elements when more than one elements present in the system [39].

3.3. Materials characterisation using XRD line profile analysis

Fig. 5 indicates the X-ray diffraction profiles and corresponding Rietveld fitting for all the conditions where peaks from α and β phases with *Miller–Bravis* indices are clearly displayed. The difference in intensity between Rietveld fitting and experimental has also been plotted under each profile. The agreement indices of the fitting show that the residual weighted profile remains between 10% and 15% for all samples whereas the Goodness of fit is lying close to 1. A summary of the Rietveld fitting representing crystallite size, microstrain, and dislocation density for β and α phases with respect to ageing time are shown in Tables 3 and 4 respectively. A reduction in dislocation densities in both phases has been occurred during ageing compared to TMP condition. The following two concurrent events determines the density of dislocations within β planes: (i) the plastically deformed β planes have relaxed/reduced stress during ageing through the recrystallisation and (ii) the fine secondary α produced during ageing have constrained the β phase. On the other hand, the first event dominates in the α phase resulting in a reduction in density of dislocations with the ageing time. The observed difference in the density of dislocations between two phases can also be explained by the evolvement of fine secondary α through constraining β which plays a significant role in the increase of dislocation density

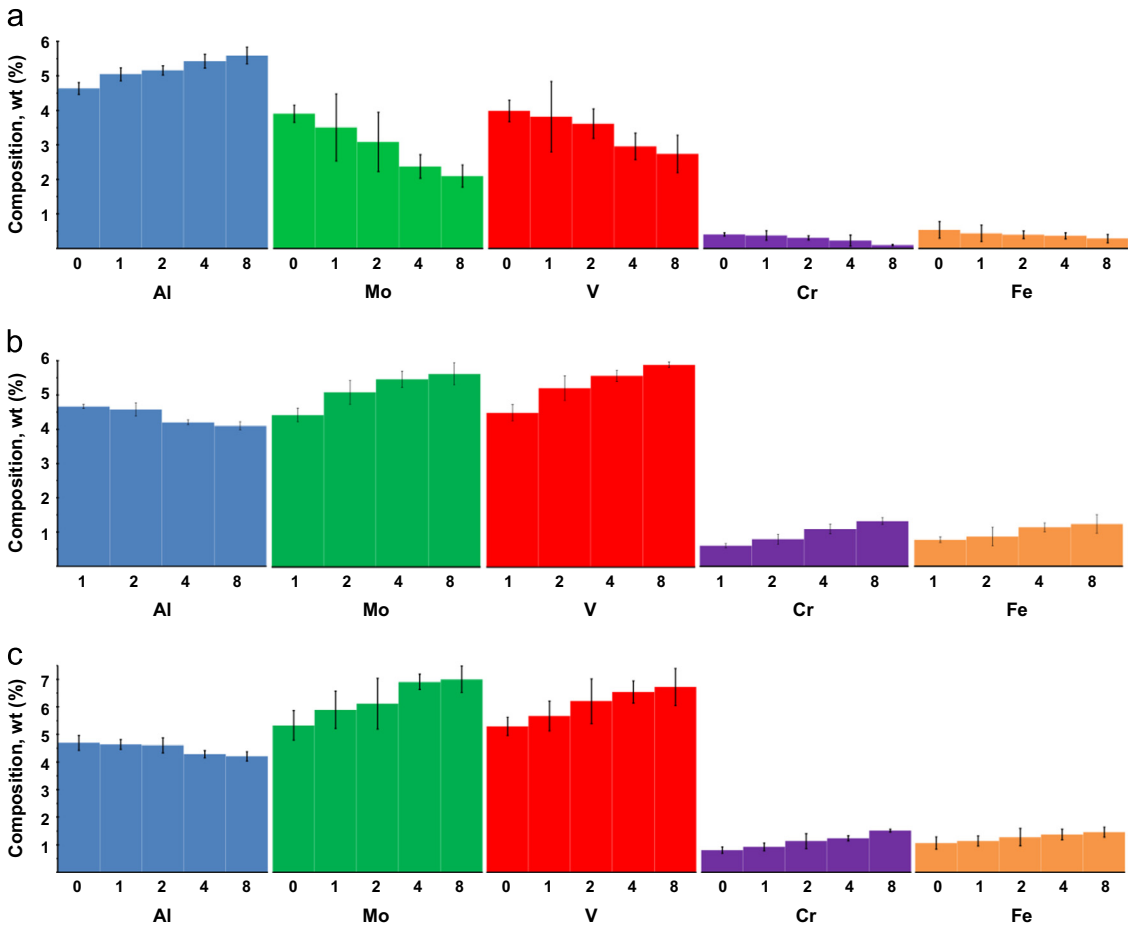

Fig. 4. The variation in phase composition with the ageing time in (a) primary α, (b) secondary α and (c) β phase.

in β phase. As expected, the crystallographic plane β (110) has the maximum dislocation density and β (200) has the minimum in all the conditions. It is mentioned in [40] that β (110) planes has the maximum compliance of strain during deformation whereas β (200) has the lowest among the bcc planes in metastable β alloy resulting in the highest dislocation density in β (110).

Table 5 presents the data of the lattice parameters of the β-Ti and α-Ti. It has been mentioned in [27] that the β lattice parameter reduced after TMP compared to unalloyed Ti. The presence of β stabilisers which have smaller atomic radii compared to elemental Ti is responsible for this event. A further reduction in β lattice parameter from 0.32 to 0.30 nm is obtained during ageing compare to the TMP condition, which can also be explained by the same reason because the β phase becomes more supersaturated with the same alloying elements. However, there was no significant effect of the ageing time on the lattice parameters of hcp crystal (α-Ti) because α stabiliser Al (143 pm) is the main alloying element in hcp lattice which has a closer atomic radius to Ti (147 pm) compared to those of β stabilising alloying elements.

3.4. Mechanical properties

A summary of the mechanical properties derived from Fig. 6 is given in Table 2. The volume fraction of α is linearly proportional to the ageing time which ultimately affects the tensile properties. The samples aged for 8 h and 1 h have yielded the maximum UTS (1298 ± 16 MPa) and the minimum UTS (1194 ± 24 MPa), respectively. Contrarily, the maximum total elongation ($14 \pm 1\%$) and the minimum total elongation ($10 \pm 1\%$) are obtained for the samples aged for 1 h and 8 h, respectively. The increasing trend of the strength and the decreasing one for the elongation with respect to α volume fraction support the second phase precipitation hardening mechanism. The obtained strength-elongation results are in good agreement with the literature [11,14,17,31]. Ivasishin et al. [14] have obtained UTS of 1410 MPa and elongation of 7.5–10% after ageing at 913 K for 8 h. The difference in UTS and elongation between the present study and Ref. [14] can be explained by analysing the heat treatment cycle of both samples. They heated the sample to 1223 K (β solution treatment) for 0.5 h resulting in a large β grain size ($\sim$200 μm) whereas in the present study only 300 s holding at the same temperature yielded much smaller β grain size ($\sim$80 µm [41]). Thereafter, the sample of Ref. [14] was cold deformed leading to α'' formation and causing poor elongation [42]. In contrast, in the present study hot plastic deformation (60%) at 1073 K is applied which fragments the primary α phase. It is well known that the fragmentation of α assists in improving the ductility of Ti. The reason behind obtaining such a good combination of total elongation (10–14%) and ultimate tensile strength (1200–1300 MPa) was the slow heating rate (0.25 K s^{-1}) to the ageing temperature. Since the slower heating rate offers the β phase decomposition to α through ω e.g. $\beta \rightarrow \beta + \omega \rightarrow \alpha + \beta$ rather than direct β phase decomposition at higher heating rate (20 K s^{-1}) [14,43] resulting in well dispersed, fine and uniform intragranular α phase which enhance both the strength and elongation. In contrast, higher heating rate leads to a coarser and non-uniformly distributed α precipitates resulting in poor balance of mechanical properties [14,31].

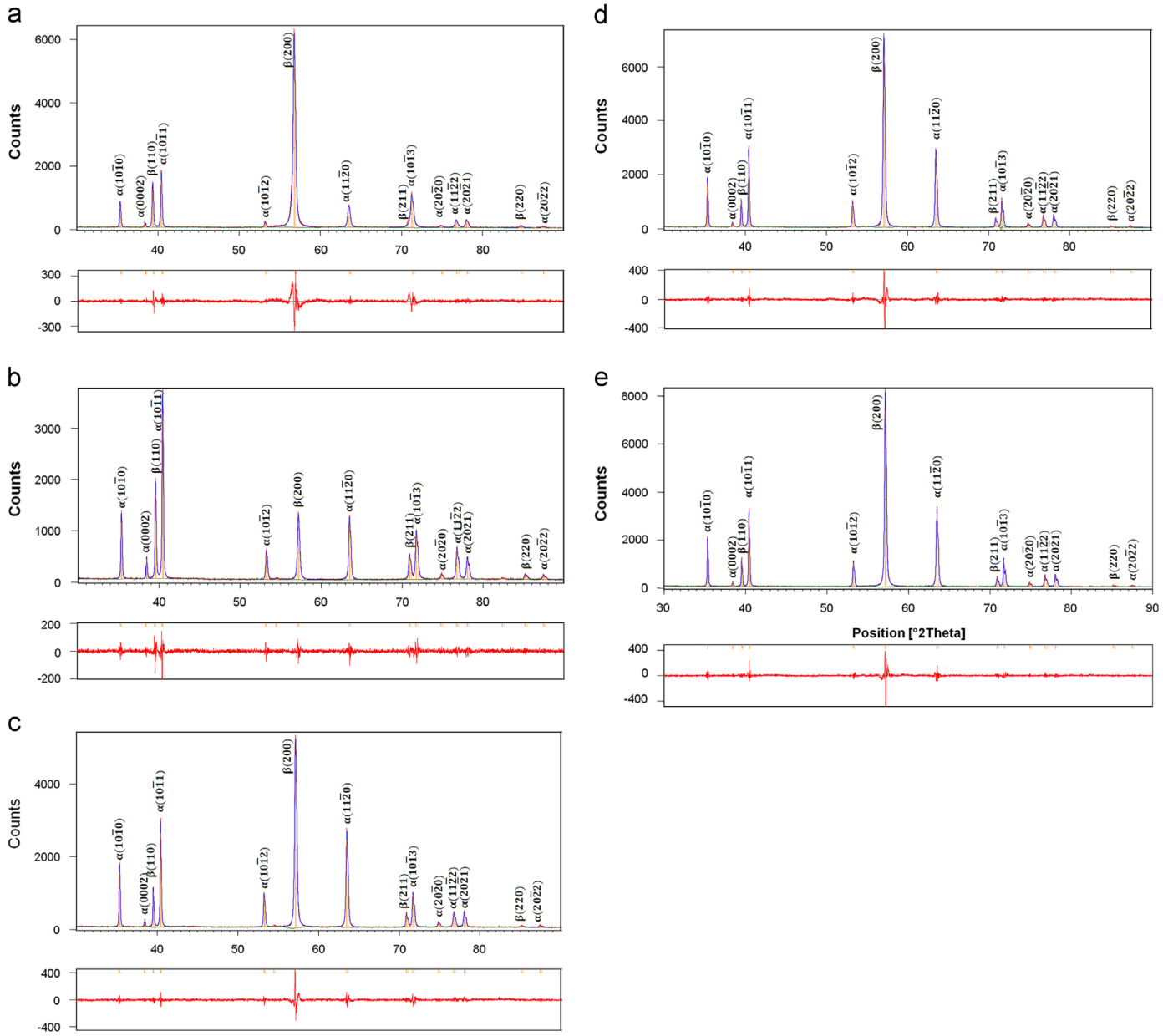

Fig. 5. XRD patterns associated with the Rietveld fitting for the samples after (a) TMP and (b–e) ageing treatment for 1 h, 2 h, 4 h and 8 h respectively. The difference between the experiment and fitting is displaying under each pattern.

The effect of the titanium carbide particles on the mechanical properties is mentioned in [20,32]. It has been shown that the addition of C reinforces the strength and reduces the elongation slightly due to the formation of titanium carbide compound. It is rather difficult to comment about the contribution of the titanium carbide particles to the mechanical properties in the present study, because C is not added deliberately and the total C amount is negligible. On the other hand, the presence of titanium carbide can enhance the high temperature strength, i.e. creep properties of an alloy [20,32]. Since the melting temperature of titanium carbide particles is 3800 K and they remain stable at high temperature, thus they will render strength at high temperature application.

The modified Crussard–Jaoul (C–J) model [44–48], which is developed to analyse work hardening (WH) behaviour of materials containing two phases, is utilised in the present study. The modified C–J model uses the following Swift equation (Eq. (3)) for the analysis [44]:

$$\varepsilon = \varepsilon_0 + C_s \sigma^m \tag{3}$$

where σ is the true stress, ε is the true strain, m is WH exponent and C_s is the material constant. The logarithmic form of the differential Swift equation with respect to strain (ε) provides the following Eq. (4):

$$\ln(d\sigma/d\varepsilon) = (1-m)\ln\sigma - \ln(C_s m) \tag{4}$$

Eq. (4) represents the linear relationship between logarithmic form of WH rate, $\ln(d\sigma/d\varepsilon)$, and logarithmic form of true stress, $\ln\sigma$, where $(1-m)$ is slope of the line. The logarithm of WH rate, $\ln(d\sigma/d\varepsilon)$, versus logarithm of true stress, $\ln\sigma$, is plotted for all the ageing conditions in Fig. 7. The curves have been fitted using Pearson IV (a–f) equation are also included in Fig. 7. Each of the curves is segmented into three distinct stages as per depicted in

Table 3
The value of crystallite size (D_s), micro-strain $\langle\varepsilon_L^2\rangle^{1/2}$, dislocation density $\langle\rho\rangle$ obtained from the Rietveld analysis and others formula for several β planes in Ti-55511 alloy.

Miller indices	Ageing condition (h)	D_s (nm)	$\langle\varepsilon_L^2\rangle^{1/2}$ ($\times 10^{-4}$)	$\langle\rho\rangle$ [$\times 10^{13}$, m^{-2}]
β (110)	0	66	10.3	53
	1	86	7.2	29
	2	110	5.8	18
	4	127	4.9	13
	8	134	3.6	9
β (200)	0	68	9.8	36
	1	90	6.5	18
	2	116	5.3	11
	4	130	4.3	8
	8	140	3.2	6
β (211)	0	45	9.5	41
	1	61	6.4	21
	2	80	5.8	14
	4	101	4.6	9
	8	113	3.4	6

Table 4
The value of crystallite size (D_s), micro-strain $\langle\varepsilon_L^2\rangle^{1/2}$, dislocation density $\langle\rho\rangle$ obtained from the Rietveld analysis and others formula for several α planes in Ti-55511 alloy.

Miller Indices	Ageing condition (h)	D_s (nm)	$<\varepsilon_L^2>^{1/2}$ ($\times 10^{-4}$)	$<\rho>$ [$\times 10^{13}$, m^{-2}]
α (10$\bar{1}$0)	0	445	14.9	9
	1	561	10.9	5
	2	756	9.8	3
	4	856	8.6	2
	8	912	5.8	1
α (0002)	0	218	5.8	7
	1	334	5.2	4
	2	354	4.6	3
	4	367	4.2	3
	8	401	3.4	2
α (10$\bar{1}$1)	0	191	11.6	15
	1	322	11.2	9
	2	365	9.2	6
	4	588	8.9	4
	8	615	6.2	2
α (11$\bar{2}$0)	0	115	11.3	25
	1	203	10.7	13
	2	325	8.8	7
	4	365	7.6	5
	8	402	6.7	4

Table 5
The lattice parameters of β- and α-Ti in Ti-55511 alloy.

Alloy	Ageing condition (h)	β-Ti lattice parameter (nm)	α-Ti lattice parameters (nm)		c/a
			a	c	
Ti-55511	0	0.32	0.293	0.469	1.60
	1	0.30			
	2	0.30			
	4	0.30			
	8	0.30			

Fig. 7 (stage I, stage II and stage III), with a maximum slope in stage II and a minimum one in stage III. It is noticeable that the duration of stage I is shortened with the ageing time, which is explained below. A summary of the results obtained from Fig. 7 is

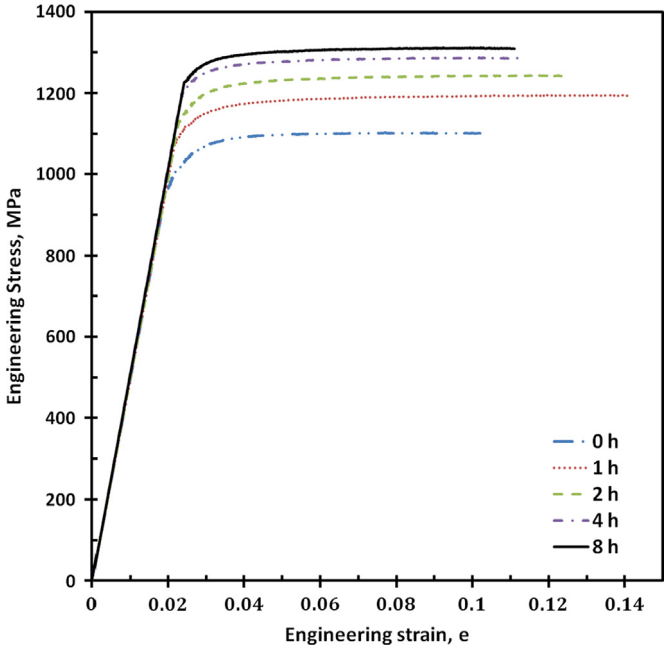

Fig. 6. The engineering stress versus engineering strain curves for different ageing conditions.

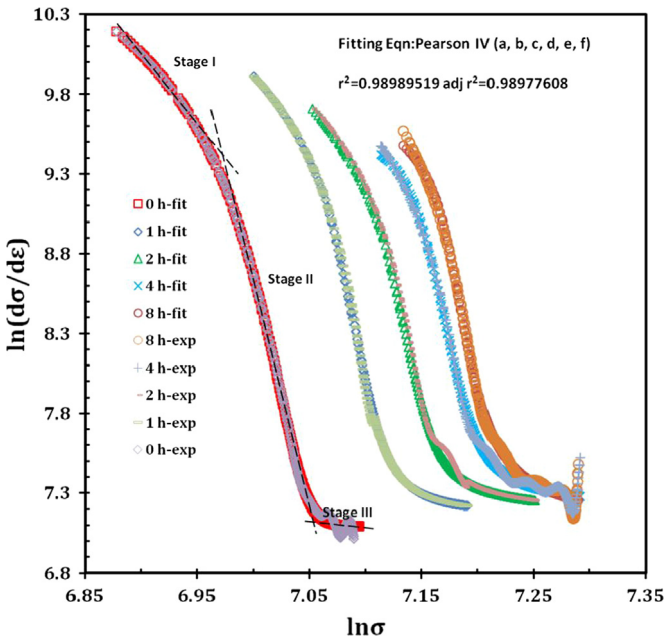

Fig. 7. $\ln(d\sigma/d\varepsilon)$ versus $\ln\sigma$ curves for all experimental conditions showing experimental and fitting curves. Three distinct stages are also distinguished.

presented in Table 6, where the WH exponent (m) values corresponding to the each stage are given together with the transition true stress and true strain values. The maximum value of the m value is obtained for stage II (m_{II}) and the minimum m value is obtained for stage III (m_{III}) in all the samples. It is mentioned in [46,47] that three stages in the WH behaviour depend upon the amount and type of the phases present in the microstructure. Stage I corresponds to the plastic deformation of β phase through gliding of dislocations. The dislocations in the β phase pile up in the vicinity of α/β interfaces and grain or laths boundaries, which act as barriers to the dislocation movement. This creates the strain gradient between the α crystals and β phase itself. However, α phase does not deform at this stage. The longevity of stage I

Table 6
The value of the work hardening exponent (m) for different stages and corresponding true stress and true strain during changing of one stage to another.

Alloy	Ageing condition (h)	Stage I, m_I	Stage II, m_{II}	Stage III, m_{III}	$m_I \Rightarrow m_{II}$		$m_{II} \Rightarrow m_{III}$	
					(σ_{tr}, MPa)	$\varepsilon_{tr} \times 10^{-2}$	(σ_{tr}, MPa)	$\varepsilon_{tr} \times 10^{-2}$
Ti-55511	0	8.7	27.2	1.9	1053	2.1	1163	5.6
	1	11.0	30.1	3.1	1164	2.6	1240	4.7
	2	11.5	33.3	3.4	1224	3.1	1299	5.4
	4	12.3	34.8	3.6	1261	3.3	1366	6.5
	8	17.6	37.5	4.4	1299	3.4	1380	5.6

depends on the amount of α phase. The higher the amount of α phase indicates the shorter free path for dislocation movement in the β phase, which ultimately reduces the duration of stage I. Once the β phase is work hardened, load transfers to α phase which undergoes elastic deformation of the phase (stage II). Raghunathan et al. [49] have also mentioned that fine secondary α lamellae significantly strengthen the material through increasing the strength of β phase by dislocation pining by fine secondary α. In the present study, secondary α phase is too large to pin dislocations so hardening was obtained through dislocation gliding where α lamellae serve as barrier. Stage III corresponds to the plastic deformation of hard α phase.

4. Conclusions

In the present study, the influence of the ageing time (1 h, 2 h, 4 h, and 8 h) at a constant temperature of 923 K is reported in terms of microstructural characterisation and mechanical properties of a powder Ti–5Al–5Mo–5V–1Cr–1Fe (VT22) alloy. The following conclusions can be drawn from this study:

- The microstructures illustrate a progression over the ageing time e.g. fine secondary α lamellae phase were formed. The amount of α phase increased over the ageing period. The microstructures contain some particles of titanium carbide due to unintentional pick up of C during processing.
- The evolution of phase compositions with ageing reflects that β stabilisers diffuse out of primary and fine secondary α phase into the retained β phase, whereas Al diffuses out of β phase being α stabiliser.
- XRD data shows reduction in dislocation density as a result of relaxation processes (recovery and recrystallisation) taking place during ageing.
- The longer the ageing time, the more secondary α is formed resulting in increase in UTS and decrease in total elongation. A good combination of strength and total elongation is achieved after 1 h ageing.

Acknowledgements

The UOW Engineering Materials Institute strategic grant financially supported this work. The use of UOW Electron Microscopy Centre facilities, in particular JEOL 7001F, which was purchased with ARC support (LE0882613) is being acknowledged. The authors are grateful to Dr. A.A. Gazder for modification of tensile stage. One of the authors (Mansur Ahmed) would like to acknowledge the University Postgraduate Award (UPA) with International Postgraduate Tuition Award (IPTA) for his Ph.D. study.

References

[1] P.J. Bania, in: D. Eylon, R.R. Boyer, D.A. Koss (Eds.), Beta Titanium Alloys in the 90's, TMS, Warrendale, PA, 1993, pp. 3–14.
[2] R.R. Boyer, Mater. Sci. Eng. A 213 (1996) 103–114.
[3] P.A. Kobryn, Casting of Titanium Alloys, A Report Submitted to DTIC, USA, , 1996.
[4] J.D. Cotton, L.P. Clark, H.R. Phelps, JOM 58 (2006) 13–16.
[5] L. Jia, D. Xu, M. Li, J. Guo, H. Fu, Met. Mater. Int. 18 (2012) 55–61.
[6] E.R. Thompson, Annu. Rev. Mater. Sci. 12 (1982) 213–242.
[7] T. Fujita, A. Ogawa, C. Ouchi, H. Tajima, Mater. Sci. Eng. A 213 (1996) 148–153.
[8] F.H. Froes, D. Eylon, Int. Mater. Rev. 35 (1990) 162–184.
[9] O.M. Ivasishin, D. Eylon, V.I. Bondarchuk, D.G. Savvakin, Defect Diffusion Forum 277 (2008) 177–185.
[10] C. Leyens, M. Peters, Titanium and Titanium Alloys: Fundamentals and Applications, John Wiley and Sons, Weinheim, Germany, 2006.
[11] V.N. Moiseev, Met. Sci. Heat Treat. 42 (2000) 81–83.
[12] Y. Ohmori, T. Ogo, K. Nakai, S. Kobayashi, Mater. Sci. Eng. A 312 (2001) 182–188.
[13] S.-z. Zhang, Z.-q. Liu, G.-d. Wang, L.-q. Chen, X.-h. Liu, R. Yang, J. Cent. South Univ. Technol. 16 (2009) 354–359.
[14] O.M. Ivasishin, P.E. Markovsky, Y.V. Matviychuk, S.L. Semiatin, C.H. Ward, S. Fox, J. Alloys Compd. 457 (2008) 296–309.
[15] S. Nag, R. Banerjee, R. Srinivasan, J.Y. Hwang, M. Harper, H.L. Fraser, Acta Mater. 57 (2009) 2136–2147.
[16] T. Furuhara, T. Maki, T. Makino, J. Mater. Process. Technol. 117 (2001) 318–323.
[17] V.N. Moiseev, Met. Sci. Heat Treat. 40 (1998) 482–485.
[18] V.N. Moiseev, N.V. Sysoeva, M.I. Ermolova, Met. Sci. Heat Treat. 38 (1996) 42–45.
[19] A.M. Parshin, S.S. Ushkov, I.I. Yarmolovich, Met. Sci. Heat. Treat. 15 (1973) 313–316.
[20] N.V. Sysoeva, V.N. Moiseev, Met. Sci. Heat Treat. 44 (2002) 304–308.
[21] V.N. Moiseev, N.V. Sysoeva, T.V. Ishun'kina, Met. Sci. Heat Treat. 37 (1995) 248–250.
[22] V.V. Shevel'kov, Met. Sci. Heat Treat. 34 (1992) 534–539.
[23] O.M. Ivasishin, P.E. Markovsky, JOM 48 (1996) 48–52.
[24] D. Savvakin, A. Carman, O. Ivasishin, M. Matviychuk, A. Gazder, E. Pereloma, Metall. Mater. Trans. A 43 (2012) 716–723.
[25] B.D. Cullity, S.R. Stock, Elements of X-ray Diffraction, third ed., Prentice Hall, Massachusetts, USA, 2001.
[26] L. Lutterotti, P. Scardi, J. Appl. Crystallogr. 23 (1990) 246–252.
[27] M. Ahmed, D.G. Savvakin, O.M. Ivasishin, E.V. Pereloma, Mater. Sci. Eng. A 576 (2013) 167–177.
[28] R.E. Smallman, K.H. Westmacott, Philos. Mag. 2 (1957) 669–683.
[29] J.K. Fan, H.C. Kou, M.J. Lai, B. Tang, H. Chang, J.S. Li, Mater. Sci. Eng. A 584 (2013) 121–132.
[30] A. Sarkar, S. Roy, S. Suwas, Mater. Charact. 62 (2011) 35–42.
[31] O.M. Ivasishin, P.E. Markovsky, S.L. Semiatin, C.H. Ward, Mater. Sci. Eng. A 405 (2005) 296–305.
[32] V.N. Moiseev, N.V. Sysoeva, I.G. Polyakova, Met. Sci. Heat Treat. 40 (1998) 107–111.
[33] I. Weiss, S.L. Semiatin, Mater. Sci. Eng. A 243 (1998) 46–65.
[34] A. Szkliniarz, W. Szkliniarz, Solid State Phenom. 176 (2011) 139–148.
[35] N. Wain, X.J. Hao, G.A. Ravi, X. Wu, Mater. Sci. Eng. A 527 (2010) 7673–7683.
[36] C.-M. Sung, M.-F. Tai, Int. J. Refract. Met. Hard Mater. 15 (1997) 237–256.
[37] P.G. Oberson, Z.W. Wyatt, S. Ankem, Scr. Mater. 65 (2011) 638–641.
[38] G. Neumann, C. Tuijn, Self-diffusion and Impurity Diffusion in Pure Metals: Handbook of Experimental Data, Elsevier Science, Pergamon Science, Amsterdam, The Netherlands, 2011.
[39] H. Nakajima, K. Ogasawara, S. Yamaguchi, M. Koiwa, Mater. Trans. 31 (1990) 249–254.
[40] R.J. Talling, R.J. Dashwood, M. Jackson, S. Kuramoto, D. Dye, Scr. Mater. 59 (2008) 669–672.
[41] M. Ahmed, A. Gazder, D. Savvakin, O. Ivasishin, E. Pereloma, J. Mater. Sci. 47 (2012) 7013–7025.
[42] O.P. Karasevskaya, O.M. Ivasishin, S.L. Semiatin, Y.V. Matviychuk, Mater. Sci. Eng. A 354 (2003) 121–132.
[43] R.R. Boyer, H.J. Rack, V. Venkatesh, Mater. Sci. Eng. A 243 (1998) 97–102.
[44] W. Nie, X. Wang, S. Wu, H. Guan, C. Shang, Sci. China Technol. Sci. 55 (2012) 1791–1796.
[45] A. Kumar, S.B. Singh, K.K. Ray, Mater. Sci. Eng. A 474 (2008) 270–282.
[46] F.H. Samuel, Mater. Sci. Eng. 92 (1987) L1–L4.
[47] A. Bag, K. Ray, E. Dwarakadasa, Metall. Mater. Trans. A 30 (1999) 1193–1202.
[48] H. Paruz, D.V. Edmonds, Mater. Sci. Eng. A 117 (1989) 67–74.
[49] S.L. Raghunathan, A.M. Stapleton, R.J. Dashwood, M. Jackson, D. Dye, Acta Mater. 55 (2007) 6861–6872.

Chapter 5

The evolution of microstructure and mechanical properties of Ti-5Al-5Mo-5V-2Cr-1Fe alloy during ageing

The evolution of microstructure and mechanical properties of Ti-5Al-5Mo-5V-2Cr-1Fe during ageing

Mansur Ahmed[1,*], Tong Li[2,3], Gilberto Casillas[4], Julie M. Cairney[2,3], David Wexler[1,4], Elena V. Pereloma[1,4]

[1]School of Mechanical, Materials and Mechatronic Engineering, University of Wollongong, New South Wales 2522, Australia

[2]Australian Centre for Microscopy and Microanalysis, The University of Sydney, NSW 2006, Australia

[3]School of Aerospace, Mechanical and Mechatronic Engineering, The University of Sydney, NSW 2006, Australia

[4]UOW Electron Microscopy Centre, University of Wollongong, New South Wales 2500, Australia

*Corresponding author: Mansur Ahmed

Postal Address: School of Mechanical, Materials and Mechatronic Engineering, University of Wollongong, NSW 2522, Australia

E-mail address: ma960@uowmail.edu.au

Tel.: +61 2 4221 5798; fax: +61 2 4221 3662.

Abstract:

The phase transformations and compositional changes occurring during thermo-mechanical processing and subsequent high temperature ageing of Ti-5Al- 5Mo-5V-2Cr-1Fe (wt. %) were investigated using scanning transmission electron microscopy (STEM) and atom probe tomography (APT). High resolution STEM revealed nano-sized α (<10 nm) and athermal ω (~1-3 nm) formed during accelerated cooling from 800°C and slow heating to an ageing temperature of 650°C. Nuclei of α were found to form heterogeneously in the β matrix as well as at the ω phase. APT revealed pronounced Mo compositional fluctuations in the β matrix. No direct connection was established between Mo-rich or Mo-lean regions and α or ω nuclei. APT also failed to detect the ω phase, which supports theories that it forms by a shuffle mechanism, without any compositional difference from the β phase. Very small α particles, after initial ageing, showed only a minute change in composition with respect to the β matrix, indicative of a displacive-diffusional transformation. With further ageing, growth of the α lamellae was accompanied by compositional changes according to the diffusion rates of β-stabilising elements. Pile-up of the slowest diffusing solutes (Mo, V) at the α/β interface were pronounced in the initial stages of ageing. The best combination of mechanical properties (1200 MPa ultimate tensile strength with 15% total elongation) was recorded after 3.6 ks of ageing.

Key words: Titanium alloy, ageing, electron microscopy, atom probe tomography.

1. Introduction:

Ti-5Al-5Mo-5V-3Cr-0.5Fe (Ti5553) is used in heavy aerospace components (e.g. bogie beams, landing gears, etc.) because of its large processing window compared to other near β Ti alloys [1, 2]. In the present study, Ti-5Al-5Mo-5V-2Cr-1Fe (Ti55521), a derivative form of commercial Ti5553 manufactured by a low cost blended elemental powder metallurgy technique [3-5], is investigated. The alloy has 2 wt% Cr and 1 wt% Fe, instead of 3 wt% Cr and 0.5 wt% Fe in Ti5553, while the concentration of other alloying elements remains the same. This change allows better densification during sintering, without significantly altering the Mo equivalent value, because Fe has the fastest diffusivity of the alloying elements used [3].

The morphology, distribution, size and amount of α largely govern the mechanical properties of near-β Ti alloys. Solution treatment and ageing (STA) is the main process to obtain fine α precipitation in near-β Ti alloys and α/β Ti alloys. For Ti alloys, the STA process has been modified to include two ageing steps to optimise properties [6, 7]. Two different schedules can be used for the two-step ageing: (i) high temperature ageing followed by low temperature ageing and inversely (ii) low temperature ageing followed by high temperature ageing; the latter one is used most frequently. Depending on the heat treatment, Ti5553 alloy possesses a wide range of mechanical properties with ultimate tensile strength of 1150-1350 MPa, 0.2% proof stress of 1100-1250 MPa and total elongations of 7-16% [8, 9] .

During the low temperature ageing followed by high temperature ageing, metastable phases, such as β′ and ω, form and act as nucleation sites for the α phase at high temperature [8,9]. Formation of metastable β′ takes place in Ti alloys with relatively high quantities of β stabilising elements in the temperature range of 200-500°C and is characterised by the appearance of coherent bcc zones depleted in β stabilisers compared to the β matrix [10]. β phase separation into solute-rich and solute-lean regions has been studied on quenching, air cooling or ageing for several model and commercial Ti alloys (Ti-16V-2.5Al [11, 12], Ti-8Al-1V-1Mo [13], Ti-20V [12], Ti-9Mo-7Mn (1-2)Al [13], Ti-13V-11Cr-3Al [14], Ti-40%Mo [15], Ti-20Mo-5Al [16], Ti-20V-10Al [17] and Ti-10V-6Cu [18] wt.%). These studies have evaluated the clustering tendency and the underlying mechanism, e.g. spinodal decomposition or nucleation and growth, as well as addressing the question of interplay between β phase separation and nucleation of ω and/or α. The ω phase can form in alloys with intermediate contents of β stabilising elements during rapid cooling from high temperature (athermal ω). On the other hand, isothermal ω forms during isothermal annealing at or below 400 ˚C [19, 20]. It is thought that athermal ω forms via a displacive mechanism with no compositional difference from the parent β phase [16, 21, 22], whereas the formation of isothermal ω is accompanied by diffusion and involves both structural and compositional changes [23, 24]. Athermal ω precipitates are typically ~2-10 nm size,

whereas some researchers have deliberately grown them to ~10-20 nm using prolonged isothermal holding for easier characterisation [23, 25]. The morphology of ω particles depends on the composition of Ti alloys and ω/β misfit, e.g. ellipsoidal in the alloys containing Mo or Nb with low misfit and cuboidal in the ones with Cr or V and high misfit [26, 27]. It is believed that the ω particles form by the displacement of two neighbouring close-packed atom rows relative to each other in the $<111>_\beta$ direction, collapsing β planes [24]. Banerjee *et al.* [28] showed that a 10° deviation from the $<111>_\beta$ direction can occur to produce ω. The recent development of aberration-corrected high resolution scanning transmission electron microscopes (HRSTEMs) now provides the means for direct observations of the collapsed atom pairs along the $<111>_\beta$ directions [24]. The well-documented orientation relationship between ω and β phases is [29]: $(111)\beta$ // $(0001)\omega$ and $[1\bar{1}0]_\beta$ //$[11\bar{2}0]_\omega$. Furuhara *et al.* [7] have reported the orientation relationship between crystal lattices of α, ω and β phases as $(\overline{11}20)\omega$ // $(0001)\alpha$ // $(0\bar{1}1)\beta$ and $[111]\beta$ // $[11\bar{2}0]\alpha$ // $[0001]\omega$ indicating that α forms at the interface of the ω and β phases. Fine, homogeneously distributed α, formed via nucleation within ω [30], at the ω/β interface [7, 19] or near this interface [31], provides high strength without impairing ductility [7, 10]. Regardless of its nucleation, the α phase is reported to grow by consuming the ω phase [25, 30]. However, the exact mechanism of α formation from ω precipitates still remains unclear, especially in alloys with multiple alloying elements where complex interactions between elements occur.

In this study, a single step of high temperature ageing with very slow heating to the ageing temperature was applied in the Ti55521 alloy. Ivasishin *et al*. [32, 33] have claimed that a good strength-ductility balance was obtained for commercial Ti alloys, which might result from formation of ω at slow heating and phase transformation into α phase during ageing.

In order to understand the evolution of microstructure during this single step ageing, both aberration corrected HRSTEM and atom probe tomography (APT) were employed here. Nag *et al.* [19, 34] and Devaraj *et al.* [24] have pioneered the study of ω-assisted α precipitation in Ti5553 and exploited the displacive-diffusional phase transformation of ω phase by a combination of HRTEM and APT. However, this was carried out using different processing schedules. In addition, limited APT data was achieved due to challenging sample preparation and statistical data analysis of solute inhomogeneity in β matrix was not considered. Therefore, the aim of this study is two-fold:

1. Combine HRSTEM and APT to study the nucleation of athermal ω and α phases after thermal-mechanical processing, and microstructure evolution during isothermal ageing.

2. Attain mechanical properties that are comparable to the existing literature by using a single-stage ageing with a slow heating rate, through the athermal formation of the ω phase [32, 33].

2. Experimental Procedure:

After sintering [35], the Ti55521 samples were thermo-mechanically processed (TMP) using a 3500 Gleeble thermo-mechanical simulator. The β transus temperature was 820 °C for the alloy [4]. They were heated to 950 °C at 10 $°Cs^{-1}$ and held for 120 s followed by cooling at 35 $°Cs^{-1}$ to 900 °C for 25% deformation. The samples were then cooled to 800 °C at 35 $°Cs^{-1}$, held for 600 s and deformed by a 60% reduction. This was followed by cooling at 10 $°Cs^{-1}$ to ambient temperature. More details are provided elsewhere [5]. Samples were encapsulated under vacuum to prevent high temperature oxidation and placed into a furnace for ageing. The ageing was performed at 650 °C by heating the samples at 0.25 $°Cs^{-1}$ and holding for 0.12 ks, 3.6 ks, 14.4 ks and 28.8 ks. Using an electrical discharge machine, sub-sized tensile specimens (gauge length 5.1 mm, width 2.18 mm and thickness 0.9 mm) were machined. Tensile tests were carried out with a μ-tweezers tensile module (Kammrath & Weiss, GmbH) at room temperature at a constant speed of 1.7 mm min^{-1}. Two samples were tested per condition.

Microstructures were observed using scanning electron microscopy (SEM), transmission electron microscopy (TEM) and scanning transmission electron microscopy (STEM). SEM was carried out with a JEOL-JSM 7001F Field Emission Gun-Scanning Electron Microscope (FEG-SEM) operating at 15 kV voltage and 10 mm working distance. Thin foils for TEM were prepared using twin jet electropolishing method with an electrolyte containing 5-7% of perchloric acid and methanol. TEM was performed on a JEOL JEM-2011 at an accelerating voltage of 200 kV. STEM images were acquired with a probe-corrected JEOL ARM200F operated at 200 kV, equipped with a cold field emission gun. High-angle annular dark field (HAADF) images were acquired with 50 and 180 mrad inner and outer collection angles respectively, while BF images used 11 mrad collection angles. Both images were recorded with a dwell time of 38 μs, and convergence semi-angle of 25 mrad resulting in a probe current of 35 pA. The microscope features a Centurio SSD Energy Dispersive X-ray Spectrometer (EDS) detector with an active area of 100 mm^2 which is equivalent to a collection angle of 0.98 sr. EDS spectra were acquired with a probe current of 290 pA.

Atom probe specimens were prepared by electropolishing in a solution containing $HClO_4$ (5%), 2-butoxyelethnol (35%) and methanol at 30 V at 233 K. The relatively blunt electropolished tips were sharpened in a Zeiss Auriga FIB, reducing the radius to less than 100 nm. Atom probe experiments were conducted in a Cameca LEAP 4000X-SI™ instrument. Data acquisition was

carried out in laser pulsing mode at a specimen temperature of 50 K with a target evaporation rate of 5 ions per 1000 pulses, a pulse rate of 250 kHz, laser energy of 70 pJ and a laser spot size of approximately 2 μm. The wavelength of the UV laser was 355 nm. The APT data were reconstructed and analysed using the commercial IVAS 3.6.6™ software. The error bars in the proxigrams have been calculated based on the statistical errors associated with APT [36].

3. Experimental Results:

3.1. Mechanical properties

The room temperature tensile test response of all samples, except the one aged for 0.12 ks, is shown in Fig. 1a. A summary of ultimate tensile strength (UTS), 0.2% proof stress and ductility for each condition is listed in Table 1. The strength of the alloy increased with ageing time. However, the change in strength from 14.4 ks to 28.8 ks was incremental. Total elongation of all aged samples was higher than that of the TMP condition. Among the ageing conditions, the sample aged for 28.8 ks has the highest strength, with a value of 1270 MPa (UTS), while 3.6 ks aged sample displayed the highest ductility (15%) (Table 1).

Table 1: The volume fraction of α, strength and ductility of TMP and aged samples

Alloy	Condition	Vol. of α (%)	0.2% Proof Stress (MPa)	UTS (MPa)	Total elongation (%)	α phase (length, width) (nm)
Ti-55521	TMP	22±3	980±15	1030±16	9.8±1.2	20-50,10-20
	3.60 ks	38±6	1080±18	1149±20	15.0±1.5	100-350, 50-80
	14.4 ks	50±3	1200±12	1245±18	12.6±1.1	250-600, 80-110
	28.8 ks	55±5	1210±14	1270±26	11.9±0.7	800-1800, 250-300

Note: for TMP sample the size mentioned is for primary α obtained during cooling to RT.

3.2. Scanning electron microscopy observations

FE-SEM images of TMP samples and the specimens aged for 3.6 ks, 14.4 ks and 28.8 ks are shown in Figs.1b-e. In the TMP sample, both β and α phases appear in the microstructure where

the α phase is present in Widmanstätten and colony morphologies (Fig.1b). Recrystallisation of the β grains occurred during accelerated cooling after hot deformation at 800 °C (Fig. 1c). Collectively, α produced prior to ageing is termed as *primary α* herein. On the other hand, *secondary α*, which evolves during ageing, is observed in all the aged samples in addition to the features in TMP microstructure described above (Fig. 1d-f). A gradual coarsening of the α phase is viewed in all aged samples. Table 1 confirms that the size and volume fraction of α increased as ageing progresses. SEM images show the general distribution, morphology and size of the α phase and more detailed characterisation of the α phase evolution with ageing is obtained using TEM.

3.3. Characterisation of samples in the TMP condition

Fig. 2 displays the microstructural features present after TMP. Bright field (BF) images (Figs. 2a-b) show intragranular α and fragmented grain boundary α and β phases. The fragmentation of grain boundary α occurred as a result of deformation at 800 °C during TMP, and has a positive influence on ductility [6, 8]. Fig. 2c is a selected area diffraction pattern (SADP) after TMP. In addition to the sharp β matrix reflections, consistent with a bcc structure, there are faint

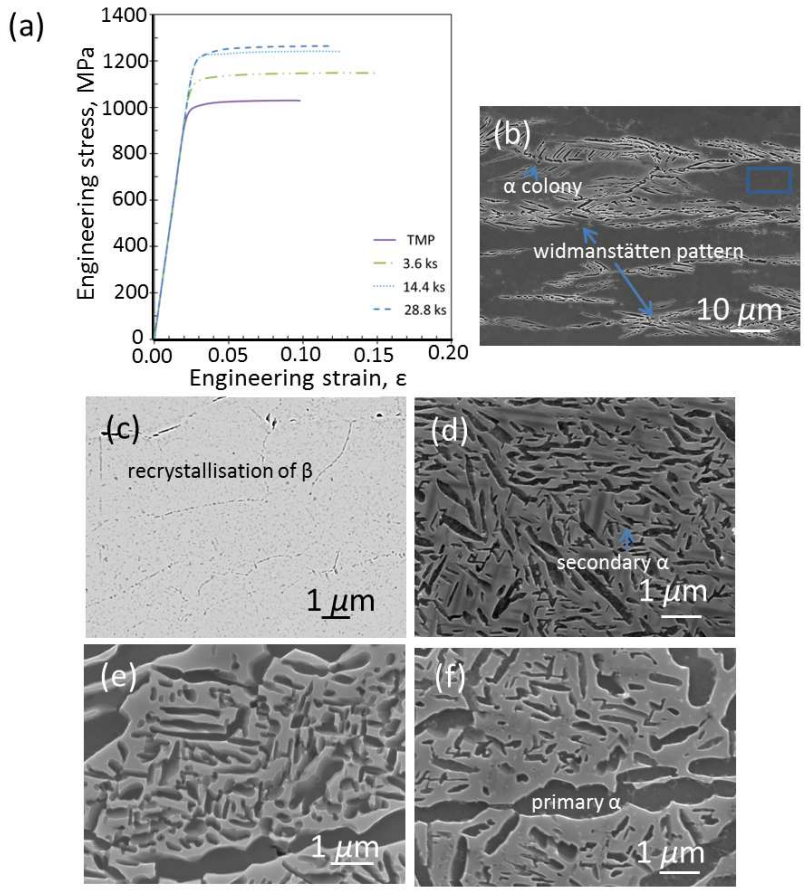

Fig.1. (a) The representative stress-strain curves for TMP and aged specimens. Secondary electron FE-SEM images of (b-c) TMP and aged sample for (d) 3.6 ks, (e) 14.4 ks and (f) 28.8 ks samples. (c) Enlarged view of a small region marked by rectangular box in Fig. 1(b) showing the recrystallised β grains.

reflections at 1/3 and 2/3 $\{112\}_\beta$ positions, which are characteristic of the athermal ω phase [29]. Moreover, the well-established orientation relationship between (111) β // (0001) ω and [110] β // $[11\bar{2}0]$ ω is also found. The dark field (DF) image (Fig. 2d) confirms the presence of a high density of homogeneously distributed ω precipitates of 2-3 nm in size with ellipsoidal/spheroidal morphology. These sizes are in good agreement with the dimensions of ω particles found upon rapid quenching of Ti5553 [28, 37]. Furthermore, the extra reflection at the 1/2 $\{112\}_\beta$ position arises from fine α precipitates also formed during cooling, as seen in the DF image shown in Fig. 2e.

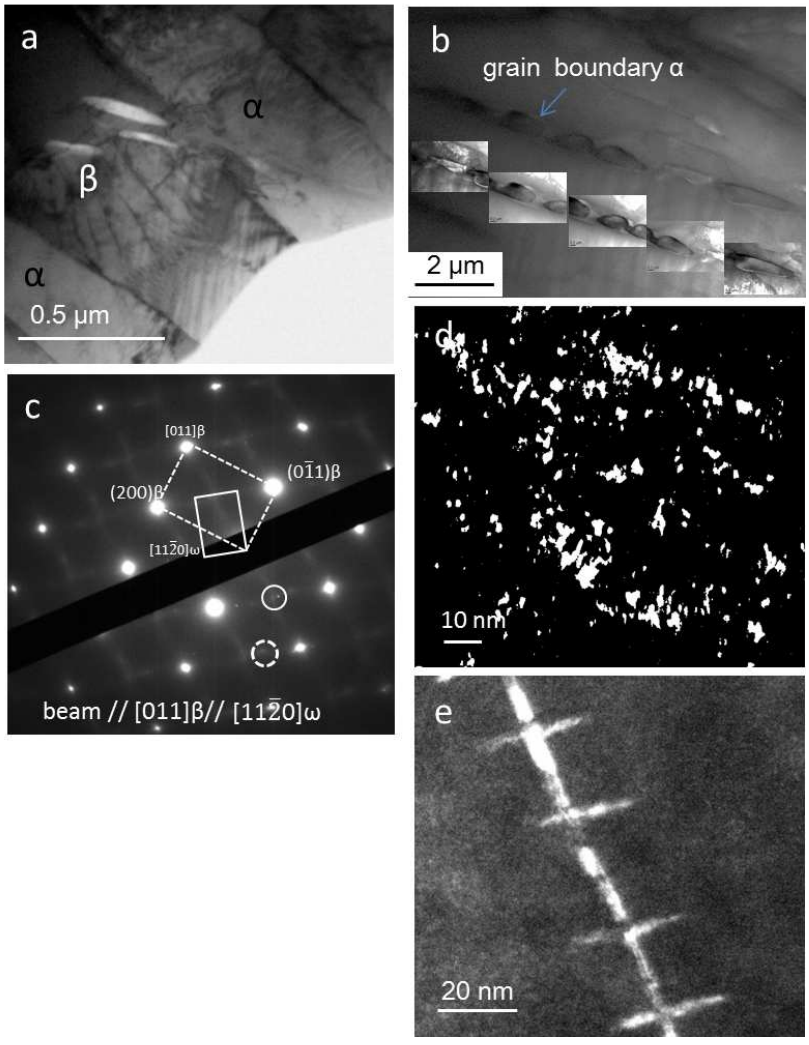

Fig.2. (a) Bright Field (BF) image showing intragranular α and β after thermo-mechanically processing. (b) A low magnification BF image capturing fragmented grain boundary α with inset

showing the same feature at a high magnification. (c) SAD pattern with $[011]_\beta$ zone axis along with faint ω reflections at 1/3 and 2/3 $\{112\}_\beta$ and α reflection at 1/2 $\{112\}_\beta$ for TMP specimen. (d) Dark field (DF) image showing ω precipitates using the reflection in dashed white circle in (c). (e) DF image revealing two orientations of fine α phase, which is taken using the solid white circle in (c).

Aberration-corrected STEM was used to investigate the nucleation stages of ω through the atomic collapse in the <002> direction (Fig. 3) on the TMP sample. The high angle annular dark field (HAADF) image shown in Fig. 3, both raw (Fig. 3a) and Fourier filtered (background subtracted, Fig. 3b), exhibits regions of brighter and darker contrast, respectively. This variation in contrast is attributed to the differences in atomic masses (Z-contrast) [24], where light regions are associated with the segregation of heavier elements. The circled regions in Figs. 3a-b show the regions with displaced atomic columns in bcc matrix. As three consecutive atom rows in <002> direction makes the ω motif, in which the adjacent two atoms in the middle row are

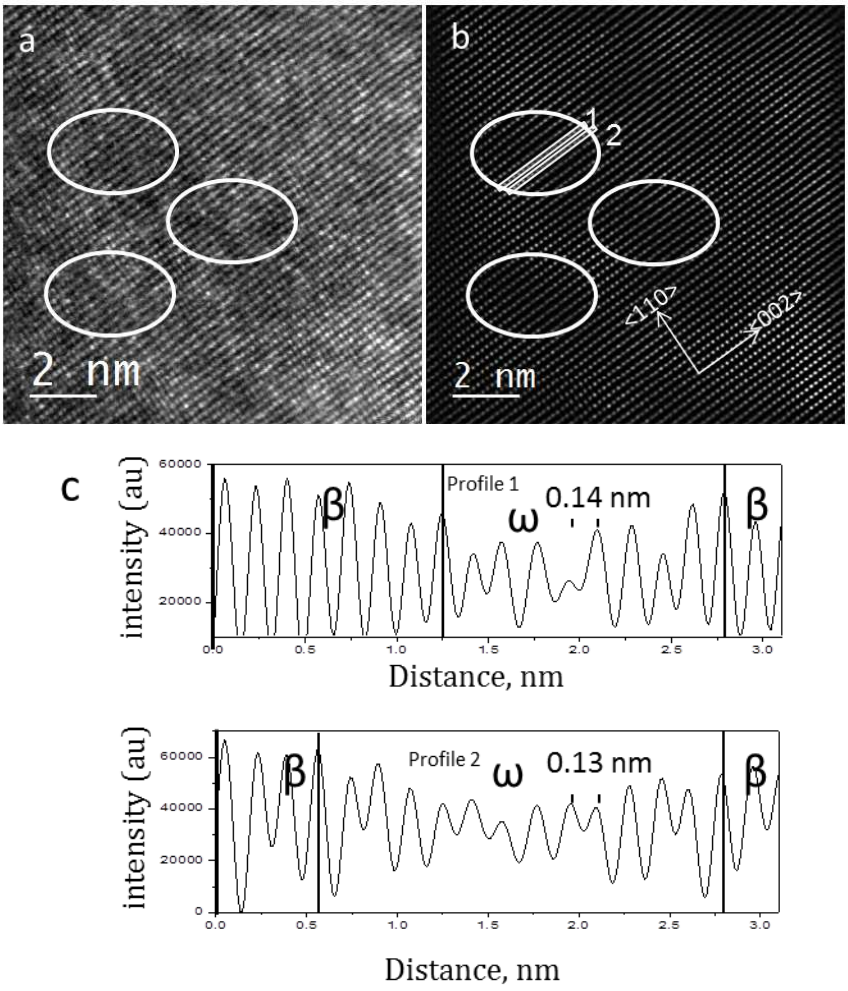

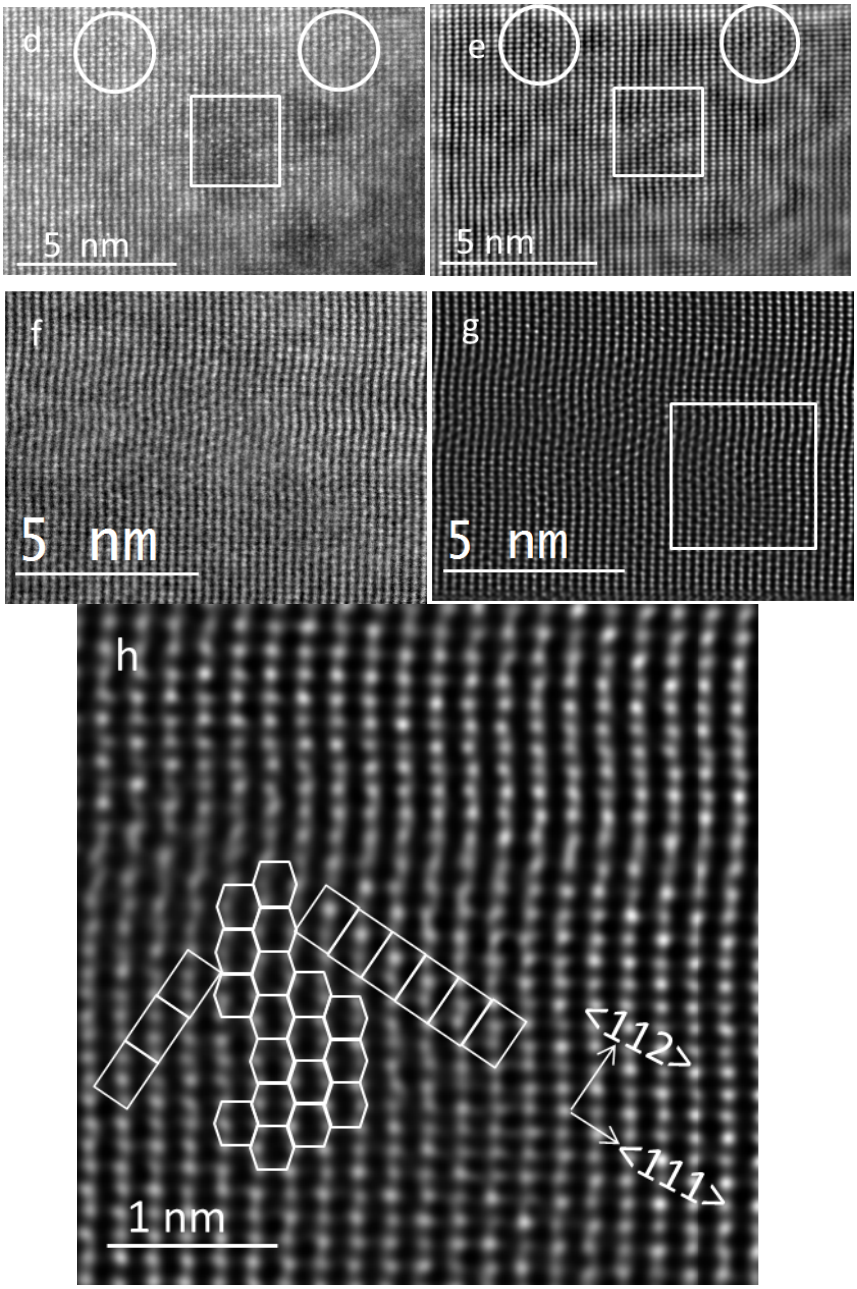

Fig.3. (a) Raw and (b) Fourier filtered HAADF-HRSTEM image of TMP sample with $[110]_{\beta}$ zone axis showing atom columns in β matrix with marked regions of the ω phase nuclei. (c) The intensity profiles along the white lines marked 1 and 2 in (b) demonstrating a very small degree of displacement of atomic planes. (d) Raw and (e) Fourier filtered HAADF-HRSTEM image in a $[011]_{\beta}$ zone axis with marked regions of α phase nuclei by circles(change the square for a circle too) in β matrix.(f) Raw and (g) Fourier filtered HAADF-STEM images . (h) Enlarged view of the rectangular box in (g) reveals adjacent ω and α motifs highlighted with white shapes.

displaced. A very small atomic displacement indicates a partial collapse at the early stages of ω formation. The intensity profiles corresponding to the lines marked by 1 and 2 in Fig. 3b are plotted along the <002> direction in order to understand the relative atomic displacements (Fig.

3c). As expected, for both lines, the distances (*d*-spacing) between two adjacent {002} planes in the β area is 0.16 nm, which indicates that the lattice parameter of the β phase is equal to $2\times d_{200}$=0.32 nm. However, the spacing between every first and fourth peak within the embryonic ω region is 0.48 nm (= 3 × 0.16 nm), while the distance between the second and third column is 0.14 nm and 0.13 nm for lines 1 and 2, respectively. This reduction in projected distance between the atomic columns (in β and ω regions) indicates that there is a collapse of the atomic planes. Fig. 3g is another region of interest in the TMP sample showing more advanced stages of ω formation. As could be seen from Fig. 3h, both α and ω motifs are present. Most interestingly, the α super cell is connected to the ω motif. In addition, the presence of ω cells at either side of the α phase supports the formation of α phase in the core of ω, as proposed by Prima *et al*. [30]. In addition, fine α phase nuclei consisting of ~2-4 layers of cells (2-3 nm size) are present in the β matrix (Fig. 3d-e). This indicates a direct β→α phase transformation on rapid cooling at heterogeneous nucleation sites, such as dislocations.

Fig. 4a shows the results of the atom probe analysis of the β phase in the TMP condition. A region of interest in Fig. 4a with 4.2 at.% Mo and 1.9 at.% Mo iso-concentration surfaces is shown in Figs. 4b and 4c, respectively, to indicate Mo-rich and Mo-lean regions. To confirm that these Mo-rich and Mo-lean regions are statistically significant, rather than simply random fluctuations in the composition of the solid solution, the experimental data was compared to a modified version of the dataset that was randomly labelled. In the randomly labelled dataset, each atom maintains its spatial co-ordinates, but is assigned as a random atomic species (while maintaining the overall measured composition). This removes the effect of preferential arrangements arising from solute-solute interactions. The same 4.2 at.% Mo iso-concentration surface is plotted in the randomly labelled data as seen in Fig. 4d, revealing only a few small Mo-rich regions.

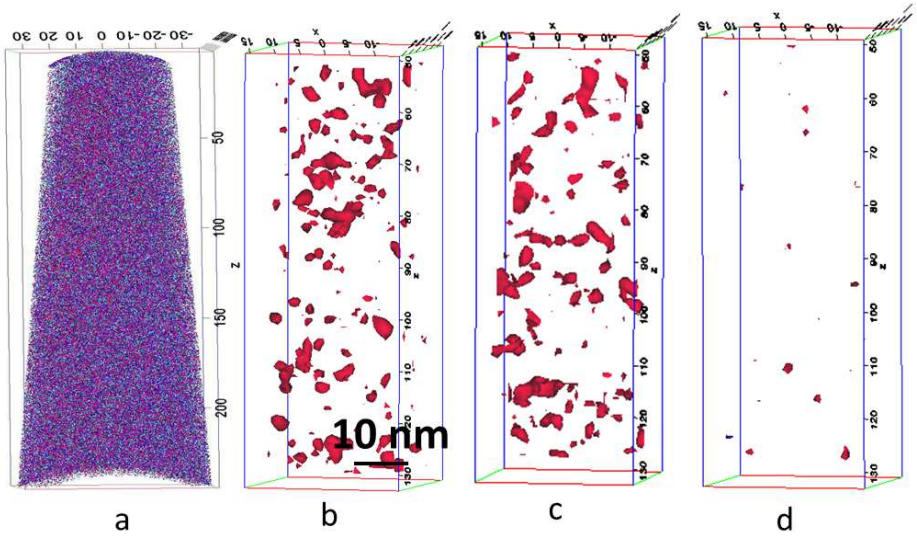

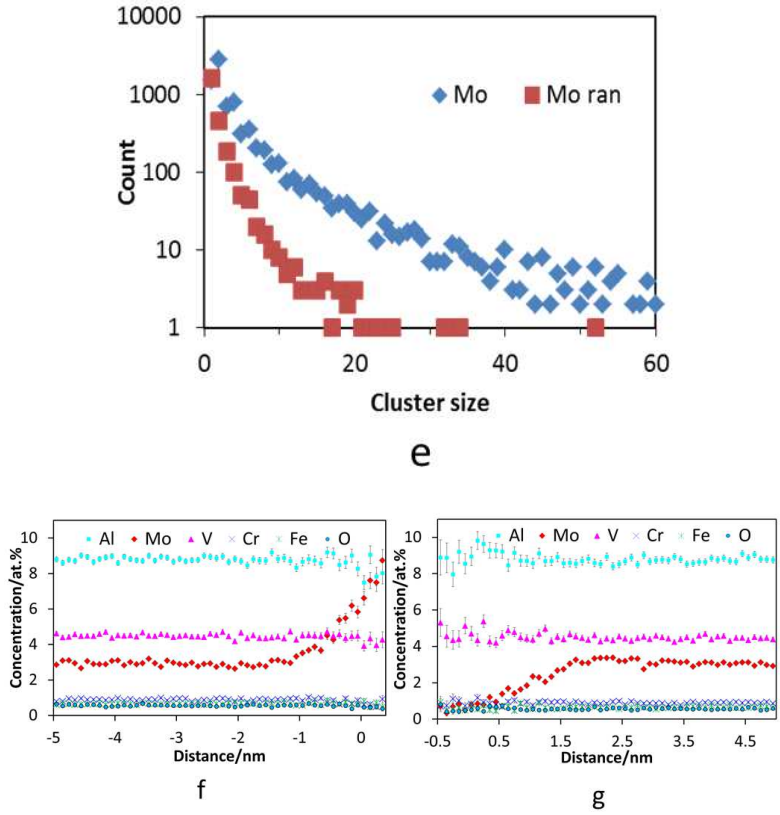

Fig. 4 Atom probe analysis of β matrix in TMP condition: (a) Selected 3D atom map of all ions with corresponding (b) 4.2 at.% Mo isoconcentration surfaces and (c) 1.9 at.% Mo isoconcentration surfaces . (d) Distribution of 4.2 at% Mo isosurfaces in random alloy of the same composition. (e) Comparison of Mo clustering in experimental and random alloys using 3D Markov chain analysis. Proximity histograms for all (f) Mo-rich and (g) Mo-lean regions.

As further verification of the significance of these compositional fluctuations, a Markov chain analysis [38] of Mo clustering (Fig. 4e) was applied, which clearly showed a significant number of clusters of more than 20 atoms, that were not observed in the randomly labelled dataset. In addition, proxigram analyses of the composition of the Mo-rich regions showed a slight depletion in all other elements (Fig. 4f), although no obvious partitioning was observed for Mo-lean regions (Fig. 4g). A much smaller extent of clustering of V and Fe atoms compared to random composition was also noted in the Markov chain analysis. Contrary to what has been previously reported for Ti5553 [19], no Cr enriched volumes were observed, which might be due to the slightly lower Cr content (2 wt%). APT observations of Mo-rich regions correlate well with the detected modulations in Z-contrast (Fig. 3a). However, there is no direct correlation of ω or α nuclei in Figs. 3a and 3d-e with segregation or depletion in heavy elements. Furthermore, the presence of ω embryos/nano-size particles was not detected by APT, which may be due to an absence in compositional variation between β and ω.

Three dimensional (3D) atom maps showing a region of the TMP sample containing several α plates are shown in Fig. 5. Fig 5a is a simple atom map, while figures 5b-5g contain 0.4 at.% Fe iso-concentration surfaces. These iso-concentration surfaces are shown alone (Fig. 5b), and together with individual elemental maps of Mo (Fig. 5c), V (Fig. 5d), Cr (Fig. 5e), Fe (Fig. 5f) and Al (Fig. 5g). In these images, the depletion of all β stabilising elements is visible in the α particles. Fig. 5h shows a representative proxigram for an α plate labelled '1' in Fig. 5b. This data is compared to elemental partitioning data from APT and STEM-EDS (Fig. 6). A comparison of the average composition of the phases is given in Table 2. Both the proxigram (Fig. 5h) and a concentration profile across a fine α particle of ~12 nm thickness (Figs. 6a and 6f) reveal a

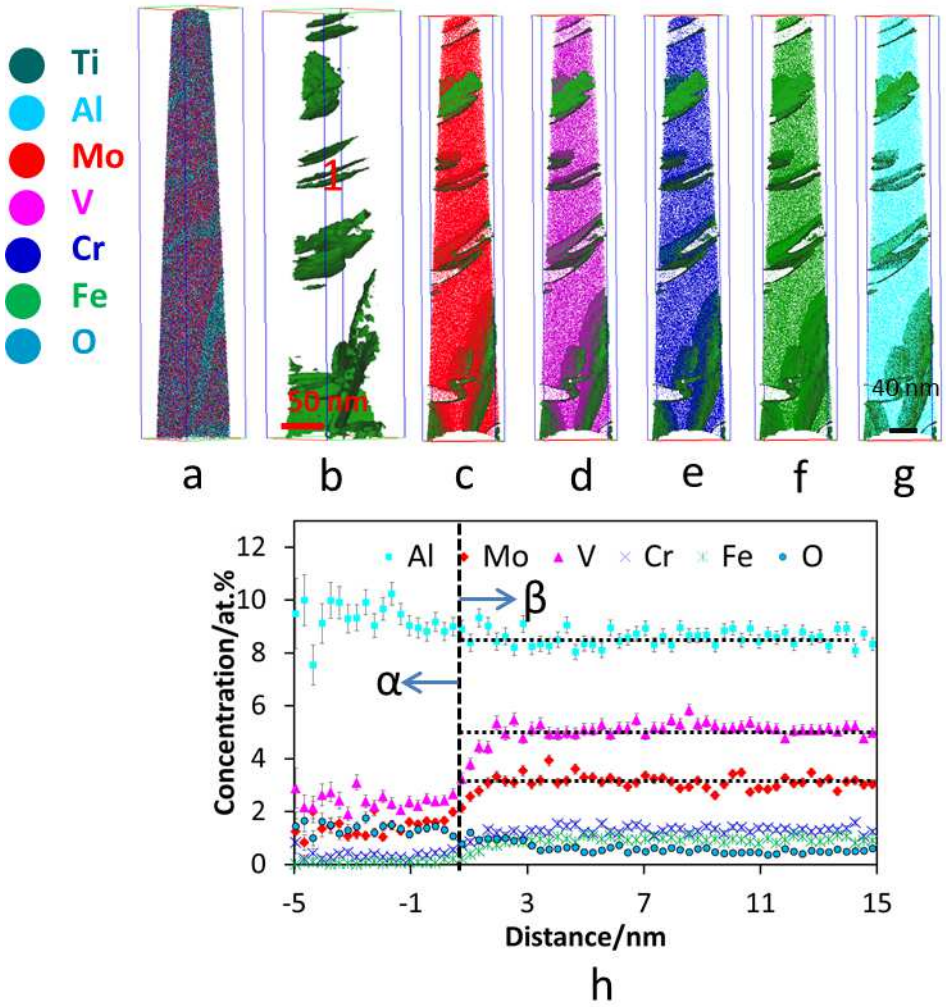

Fig.5. (a) A representative 3D atom map (94 millions ions) of all elements and (b) corresponding 0.4 at. % Fe isoconcentration surfaces. Overlap of 0.4 at.% Fe isosurfaces on elemental atom maps of (c) Mo, (d) V, (e) Cr, (f) Fe and (g) Al. (h) Proxigram showing elemental partitioning across the α/β interface of lath 1 in (b).

slight enrichment in Al and slight depletion in β stabilising elements. APT also revealed a higher concentration of O in the α particle compared to the β matrix, as O is also an α stabiliser. There is a rise in the concentration of β stabilisers in the vicinity of the α/β interface on the β side (Fig. 5h), until all the concentrations reach constant values. While the trend in redistribution of alloying elements between phases was found to be the same by both techniques, the exact values were slightly different, with APT data showing a higher level of enrichment with Al and lower levels of Mo and V compared to STEM-EDS data. This could be related to the slightly larger size of the α particle analysed by APT, which thus had more time for growth and the associated diffusion of alloying elements. There is less difference for both Cr and Fe, as they have much faster diffusion rates compared to Mo and V [39], as well as being present in lower initial amounts.

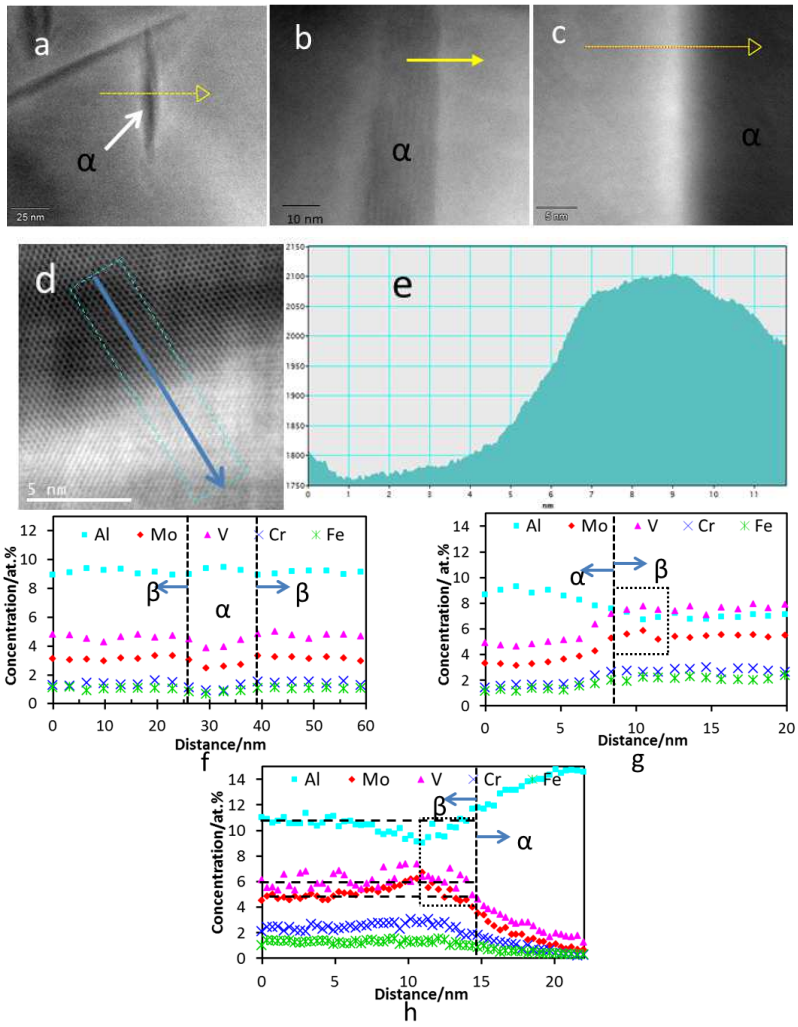

Fig.6. (a-c) HAADF-STEM images showing α phase formed during cooling in TMP, aged for 0.12 ks and 3.6 ks samples, respectively. (d) A representative image showing dark and bright contrast at α/β interface. (e) The intensity profile along the line shown in (d) confirms the

segregation of heavier elements in the bright contrast regions. (f-h) The composition profiles along the arrows shown in (a-c), respectively.

3.4 Microstructural and compositional changes with ageing

3.4.1 Electron microscopy

The HAADF-STEM image in Fig. 7a depicts secondary α laths with two orientations in a retained β matrix in the sample aged for 0.12 ks. The average size of the secondary α formed at this stage is ~200 nm in length by ~20 nm in width. The secondary α phase shown is formed during heating and ageing. A SADP, similar to that shown for the TMP condition, taken with the beam direction parallel to [011] $_{\beta}$ zone axis shows 1/3 {112} $_{\beta}$ and 2/3 {112} $_{\beta}$ diffusive spots, consistent with the athermal ω phase (Fig. 7b). The DF image confirms the presence of ω precipitates less than 5 nm in size (Fig. 7c). The observed ω phase displays two out of four possible variants, as was observed for the TMP condition. However, the ω phase was detected only in few areas, compared to a nearly uniform distribution for the TMP condition. The SADP in Fig. 7d shows the presence of extra reflections at 1/2 {200} $_{\beta}$ positions, which is consistent with the characteristics of the α phase. No reflections corresponding to ω are present in this SADP. Like for the TMP condition, HRTEM reveals the presence of ω (Fig. 7e). Two regions of interest in Fig. 7e are marked by rectangular boxes and their enlarged views are shown in Figs. 7f and 7g. Fig. 7f clearly displays two rows of ω super cells, though the stacking sequence shows partially transformed ω. Significantly, the concurrent presence of adjacent ω and α motifs is also shown in the HRTEM image (Fig 7g).

Following 3.6 ks of ageing, the average size of the α plates increased to ~350×70 nm (Fig. 8a). The BF image in Fig. 8a, and the corresponding SADP (Fig. 8b) and DF images (Figs. 8c and 8d) clearly indicate the presence of two orientations of α laths in retained β. No evidence of reflections from the ω phase was found in any SADPs or HR imaging after 3.6 ks ageing, which indicates that all the ω precipitates had dissolved by this point. Further ageing up to 14.4 ks, led to an increase in the size of the α precipitates to ~600 nm in length and ~100 nm wide (Fig. 8e). Two variants of α are clearly visible in Fig. 8e, where one of the variants is in diffraction condition (dark contrast) and other is not (bright contrast). As expected, ageing for 28.8 ks resulted in growth of α to a mean size of ~1.8×0.3 μm (Fig. 8f). Two variants of intragranular α were observed in all conditions.

3.5. Solute redistribution during ageing

Line profiles across the α-β interfaces, as shown in HAADF images (Figs. 6b-d) were acquired in order to examine the partitioning of the alloying elements between phases as a function of

ageing time (Figs. 6g-h). Layers of a bright contrast at the α/β interfaces were indicative of the segregation of heavier elements. An increase in intensity counts (Fig. 6e) in the β phase adjacent

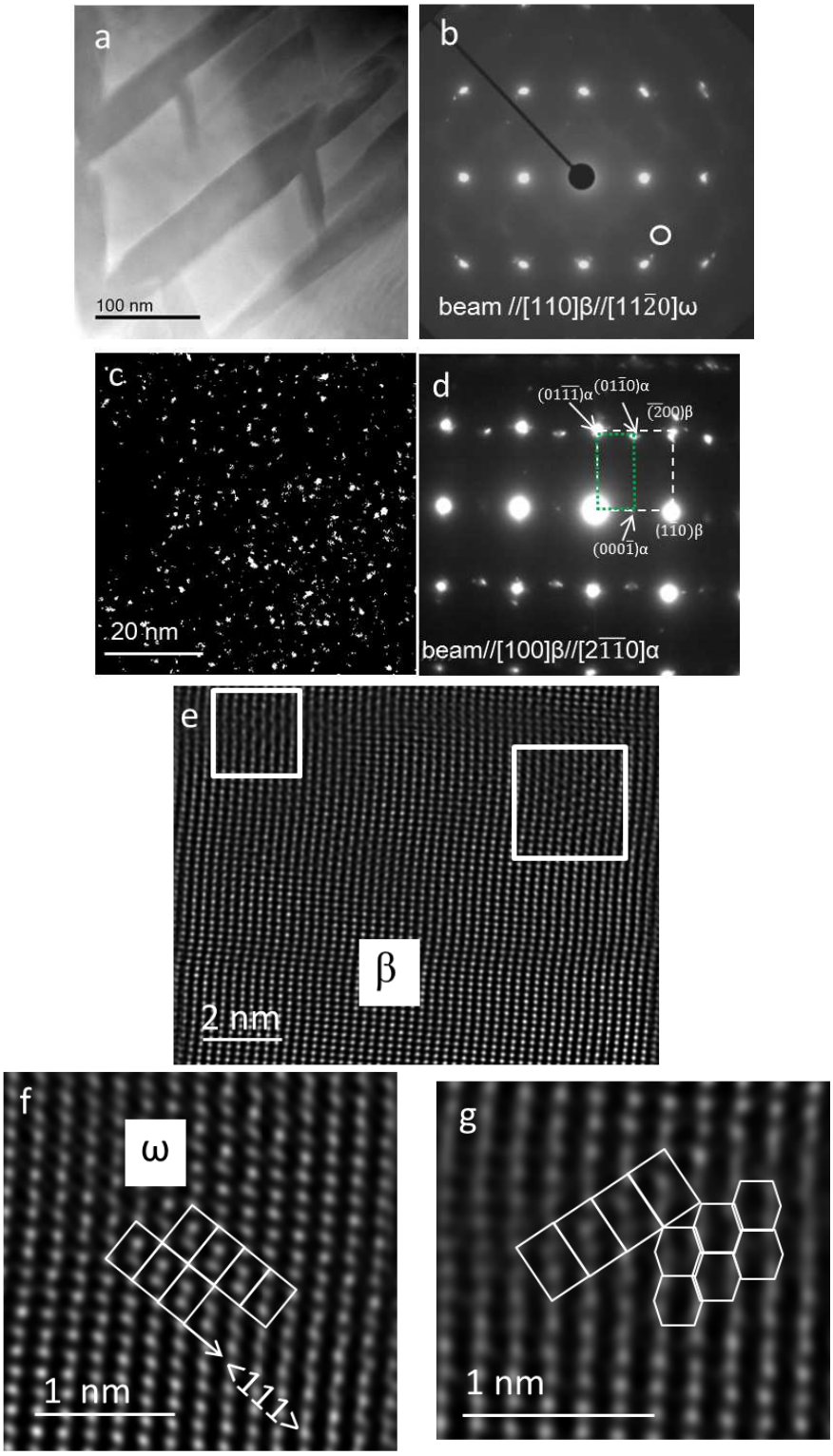

Fig.7. (a) HAADF-STEM image showing two variants of secondary α laths in 0.12 ks aged sample. (b) SAD pattern captured in a $[110]_{\beta}$ zone axis with ω reflections at 1/3 and 2/3 $\{112\}_{\beta}$

positions. (c) DF image taken from the reflection in the circle in (b) illustrating nanosized ω particles. (d) SAD pattern taken in a $[100]_{\beta}//[2\bar{1}\bar{1}0]_{\alpha}$ zone axis. (e) Fourier filtered HAADF image of 0.12ks aged sample showing atom columns of β and marked areas with ω and α motifs. (f) Enlarged view of large rectangular box in (e) displaying ω super cells. (g) Enlarged view of small rectangular box in (e) illustrating adjacent ω and α motifs in β matrix.

to the α/β interface also confirms the segregation of heavier elements. The concentration profiles (Fig. 6h) reveal segregation of Mo and V and depletion of Al in these regions. Whereas pile-up of Mo and V is pronounced in 3.6 ks aged sample, it was less evident for 0.12 ks condition. As expected, the concentrations of Fe and Cr in α phase reached nearly zero levels after 3.6 ks ageing, whereas the difference between Mo, V and Al contents in the α and β phases has increased. While this was the observed trend, it is noted that these are local variations in composition. Thus, the average phase compositions obtained from EDS maps are summarised in Table 2.

Atom probe maps for the 0.12 ks, 3.6 ks and 14.4 ks aged samples are shown in Figs. 9a, 9d-h, 10a and 10c. 0.5 at.% Fe iso-concentration surfaces (Fig. 9b, d-h) and 0.8 at.% Fe iso-concentration surfaces (Figs. 10a and 10c) clearly delineate α/β interfaces and reveal a complex arrangement of several parallel α particles. A concentration profile along the cylinder shown in Fig. 9b is displayed in Fig. 9c. Interestingly, there is a difference in the compositional profile depending on the thickness of the β phase regions between α particles; in thin ones a very sharp gradient in Mo and Al concentrations was observed, with Al rapidly decreasing from interface towards the centre and Mo exhibiting the opposite trend. The corresponding maximum and minimum values achieved in the centre are higher and lower, respectively, than the ones in the larger remaining areas of β phase. The composition is more uniform in larger β and α regions.

The partitioning of alloying elements between phases becomes more pronounced as ageing progresses, i.e. the α phase becomes progressively more enriched in Al and O, and depleted in Mo, V, Cr and Fe, whereas the opposite occurs for the β phase (Figs. 9c, 10b and 10d). The compositional uniformity of phases increased at prolonged ageing time to 3.6 ks, together with the coarsening of α particles (Table 2). However, the proxigram (Fig. 10d) for 14.4 ks aged samples showed a relatively high concentration of ~2 at.% Mo, 1.5 at.% V, 13 at.% Al in α compared to the 3.6 ks aged condition (Fig. 10b). As only a small volume of α was in the analysed APT tip, it is possible the data might be skewed as the data only comes from α that is near the α/β interface. Another explanation might be that this particular α particle was newly-formed and the higher content of Mo and V is associated with their slow diffusion out of α. The specimen aged for 14.4 ks also displayed the most pronounced pile-up of V in the β phase, with

the average V content being lower than it was in the 3.6 ks aged sample (Fig. 10b). The average compositions of phases were calculated for each condition from APT data and a summary is given in Table 2. As oxygen was not measured by EDS, there is some variation in values obtained from both techniques. However, the trends are similar.

Table 2: Compositions of the phases in atomic percentage (at. %) obtained using both APT and TEM techniques

	TMP				**0.12 ks**				**3.6 ks**				**14.4 ks**	
Elements	α		β		α		β		α		β		α	β
	APT	TEM	APT	TEM	APT	TEM	APT	TEM	APT	TEM	APT	TEM	APT	
Al	9.2	9.9	8.4	7.2	11.0	13.0	6.8	7.4	11.3	14.4	6.5	8.9	12.0	5.8
Mo	1.3	1.0	3.2	2.4	0.4	0.6	4.8	2.7	0.2	0.3	4.8	2.1	0.1	4.3
V	2.2	1.9	5.2	6.0	1.5	1.6	8.0	7.6	1.5	1.9	8.4	7.1	1.2	7.8
Cr	0.3	0.3	1.1	1.7	0.2	0.2	3.6	2.6	0.3	0.4	3.2	3.4	0.2	4.5
Fe	0.1	0.1	0.9	1.2	0.04	0.4	1.7	1.9	0.2	0.3	1.8	1.7	0.03	1.5
O	1.9	*	0.5	*	1.6	*	0.2	*	1.3	*	0.7	*	1.7	0.3

* O is not included in TEM analysis. Standard deviation varies between 0.1-0.2 for all elements except Fe; for Fe it is 0.01-0.1. All α phase above will be called as secondary α phase except for TMP in which it is a primary α phase. The amount of Ti is a balance. Data from APT is based on the number of ions in the analysed volume.

4. Discussion:

4.1 Early stages of β phase decomposition

Coupled HRSTEM and APT analysis of the TMP sample and the sample aged for 0.12 ks revealed the simultaneous occurrence of the following events: (i) decomposition of β to form solute rich and solute lean regions (only for TMP); (ii) the formation of nanosized athermal ω; (iii)

nucleation of a new α phase and (iv) the growth of pre-existing α particles. β phase decomposition to either solute separation (forming solute rich and lean regions), or ω phase formation, depends on the alloy composition and heat treatment temperatures. Below, a more detailed discussion of the processes taking place on cooling during TMP and on heating to the ageing temperature is provided.

4.1.1 Decomposition of β to form solute rich and solute lean regions

During TMP processing (isothermal holding in α/β region at 800°C and subsequent cooling at 10 $°Cs^{-1}$); solute redistribution takes place within the β phase as a result of the exit of β stabilising elements (Mo, V, Cr and Fe) from the α phase. Mo and V result in the isomorphous-type phase diagram for binary Ti alloys, whereas Fe and Cr favour the formation of a β eutectoid. This system is also interesting from the perspective of the thermodynamic interaction parameters of the elements present. As binary Ti-V (+7.6 KJ/mol), Ti-Mo (+12.1 KJ/mol), Ti-Fe (+33.9 KJ/mol) and Ti-Cr (+7.5 KJ/mol), have positive enthalpies of mixing [40], it could be expected that this alloy has a limited tendency for de-mixing, except for in the case of Al, as Ti-Al (-37.7 KJ/mol) has negative enthalpy of mixing. However, the binding energies of Mo-Mo (796 MeV), Fe-Fe (471 MeV), V-V (425 MeV), and Cr-Cr (411 MeV) are higher than that of Ti-Ti (375 MeV), which could lead to their preferential clustering at relatively high temperatures [41]. APT data (Fig. 4) has confirmed significant compositional fluctuations of Mo, and to a much lesser extent, Fe, V and Cr. Contrary to our observations, the solute rich regions in a Ti-20Mo-5Al alloy [16, 42] were enriched with both Mo and Al. Additionally, there was no satellite reflections from β lattice in DPs (Figs. 2, and 8), which is usually evidence of a spinodal decomposition, as the processing temperatures here are much higher than the temperatures at which spinodal decomposition is likely to occur. Unlike for the TMP condition, clustering of alloying elements was not detected in the β matrix in aged samples. There are several possible reasons for this, all of which affect diffusion and distribution of alloying elements, including slow heating rates, long holding times and diffusion patterns arising from partitioning of elements between α and β.

4.1.2 Formation of athermal ω

Typically, the formation of ω phase is suppressed in Ti alloys containing α stabilisers, e.g. Al, O etc [11]. The starting temperature for ω formation decreases with increasing O content [43]. As O is present in our case, it can be speculated that the ω formation temperature will be lowered. Ti55521 is a near-β alloy, and the β matrix depletes in Al due to the formation of α phase during holding at 800°C, thus opening the pathway for ω phase formation at a later stage of TMP (during accelerated cooling). The size and shape of the athermal ω precipitation are identical to that formed on quenching [19, 28, 29]. SADP also reveals similar weak reflections upon

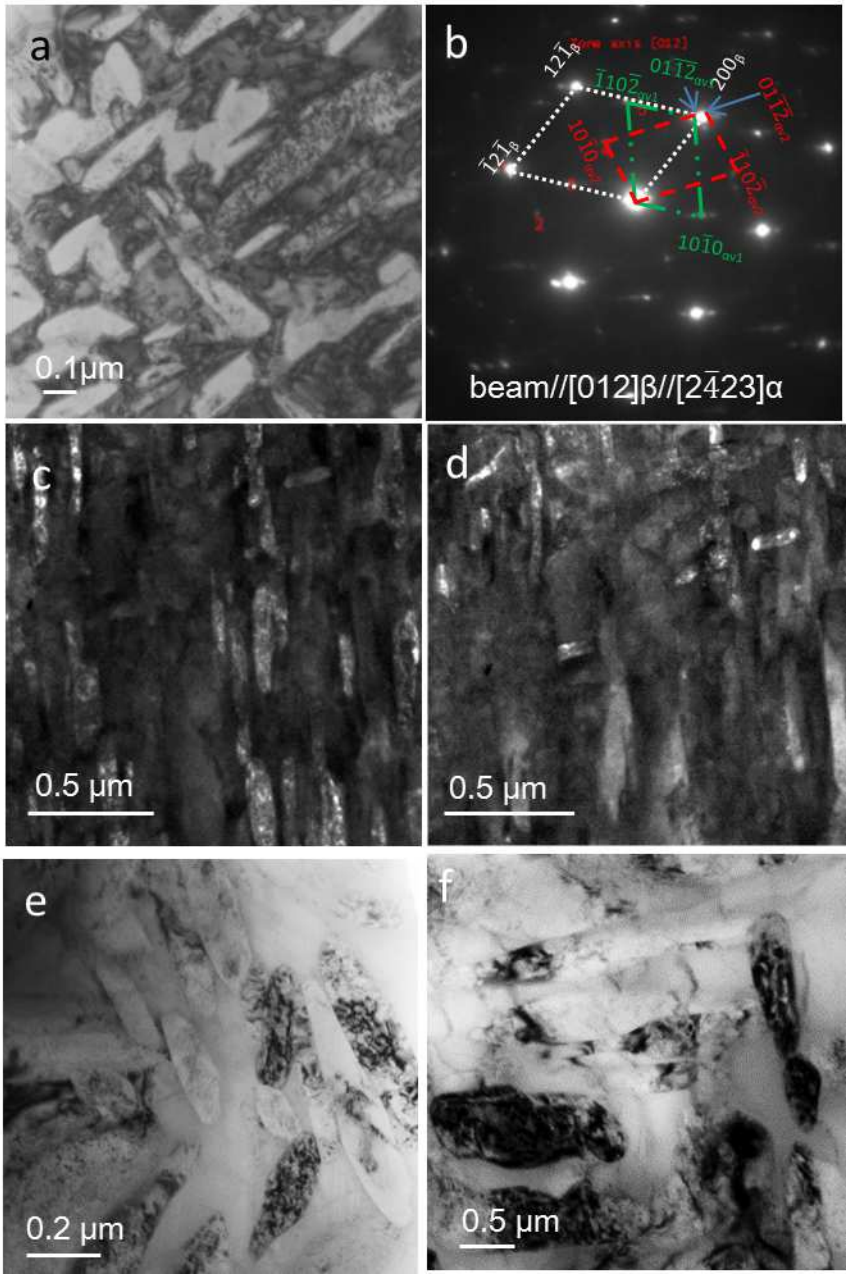

Fig.8. (a) Bright field (BF) image showing two variants of α laths in β matrix after 3.6 ks aging. (b) SAD pattern taken with $[012]_\beta$ zone axis; two variants of α phase with $[2\bar{4}23]_\alpha$ zone axis sketched on the pattern and corresponding (c-d) DF images showing two α variants. (e) BF image revealing β and two variants of α phase in 14.4 ks aged sample. (f) BF image showing β and two variants of α phase in 28.8 ks aged sample.

quenching [8]. In contrast, this accelerated cooling allows α nuclei to form from athermal ω, which has never before been reported for quenched alloys.

Contrary to the conclusions of Devaraj *et al.* [24], that formation of athermal ω was linked with Mo-lean pockets in β phase of binary Ti-Mo alloy, our HRSTEM and APT investigations have failed to elucidate such a link. The shape, size and distribution of Mo-lean volumes resolved by

APT (Fig. 4c) didn't resemble the ones for the ω particles detected using electron microscopy (Figs. 2d and 3h). Partially collapsed rows of β lattice forming coherent ω structure (Fig. 3) were associated with both light and dark areas of the HAADF micrographs (Z-contrast), thus the role of compositional fluctuation in the formation of athermal ω phase is disregarded in the studied alloy. Similar to previous reports [16, 21, 22], it could be suggested that observed athermal ω formed via the displacive collapse of the $\{111\}_{\beta}$ plane and without compositional changes. However, compositional partitioning in β matrix may result in different local lattice parameters causing hydrostatic pressure, which could assist formation of ω phase as was reported in ref. [24].

The size of ω nuclei (~3 nm) did not change much in the 0.12 ks aged samples compared to the TMP condition. However, the nuclei were found only in specific areas. This could be explained by the ageing temperature (650 °C) being well above the dissolution temperature of athermal ω. During heating at 0.25 $°Cs^{-1}$ through a ~100-400 °C temperature interval pre-existing athermal ω particles grow and new ones nucleate. However, above this temperature range, two events concurrently occur: nucleation of new α, which consumes ω if it is formed there, and dissolution of ω. With longer ageing times (up to 3.6 ks) ω is either completely dissolved or consumed by the growing α laths.

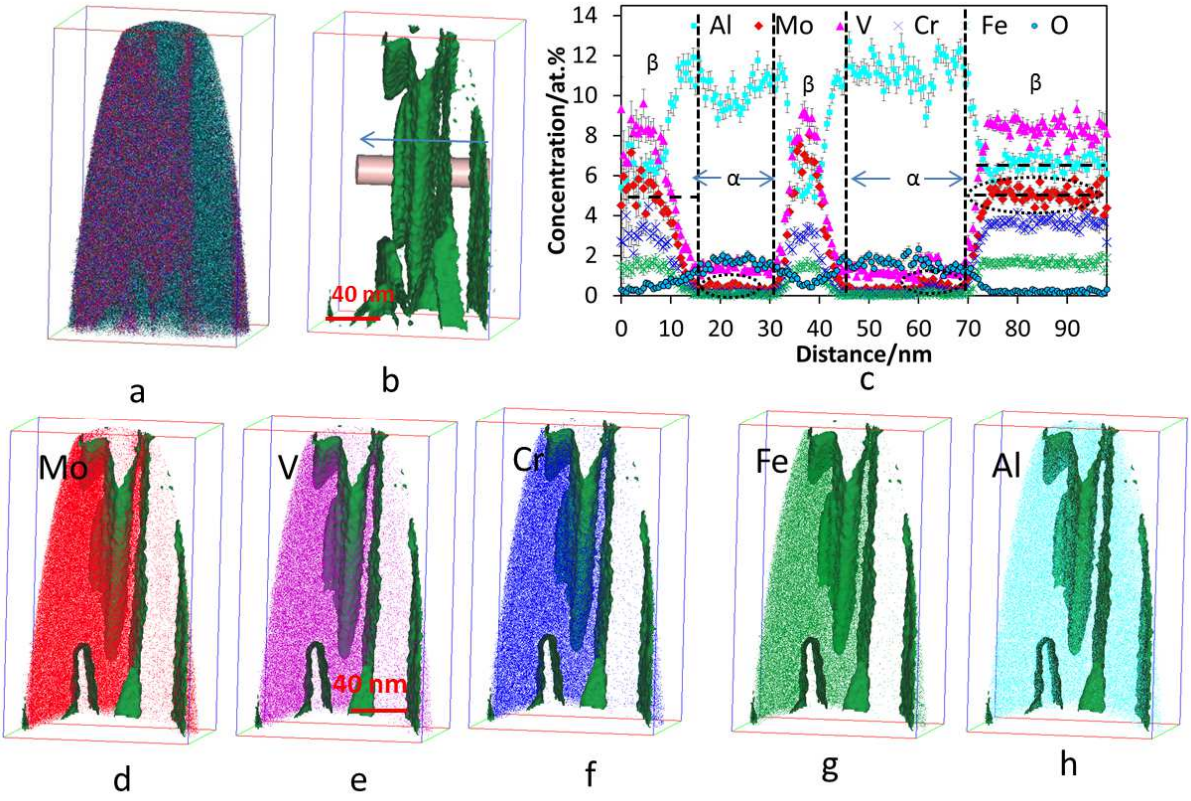

Fig. 9. (a) Three-dimensional atom map (60 million ions) of all elements and (b) corresponding 0.5 at.% Fe isoconcentration surfaces for 0.12ks aged sample. (c) Composition profile along the cylinder (from right to left) shown in (b). Elemental maps with overlapped 0.5 at.% Fe isoconcentration surfaces for (d) Mo, (e) V, (f) Cr, (g)Fe and (h) Al.

4.1.3 Nucleation of α

In the TMP condition, a range of α particles of different sizes and compositions was present, ranging from nano-sized nuclei only visible in aberration corrected HRSTEM to coarse grain boundary α. This is associated with a) undissolved α after solution treatment at 950 °C, b) intragranular α precipitation during isothermal holding at 800 °C and c) the finest α, which forms on cooling to ambient temperature. Focusing on the latter one, two groups are defined: (i) α laths (10-30 nm length and up to 10 nm width) typically of two orientations and (ii) 2-5 nm α nuclei. It is assumed that the former ones formed at early stage of cooling as they had time to grow before cooling to temperatures where diffusion of alloying elements is very limited. The line profile (Fig. 6f) and proxigram (Fig. 5h) analyses suggest that the elemental partitioning between α and β phases took place during their growth. During cooling after deformation at 800°C, the nucleation of α may take place at different heterogeneous nucleation sites, such as (i) dislocation substructure, (ii) at ω/β interfaces or within the ω phase and (iii) Mo-lean volumes. The preferred nucleation site will depend on the temperature. Immediately after 60% deformation at 800°C, dislocations will be present in β matrix, serving as potent nucleation sites for α. However, as the temperature is lowered, recovery and even recrystallisation takes place, resulting in defect-free β grains (Fig. 1c). Thus, the number of such nucleation sites decreases as cooling progresses. Therefore, the preferential heterogeneous nucleation sites for the first group of 10-30 nm α laths existing in TMP sample would be the remaining dislocation substructure developed as a result of 60% reduction, as some dislocation cells remain at room temperature.

On another hand, Mo-lean regions (Fig. 4) may also serve as precursors/preferential nucleation sites for the formation of α or ω. Although nucleation of α in solute lean regions in Ti-10Mo-6Al [17] and in Ti-20Mo-5Al alloy [16] has been reported, those solute lean regions were homogeneously distributed and developed after much longer isothermal holdings at 350-400°C, which is very different from the non-uniform distribution of Mo-lean volumes in the alloy studied here. Although some observed α nuclei were in the areas of darker contrast (Fig. 3d-e), linked with Mo-lean pockets, others were in the areas of lighter contrast. Thus nucleation of the latter ones is also probably at defects.

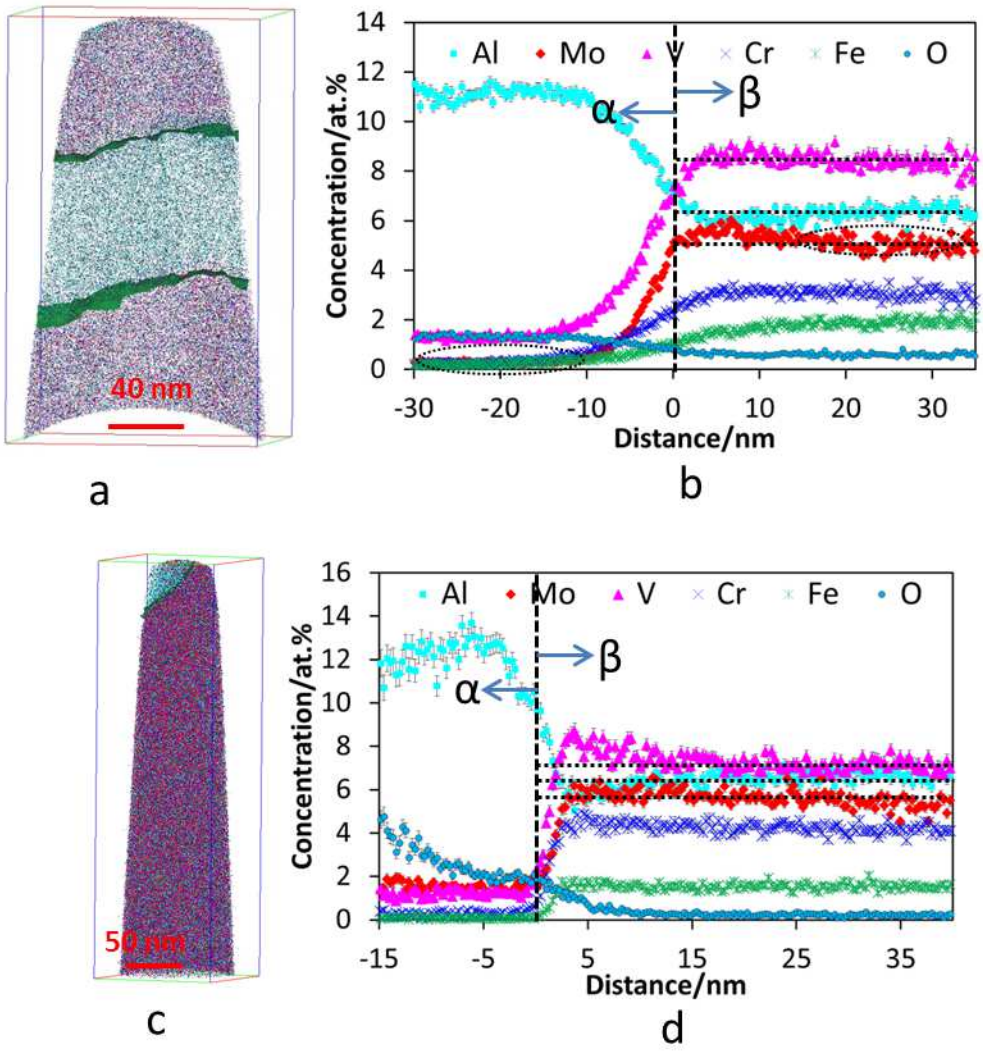

Fig. 10. Atom maps of samples after ageing for (a) 3.6 ks and (c) 14.4 ks with overlapped 0.8 at.% Fe and 0.4 at.% Fe isoconcentration surfaces in (a) and (c) correspondingly. (b) Proxigram taken across the lower isosurface in (a). (d) Proxigram taken across the isosurface in (c). Total number of ions collected is 72 million in (a) and 105 million in (c).

In addition to the aforementioned discussion, two other possible nucleation sites for α in the aged sample, e.g. formation of α within ω or at ω/β interface, should be addressed for the TMP (Fig. 3h) and 0.12 ks (Fig. 7g) samples. The presence of ω super cells at either side of α confirms the possibility of α nucleation within ω, as previously reported by [30] and the consumption of ω during the growth of α [25, 30]. The crystallographic relationships between β/α/ω were determined to be: (111) β → (0001) ω and $[1\bar{1}0]$ β // $[11\bar{2}0]$ ω and $(11\bar{2}0)$ ω→ (0001) α and [0001] ω // $[11\bar{2}0]$ α. As some α super cells were found only adjacent to nano-sized nuclei ω, with coherent interfaces with both ω and β, it can be also suggested that nucleation of α takes

place not only within the ω but also at ω/β interfaces. However, it should be noted that from the thermodynamic point of view, nucleation at the interface is preferred. Composition profile analysis for a fine (~12 nm thick) α in 0.12 ks aged sample also shows only a minute compositional change with respect to the matrix (Fig. 6g). It might be that the α plate shown in Fig. 6b precipitates via athermal ω with no compositional change and starts to expel the β stabilisers. Since α nucleates with a composition that is very close to the surrounding β phase, which is very far from equilibrium, this does not support a diffusional phase transformation mechanism. It is expected that the second phase produced by diffusional transformation should have a composition close to its equilibrium value predicted by the phase diagram with alterations due to Gibbs-Thompson impact [44]. Nag *et al.* [19] also reported a small compositional transition while α forms via ω (a displacive-diffusional transformation).

Based on the above, dislocations, ω particles and/or β/ω interfaces and solute-lean regions are the possible nucleation sites of α during cooling in TMP. On the other hand, it can be concluded that ω particles are the dominant nucleation site for α formation in 0.12 ks aged samples, leading to more uniformly distributed fine α structure.

4.2 Partitioning of alloying elements during ageing

The observed changes in the composition of α and β with ageing time (Table 2) are evidence of the diffusion-controlled character of α nucleation and growth during isothermal holding at 650 °C, in agreement with the literature [42, 45]. As expected, with prolonged ageing, the average compositions of the α and β phases become more enriched in α and β stabilisers, respectively. However, in the early stages of formation, each newly formed α lath was more enriched in β stabilisers, as it forms in β matrix, which has a higher β stabiliser content due to their exit from the α phase formed earlier. Thus, at the same stage of ageing, finer α laths typically show a higher residual content of β stabilisers than coarser ones, which have had time for growth and accompanying elemental diffusion. Taking into account the variation in volume fraction of α and its size with ageing time (Table 1), it could be suggested that the majority of α nucleation activity is completed by 3.6 ks of ageing and further increase in volume fraction is mainly due to growth.

The diffusion rate of the alloying elements in both phases determines the evolution of compositions of the phases and interfaces throughout ageing. The diffusion rate of a solute can be obtained from an Arrhenius equation. The diffusion rate of Mo, V, Cr, Fe and Al in β Ti phase at 650 °C are 5.2×10^{-17}, 7.3×10^{-16}, 1.1×10^{-15}, 2.2×10^{-13} and 1×10^{-17} m^2s^{-1} , respectively [39, 46, 47]. On the other hand, the diffusivity of Mo, V, Cr, Fe and Al in α Ti are 6.25×10^{-19}, 4.3×10^{-19},

7.33×10^{-16}, 1.22×10^{-13} and 3.92×10^{-16} m^2s^{-1}, correspondingly [39, 46, 47]. These diffusion data were obtained by extrapolating the data available in ref. [39, 46, 47], in which the data were calculated at 900-1600 ºC in β Ti and 600-1200ºC in αTi in binary systems. Thus, the solute diffusivity data in β Ti are not fully reliable. However, it is apparent that Fe has the fastest diffusivity in both phases, followed by Cr in β and Al in α. Interestingly, Mo has the slowest diffusivity in β Ti but V has the slowest diffusivity in α Ti. Therefore, the fastest approach to equilibrium concentration contents in α and β phases was achieved for Fe and Cr, whereas Mo, V and Al were much further behind in reaching their equilibrium contents. With increased ageing time, the pile-ups of Mo, V and Al gradually decreased and homogeneity was achieved at the interface (Fig. 10b, d). At the same time, compositional partitioning between the phases becomes more pronounced with ageing (Table 2).

Similar pile-up of Mo in the β phase near the α/β interface in furnace cooled Ti5553 was observed by APT [45]. The authors of [45] have also noted the limited elemental partitioning between phases during subsequent ageing, explaining it by low diffusion rates at their 400 °C ageing temperature. However, in our case, the ageing temperature is much higher, leading to more pronounced partitioning between phases as ageing progresses. As V is the slowest diffusing solute in α, pile-ups of V were also occasionally detected (Fig. 10d), which might be associated with the early stage of α growth. A simple case could be discussed based on diffusivity to clarify the diminishing interfacial compositional changes. A 20 nm wide α lath (obtained after 0.12 ks ageing) increased to 80 nm after 3.6 ks, so Mo atoms/ions in the core of the α lath have to pass 40 nm in the α Ti phase and then in the β Ti phase. By using the diffusivity of Mo in α Ti, it is calculated that 2.48 ks is needed to travel 40 nm (half of the total width). In the rest of the time, it can cover a maximum of 20 nm in the β phase. However, the pile up of Mo appeared at about 10 nm (Fig. 9b) from the interface. The difference is attributed to the fact that the diffusivity used to calculate the distance was based on that in the binary system, while the present system is more complex. In contrast, Fe needs only 0.013 s to cover 40 nm distances in α Ti and during the remaining time it may diffuse 0.2 μm distance, resulting in its more uniform distribution within β matrix and an absence of pile-up at the interface.

5.3 Effect of ageing on the microstructure-property relationships in Ti55521

The age hardening response is clearly manifested by the linear relationship between strength (UTS / 0.2% proof strength) and volume fraction of α (Table 1). Similar results describing an increase in α volume fraction during ageing were reported in [48]. The tensile mechanical properties obtained for aged samples are in good agreement with the existing literature for Ti-5553 [8, 9, 49-51]. Huang *et al.* [50] mentioned an UTS of 1316 MPa with a high ductility (~18%) and reported that bi-modal microstructure consisting of both equiaxed and lath α in the

matrix is responsible for such a combination of high ductility with high strength. Contrarily, Clement *et al.* [8] did not find a significant improvement in ductility for a similar bi-modal microstructure, as only 8% total elongation was recorded for 1320 MPa. It was suggested that a continuous form of grain boundary α is responsible for the severe embrittlement. In the present study, only 10 % total elongation was recorded with a UTS of 1024 MPa in the TMP condition, despite the presence of fragmented grain boundary α [6, 8]. As ω negatively affects ductility [52], the low ductility of the TMP samples is attributed to the presence of athermal ω. Improvement in ductility after ageing for 3.6 ks is thought to be associated with the disappearance of ω as well as the presence of fine and uniformly distributed α, previously formed on a large number of available heterogeneous nucleation sites (defects, ω/β interfaces, and Mo-lean regions). In addition, fragmented grain boundary α becomes increasingly spheroidal during TMP during the slow heating and ageing, thus also contributing to improved elongation. Although the 3.6 ks aged sample attains the best combination of properties, the other ageing conditions also achieved mechanical properties lying within the range specified by Fanning *et al*. for Ti-5553 (UTS=1179-1304 MPa, Total elongation=11-16%) [9]. With further ageing, the existing α plates grow, leading to an increase in strength and deterioration in ductility [32, 53].

Oxygen content is crucial not only in powder processed samples but also in the wrought titanium alloys because it considerably affects the tensile elongation. The amount of oxygen found in the present study was ~0.38 wt. % (Refer to Table 6 of Chapter 1). The obtained oxygen might be picked up during different stages of processing [5]. The absence of α_2 precipitation clusters inside the α phase indicates that the measured oxygen content was lower in the study than the critical limit for ductility for this alloy[54]. Since the critical limit of oxygen is alloy dependent, the determination of critical oxygen concentration for this alloy needs further investigation. Based on the elongation (10-15%) obtained in the present study, it can be claimed that such level of oxygen content is not harmful for this alloy.

Conclusions:

1. Significant improvement in the mechanical properties, especially ductility, was found in aged samples which is due to the processing e.g. accelerated cooling in TMP and slow heating in ageing allow the formation of α via ω, high temperature deformation provides fragmented grain boundary α.
2. Accelerated cooling at 10 $°Cs^{-1}$ to RT during TMP resulted in the partial decomposition of the parent β phase, manifested in the form of compositional fluctuations, nano-sized athermal ω and α phases. These α nuclei were observed to form both individually in the β matrix and in conjunction with the ω phase.

3. Negligible difference between α nuclei and β phase composition at early stages of α formation and subsequent deviation in their compositions with α growth support displacive-diffusional mechanism of α formation.
4. On slow heating to an ageing temperature of 650 °C, two competing processes for athermal ω phase occur: (i) the growth of pre-existing ω and the nucleation and growth of new athermal ω particles at temperatures below ~400 °C and (ii) dissolution of ω at temperatures above ~400 °C.
5. A change in the α phase composition from TMP to 14.4 ks indicated a gradual depletion in β stabilising elements with growth of α. Each newly formed α was initially enriched in β stabilisers due to their high content in the parent β phase.
6. Both HRSTEM and APT showed the difference in diffusion rate for the β stabilisers on their exit from α, with Fe and Cr being the fastest and most uniformly distributed in the β phase while Mo, and occasionally V, built-up in the vicinity of α/β interface.

Acknowledgements: The UOW Engineering Materials Institute strategic grant and the ARC (DP120100206) financially supported this work. The authors are grateful to Prof. O.M. Ivasishin and Dr. D.G. Savvakin, Institute of Metal Physics, National Academy of Sciences, Ukraine for provision of the alloy. The use of UOW Electron Microscopy Centre facilities and ARC support (LE120100104) for JEM-ARM200F purchase are being acknowledged. The authors thank Dr. A. A. Gazder, UOW for modification of tensile stage. The authors acknowledge the facilities and the scientific and technical assistance, of the Australian Microscopy & Microanalysis Research Facility at the Australian Centre for Microscopy and Microanalysis at the University of Sydney.

References

[1] R. R. Boyer and R. D. Briggs, The use of β titanium alloys in the aerospace industry, J. of Materi Eng and Perform, 14 (2005) 681-685.

[2] N. G. Jones, R. J. Dashwood, M. Jackson, and D. Dye, β Phase decomposition in Ti–5Al–5Mo–5V–3Cr, Acta Materialia, 57 (2009) 3830-3839.

[3] M. Ahmed, A. Gazder, D. Savvakin, O. Ivasishin, and E. Pereloma, Microstructure evolution and alloying elements distribution between the phases in powder near-β titanium alloys during thermo-mechanical processing, Journal of Materials Science, 47 (2012) 7013-7025.

[4] M. Ahmed, D. G. Savvakin, O. M. Ivasishin, and E. V. Pereloma, The effect of cooling rates on the microstructure and mechanical properties of thermo-mechanically processed Ti–Al–Mo–V–Cr–Fe alloys, Materials Science and Engineering: A, 576 (2013) 167-177.

[5] M. Ahmed, D. G. Savvakin, O. M. Ivasishin, and E. V. Pereloma, The effect of ageing on microstructure and mechanical properties of powder Ti–5Al–5Mo–5V–1Cr–1Fe alloy, Materials Science and Engineering: A, 605 (2014) 89-97.

[6] C. Sauer and G. Luetjering, Thermo-mechanical processing of high strength β-titanium alloys and effects on microstructure and properties, Journal of Materials Processing Technology, 117 (2001) 311-317.

[7] T. Furuhara, T. Maki, and T. Makino, Microstructure control by thermomechanical processing in β-Ti–15–3 alloy, Journal of Materials Processing Technology, 117 (2001) 318-323.

[8] N. Clément, A. Lenain, and P. J. Jacques, Mechanical property optimization via microstructural control of new metastable beta titanium alloys, JOM, 59 (2007) 50-53.

[9] J. C. Fanning, Properties of TIMETAL 555 (Ti-5Al-5Mo-5V-3Cr-0.6Fe), J. of Materi Eng and Perform, 14 (2005) 788-791.

[10] M. Okada, Tetsu-to-Hagane, 76 (1991) 614.

[11] E. L. Harmon and A. R. Troiano, Trans. ASM, 53 (1961) 43.

[12] E. L. Tanner, Trans. TMS:AIME, 221 (1961) 74.

[13] N. E. Ageyev and P. K. Novik, Russian Metallurgy, 5 (1965) 46.

[14] G. H. Narayanan and T. F. Archbold, Decomposition of the metastable beta phase in the all-beta alloy Ti-13V-11Cr-3Al, MT, 1 (1970) 2281-2290.

[15] T. Furuhara, T. Makino, Y. Idei, H. Ishigaki, T. A., and M. T., Morphology and Crystallography of α Precipitates in β Ti-Mo Binary Alloys, Materials Transactions JIM, 39 (1998) 31.

[16] A. Devaraj, PhD, Department of Materials Science and Engineering University of North Texas, Denton, 2011.

[17] J. C. Williams, B. S. Hickman, and D. H. Leslie, The effect of ternary additions on the decompositon of metastable beta-phase titanium alloys, MT, 2 (1971) 477-484.

[18] H. P. Ng, A. Devaraj, S. Nag, C. J. Bettles, M. Gibson, H. L. Fraser, B. C. Muddle, and R. Banerjee, Phase separation and formation of omega phase in the beta matrix of a Ti–V–Cu alloy, Acta Materialia, 59 (2011) 2981-2991.

[19] S. Nag, R. Banerjee, R. Srinivasan, J. Y. Hwang, M. Harper, and H. L. Fraser, ω-Assisted nucleation and growth of α precipitates in the Ti–5Al–5Mo–5V–3Cr–0.5Fe β titanium alloy, Acta Materialia, 57 (2009) 2136-2147.

[20] Y. Zheng, "Nucleation Mechanisms of Refined Alpha Microstructure in Beta Titanium Alloys," PhD, Materials Science and Engineering, Ohio State University, Ohio, 2013.

[21] G. Welsch, R. Boyer, and E. W. Collings, *Materials Properties Handbook: Titanium Alloys*: ASM International, 1993.

[22] S. L. Sass, The structure and decomposition of Zr and Ti b.c.c. solid solutions, Journal of the Less Common Metals, 28 (1972) 157-173.

[23] A. Devaraj, R. E. A. Williams, S. Nag, R. Srinivasan, H. L. Fraser, and R. Banerjee, Three-dimensional morphology and composition of omega precipitates in a binary titanium–molybdenum alloy, Scripta Materialia, 61 (2009) 701-704.

[24] A. Devaraj, S. Nag, R. Srinivasan, R. E. A. Williams, S. Banerjee, R. Banerjee, and H. L. Fraser, Experimental evidence of concurrent compositional and structural instabilities leading to ω precipitation in titanium–molybdenum alloys, Acta Materialia, 60 (2012) 596-609.

[25] Y. Ohmori, T. Ogo, K. Nakai, and S. Kobayashi, Effects of ω-phase precipitation on β→α, α″ transformations in a metastable β titanium alloy, Materials Science and Engineering: A, 312 (2001) 182-188.

[26] M. J. Blackburn and J. C. Williams, Trans. Met. Soc. AIME, 242 (1968) 2461.

[27] G. M. Pennock, H. M. Flower, and D. R. F. West, presented at the Titanium'80 Science and Technology, 1980.

[28] S. Banerjee, R. Tewari, and G. K. Dey, Omega phase transformation – morphologies and mechanisms, International Journal of Materials Research, 97 (2006) 963-977.

[29] D. De Fontaine, N. E. Paton, and J. C. Williams, The omega phase transformation in titanium alloys as an example of displacement controlled reactions, Acta Metallurgica, 19 (1971) 1153-1162.

[30] F. Prima, P. Vermaut, G. Texier, D. Ansel, and T. Gloriant, Evidence of α-nanophase heterogeneous nucleation from ω particles in a β-metastable Ti-based alloy by high-resolution electron microscopy, Scripta Materialia, 54 (2006) 645-648.

[31] S. Azimzadeh and H. J. Rack, Phase transformations in Ti-6.8Mo-4.5Fe-1.5Al, Metall and Mat Trans A, 29 (1998) 2455-2467.

[32] O. M. Ivasishin, P. E. Markovsky, Y. V. Matviychuk, S. L. Semiatin, C. H. Ward, and S. Fox, A comparative study of the mechanical properties of high-strength β-titanium alloys, Journal of Alloys and Compounds, 457 (2008) 296-309.

[33] O. M. Ivasishin, P. E. Markovsky, S. L. Semiatin, and C. H. Ward, Aging response of coarse- and fine-grained β titanium alloys, Materials Science and Engineering: A, 405 (2005) 296-305.

[34] S. Nag, A. Devaraj, R. Srinivasan, R. E. A. Williams, N. Gupta, G. B. Viswanathan, J. S. Tiley, S. Banerjee, S. G. Srinivasan, H. L. Fraser, and R. Banerjee, Novel Mixed-Mode Phase Transition Involving a Composition-Dependent Displacive Component, Physical Review Letters, 106 (2011) 245701.

[35] A. Carman, L. C. Zhang, O. M. Ivasishin, D. G. Savvakin, M. V. Matviychuk, and E. V. Pereloma, Role of alloying elements in microstructure evolution and alloying elements behaviour during sintering of a near-β titanium alloy, Materials Science and Engineering: A, 528 (2011) 1686-1693.

[36] M. K. Miller, *Atom Probe Tomography: Analysis at the Atomic Level*: Springer US, 2000.

[37] N. Wain, X. J. Hao, G. A. Ravi, and X. Wu, The influence of carbon on precipitation of α in Ti–5Al–5Mo–5V–3Cr, Materials Science and Engineering: A, 527 (2010) 7673-7683.

[38] A. V. Ceguerra, M. P. Moody, L. T. Stephenson, R. K. W. Marceau, and S. P. Ringer, A three-dimensional Markov field approach for the analysis of atomic clustering in atom probe data, Philosophical Magazine, 90 (2010) 1657-1683.

[39] G. Neumann and C. Tuijn, *Self-diffusion and Impurity Diffusion in Pure Metals: Handbook of Experimental Data*: Elsevier Science, 2011.

[40] E. W. Collings, *Applied Superconductivity, Metallurgy, and Physics of Titanium Alloys: Volume 1: Fundamentals*: Springer London, Limited, 1986.

[41] http://hyperphysics.phy-astr.gsu.edu/hbase/hph.html,

[42] A. Devaraj, S. Nag, and R. Banerjee, Alpha phase precipitation from phase-separated beta phase in a model Ti–Mo–Al alloy studied by direct coupling of transmission electron microscopy and atom probe tomography, Scripta Materialia, 69 (2013) 513-516.

[43] N. E. Paton and J. C. Williams, The influence of oxygen content on the athermal β-ω transformation, Scripta Metallurgica, 7 (1973) 647-649.

[44] D. A. Porter and K. E. Easterling, *Phase transformations in metals and alloys*: Chapman & Hall, 1992.

[45] S. Nag, R. Banerjee, J. Y. Hwang, M. Harper, and H. L. Fraser, Elemental partitioning between α and β phases in the Ti–5Al–5Mo–5V–3Cr–0.5Fe (Ti-5553) alloy, Philosophical Magazine, 89 (2009) 535-552.

[46] R. P. Elliott, "Diffusion in Titanium and Titanium Alloys," 1962.

[47] D. Goold, J. Inst. Metals, 88 (1959) 444.

[48] X. Zhang, H. Kou, J. Li, F. Zhang, and L. Zhou, Evolution of the secondary α phase morphologies during isothermal heat treatment in Ti-7333 alloy, Journal of Alloys and Compounds, 577 (2013) 516-522.

[49] D. Qin, Y. Lu, Q. Liu, and L. Zhou, Effects of Si addition on mechanical properties of Ti–5Al–5V–5Mo–3Cr alloy, Materials Science and Engineering: A, 561 (2013) 460-467.

[50] J. Huang, Z. Wang, and K. Xue, Cyclic deformation response and micromechanisms of Ti alloy Ti–5Al–5V–5Mo–3Cr–0.5Fe, Materials Science and Engineering: A, 528 (2011) 8723-8732.

[51] S. L. Nyakana, J. C. Fanning, and R. R. Boyer, Quick reference guide for β titanium alloys in the 00s, J. of Materi Eng and Perform, 14 (2005) 799-811.

[52] J. C. Williams, B. S. Hickman, and H. L. Marcus, The effect of omega phase on the mechanical properties of titanium alloys, MT, 2 (1971) 1913-1919.

[53] C. Leyens and M. Peters, *Titanium and titanium alloys: fundamentals and applications*: Wiley-VCH, 2003.

[54] M. Yan, M. S. Dargusch, T. Ebel, and M. Qian, A transmission electron microscopy and three-dimensional atom probe study of the oxygen-induced fine microstructural features in as-sintered Ti–6Al–4V and their impacts on ductility, Acta Materialia, 68 (2014) 196-206.

Chapter 6

A comparative study of near-β Ti alloys produced by cost effective blended elemental powder metallurgy technique

A comparative study of near-β Ti alloys produced by cost effective blended elemental powder metallurgy technique

Mansur Ahmed[a], Dmytro G. Savvakin[b], Orest M. Ivasishin[b], Elena V. Pereloma[a]

[a] School of Mechanical, Materials & Mechatronic Engineering, University of Wollongong, NSW 2522, Australia

[b] Institute for Metal Physics, National Academy of Sciences of Ukraine, UA-03142 Kiev, Ukraine

[c] Electron Microscopy Centre, University of Wollongong, NSW 2500, Australia

Keywords: powder Ti alloys, ageing, microstructure, mechanical properties.

Abstract:

Manufactured by blended elemental powder metallurgy technique and thermo-mechanically processed Ti-5Al-5Mo-5V-1Cr-1Fe and Ti-5Al-5Mo-5V-2Cr-1Fe (in wt.%) alloys were investigated to establish the microstructure-mechanical properties relationships during ageing. The ageing was performed at 650°C from 1 to up to 8 hrs. Thereafter, the alloys were characterised using scanning electron microscopy and tensile testing. The microstructures contain primary α, secondary α and retained β phase. The secondary α nucleated intragranularly and at the grain boundaries of recrystallised β during ageing. The obtained optimum combination of ultimate tensile strength and total elongation was after ageing for 1 and 2 hrs for both alloys. There is a variation in tensile properties of the alloys associated with the different volume fractions of α phase formed in these alloys, which is related to the difference in the Cr content.

Introduction:

Due to the excellent mechanical, thermal and bio-compatibility properties of titanium alloys, they have been used in aerospace, chemical and biomedical industries. The production cost of titanium components hinders the expansion of their applications. For the last decade, it has been attempted to reduce the manufacturing cost of titanium components by using alternative to casting processes. The blended elemental powder metallurgy (BEPM) is one of such processes [1, 2].

The authors have systematically studied two near-β titanium alloys with the nominal composition of Ti-5Al-5Mo-5V-1Cr-1Fe (Ti55511) and Ti-5Al-5Mo-5V-2Cr-1Fe (Ti55521) which are produced by BEPM technique. In our previous investigations [3, 4], microstructures of these alloys have been tailored by varying thermo-mechanical processing (TMP) parameters. In the present study, these TMP samples have been subjected to ageing. The effect of ageing on the microstructure and mechanical properties of Ti55511 alloy is discussed to some extent in the literature [5, 6] so far for the alloy being produced by either casting or wrought process. Thus, the aim of the present study is to investigate the microstructure and mechanical properties of BEPM-produced Ti55511 and Ti55521 alloys during ageing. Moreover, the influence of Cr addition is also determined.

Experiments and Materials:

In order to prepare the green compact of alloys, Ti powders containing 3.5 wt.% hydrogen were mixed with Mo, Cr, Fe (<40 μm) and 50Al-50V master alloy powders (40-63 μm). Afterwards, the green compacts were blended and die pressed under 650 MPa. The sintering of green compacts was accomplished in two steps: (i) heating to 1020°C for 1 h followed by (ii) heating to 1250°C for 6 h. Thereafter a Gleeble 3500 thermo-mechanical simulator was used to perform TMP under ~0.05 Pa vacuum to prevent oxidation and atmospheric contamination. The dimensions of cylindrical sample used for the TMP were 12 mm×ø8 mm. The samples were heated at $10°Cs^{-1}$ to 950°C, held for 120s, then cooled to 900°C at $35°Cs^{-1}$ where 25% deformation took place, then further cooled to 800°C at $35°Cs^{-1}$ where after 600s hold they were subjected to 60% reduction followed by cooling at $10°Cs^{-1}$ to room temperature. After the TMP, the samples were encapsulated into a quartz tube under a vacuum. Thereafter, the samples were heated at $0.25°Cs^{-1}$ to 650°C and aged for 1, 2, 4 and 8 hrs.

After the ageing, the samples were cut and prepared by using conventional metallographic techniques. Scanning electron microscopy (SEM) was used to investigate the microstructures of the alloys. SEM observations were conducted using a JEOL-JSM 7001F Field Emission Gun-Scanning Electron Microscope (FEG-SEM) operating at 15 kV voltage and 10 mm working distance. The sub-sized tensile samples were wire cut with the gauge length, width and thickness of 5.1 mm, 2.18 mm and 0.9 mm, respectively. Tensile tests were performed at room temperature using a μ-Tweezer Tensile Module at

a constant speed of 1.7 mm min^{-1}. The volume fraction of α has been measured by direct comparison method using the x-ray data.

Results and Discussion:

Mechanical properties and hardness:

Figs. 1a and 1b show the effect of ageing time on the ultimate tensile strength (UTS) and total elongation, correspondingly. The increasing trend for strength and the decreasing trend for elongation with respect to ageing time are related to the progress of α phase formation, thus follow the second phase precipitation hardening mechanism.

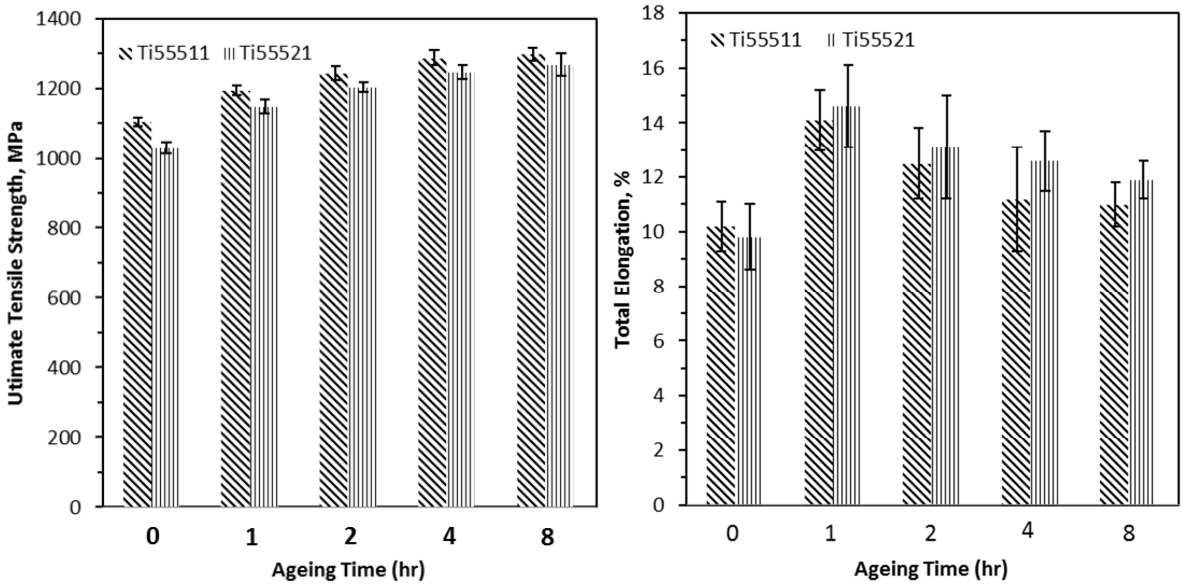

Fig.1 Variation of the utlimate tensile strength (a) and total elongation (b) with ageing time for both alloys.

The highest UTS for Ti55511 and Ti55521 are 1298 and 1267 MPa which are obtained for 8hrs sample. On the other hand, the maximum total elongation for Ti55511 and Ti55521 are 14 and 15% achieved for 1hr aged sample. The change in Vickers Hardness Number (VHN) with ageing time is shown in Fig. 2a. It is evident that VHN increases with the ageing time which implies increasing resistance to plastic deformation due to the increasing amount of α phase, as discussed below. Similar to UTS, highest hardness values were achieved after 8 hrs ageing, 379±4 and 374±8 VHN, for Ti55511 and Ti55521 alloy respectively. The obtained VHN are in good agreement with the literature [7].

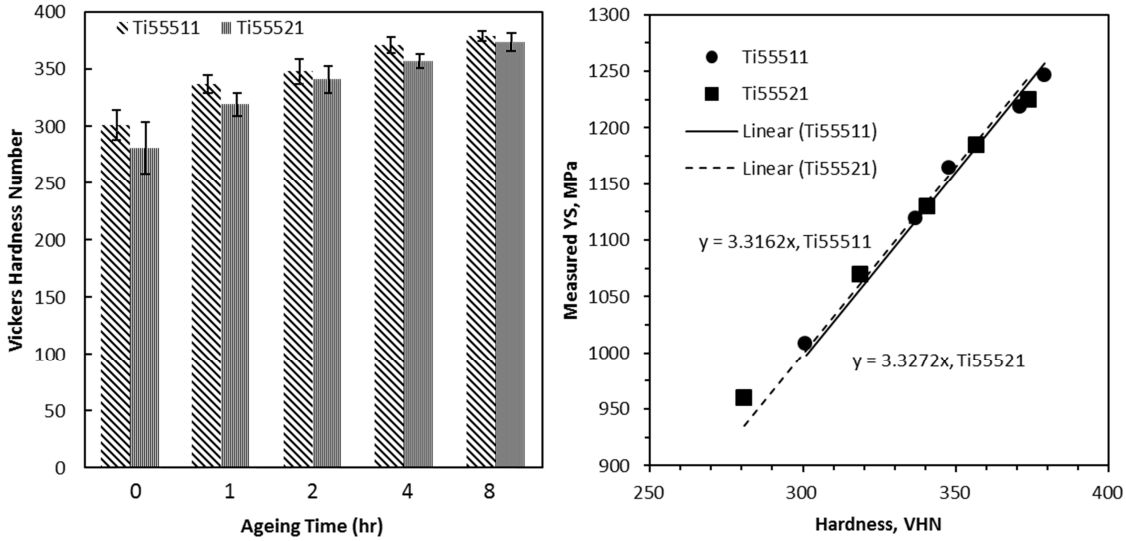

Fig.2 The effect of ageing time on Vickers hardness for both alloys (a) and the relationship between yield strength and hardness (b).

Thereafter, VHN and Yield strength (YS) are plotted in Fig. 2b in order to determine the empirical relation between VHN and YS for these alloys. The obtained correction factors for Ti55511 and Ti55521 are 3.32 and 3.33, respectively.

Microstructural characterisation:

The microstructures after TMP of both alloys consist of β and α phase having basket weave and colony type morphology (Fig. 3). The TMP microstructures include fragmented grain boundary α, partially recrystallised β grains, intra-granular α and fine α phase. All categories of α present in TMP condition terms as primary α in the present study. The volume fractions of primary α phase for Ti55511 and Ti55521 alloys after TMP are 26 and 22%, respectively [4]. Figures 4 and 5 show the microstructures of Ti55511 and Ti55521 alloys after ageing at 650°C for 1, 2, 4 and 8 hrs, respectively. The amount of α produced as a function of ageing time is depicted in Fig. 6. The microstructures of the alloys after ageing include secondary α in addition to all other TMP features. It can also be noted that some of the primary α change their shape from lamellae to globular during ageing through decreasing surface-to-volume ratio.

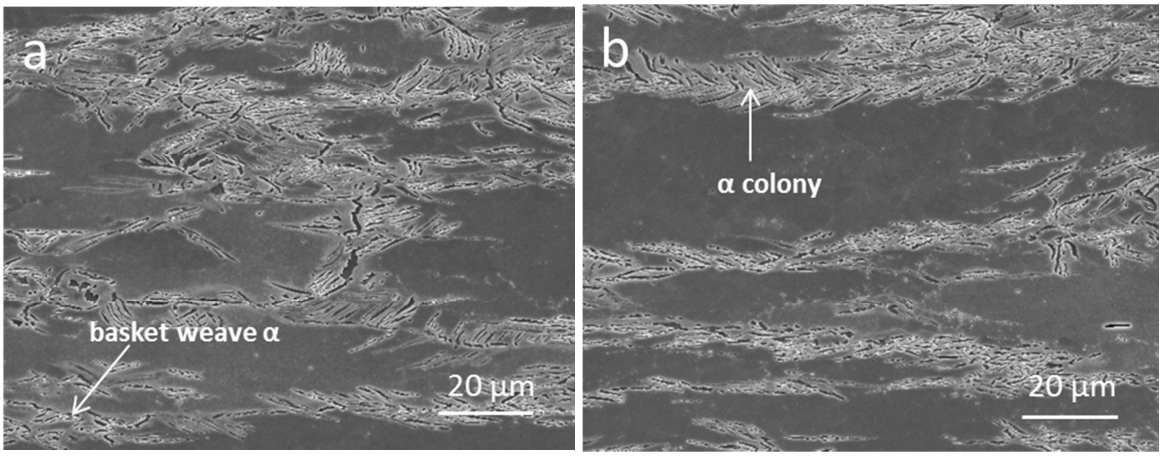

Fig. 3 Secondary electron (SE) micrographs of Ti55511 (a) and Ti55521 (b) after TMP.

These globular-shaped primary α positively affect the ductility of the alloys [8]. The morphology of secondary α formed during ageing is typically a basket weave with some colonies. It is obvious that recrystallisation of deformed β phase happens during ageing in both alloys. The similar results indicating the recrystallisation of β phase after cold rolling are reported in [9]. It is also clear that secondary α nucleated both intra-granularly (large extent) and at grain boundaries of recrystallised β phase (some extent) which is similar to other investigations [7, 9]. The partial recrystallisation of β

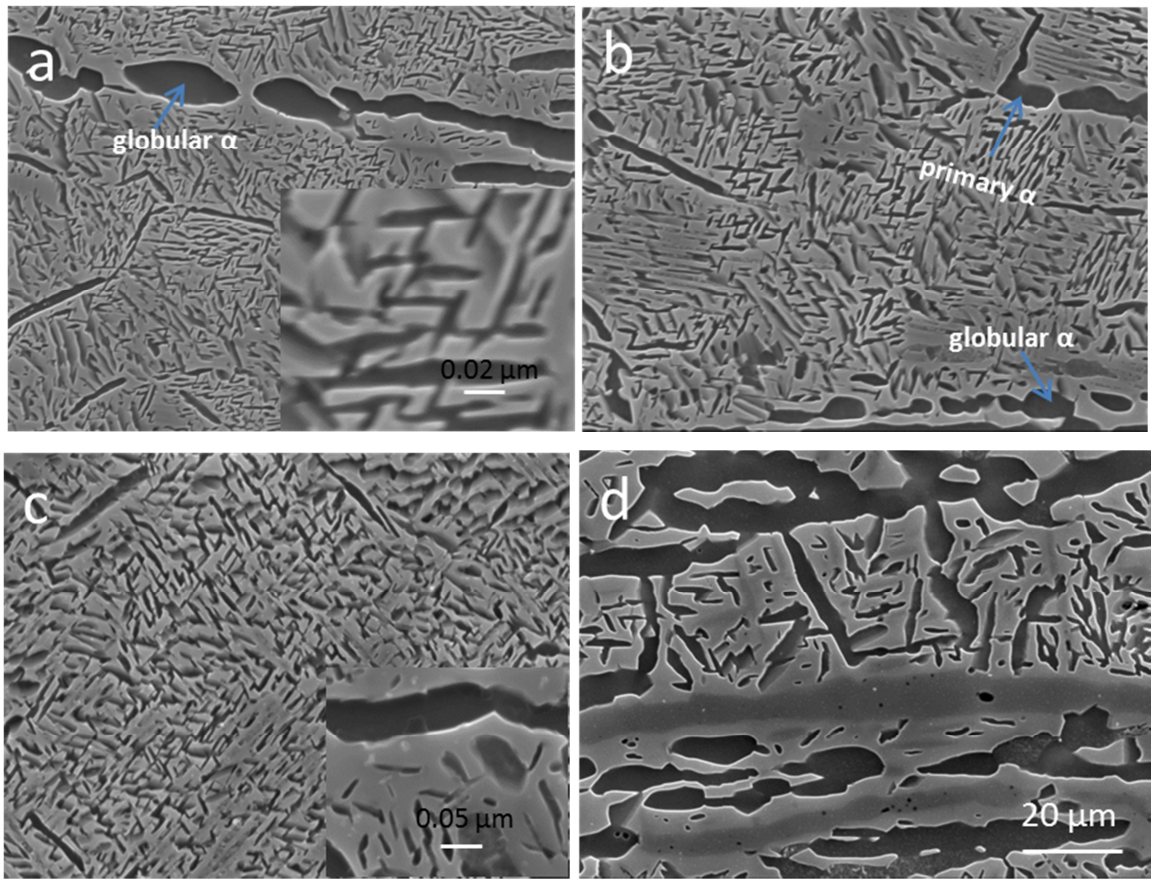

Fig. 4 The SE microstructures of Ti55511 alloy after ageing for 1 hr (a), 2 hrs (b), 4 hrs (c) and 8 hrs (d). The inset of Fig. 4a and 4c show the secondary α.

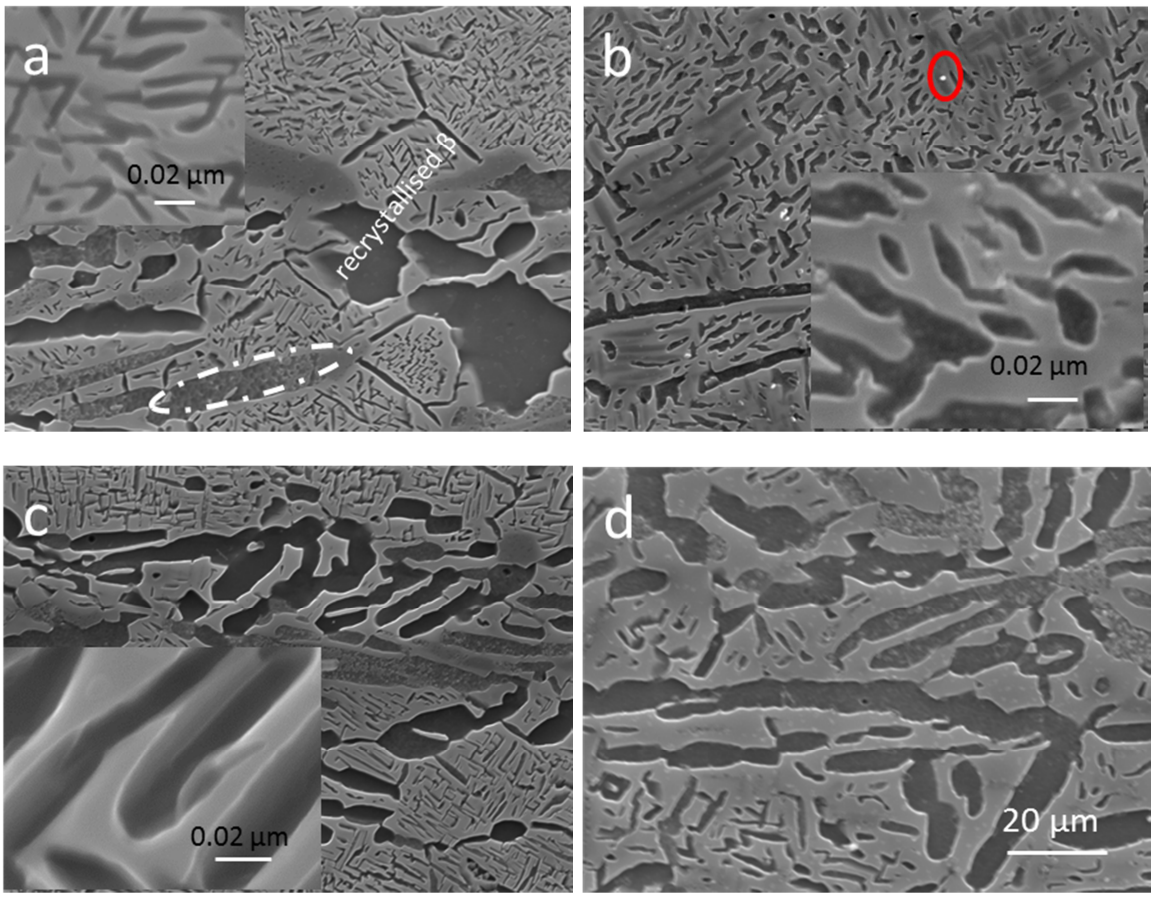

Fig. 5 The SE microstructures of Ti55521 alloy after ageing for 1 hr (a), 2hrs (b), 4 hrs (c) and 8 hrs (d). The red circle in Fig. 5b indicates the TiC particle and the insets in Fig 5 (a,b,c) show the enlarged view of secondary α. White ellipse in Fig. 5a denotes an incomplete phase transformation of α.

grains occurred during cooling to room temperature during TMP resulting in less amount of α nucleated at grain boundaries. The width and length of fine secondary α for the aged up to 4hrs samples are 0.02±0.01 μm and ~0.6±0.2 μm, correspondingly. On the other hand, width and length of fine secondary α in the sample aged for 8 hrs increased to~0.05±0.03 and 0.6±0.3 μm due to the coarsening. Furthermore, some small white particles can be observed in the aged microstructures of both alloys (Fig 5b). Moiseev et al. [10, 11] clearly indicated that these particles are titanium carbide. Furthermore, incomplete phase transformation in a single α lamellae is another feature in the microstructures (Fig. 5a and b). The segregation of interstitials, e.g. C and/or O, is responsible for this event [4]. As C and O are α stabilisers, formation of their segregation

reduces concentration of α stabilisers in the surrounding β matrix phase. Thus, in such local region β matrix is more stable (with increased Mo equivalent and, hence, the decreased β-transus temperature), which results in a delay in the β→α transformation compared to the area containing no C and/or O segregation.

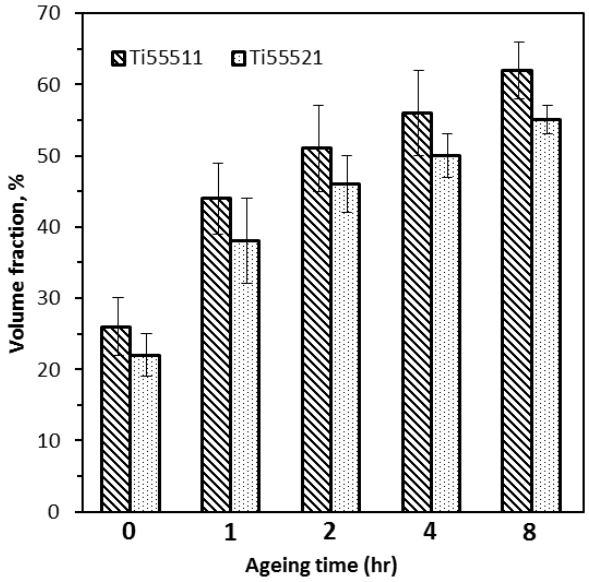

Fig. 6 The change in the volume fraction of α phase in both alloys with the ageing time.

It is reported in [8, 10, 12-15] that UTS and elongation for Ti55511 and Ti5553 alloys are in the range of 1100-1250 MPa and 12-20%. The best combination of strength and ductility is deemed to be achieved after 1 hr ageing. After 2 hrs ageing, the combination of strength and ductility is still very good with UTS in the range of 1203-1243 MPa and total elongation of ~12%. Thus, it can be claimed that 1 and 2 hrs are the optimal ageing times at 650°C displaying the best balance of UTS and elongation.

The slow cooling during TMP ($10°Cs^{-1}$) and slow heating ($0.25°Cs^{-1}$) to ageing temperature was the underlying reason obtaining such a good combination of UTS (1150-1250 MPa) and elongation (12.5-15%) in the present study. During slow cooling to TMP and slow heating to ageing temperature, ω precipitates which later on acts as nucleation sites for fine α phase [9]. These fine and well-dispersed intragranular α enhance both the strength and elongation [5, 9]. In contrast, two step ageing is usually performed in order to obtain such a good combination of strength and elongation where low temperature ageing provides ω phase and then fine α is produced by high temperature ageing [16]. The reason for the difference in mechanical properties (strength, elongation, hardness) between the alloys is the variation in α volume fraction.

As could be seen in Fig. 6 the Ti55521 has less amount of α compared to the Ti55511 alloy. This could be explained based on the β→α phase transformation kinetics of these alloys. The additional (1%) Cr in Ti55521 lowers the β-transus temperature compared to that in the Ti55511 [17]. Hence, in addition to higher volume fraction of β phase in α+β condition, β phase in the Ti55521 becomes more stable than in the Ti55511 at any temperature and basically responds slower to phase transformation than that in Ti55521 alloy.

Conclusions:

The following conclusions can be drawn from this study:

- The strength (UTS, YS) of both alloys increases and the total elongation reduces with ageing time and these changes are directly proportional to the volume fraction of α phase present in the microstructure.
- Hardness of both alloys increases with the ageing time and the empirical relation between VHN and YS has been established with correlation factors of 3.32 and 3.33 for Ti55511and Ti55521 alloy, respectively.
- It is suggested that a good combination of strength and elongation is due to the slow heating rate to ageing temperature and slow cooling rate during TMP, which allow nucleation of ω which later on turns into fine α phase during ageing.
- Increase in Cr content reduces the amount of α phase in the alloy leading to the lower strength.

References:

[1] F.H. Froes, D. Eylon, Powder metallurgy of titanium alloys, Int.Mater. Rev. 35 (1990) 162-184.

[2] T. Fujita, A. Ogawa, C. Ouchi, H. Tajima, Microstructure and properties of titanium alloy produced in the newly developed blended elemental powder metallurgy process, Mater. Sci. Eng. A 213 (1996) 148-153.

[3] M. Ahmed, A.A. Gazder, D.G. Savvakin, O.M. Ivasishin, E.V. Pereloma, Microstructure evolution and alloying elements distribution between the phases in powder near-β titanium alloys during thermo-mechanical processing, J. Mater. Sci. 47 (2012) 7013-7025.

[4] M. Ahmed, D.G. Savvakin, O.M. Ivasishin, E.V. Pereloma, The effect of cooling rates on the microstructure and mechanical properties of thermo-mechanically processed Ti–Al–Mo–V–Cr–Fe alloys, Mater. Sci. Eng. A 576 (2013) 167-177.

[5] O.M. Ivasishin, P.E. Markovsky, Y.V. Matviychuk, S.L. Semiatin, C.H. Ward, S. Fox, A comparative study of the mechanical properties of high-strength β-titanium alloys, J. Alloys Compds. 457 (2008) 296-309.

[6] O.M. Ivasishin, P.E. Markovsky, Enhancing the mechanical properties of titanium alloys with rapid heat treatment, JOM 48 (1996) 48-52.

[7] S.-z. Zhang, Z.-q. Liu, G.-d. Wang, L.-q. Chen, X.-h. Liu, R. Yang, Microstructural evolution during aging of Ti-5Al-5Mo-5V-1Cr-1Fe alloy, J. Cent. South Univ. Technol. 16 (2009) 354-359.

[8] J. Huang, Z. Wang, K. Xue, Cyclic deformation response and micromechanisms of Ti alloy Ti–5Al–5V–5Mo–3Cr–0.5Fe, Mater. Sci. Eng. A 528 (2011) 8723-8732.

[9] T. Furuhara, T. Maki, T. Makino, Microstructure control by thermomechanical processing in β-Ti–15–3 alloy, J. Mater. Process. Technol. 117 (2001) 318-323.

[10] V.N. Moiseev, N.V. Sysoeva, I.G. Polyakova, Effect of additional carbon and boron alloying on the structure and mechanical properties of alloy VT22, Met. Sci. Heat Treat. 40 (1998) 107-111.

[11] N.V. Sysoeva, V.N. Moiseev, High-Strength Granulated Titanium Alloys with the Intermetallic Type of Hardening, Met. Sci. Heat Treat. 44 (2002) 304-308.

[12] V.N. Moiseev, Beta-titanium alloys and prospects of their development, Met. Sci. Heat Treat. 40 (1998) 482-485.

[13] V.N. Moiseev, High-strength titanium alloys for large parts of aircraft engines, Met. Sci. Heat Treat. 42 (2000) 81-83.

[14] S.L. Nyakana, J.C. Fanning, R.R. Boyer, Quick reference guide for β titanium alloys in the 00s, J. Mater. Eng. Perform. 14 (2005) 799-811.

[15] J.C. Fanning, Properties of TIMETAL 555 (Ti-5Al-5Mo-5V-3Cr-0.6Fe), J. Mater. Eng. Perform. 14 (2005) 788-791.

[16] M. Okada, Acceleration of alpha precipitation and strengthing of Ti-15V-3Cr-3Sn-3Al alloy by two step aging, Tetsu-to-Hagane 76 (1990) 614.

[17] I. Weiss, S.L. Semiatin, Thermomechanical processing of beta titanium alloys—an overview, Mater. Sci. Eng. A 243 (1998) 46-65.

Chapter 7

The influence of β phase stability on deformation mode and compressive mechanical properties of Ti-10V-3Fe-3Al alloy

Available online at www.sciencedirect.com

ScienceDirect

Acta Materialia 84 (2015) 124–135

Acta MATERIALIA

www.elsevier.com/locate/actamat

The influence of β phase stability on deformation mode and compressive mechanical properties of Ti–10V–3Fe–3Al alloy

Mansur Ahmed,[a,*] David Wexler,[a,b] Gilberto Casillas,[b] Orest M. Ivasishin[c] and Elena V. Pereloma[a,b]

[a]*School of Mechanical, Materials and Mechatronic Engineering, University of Wollongong, Wollongong, NSW 2522, Australia*
[b]*UOW Electron Microscopy Centre, University of Wollongong, Wollongong, NSW 2500, Australia*
[c]*Institute for Metal Physics, National Academy of Sciences of Ukraine, UA-03142 Kiev, Ukraine*

Received 30 August 2014; accepted 14 October 2014

Abstract—A metastable β-Ti alloy, Ti–10V–3Fe–3Al (wt.%), was subjected to thermomechanical processing (TMP), where the temperature of isothermal holding in the α + β phase field was varied in order to change the volume fraction of the α phase and, correspondingly, the β phase stability. Following TMP, compression tests were performed at room temperature to evaluate the deformation mode. Microstructural features induced by compression were identified using transmission electron microscopy. It was found that {332}⟨113⟩β deformation twinning along with stress-induced products (α″ martensite and ω lamellae) and slip were operational in the least stable β. The co-existence of {332}⟨113⟩β and {112}⟨111⟩β twinning was found at intermediate β stability along with other deformation products. With further increasing of β phase stability, no {332}⟨113⟩β twinning was detected whereas other deformation modes remained unchanged. In stable β phase, dislocation glide was the only deformation mode to be found. It was revealed that triggering stress required inducing the deformation products increases with the β phase stability. Based on the findings, a modification of the lower portion of the Bo–Md phase stability diagram is proposed.

Keywords: Ti alloys; Compression; Twinning; Stress-induced martensite; β phase stability

1. Introduction

Metals typically deform by different mechanisms: twinning, deformation-induced martensite, dislocation glide on slip planes or a combination of these. These deformation mechanisms strongly rely on the matrix condition: on the one hand, on the critical stresses that trigger slip and twinning and, on the other hand, on the ability of a metastable matrix to transform into martensite [1]. The mechanical behavior of the materials largely depends on the interaction between the different deformation mechanisms. In the case of ferrous alloys, the influence of external load and plastic strain on the martensitic and twinning transformation has been extensively studied, where the phase transformation kinetics and the mechanical behavior resulting in transformation-induced twinning and plasticity are discussed [2–4].

In contrast, limited research has so far been conducted to understand the deformation mechanism in Ti alloys of the metastable β class. These metastable β Ti alloys can be divided into two categories: β phase with α phase prior to deformation or β phase without α prior to deformation. The deformation mechanisms of metastable β Ti alloys without any α phase, e.g., Ti–Nb–Ta–Zr–O (gum metal series) [5–13], Ti–Mo [14–17], Ti–V [15,16] and Ti–15V–3Cr–3Sn–3Al [18,19] alloys, have been revealed. For the Ti–Nb–Ta–Zr–O system, {332} ⟨113⟩β deformation twinning [10] and stress-induced α″ martensite [9] were observed in Ti–21Nb–0.7Ta–2Zr–1.2O (at.%) alloy with unstable β. In Ti–23Nb–0.7Ta–2Zr–1.2O (at.%) alloy (gum metal), stress-induced α″ martensite phase, 1/2⟨111⟩ dislocations slipping, stress-induced ω phase and {112} ⟨111⟩β deformation twinning were found [11–13]. Kuramoto et al. [10] found only dislocation glide in Ti–25Nb–0.7Ta–2Zr–1.2O (at.%) alloy. It was found in Ref. [5] that both {332}⟨113⟩β and {112} ⟨111⟩β twinning systems co-exist in Ti–22.4Nb–0.73Ta–2Zr–1.34O (at.%), an alloy with intermediate β phase stability. The above results indicate that the deformation mechanism operative in the Ti–Nb–Ta–Zr–O system is dependent on the β stability. For the Ti–Mo system, Hanada et al. [15,16] reported that the formation of {332}⟨113⟩β deformation twinning is accompanied by stress-induced ω phase formation when β phase contains 11–14 wt.% Mo. It is also mentioned that {332}⟨113⟩ β deformation twins tend to appear in Ti–Mo alloys having a ratio of the lattice *d*-spacing, $d_{0002\omega}/d_{222\beta}$, larger than 0.66. Sun et al. [8] recently reported that {332}⟨113⟩β and {112}⟨111⟩β deformation twinning, primary stress-induced α″ martensite and

* Corresponding author. Tel.: +61 242215798; fax: +61 2 4221 3662; e-mail: ma960@uowmail.edu.au

http://dx.doi.org/10.1016/j.actamat.2014.10.043
1359-6462/

stress-induced ω are formed in the early stage of deformation ($\varepsilon = \sim 0.04$) in Ti–12Mo alloy. With further straining, secondary $\{3\,3\,2\}\langle 1\,1\,3\rangle\beta$ twinning and secondary stress-induced α″ martensite developed [5,8]. For Ti–15V–3Cr–3Sn–3Al alloy, Furuhara et al. [18] observed $\{3\,3\,2\}\langle 1\,1\,3\rangle\beta$ deformation twinning, secondary twinning with the $\{3\,3\,2\}\langle 1\,1\,3\rangle\beta$ system and dislocation loops.

On the other hand, only two metastable β Ti alloys containing α phase, Ti–5Al–2Sn–5Zr–4Mo–2Cr–1Fe (β-Cez) [1,20–22] and Ti–10V–2Fe–3Al [23–28], have been studied to understand the deformation mechanism operative in this type of metastable β. In such Ti–10V–2Fe–3Al alloy (wt.%), Duerig et al. [23] mentioned that β phase transforms into α″ martensite phase with orthorhombic structure upon tension. Such a $\beta \rightarrow \alpha''$ phase transformation is induced by stress, which is accompanied by lattice strains in the three principal lattice directions of $\varepsilon_1 = -7.1\%$, $\varepsilon_2 = +7.2\%$ and $\varepsilon_3 = +1.1\%$. It was reported that the stress required to induce α″ martensite depends on the β domain/grain size and β stability [1,20]. In β-Cez alloy, the deformation mode changes from stress-induced α″ martensite to slip with increasing β stability (increasing the fraction of α precipitates). Neelakantan et al. [28] also explained that it becomes difficult to transform the β phase to martensite with increasing the α phase fraction in Ti–10V–2Fe–3Al alloy as increasing the α fraction increases β phase stability and decreases the effective β domain size. Li et al. [24,29] has hypothesized that the alloy containing more than 50% of α phase does not transform into the α″ martensite by external stress. It is pertinent to note that neither β deformation twinning nor stress-induced ω was found in the aforementioned studies in Ti–10V–2Fe–3Al and β-Cez alloys.

A metastable β Ti–10V–3Fe–3Al (wt.%) alloy, which is a modified form of the more common alloy, Ti–10V–2Fe–3Al (wt.%), is investigated in the present study. The alloy was produced by the cost-effective blended elemental powder metallurgy technique, as described in Ref. [30]. The Fe content in the studied alloy has deliberately been increased by 1 wt.% to improve the powder compact density during sintering as Fe has the fastest diffusivity among the elements used [30]. In addition, the Fe content further increases the β stability through increasing the Mo equivalent. Therefore, the present study aims to investigate the evolution of the deformation mechanisms with respect to the β phase stability in a metastable β Ti alloy containing α phase.

2. Experiments

A Gleeble 3500 thermomechanical simulator was used for processing the alloy after sintering. The dimensions of the cylindrical samples were 10 mm in length by 8 mm in diameter. Thermomechanical processing consisted of heating at 10 °C s^{-1} to 900 °C (β phase region), holding for 300 s then lowering the temperature to 850 °C at 20 °C s^{-1} where 40% reduction in length was imparted. Thereafter, the specimens were cooled at 20 °C s^{-1} to the temperature in the α + β phase region (725, 700, 675, 650, 625 or 500 °C), held for 300 s and then water-quenched. The samples will be hereafter referred to as 725, 700, 675, 650, 625 and 500 °C in the text.

Samples were then machined to reduce the size to 7 mm length and 4 mm diameter. The uniaxial compression test was performed at room temperature using Gleeble 3500. Each sample was strained to 0.4 (true strain) at a (constant) strain rate of 10^{-3} s^{-1}.

The samples were cut perpendicular to the compression axis, prepared using metallographic techniques and etched using Kroll reagent (2HF: $5HNO_3$:$93H_2O$). The polished surfaces were then observed under a Leica optical microscope. Thin films for transmission electron microscopy (TEM) were prepared using twin-jet electropolishing. The electrolyte comprised of 5% $HClO_4$ in CH_3OH. TEM observations were performed on a JEOL JEM 2011 analytical instrument using an accelerating voltage at 200 kV. High resolution scanning TEM (HRSTEM) was carried out using a probe-corrected JEOL ARM200F operated at 200 kV and equipped with a cold field emission gun. High-angle annular dark field (HAADF) images were acquired with 50 and 180 mrad inner and outer collection angles, respectively, while bright field (BF) images used 11 mrad collection angles. Both types of images were recorded with a dwell time of 38 μs and convergence semi-angle of 25 mrad, resulting in a probe current of 35 pA. The microscope features a Centurio SSD energy dispersive X-ray spectrometer (EDS) detector with an active area of 100 mm^2, which is equivalent to a collection solid angle of 0.98 sr. EDS spectra were acquired with a probe current of 290 pA.

3. Experimental results

3.1. Mechanical properties and optical microscopy

Fig. 1a shows the compression test response at ambient temperature (~20 °C) for various conditions. These stress–strain curves exhibit a very slowly raising stress region (called a stress plateau [5]), which is ascribed to stress-induced martensite formation and β mechanical twinning [5,20], except for the 500 °C sample. The stress required to induce such a plateau on a stress–strain curve will hereafter be referred to as the "triggering stress". It is defined as the intersection of the elastic modulus tangent and the tangential extension of the slope of the slowly raising stress region (as illustrated in the inset of Fig. 1a). Similar plateau on stress–strain curves have been reported in Ti–22.4Nb–0.73Ta–2Zr–1.34O (at.%) [5] and Ti–10V–2Al–3Fe [23]. Triggering stresses ranging from ~180 to 310 MPa (Fig. 1a, Table 1) were found to be dependent upon the heat-treatment temperature in the α + β phase field, e.g., stress increases with the lowering of temperature.

Fig. 1b shows the corresponding work-hardening rate for 725, 625 and 500 °C samples. It is evident that work-hardening rate (for 725 and 625 °C samples) first decreases in the elasto-plastic transition region, then starts increasing from the elastic limit to a certain value of strain and then again abruptly drops. Thus, similar to the investigations [17,31], three stages of work-hardening rate are found for 725 and 625 °C samples. The strain value (0.1 for 725 and 0.08 for 625 °C samples) where the work-hardening rate is maximum depends on the α volume. Although the trend in work-hardening rate is similar to the ones observed for metastable β Ti alloys in Refs. [17,31], much higher maximum work-hardening rates achieved in the present study could be attributed to the presence of α phase. However, it has been mentioned in Ref. [31] that deformation twinning and martensitic transformation together with their

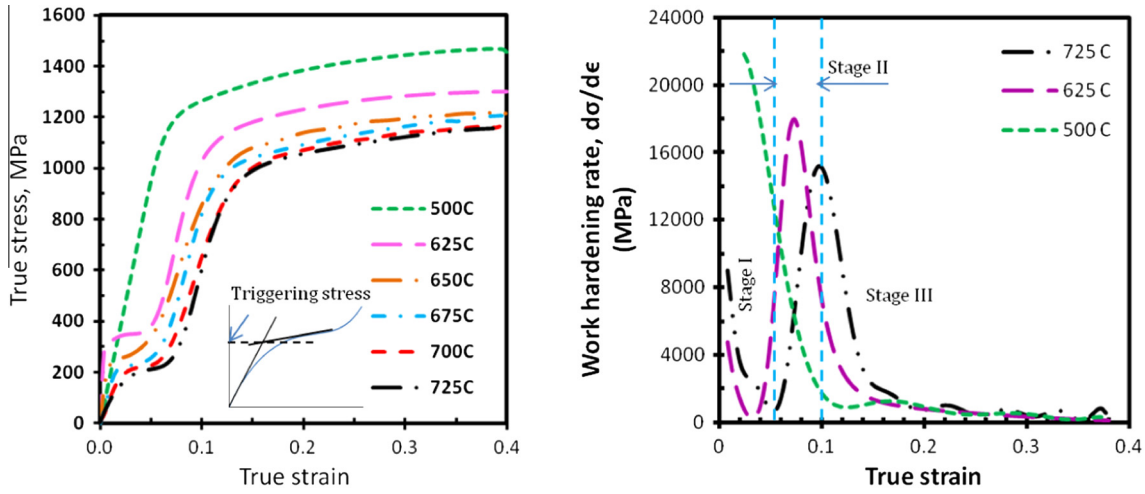

Fig. 1. Ambient temperature compression test results (a) stress–strain curves for all the experimental conditions where inset shows the intersection of elastic modulus and strain plateau; (b) corresponding work-hardening rate behavior for 725, 625 and 500 °C samples; stage indication by using dashed lines was only for 725 °C sample.

Table 1. The amount of prior α phase and triggering stress with respect to the samples processed at various temperatures.

Temperature in α + β phase field (°C)	Amount of prior α phase (%)	Triggering stress (MPa)
725	9 ± 3	180 ± 3
700	14 ± 2	203 ± 5
675	21 ± 3	228 ± 4
650	30 ± 2	248 ± 6
625	38 ± 4	309 ± 4
500	62 ± 4	N/A

constant interactions are responsible for the continuous increase of work-hardening rate during stage II. On the other hand, only two stages of work-hardening rate are found for 500 °C sample as described in the previous study [32]. These two stages are exponential decrease in work-hardening rate followed by a slower, nearly plateauing decrease. In contrast to the samples showing twinning and martensitic phase transformation (725 and 625 °C), the 500 °C sample does not contain stage II where work-hardening rate increases.

Fig. 2a–c shows optical micrographs after room temperature compression. The micrographs (Fig. 2a and b) for the 725 and 700 °C samples demonstrate similar microstructures, with parallel thin lines and thick laths induced by compression readily observed in these two microstructures. These lines are characteristics of either twins or stress-induced α″ martensite [5,8]. It is pertinent to mention that these lines (twin or stress-induced α″ martensite) evolve from β grain boundaries and are stopped at the grain boundary as well. Furthermore, a few small parallel lines inside the thick laths are also visible in the samples (Fig. 2a and d). According to Refs. [14,17,18], these small lines may be secondary twins, or secondary α″ or stress-induced ω plates located inside the primary products. It should be stated that each β grain deforms differently, as shown in Fig. 2c, which might be a result of their orientation, as was pointed out in Ref. [17]. Representative secondary electron images (Fig. 2d and e) taken from the 700 °C sample are shown to identify more clearly the aforementioned features. Scanning electron microscopy (SEM) imaging also highlights the presence of some long lines crossing each other, which might be either twins or α″ martensite (Fig. 2e). Furuhara et al. [18,19] mentioned the appearance of the similar twinning induced by cold rolling in a Ti–15V–3Cr–3Sn–3Al alloy.

On the other hand, the 675, 650 and 625 °C samples show near-identical microstructures, which are different from the 725–700 °C samples. Representative optical micrographs for the 675 and 625 °C samples are displayed in Fig. 3a and b, respectively. These microstructures contain differently etched (light) α-like small features in addition to α phase (Fig. 3a and b). It is worth mentioning that some thick laths belonging to twins were also detected in the 675 and 650 °C samples (inset of Fig. 3a). No such laths were observed in the 625 °C sample. However, the microstructure consists of only α phase in a β matrix in the 500 °C sample (Fig. 3c). All the experimental conditions contain different amounts of α phase as the samples were held at different temperatures in the α + β phase region. The area fraction of α phase calculated from optical microstructures is found to increase with lowering of the temperature. The calculated area fractions are 9%, 14%, 21%, 30%, 38% and 62% for the 725, 700, 675, 650, 625 and 500 °C samples, respectively (Table 1). TEM has been used to identify precisely the aforementioned compression-induced products, as described below.

3.2. Microstructural characterization using TEM and STEM

By morphology, ω phase found in the present study can be divided into two types: spheroidal athermal ω, which forms during rapid quenching from α + β temperature field, and ω induced by compression in the form of thin long lamellae. While the athermal ω is randomly distributed in the β matrix (Fig. 4a), the latter is present not only in β matrix (Fig. 4b–d) but also inside the $\{3\,3\,2\}\langle 1\,1\,3\rangle\beta$ deformation twins (Fig. 4e). All these ω in the present study show the typical $(1\,1\,1)_\beta//(0\,0\,0\,1)_\omega$ and $[0\,1\,1]_\beta//[1\,1\bar{2}0]_\omega$ orientation relationship

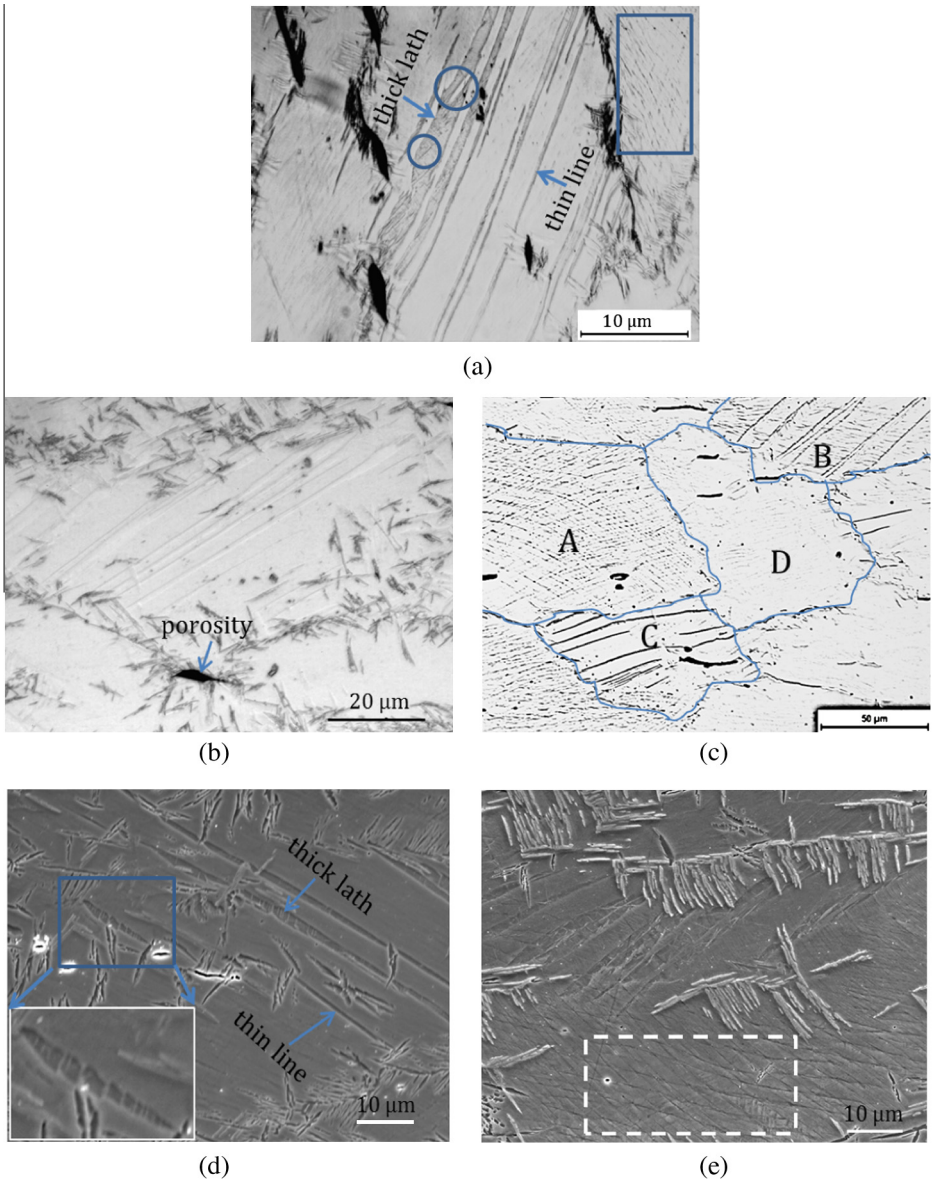

Fig. 2. (a, b) Representative optical microstructures for the samples heat-treated at 725 and 700 °C respectively. The circles within the thick lath in (a) represent small parallel lines. The rectangle box in (a) shows thin lines intersecting each other in a different β grain. Porosity is also shown by an arrow in (b). (c) Optical microstructure of the sample processed at 725 °C showing several β grains with different deformation behavior. (d, e) Representative SEM microstructures showing the thick laths and thin lines formed after deformation in 700 °C sample. The inset in (d) shows an enlarged view of a thick lath containing small parallel thin lines. The rectangular box in (e) shows thin lines of deformation products intersecting each other in β matrix.

(Fig. 4c–e). Fig. 5a shows a BF image of β deformation twinning taken from the sample processed at 725 °C. A selected area diffraction pattern (SADP) along the $[1\,1\,0]_{\beta T}//[1\,1\,0]_{\beta M}$ zone axis (where T and M indicate twinning and matrix, respectively) confirms the presence of a $\{3\,3\,2\}\langle 1\,1\,3\rangle\beta$ twinning system (Fig. 5b). A DF image of twins in Fig. 5a is shown in Fig. 5c. It is important to mention that we are reporting twinning observation in a metastable β Ti alloy containing α phase for the first time. The HRSTEM image in Fig. 5d further confirms the occurrence of $\{3\,3\,2\}\langle 1\,1\,3\rangle$ β twinning. The sample heat-treated at 700 °C also shows the same twinning system. Fig. 6a shows a BF image of the stress-induced α″ martensite needles with corresponding DF image shown in Fig. 6b. This needle-like martensite will hereafter be referred to as primary stress-induced α″ martensite. A SADP captured along the $[0\,1\,1]_{\beta}$ zone axis shows reflections characteristic of orthorhombic structure (α″) in addition to the spots belonging to body centred cubic (bcc) structure (Fig. 6c). A schematic of the relation between β and stress-induced α″ martensite is shown in Fig. 6d. Similar to Refs. [14,17], another type of stress-induced α″ martensite is noticed inside the primary twins (Fig. 7a). A SADP along the $[0\,1\,2]_{\beta}$ zone axis in Fig. 7b shows the reflections with characteristics of orthorhombic structure, i.e., stress-induced α″ phase. According to previous works [17,18], these are called secondary stress-induced α″ martensite. All the aforementioned features are also observed in the sample heat-treated at 700 °C.

Representative TEM micrographs of the 675–625 °C samples are shown in Figs. 8 and 9. The BF image in

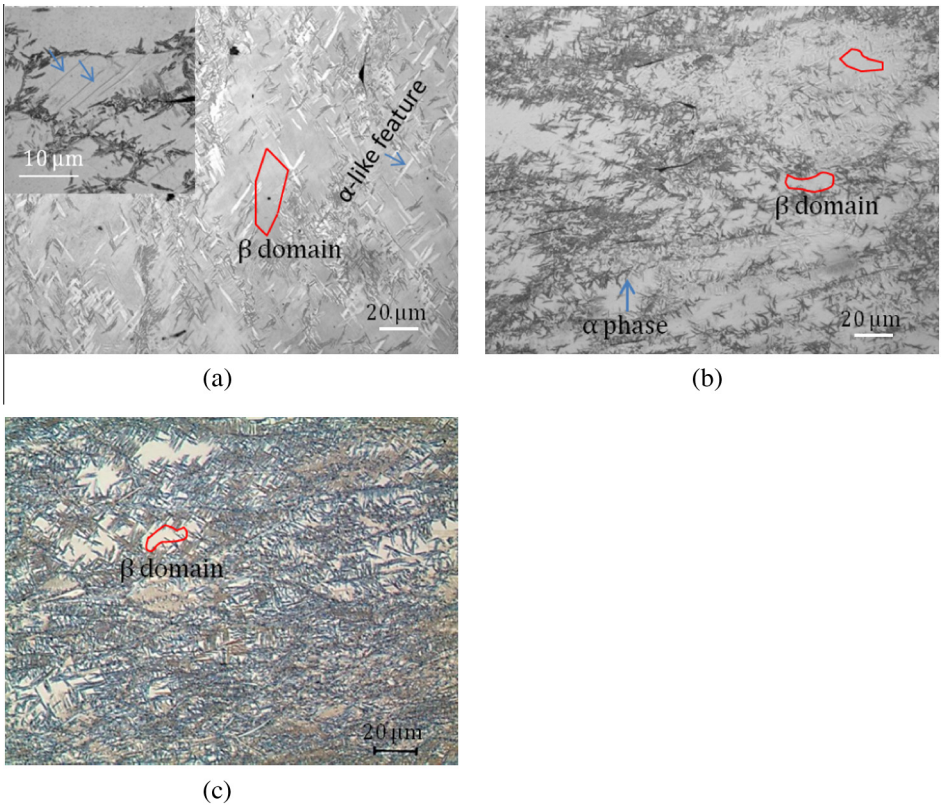

Fig. 3. Representative optical microstructures of deformed samples heat treated at (a) 675, (b) 625 and (c) 500 °C, respectively. The free-form sketch in each image shows the active β domain size. The inset in (a) delineates the thick laths in the 675 °C sample.

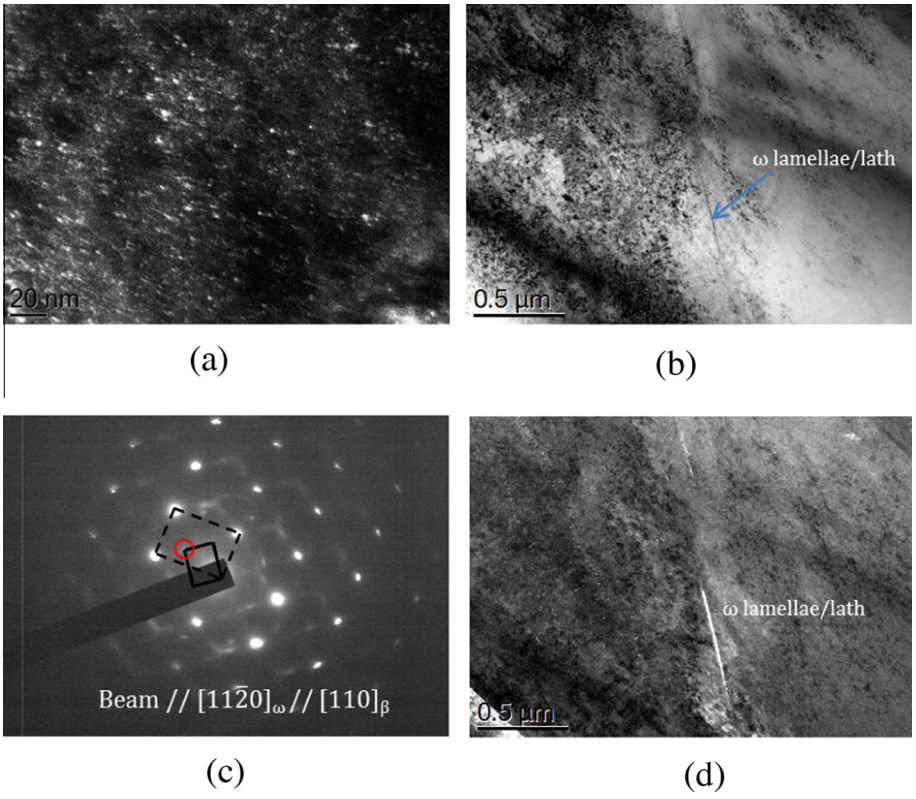

Fig. 4. ω Phase formation: (a) dark field (DF) TEM image showing athermal ω particles in β phase in the 725 °C sample. (b) Bright field (BF) image showing the needle-shaped ω lamellae. (c) A SADP pattern along $[1\,1\,0]_\beta$//$[11\bar{2}0]_\omega$ zone axis illustrating the orientation relationship between ω and β. (d) DF image taken from the circled spot in (c) showing the stress-induced ω. (e) A HRSTEM image of a twin and the corresponding FFT diagram (below) showing the ω reflections (red circled). Areas of ω lattice are circled and shown by the arrangement of supercells. (For interpretation of the references to color in this figure legend, the reader is referred to the web version of this article.)

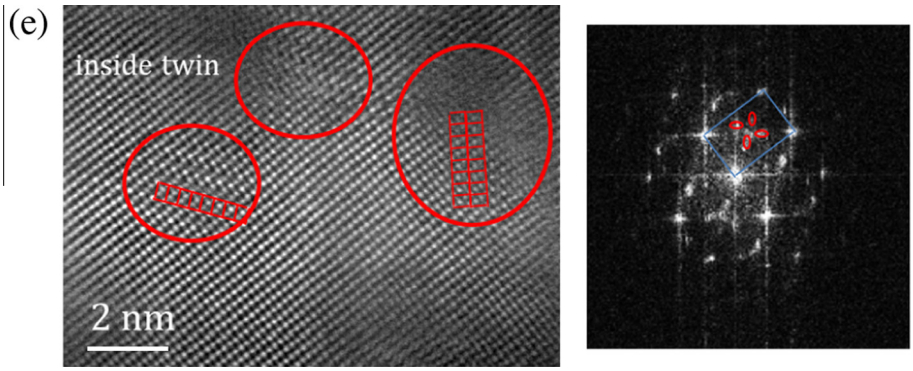

Fig 4. *(continued)*

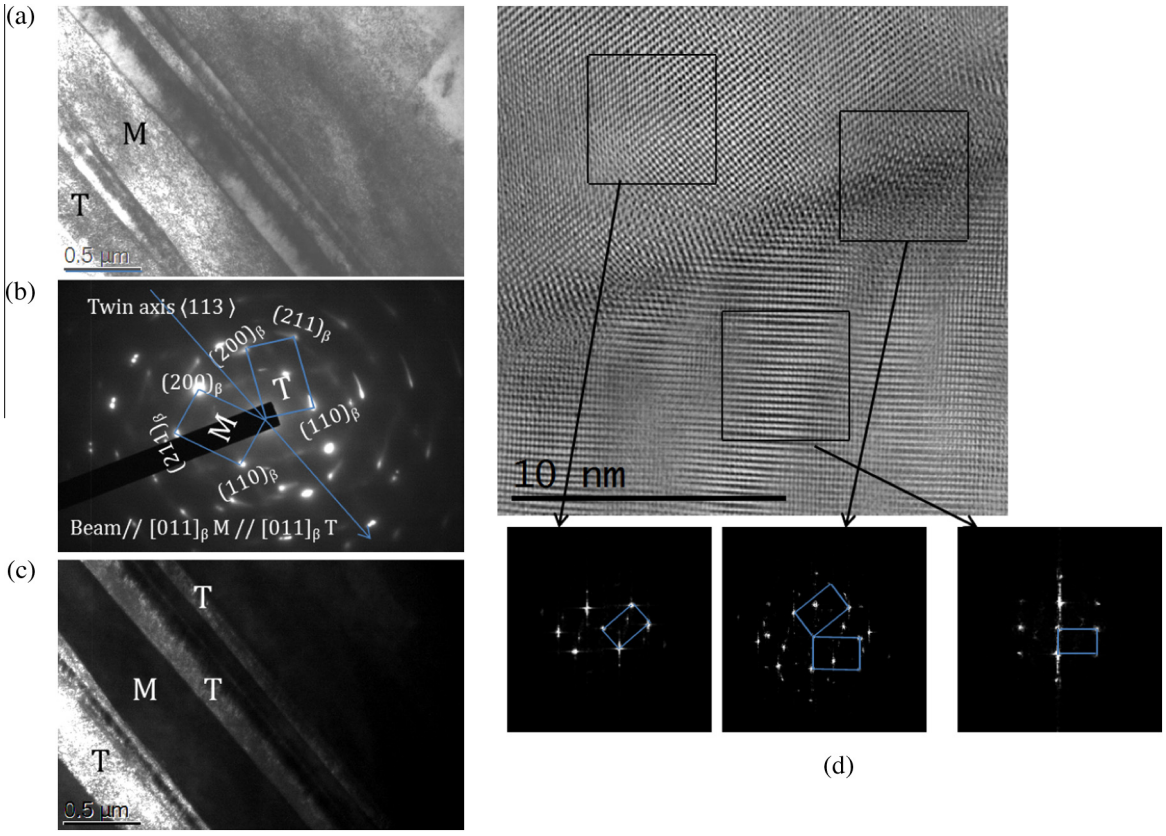

Fig. 5. Twin formation: (a) BF image of $\{332\}\langle 113\rangle\beta$ twins where letters T and M denote the twin and matrix, respectively. (b) A SADP pattern along the $[110]_\beta$ zone axis showing both the twin and matrix lattices. (c) A DF image shows the twins using the $(2\bar{1}1)_\beta$ spot of the twin lattice in (b). (d) An HRSTEM image showing an $\{332\}\langle 113\rangle\beta$ twin. Diffraction spots corresponding to the ω phase are also visible on the power spectra.

Fig. 8a reveals the nano-sized $\{112\}\langle 111\rangle\beta$ deformation twins, which were not visible in the optical microscopy investigation. A SADP along $[012]_\beta$T//$[012]_\beta$ M zone axis taken from the 625 °C sample confirms the occurrence of deformation twinning on the $\{112\}\langle 111\rangle\beta$ system (Fig. 8b), which is different from the system observed for the 700–725 °C samples. The size of the $\{112\}\langle 111\rangle\beta$ twins appeared herein much smaller than that of $\{332\}\langle 113\rangle\beta$ twins. Although $\{332\}\langle 113\rangle\beta$ deformation twinning in the 675 and 650 °C samples was not captured by TEM, it can be assumed based on similarity of morphology and size with the ones in Fig. 2a–c that the thick lines appearing in the inset of Fig. 3a are of $\{332\}\langle 113\rangle\beta$ twins. Furthermore, the BF image (Fig. 8d) indicates two variants of stress-induced α″ martensite. An associated SADP along the $[001]_\beta$//$[001]_{\alpha''}$ zone axis shows the diffraction spots corresponding to the orthorhombic structure (α″) in addition to strong bcc spots. The associated DF image confirms the presence of two variants of stress-induced α″ martensite (Fig. 8f). Deformation-induced ω also appeared under these processing conditions in the form of very thin parallel lines/lamellae (Fig. 9a and b). The associated SADP shows reflections corresponding to the β and ω phase (inset of Fig. 9a). Fig. 9c shows a BF image of deformed α phase in β phase. The corresponding SADP along the $[113]_\beta$ and $[01\bar{1}0]_\alpha$ zone axis is shown in Fig. 9d.

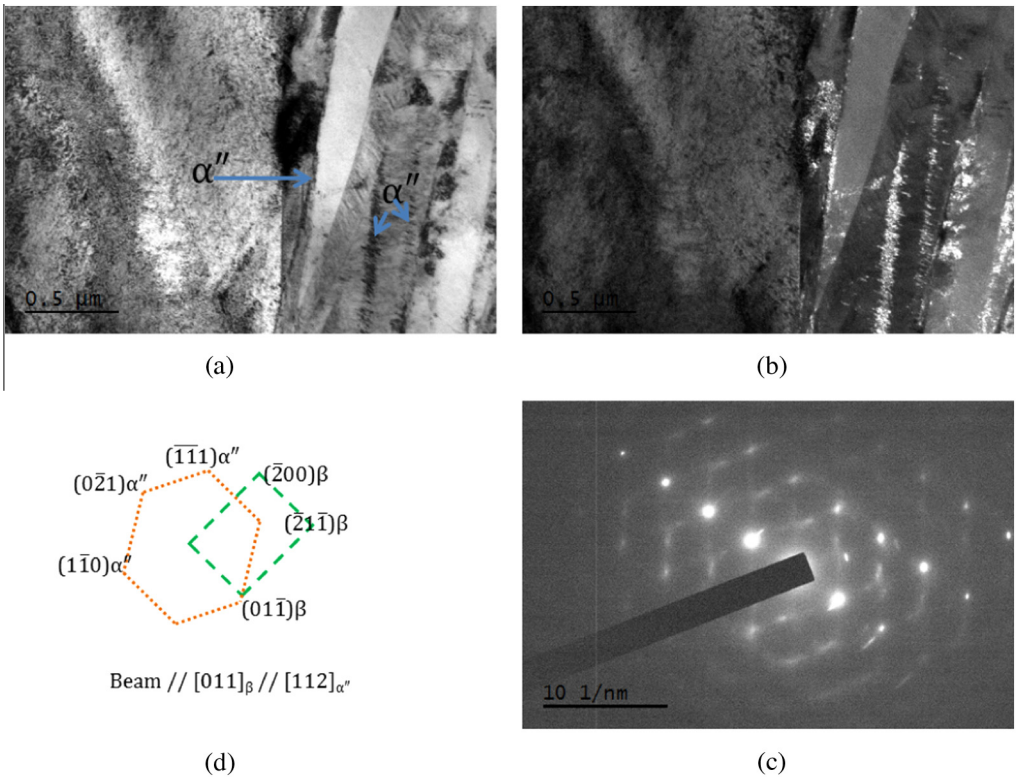

Fig. 6. Stress-induced α″ martensite formation: (a, b) BF and DF images of primary stress-induced α″ martensite, respectively, in the 725 °C sample. (c) A SADP along the $[0\,1\,1]_{\beta}//[1\,1\,2]_{\alpha''}$ zone axis taken from the region of Fig. 4(a). (d) A schematic of (c) showing the relation between the stress-induced α″ martensite and β phase.

Arrangements of dislocations including tangles were observed in the remaining deformed β matrix (Figs. 4b, 6a, 7a and 9c) in all the samples, which is an indication of slip activity. Similarly, deformation substructure is also visible in deformed α plates (Fig. 9c).

4. Discussion

4.1. Formation of stress-induced α″ martensite and corresponding triggering stress

Grosdidier et al. [1,20–22] reported that two factors independently govern the triggering stress for the formation of stress-induced martensite in metastable β Ti alloys. The factors are: (i) the stability of the β phase, i.e., the chemical composition of β phase, and (ii) β domain size (in our study it is defined as the remaining β surrounded by α before compression). These two aspects vary with the α phase fraction [24,25,28]. The authors of Refs. [24,25,28] reported that with an increasing amount of α, β phase becomes more stable while β domain size decreases. Both events oppose stress-induced α″ martensite formation, as chemically stable β tends to hinder β → α″ phase transformation and the accommodation of the shape changes associated with β → α″ phase transformation is more difficult with decreasing β domain size [1,20–22]. Additionally, decreasing parent domain size confines the number of available nucleation sites for martensite and also controls the interfacial energy of martensite, resulting in lower martensite start temperature, M_s [33]. Considering stress-induced α″ martensite, a lowering of M_s increases critical stress and requires greater mechanical work [1]. In the present study, β phase became enriched in β stabilizers (alternatively, the stability of the β phase increased) with increasing α fraction. For instance, EDS analysis (using STEM) indicates that the β phase in the 625 °C sample contains more β stabilizers (V, Fe) than in that of the 725 °C sample (Table 2). For the case of low volume of α, where α has precipitated mainly at the β grain boundaries, the actual β domain size is the prior β grain size minus the α size. But for the case where there is a high amount of α phase, and α has precipitated intragranularly, the β domain size will be much smaller. In the present study it is evident that the β domain size decreased with increasing α fraction (decreasing temperature in α + β phase field) (Fig. 3a–c). Consequently, the formation of stress-induced α″ martensite will be more difficult with increasing α fraction. Thus, higher triggering stress (180 MPa at 725 °C vs. 309 MPa at 625 °C) was required in the present study with higher α fraction. In the present study, the difference in triggering stress for 725 and 700 °C samples was small (~20 MPa) because of the minute difference in α phase resulting in a small difference in the β domain size and β stability. But the 675–625 °C samples show higher values and a larger difference of triggering stress (218 MPa vs. 309 MPa) needed to induce α″ martensite because the β phase was more stable in the 625 °C sample due to it having nearly twice the amount of α compared to that in the 675 °C sample, and because of the corresponding reduction in β domain size (Fig. 3a–c). On the other hand, the 500 °C sample did not show a β → α″ phase transformation. This is attributed to the fact that the amount of α fraction (62%) in the 500 °C sample crosses the barrier of 50%, at which the β → α″ martensitic trans-

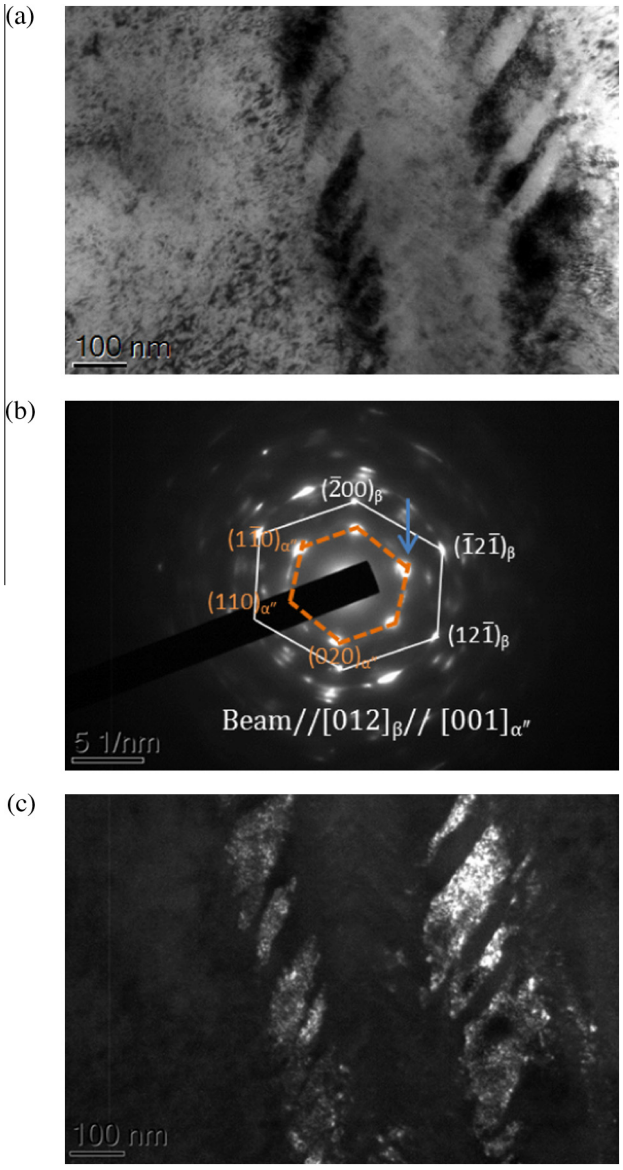

Fig. 7. Scondary α″: (a) BF image shows the secondary α″ martensite within the primary twins in the 725 °C sample. (b) A SADP along $[012]_\beta//[001]_{\alpha''}$ taken from Fig. 6(a). (c) DF image showing the secondary α″ using the spot indicated by an arrow in Fig. 6(b).

formation is impeded [24,25] and that the β domain size is much smaller than the ones in all other studied conditions.

Ishiyama et al. [34] mentioned that athermal ω also governs the β phase to stress-induced α″ martensite phase transformation. It was also reported that martensitic phase transformation appears to be impeded in alloys containing a large amount of athermal ω. In the present study, athermal ω particles were precipitated under all the conditions during water-quenching after α + β heat treatment (Fig. 4a), except for the 500 °C sample. Harmon and Troiano [35] mentioned that Al and other α stabilizers in β phase suppress athermal ω formation. In the present study, it has already been shown in Table 2 that β phase in a sample heat-treated at 625 °C has less Al content than in 725 °C. Therefore, the 625 and 725 °C heat-treated samples should contain the highest and lowest amounts of athermal ω particles. Thus, according to Ref. [34], the difficulty in formation of stress-induced α″ martensite will be maximum in the 625 °C sample and minimum in the 725 °C sample among the studied samples. However, despite having the lowest Al content in the 500 °C sample, no athermal ω was found because the β phase in the 500 °C sample became fully stable, causing the hindrance of such phase transformation.

Recently, Sun et al. [17] reported that concurrently activated primary twinning and stress-induced α″ require similar stresses for twinning and α″ formation. Such low stress (~180–200 MPa) for the 725 and 700 °C samples can be explained using the dislocation model introduced by Litvinov and Rusakov [36], where they proposed that a $\{3\,3\,2\}\langle 1\,1\,3\rangle\beta$ twin is formed by successive slip of partial dislocation $\pm a/22\langle 1\,1\,3\rangle$ in pairs on $\{3\,3\,2\}$ planes. The small value of the Burgers vector of $a/22\langle 1\,1\,3\rangle$ twinning dislocation produced from a grain boundary or from primary twins causes the low stress required for nucleation and growth of $\{3\,3\,2\}\langle 1\,1\,3\rangle\beta$ twins. In another study [14] by the same group, it was mentioned that the formation of $\{3\,3\,2\}\langle 1\,1\,3\rangle\beta$ twins is easier in metastable β phase and becomes more difficult with increasing the stability of the β phase. It is the metastability of β phase which is responsible for the low resistance to shifting plane $\{3\,3\,2\}$ in the $\langle 1\,1\,3\rangle$ direction and the reshuffling shifts of $\pm a/22$, on the other hand, would be hindered in a stable β phase because of its low toughness [14,36]. On the other hand, slip of $a/6\langle 1\,1\,1\rangle$ dislocation on a $\{1\,1\,2\}$ plane is responsible for the formation of $\{1\,1\,2\}\langle 1\,1\,1\rangle\beta$ twins [7]. The size of twinning displacement $(1/2\sqrt{2})$ is twice smaller for $\{3\,3\,2\}\langle 1\,1\,3\rangle\beta$ twins compared to $\{1\,1\,2\}\langle 1\,1\,1\rangle\beta$ ones. Thus the former is easier to form due to the lower stress required for their nucleation and growth. This is why the $\{3\,3\,2\}\langle 1\,1\,3\rangle\beta$ twinning system is dominant for those conditions experiencing lower triggering stress (725–700 °C samples) compared to conditions associated with the 625 °C sample. In conditions with intermediate triggering stresses (675–650 °C samples) both types of twins co-exist.

4.2. Stress-induced ω phase

Two types of stress-induced ω, one located inside the twins and one in the β matrix, were produced during compression. Fig. 4 shows an HRSTEM image containing ω inside the $\{3\,3\,2\}\langle 1\,1\,3\rangle\beta$ twins. Similar stress-induced ω phase with a single variant inside the twins was also found in Refs. [18,37,38]. The authors of Refs. [18,37,38] confirmed that such ω are induced by stress. Oka and Taniguchi [37] proposed that the instability of β phase with respect to ω phase facilitates the shuffling motion of the atoms in $\{3\,3\,2\}\langle 1\,1\,3\rangle\beta$ twinning. Due to such an instability, the shuffling in $\{3\,3\,2\}\langle 1\,1\,3\rangle\beta$ twinning may cause the formation of stress-induced ω. Takemoto et al. [38] reported that local relaxation happens through the atomic displacements along $\langle 1\,1\,1\rangle$ when the atomic shuffling occurs to form $\{3\,3\,2\}\langle 1\,1\,3\rangle\beta$ twinning, thus ω can be formed due to the displacements along $\langle 1\,1\,1\rangle$. The ω phase presence only inside the twin in β grain indicates that such relaxation predominantly takes place in the twin [38]. In the present study, we also obtained the typical orientation relationship between β and ω, which indicates that ω inside the primary twins formed due to the atomic displacements along $\langle 1\,1\,1\rangle$ during the twin formation (Fig. 4e) Dislocation stress fields could be another possible reason to form such ω phase.

On the other hand, deformation-induced ω lamellae in the β matrix of similar type to that observed in the current investigation has been observed to occur in Ti–12Mo [17], Mo-based [39] and Ta-based [40] alloys after severe plastic deformation. Similar to athermal ω phase, the formation mechanism of stress-induced ω involves the shuffle of atoms in {1 1 2} planes in the direction of ⟨1 1 1⟩ [39,40]. A dislocation mechanism was illustrated during atomic displacement of {1 1 2} planes along ⟨1 1 1⟩ direction [39,40]. The authors of Refs. [39,40] mentioned that glide of partial dislocations of type 1/3⟨1 1 1⟩, 1/6⟨1 1 1⟩ and 1/12⟨1 1 1⟩, which are dissociated from 1/2⟨1 1 1⟩ perfect dislocations, are responsible for such a transformation. Gysler et al. [41] mentioned that the ω disappears with increasing stability of the β phase as dislocation slip would be the active deformation mode therein. Accordingly, in our case stress-induced ω was found in the samples heat-treated in the temperature interval from 725 to 625 °C, but not in the 500 °C condition. Contrary to Ref. [17], which reported a disappearance of stress-induced ω after reaching 0.4 strain due to the shear band activity, in the present study such ω was still present because of either the absence of the shear bands or the difference in the stress state (tension/compression).

4.3. Deformation mechanism

As mentioned in Section 3, similarly to Ref. [17], some β grains undergo only twinning (thick laths) or stress-induced α″ martensite formation while other grains show a mixture of twinning and martensite formation, and some deform by slip only (Fig. 2c). This means that different β grains accommodate plastic deformation in different manners. Bernard et al. [42] reported that the preferential activation of a specific deformation mechanism in different β grains is dependent on the crystallographic orientation with respect to the direction of applied stress. The authors in Ref. [42] have also mentioned that grains with a minimum Schmid factor (SF) of 0.38 led to the activation of twinning. The origin of secondary twinning or of secondary α″ martensite in the primary twinning can be explained using the same orientation factor. As was mentioned in Ref. [17], primary twinning and stress-induced α″ martensite activated simultaneously during an early stage of straining result in a modified orientation factor. Secondary products such as secondary twinning or secondary α″ can be activated with further straining in the primary twins, depending on the modified orientation factor of the secondary twinning plane [14,17]. However, it is worth mentioning that only secondary α″ martensite was noticed inside the {3 3 2}⟨1 1 3⟩β twins in the present study. For the studied alloy, the correlation of the orientation of β grains with the deformation operating mechanism requires further investigation.

Both TRIP and TWIP effects were found in the present study for all the conditions, except the one heat-treated at 500 °C, which, as reported [17,31], may lead to the improvement of the plasticity of the alloy. This is the first time that the combination of TRIP and TWIP has appeared in metastable β Ti alloys containing α phase. In addition, limited examples have been found showing both TRIP and TWIP effects simultaneously in single β phase metastable β Ti alloys. The reason for the co-existence of twinning and stress-induced martensite in the microstructures can be explained using the phase stability diagram

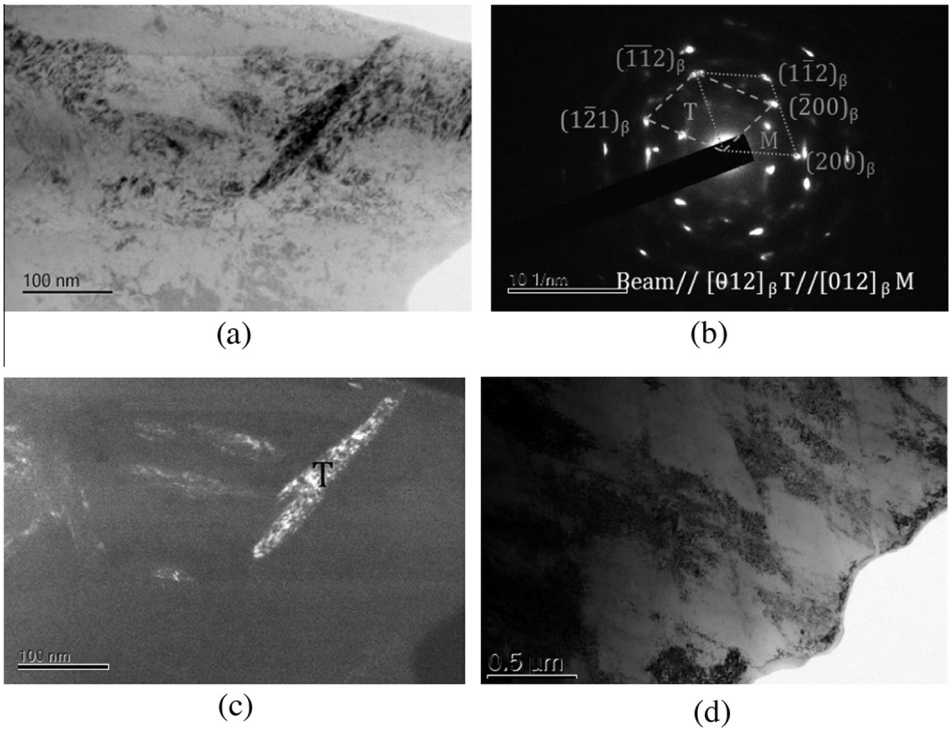

Fig. 8. (a) BF image of a nano-sized {1 1 2}⟨1 1 1⟩β twin in the 625 °C sample. (b) A SADP along the $[0\,1\,2]_\beta$ zone axis showing both the twin and matrix lattices. (c) DF image of the twin in (a) using the $(1\bar{2}1)_\beta$ spot of the twin lattice. (d) BF image showing two variants of stress-induced α″ martensite in the 625 °C sample. (e) A SADP of region (d) along $[0\,0\,1]_\beta$//$[0\,0\,1]_{\alpha''}$ showing the two variants of the α″. (f) A DF image associated with (d) and (e) with the two α″ variants shown in (e) illuminated using the spots circled in (e).

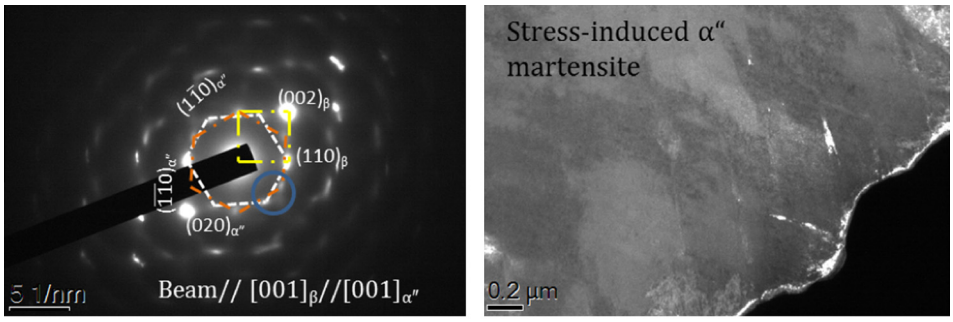

Fig 8. *(continued)*

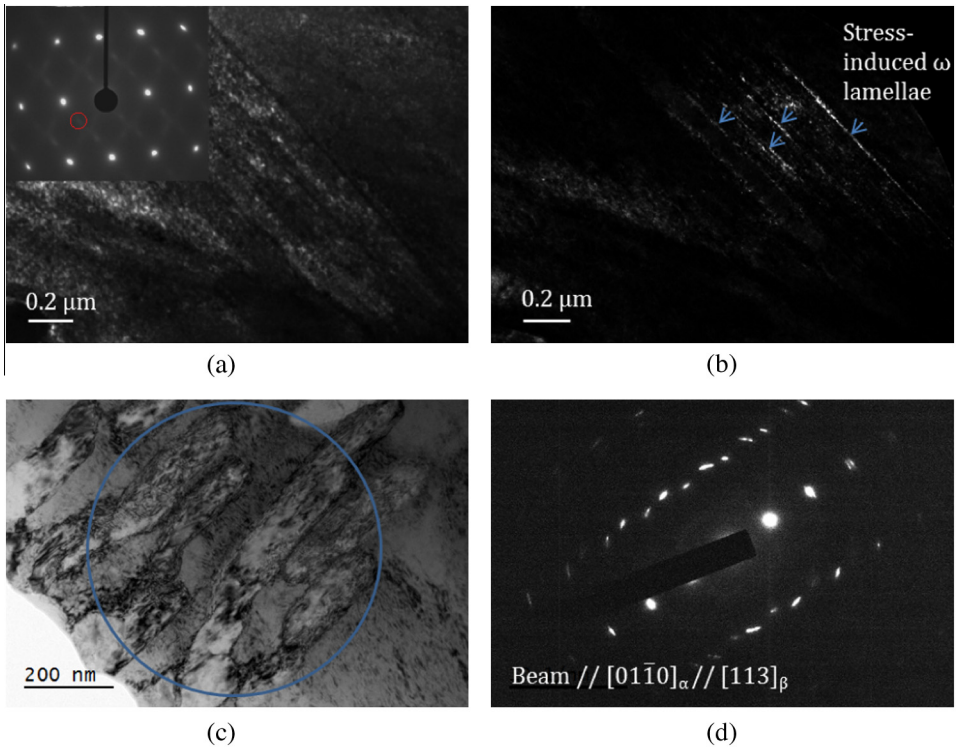

Fig. 9. (a) DF image of the stress-induced ω phase, where the inset shows the SADP displaying typical orientation relation between β and ω. (b) DF image showing the ω needles using the circled spot in inset of (a). (c) BF image showing the deformed α phase in β phase. (d) A SADP taken from the region circled in Fig. 8c.

Table 2. The composition of β phase in wt.%, $\overline{Md}$ and $\overline{Bo}$, and Mo equivalent for selected conditions.

Temperature (°C)	Al	V	Fe	Ti	$\overline{Md}$	$\overline{Bo}$	$Mo_{eq.}$
725	2.6 ± 0.2	11.6 ± 0.5	4.1 ± 0.2	Bal.	2.322	2.773	17.1
625	2.2 ± 0.3	13.1 ± 0.4	5.3 ± 0.3	Bal.	2.293	2.771	21.9
500	2.0 ± 0.1	16.2 ± 0.5	6.4 ± 0.2	Bal.	2.270	2.770	27.4

proposed by Morinaga et al. [43]. The authors of Ref. [43] discussed the stability of the different deformation mechanisms with respect to the electronic properties of the materials. The following equations were used to calculate the average metal d-orbital energy level ($\overline{Md}$) and bond order ($\overline{Bo}$) values in Ref. [43]:

$$\overline{Md} = \sum_{i=1}^{n} x_i (Md)_i$$

$$\overline{Bo} = \sum_{i=1}^{n} x_i (Bo)_i$$

Here, x_i is the atomic fraction of element i in the alloy and $(Md)_i$ and $(Bo)_i$ are the metal d-orbital energy level and Bond order values for element i, respectively.

The calculated values of $\overline{Bo}$ and $\overline{Md}$ for 725, 625 and 500 °C samples are presented in Table 2. It is evident that the $\overline{Md}$ value reduces from 2.32 to 2.27 for the 725 and

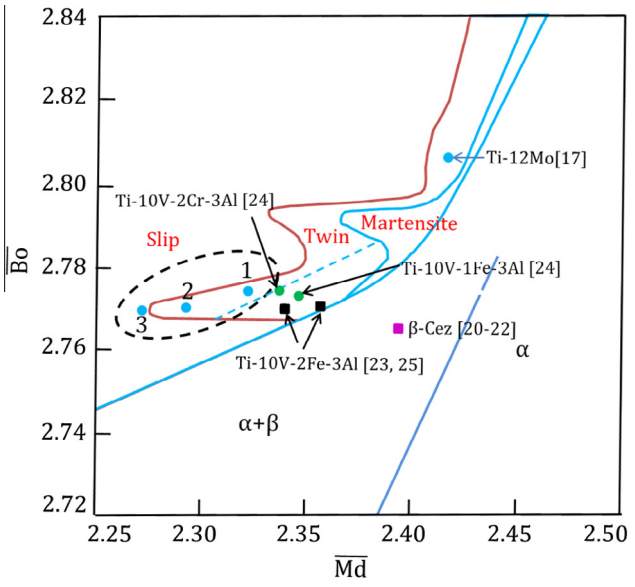

Fig. 10. The $\overline{Bo}$ vs. $\overline{Md}$ phase stability map adopted from Ref. [43]. The points 1, 2 and 3 correspond to the 725, 625 and 500 °C processed samples, respectively.

500 °C samples, respectively, with increasing the β stability (decreasing heat-treatment temperature, increasing α volume fraction), while $\overline{Bo}$ changes a little (2.774–2.771). The obtained three points were superimposed on Morinaga's $\overline{Bo}$ - $\overline{Md}$ map (Fig. 10). Two of the points corresponding to the 725 and 625 °C samples (indicated by 1 and 2) are located in the twinning region, whereas point 3 for the 500 °C sample is in the region designated for slip. It is important to mention that the twinning region of points 1 and 2 is surrounded by slip and α + β phase. Similarly to our results, Ti–12Mo also showed a combination of twinning and martensite formation in the microstructure after room temperature deformation [17,31]. Interestingly, Ti–12Mo is also located in the twinning region surrounded by martensite and slip regions in Morinaga's diagram, which indicates the possibility of their formation as well (Fig. 10). Based on this observation and our results, an expansion of the stress-induced martensite region on Morinaga's map could be suggested, especially in the lower part of the diagram. This proposal can be further supported by including some other experimental results, e.g., for Ti–10V–2Fe–3Al [23,25], Ti–10V–2Cr–3Al [24] and Ti–10V–1Fe–3Al [24] in the $\overline{Bo}$–$\overline{Md}$ map. According to the $\overline{Bo}$–$\overline{Md}$ phase stability diagram, Ti–10V–2Fe–3Al alloy positions on the intersection line of twinning and α + β phase. Further, points corresponding to Ti–10V–2Fe–3Al (with 30% of α), Ti–10V–2Cr–3Al and Ti–10V–1Fe–3Al lie within the twin region. In reality, all these conditions showed stress-induced α″ martensite in the microstructure after room temperature deformation [23–25,27,28]. The new boundary of the martensite region on the phase stability map will definitely lie in between the Ti–10V–2Cr–3Al point and the points for the studied Ti–10V–3Fe–3Al conditions. However, further study is needed to determine the exact border line of the extended stress-induced α″ martensite region.

On the other hand, with increase of Mo equivalent from ~17.1 to 21.9 corresponding to the 725 and 625 °C samples the twinning system changes from {3 3 2}⟨1 1 3⟩β to {1 1 2}⟨1 1 1⟩β while stress-induced ω and martensite transformations operate in the same manner. As in the investigation of Ref. [5], both twinning systems were found to co-exist in the intermediate conditions (675 and 650 °C samples) where the {3 3 2}⟨1 1 3⟩β twinning system was less dominant. Finally, when β phase becomes stable (Mo equivalent = 27.4 at 500 °C sample), deformation of β phase occurs only by slip. It appears that the deformation modes of the present system are similar to those of the gum metal series, although the Mo_{eq} value of the Ti–Nb–Ta–Zr–O system (~5.9) is much less than in the studied alloy. Furthermore, the same deformation features were found in Ti–12 Mo where the Mo_{eq} value is 12, which is also less than that for the studied alloy but higher than that for the gum metal system. This means that each alloy has a critical value of Mo_{eq} corresponding to the operation of all the deformation mechanisms and which is compositionally dependent. Above this critical Mo_{eq} the deformation occurs only by slip. In addition, with increasing the Mo_{eq} value e.g., the β phase stability, the operating deformation modes follow the sequence ({3 3 2}⟨1 1 3⟩β twinning + stress-induced martensite formation + slip → co-existence of both {3 3 2}⟨1 1 3⟩β and {1 1 2}⟨1 1 1⟩β types of twinning + stress-induced α″ martensite + slip → {1 1 2}⟨1 1 1⟩β twinning + stress-induced α″ martensite + slip → slip). As is shown in the present study, varying β phase composition via heat treatment results in changes of its characteristics and correspondingly in the operating deformation mechanisms.

5. Conclusions

- The stress–strain curve shows a stress plateau, which is attributed to the formation of twins and martensite in the samples heat-treated in the 725–625 °C range and containing 9–38% of α phase. The triggering stress to induce deformation products depends on the amount of α phase.
- The β phase of the sample treated at 725 °C possesses the highest metastability and, with lowering the temperature of heat treatment, the stability of β phase increases until it becomes stable in samples heat-treated at 500 °C. With increasing β phase stability $Mo_{eq.}$ increases and both the electronic parameters ($\overline{Bo}$and$\overline{Md}$) decrease.
- Deformation twinning has been observed for the first time in a metastable β Ti containing α phase. In addition, {3 3 2}⟨1 1 3⟩β deformation twinning along with primary and secondary α″, stress-induced ω were predominantly found to be additional to slip deformation mechanisms in the samples heat-treated at 725 and 700 °C (where the least amounts of α phase was present among the conditions studied).
- Two types of twinning were deemed to occur in the 675 and 650 °C samples with intermediate β stability. With further increases in β stability (625 °C), only {1 1 2}⟨1 1 1⟩β twinning operates along with stress-induced transformation products.
- Stress-induced ω phase was found to be present in all the samples exhibiting stress plateau phenomena. Further increase in stability of the β phase suppresses twinning and stress-induced phase transformations for the sample treated at 500 °C, which is reflected in the corresponding stress–strain curve.

- A modification of Morinaga's phase stability map has been proposed based on the findings of the present study and other results reported in the literature.

Acknowledgements

The authors thank Mr Andrew Scobie, UOW for machining the samples. This research used equipment funded by the Australian Research Council (LE120100104 and LE0237478), which is located at the UOW Electron Microscopy Centre.

References

[1] T. Grosdidier, Y. Combres, E. Gautier, M.J. Philippe, Metall. Mater. Trans. A 31 (2000) 1095.
[2] J.R. Patel, M. Cohen, Acta Metall. 1 (1953) 531.
[3] G.B. Olson, M. Cohen, Metall. Trans. A 13 (1982) 1907.
[4] V.F. Zackay, E.R. Parker, D. Farh, R. Bush, Trans. ASM 60 (1967) 252.
[5] Y. Yang, S.Q. Wu, G.P. Li, Y.L. Li, Y.F. Lu, K. Yang, et al., Acta Mater. 58 (2010) 2778.
[6] T. Saito, T. Furuta, J.-H. Hwang, S. Kuramoto, K. Nishino, N. Suzuki, et al., Science 300 (2003) 464.
[7] Y. Yang, G.P. Li, H. Wang, S.Q. Wu, L.C. Zhang, Y.L. Li, et al., Scr. Mater. 66 (2012) 211.
[8] Y. Yang, G.P. Li, G.M. Cheng, Y.L. Li, K. Yang, Appl. Phys. Lett. 94 (2009) 061901-1.
[9] T. Furuta, S. Kuramoto, J.H. Hwang, K. Nishino, T. Saito, Mater. Trans. 46 (2005) 3001.
[10] S. Kuramoto, T. Furuta, J. Hwang, K. Nishino, T. Saito, J. Jpn. Inst. Met. Mater. 69 (2005) 953.
[11] R.J. Talling, R.J. Dashwood, M. Jackson, D. Dye, Acta Mater. 57 (2009) 1188.
[12] R.J. Talling, R.J. Dashwood, M. Jackson, S. Kuramoto, D. Dye, Scr. Mater. 59 (2008) 669.
[13] H. Xing, J. Sun, Q. Yao, W.Y. Guo, R. Chen, Appl. Phys. Lett. 92 (2008) 151905-1.
[14] G.M. Rusakov, A.V. Litvinov, V.S. Litvinov, Met. Sci. Heat Treat. 48 (2006) 244.
[15] S. Hanada, O. Izumi, Metall. Trans. A 17 (1986) 1409.
[16] S. Hanada, O. Izumi, Metall. Trans. A 18 (1987) 265.
[17] F. Sun, J.Y. Zhang, M. Marteleur, T. Gloriant, P. Vermaut, D. Laillé, et al., Acta Mater. 61 (2013) 6406.
[18] T. Furuhara, K. Kishimoto, T. Maki, Mater. Trans. JIM 35 (1994) 843.
[19] T. Furuhara, H. Nakamori, T. Maki, Mater. Trans. JIM 33 (1992) 585.
[20] T. Grosdidier, C. Roubaud, M.-J. Philippe, Y. Combres, Scr. Mater. 36 (1997) 21.
[21] T. Grosdidier, M.J. Philippe, Mater. Sci. Eng. A 291 (2000) 218.
[22] T. Grosdidier, C. Roubaud, M.-J. Philippe, S. Zaefferer, M. Zandona, E. Gautier, Y. Combres, J. Phys. IV France 06 (1996) C1-435–C431-444.
[23] T.W. Duerig, J. Albrecht, D. Richter, P. Fischer, Acta Metall. 30 (1982) 2161.
[24] C. Li, J.H. Chen, X. Wu, W. Wang, S. van der Zwaag, J. Mater. Sci. 47 (2012) 4093.
[25] C. Li, X. Wu, J.H. Chen, S. van der Zwaag, Mater. Sci. Eng. A 528 (2011) 5854.
[26] S. Neelakantan, P.E.J. Rivera-Díaz-del-Castillo, S. van der Zwaag, Scr. Mater. 60 (2009) 611.
[27] S. Neelakantan, P.E.J. Rivera-Díaz-del-Castillo, S. Van Der Zwaag, Adv. Mater. Res. 89–91 (2010) 405.
[28] S. Neelakantan, D. San Martin, P.E.J. Rivera-Díaz-del-Castillo, S. van der Zwaag, Mater. Sci. Technol. 25 (2009) 1351.
[29] C. Li, J.H. Chen, X. Wu, S. van der Zwaag, Mater. Sci. Eng. A 573 (2013) 111.
[30] D. Savvakin, A. Carman, O. Ivasishin, M. Matviychuk, A. Gazder, E. Pereloma, Metall. Mater. Trans. A 43 (2012) 716.
[31] M. Marteleur, F. Sun, T. Gloriant, P. Vermaut, P.J. Jacques, F. Prima, Scr. Mater. 66 (2012) 749.
[32] M. Ahmed, D.G. Savvakin, O.M. Ivasishin, E.V. Pereloma, Mater. Sci. Eng. A 605 (2014) 89.
[33] J. Wang, S. Van Der Zwaag, Metall. Mater. Trans. A 32 (2001) 1527.
[34] S. Ishiyama, S. Hanada, O. Izumi, ISIJ Int. 31 (1991) 807.
[35] E.L. Harmon, A.R. Troiano, Trans. ASM 53 (1961) 43.
[36] V.S. Litvinov, G.M. Rusakov, Phys. Met. Metallogr. 90 (2000) 96.
[37] M. Oka, Y. Taniguchi, J. Jpn. Inst. Met. 42 (1978) 814.
[38] Y. Takemoto, M. Hida, A. Sakakibara, J. Jpn. Inst. Met. 57 (1993) 1471.
[39] G.M. Cheng, H. Yuan, W.W. Jian, W.Z. Xu, P.C. Millett, Y.T. Zhu, Scr. Mater. 68 (2013) 130.
[40] L.M. Hsiung, D.H. Lassila, Acta Mater. 48 (2000) 4851.
[41] A. Gysler, G. Lütjering, V. Gerold, Acta Metall. 22 (1974) 901.
[42] E. Bertrand, P. Castany, I. Péron, T. Gloriant, Scr. Mater. 64 (2011) 1110.
[43] M. Morinaga, N. Yukawa, T. Maya, K. Sone, H. Adachi, Theoretical design of titanium alloys, in: presented at the Sixth World Conference on Titanium Alloys, Cannes, 1988.

Chapter 8

Synopsis and Future Work

This study investigates the evolution of microstructure and mechanical properties of BEPM-processed Ti-55511, Ti-55521 alloys after thermo-mechanical processing and ageing. Further, the deformation mechanisms of BEPM processed Ti-1033 alloy are interpreted and discussed. This chapter outlines the general conclusions and the most significant contributions to the original knowledge. Additionally, possible future research directions are proposed.

8.1. Conclusions

The following effects of the TMP processing parameters on the microstructure of Ti-55511 and Ti-55521 near β Ti-alloys were observed:

- Deformation in the β region resulted in reduction of both porosity and β grain size.
- Deformation in the α + β phase field led to fragmentation of grain boundary α. Higher amounts of deformation (60 vs 40%) intensified the fragmentation resulting in globular-shaped α. Simultaneously, the remained β phase was deformed resulting in the increase in dislocation density.
- Cooling rates (10 Ks^{-1} vs 1 Ks^{-1}) after deformation affect α phase formation. More α lamellae were obtained when the samples were cooled slowly. Recrystallisation of deformed β occurred under both cooling conditions but was more pronounced in the sample cooled at 1 Ks^{-1}. Additionally, a larger α crystallite size was found in samples cooled at 1Ks^{-1}. This was attributed to the annihilation of dislocations and the formation of dislocation cell structures.

During heat treatment in the α+β phase field in TMP schedules, β to α phase transformation occurred by means of diffusion. However, during the accelerated cooling at 10 Ks^{-1} from high temperature athermal phases have formed. Coupling aberration-corrected STEM analysis and atom probe tomography allowed elucidation of compositional changes and phase transformation events at an atomic scale. Nano-sized α nuclei are believed to have nucleated at dislocations in the β matrix. Athermal spheroidal- shaped ω particles of size ~3 nm were found to be uniformly distributed in the β matrix. Simultaneously, α nuclei associated with ω super cells have also been found, which indicates the possibility of α nucleation at the ω/β interface and/or inside the ω. The formation mechanism of observed ω was concluded to be via simple atomic displacement along $<111>_{\beta}$ direction. , Both Z-contrast imaging and APT could not reveal

any corresponding compositional difference within the parent phase. Moreover, APT showed compositional fluctuations (Mo-rich and Mo-lean regions) in β phase in the TMP condition.

In order to improve the mechanical properties by completing the typical processing schedule for near-β Ti alloys, ageing was performed at 650 °C with slow heating (0.25 Ks^{-1}) to the ageing temperature. The following microstructural changes did occur during ageing:

- At the initial stage (120 s) of ageing, partially transformed ω super cells were observed both individually and in connection with an α motif, which means two concurrent events: the remaining ω particles carried over from TMP grow and then act as nucleation sites for α; the slow heating up to a certain temperature (~400 °C) induced ω which also can act as nucleation sites for α. However, during further heating and holding at 650 °C the concurrent process of ω dissolution takes place. APT did not reveal any compositional fluctuations in β phase at early stage of ageing. Hence, it was claimed that α forms at this stage preferentially at β/ω interfaces or remaining dislocations. Associated composition differences between β and newly formed α were only slight and consistent with a mixed displacive-diffusional transformation mechanism. With increasing ageing time the volume fraction of α phase increases. The growth of α particles was predominantly responsible for this after 3.6 ks of ageing.

Elemental partitioning between α and β phases took place during TMP and ageing at 650°C. The α phase grew via a diffusional mechanism, as evidenced by the fact that late stage growth, characterised by coarser α, resulted in pronounced increased in solute stabilisation of the β phase. Whereas Fe has fastest diffusivity in both phases, Mo and V have the lowest diffusion rates in β and α phase, respectively. The composition of α also depends at which stage of processing it was formed and what the composition of the parent β phase was at that moment. Mo (and sometimes V) pile-up at the α/β interface was noticed after TMP and at the early stage of ageing, and this pile-up diminished with increased ageing.

Mechanical properties of the TMP and aged samples were found to be dependent on the α volume fraction, such that strength increases while ductility reduces with increase of α phase amount. However, ageing of the TMP samples resulted in significant improvements in mechanical properties. This can be attributed to ω- assisted α phase nucleation where processing (slow heating to ageing temperature and accelerated cooling from high temperature) plays a vital role to induce ω phase formation. Three stages of work hardening behavior are found. Stage I corresponds to the plastic deformation of β phase through gliding of dislocations to work harden the β phase. Stage II corresponds to the elastic deformation of α phase and Stage III indicates the plastic deformation of α phase.

The Cr content was found to govern the β to α phase transformation. For instance, isothermal holding in α + β phase field during TMP and ageing returned a slightly higher amount of α in the case of Ti-55511 than that of Ti-55521 alloy. Such a lagging in α phase formation in Ti-55521 alloy is attributed to the presence of more stable retained β phase in the α+β phase region as the additional 1% Cr content reduces the β-transus temperature. Consequently, different mechanical properties are reflected in the different compositions, i.e., Ti-55511 gained slightly higher strength and lower ductility compared to Ti-55521.

The deformation behaviour of Ti-1033 alloy was evaluated by varying β phase stability. With the least stable β phase (samples heat-treated at 725°C (Moeq=17.1, Md=2.322, Bo = 2.773) and 700 °C), {332}⟨113⟩β deformation twinning along with primary and secondary stress-induced α″ martensite, as well as stress-induced ω, were found to be the deformation mechanisms in addition to slip. With increasing the β stability by inducing more α in the samples heat-treated at 675 – 650 °C the co-existence of both twinning system were found. At 625 °C (Mo eq=21.9, Bo=2.771, Md=2.293 for) it was found that the deformation mode shows only {112}⟨111⟩β twinning, while the mechanisms of slip, stress induced α" and stress-induced ω remain operational. Finally, deformation of the sample (heat-treated at 500 °C, Moeq=27.4, Md=2.270, Bo= 2.770) with a maximum β stability occurs only by slip.

8.2. Contributions to original knowledge

In order to assess the microstructure-mechanical properties relationship and room temperature deformation mechanism of near-β Ti alloys (Ti-55511, Ti-55521 and Ti-1033) manufactured by the cost effective BEPM method, different experimental techniques have been applied. The original contributions of this study are stated as follows:

- This is one of the first studies to characterise both qualitatively and quantitatively the microstructural and compositional changes which occurred after each step of thermo-mechanical processing of near-β Ti alloys (Ti-55511 and Ti-55521). The influence of Cr content on the β → α phase transformation is described.
- This is one of the first studies on Ti alloys that discusses the effects of cooling rates during thermo-mechanical processing on microstructural evolution and mechanical properties. X-ray line profile analysis with Rietveld fitting was performed to observe the effect of cooling rates on the microstructural features e.g. domain size, dislocation density etc. Mechanical properties were correlated with the cooling rates. Work hardening behaviour of Ti alloy was evaluated using the modified Crussard–Jaoul model.
- The present study is one of first studies on Ti alloys that describes the influence of single-step high temperature ageing on mechanical properties. For the first time, Rietveld analysis was applied to characterise the microstructural changes which occurred over the ageing period. Compositional changes were monitored to understand the mechanism of newly formed α phase. Comparison of results with those in existing literature revealed that obtained properties of these powder Ti alloys are comparable to those of wrought materials.
- This is one of the first studies to characterise the aged microstructures of the novel powder Ti-55521 alloy through application of state-of-the art techniques of aberration corrected STEM and APT. For the first time, nanosized athermal ω phase was reported to be adjacent to the α nucleus, which is consistent with the assumption of possible nucleation at the ω/β interface. APT observations revealed the build-up of slow diffusing elements, such as Mo and V, near the α/β interface in the β phase.
- This is one of the first studies where deformation mechanism of metastable β Ti alloy containing α phase has been evaluated with respect to the stability of the matrix phase. This is the first study to show the simultaneous operation of different deformation mechanisms including stress-induced twinning and stress-induced phase transformation in metastable β Ti alloys containing α phase. The latter one produced two products: ω and martensite. It is also highlighted that the co-existence of both

twinning and thereafter change in twinning system does occur with increasing the β stability. A modification/expansion of the existing Bo-Md diagram proposed by Morinaga *et al.* [1], used to design the new Ti based alloys, has been suggested.

- The importance of the findings of the present study is the further advance of the knowledge of physical metallurgy of Ti products made using powder metallurgy. Based on the findings of the present study, the fundamental science of near β titanium alloys produced via powder metallurgy technique appears to be similar to that of Ti alloys manufactured through conventional ingot metallurgy.

8.3. Future Work

In the present study, spectral/peak overlaps (e.g. Ti and V, V and Cr) in SEM-EDS were a common problem, which occurs when emission lines from two different elements share the same energy. This leads to ambiguity and misidentification of elements in the system. The energy resolution (the degree of sharpness) of Wavelength Dispersive Spectrometry (WDS) is superior to EDS by a factor of 30, leading to improved peak separation [2]. Other problems arise when attempting to measure low concentrations of elements using EDS in a sample. WDS is also able to process higher numbers of X-ray events than EDS, leading to a greater sensitivity in this instance. Thus the use of WDS is suggested to measure the composition.

The ageing temperature (650 °C) in the present study was too high to clearly observe the $\beta \rightarrow \omega \rightarrow \alpha$ phase transformation during slow heating to ageing temperature. Therefore, a low temperature ageing (at ~450 °C) with interrupted at lower temperatures heating in order to monitor the process is recommended for detection and detailed characterisation of the aforementioned phase transformation. In order to obtain better results, Focused Ion Beam (FIB) can be used to prepare the sample used in APT and STEM.

In Chapter 6, deformation in β phase field (850 °C) was used to close the residual porosity carried over from the as-sintered sample. It may have effect on the deformation mechanisms during room temperature deformation because it may change the crystallographic orientation of β grains [3]. So, it is suggested to investigate the deformation mechanisms in 1033 alloy without such prior deformation at 850 °C and compare the results with the present study.

In the present study, there was a small difference in lattice parameters of α and stress-induced α" martensite (Chapter 7) which creates problem to calculate the changes in volume fraction of stress-induced α" martensite with increasing the β stability/α phase fraction. Thus, synchrotron diffraction can be used instead of XRD to solve the problem.

Since it is mentioned in [4] that the occurrence of the both deformation twinning and stress-induced martensite improves the mechanical properties of the materials, especially their plasticity, so it is recommended to perform tensile test to observe the effect in the case of studied alloy. In order for this, three of the representative conditions heat treated at 725, 625 and 500 °C can be tested. Additionally, tensile tests undertaken on these samples with the same strain and strain rate parameters used in compression will provide insight into effect of the stress state on the operation of deformation mechanisms in the metastable β.

References

[1] M. Morinaga, N. Yukawa, T. Maya, K. Sone, and H. Adachi, "Theoritical Design of Titanium alloys," presented at the Sixth world conference on Titanium alloys, Cannes, France, 1988.

[2] J. Goldstein, *Scanning Electron Microscopy and X-ray Microanalysis: Third Edition*: Springer US, 2003.

[3] E. Bertrand, P. Castany, I. Péron, and T. Gloriant, Twinning system selection in a metastable β-titanium alloy by Schmid factor analysis, Scripta Materialia*,* 64 (2011) 1110-1113.

[4] F. Sun, J. Y. Zhang, M. Marteleur, T. Gloriant, P. Vermaut, D. Laillé, P. Castany, C. Curfs, P. J. Jacques, and F. Prima, Investigation of early stage deformation mechanisms in a metastable β titanium alloy showing combined twinning-induced plasticity and transformation-induced plasticity effects, Acta Materialia*,* 61 (2013) 6406-6417.